Multiscale Characterization of Anisotropic Rocks with Emphasis on Phyllite and Shale from the Lesser Himalaya, Uttarakhand, India

Thesis submitted in partial fulfilment

For the Award of a Degree

Doctor of Philosophy

By

DIVYANSHOO SINGH

RAJIV GANDHI INSTITUTE OF PETROLEUM TECHNOLOGY

JAIS, AMETHI, INDIA- 229304

21PE0005 2026

CERTIFICATE

It is certified that the work contained in the thesis titled "***Multiscale Characterization of Anisotropic Rocks with Emphasis on Phyllite and Shale from the Lesser Himalaya, Uttarakhand, India***" by "***Divyanshoo Singh***" has been carried out under my supervision and that this work has not been submitted elsewhere for a degree.

It is further certified that the student has fulfilled all the requirements of Comprehensive, Candidacy, and SOTA.

Dr. Hemant Kumar Singh
Thesis Supervisor
Rajiv Gandhi Institute of Petroleum Technology,
Jais, Amethi, Uttar Pradesh, India

DECLARATION BY THE CANDIDATE

I, ***Divyanshoo Singh***, certify that the work embodied in this thesis is my own bona fide work and carried out by me under the supervision of ***Dr. Hemant Kumar Singh*** from *2021* to *2026*, at the Department of Petroleum Engineering & Geoengineering, Rajiv Gandhi Institute of Petroleum Technology, Jais, Amethi, Uttar Pradesh, India (229304). The matter embodied in this thesis has not been submitted for the award of any other degree. I declare that I have faithfully acknowledged and given credit to the research workers wherever their works have been cited in my work in this thesis. I further declare that I have not wilfully copied any other's work, paragraphs, text, data, results, *etc.,* reported in journals, books, magazines, reports, dissertations, thesis, *etc.,* or available at websites, and have not included them in this thesis and have not cited them as my own work.

Date:
Place: Jais, Amethi

Divyanshoo Singh
Roll No: 21PE0005

CERTIFICATE BY THE SUPERVISOR

It is certified that the given declaration by the student is correct to the best of my knowledge.

Dr. Hemant Kumar Singh
Thesis Supervisor

Head of Department (HoD)
Department of PEGE

CERTIFICATE

CERTIFIED that the work contained in the thesis titled "**Multiscale Characterization of Anisotropic Rocks with Emphasis on Phyllite and Shale from the Lesser Himalaya, Uttarakhand, India**" by **Mr. Divyanshoo Singh** has been carried out under my supervision. It is also certified that he fulfilled the mandatory requirement of TWO quality publications arose out of his thesis work.

It is further certified that the two publications (copies enclosed) of the aforesaid **Mr. Divyanshoo Singh** have been published in the Journals indexed by -
(a) SCI
(b) SCI Extended
(c) SCOPUS
(d) Emerging SCI

Dr. Hemant Kumar Singh
Thesis Supervisor

Convenor, DPGC
Department of PEGE

COPYRIGHT TRANSFER CERTIFICATE

Title of the Thesis: **Multiscale Characterization of Anisotropic Rocks with Emphasis on Phyllite and Shale from the Lesser Himalaya, Uttarakhand, India**

Name of the Student: **Divyanshoo Singh**

Copyright Transfer

The undersigned hereby assigns to the Rajiv Gandhi Institute of Petroleum Technology, Jais, all rights under copyright that may exist in and for the above thesis submitted for the award of the "Doctor of Philosophy".

Date: **Divyanshoo Singh**
Place: **Jais, Amethi** Roll No: **21PE0005**

Note: However, the author may reproduce or authorize others to reproduce material extracted verbatim from the thesis or derivative of the thesis for author's personal use provided that the source and the Institute's copyright notice are indicated.

Dedicated To

My Beloved

Parents

For their endless love, support, and encouragement

&

In the Loving Memories

of

बाबा, दादी, और बड़े पापा

Acknowledgements

First and foremost, I express my heartfelt gratitude to the Almighty God for the grace and blessings that have strengthened my determination to pursue my academic journey.

I would like to express my deepest gratitude to my supervisor, **Dr. Hemant Kumar Singh**, for his exceptional guidance, unwavering support, and profound mentorship throughout my doctoral journey. His expertise, dedication, and encouragement have been the cornerstone of my academic progress and research endeavours. Without his persistent support, valuable suggestions, and insightful guidance, the completion of this thesis would not have been possible.

I extend my thanks to the Honourable Director, **Prof. Harish Hirani**, for providing the necessary research facilities at RGIPT. I also wish to express my appreciation to **Prof. Tushar Sharma**, Head of the Department, Petroleum Engineering and Geoengineering, for his excellent motivation and encouragement during my research work. My sincere thanks go to the members of the research progress evaluation committee (RPEC) and the comprehensive examination committee, **Dr. Piyush Sarkar, Dr. Gobinda Rakshit**, and **Dr. Siddhant Prasad**, for their valuable direction, wisdom, and moral support throughout my research.

I am grateful to the anonymous reviewers, chief editors, and associate editors of various journals for their valuable suggestions and reviews, which helped improve the quality of my published research articles included as part of this thesis. Special thanks to **Prof. Vikram Vishal** from IIT Bombay, **Prof. Deepak Amban Mishra** from IIPE Visakhapatnam, **Prof. Khairul Azlan Mustapha** from University of Malaya, **Dr. Rakesh Kumar** from IIT Kharagpur, **Dr. Alok Kumar** from IIT (ISM) Dhanbad, and **Dr. Bikash Kumar Ram** from NTPC Limited, for their research collaboration and continuous support.

I appreciate the help and cooperation of my lab mate, **Mr. Kumar Nilankar,** and all the other Research Scholars at RGIPT. I also extend my gratitude to all others who have supported me but are not mentioned here.

My heartfelt gratitude goes to my Parents, who have been a constant source of inspiration. I would never have been able to accomplish this work without their blessings.

I also gratefully acknowledge the Department of Science and Technology (DST), Govt. of India, New Delhi, for the financial support (DST Inspire Fellowship: **IF190992**) provided for my research.

Finally, I express my sincere thanks to the **reviewers** for their detailed and constructive comments, which have improved the quality and readability of my PhD Thesis.

Divyanshoo Singh

Contents

Acknowledgements ..... **xi**

Contents ..... **xiii**

List of Figures ..... **xix**

List of Tables ..... **xxvii**

List of Abbreviations and Symbols ..... **xxix**

Preface ..... **xxxiii**

Chapter: 1 Introduction **1**

1.1. Definition of the Problem 1

1.2. Importance/Significance of the Himalaya 4

1.3. Research Gap 10

1.4. Research Objectives 11

Chapter: 2 Selection and Collection of Rock Samples **13**

2.1. Chandpur Phyllite from the Srinagar area, Uttarakhand 13

2.2. Krol Shale from the Kaudiyala area, Uttarakhand 16

Chapter: 3 Multiscale Weathering-grade Classification of Chandpur Phyllite: Insights from *In situ* Observation and Laboratory Investigation **19**

3.1. Introduction 19

3.2. Methodology 22

3.2.1. In situ classification of Weathering-grades 25

3.2.2. Laboratory Investigations of In situ Categorized Weathered Samples 25

3.3. Results 29

3.3.1. Stage 1: In situ Weathering-grade Classification 29

3.3.2. Stage 2: Validation of In situ Weathering-grades using Multiscale Analysis 30

3.4. Discussions 42

3.4.1. Quantitative Investigation 42

3.4.2. Qualitative Interpretation 47
3.5. Summary 55
Chapter: 4 Impact of Water Saturation on Physico-mechanical Properties of Chandpur Phyllite at Varying Foliation Angles.....57
4.1. Introduction 57
4.2. Methodology 61
4.2.1. Specimen Preparation.....61
4.2.2. Experimental Test and Procedures 63
4.3. Results 65
4.3.1. XRD characteristics and FE-SEM analysis of the Chandpur Phyllite 65
4.3.2. Variation in Ultrasonic P-wave Velocities with Foliation Angle.....67
4.3.3. Strength and Deformation Behavior with Foliation Angle 69
4.3.4. Rock Failure Modes under UCS and BTS at Different Foliation Angles 71
4.3.5. Brittleness Index, Elastic Modulus, and Proneness to Rockburst 73
4.4. Comparison of the Present Study with Existing Literature.....75
4.5. Discussions.....77
4.6. Summary 82
Chapter: 5 Influence of Specimen Geometry on the Point Load Strength Anisotropy of Phyllite.....85
5.1. Introduction 85
5.2. Methodology 89
5.2.1. Preparation of the Test Specimens 89
5.2.2. PLI test 91
5.2.3. Mathematical analyses 91
5.3. Results 93
5.3.1. Characterization of Phyllite.....93
5.3.2. Effect of t/d ratios on Axial PLI test.....95
5.3.3. Rock Failure Modes with varying β and t/d ratios 96

5.3.4. Student's t-test and F-test 101

5.4. Discussions 103

5.4.1. Generalized Empirical Relation between t/d ratio and β 107

5.5. Summary 109

Chapter: 6 Multiscale Mechanical Characterization of Krol Shale using Brazilian Tensile Strength and Nano-indentation Tests: Implications in Hydrocarbon Recovery and CO_2 Sequestration 111

6.1. Introduction 111

6.2. Sample Preparation and Nature of Krol Shale 115

6.2.1. Sample Preparation 115

6.2.2. Nature of the Krol Shale 116

6.3. Laboratory investigation 120

6.3.1. Brazilian Tensile Strength (BTS) Test 120

6.3.2. Nano-indentation Test 121

6.3.3. AFM analysis 123

6.4. Results and Discussions 124

6.4.1. Macroscale Mechanical Characteristics using the BTS Test 124

6.4.2. Microscale Mechanical Characteristics using Nano-indentation Test 128

6.4.3. Determination of Multiscale Brittleness Index (BI) based on Load vs. Displacement Curve 137

6.4.4. Surface Heterogeneity using AFM 140

6.5. Integration of Multiscale Elastic Modulus and Brittleness Index 143

6.6. Summary 147

Chapter: 7 Pore System Characterization of Untapped Krol Shale Using an Integrated Multi-analytical Approach: Bridging Nano-to Macro Scale Investigation 149

7.1. Introduction 149

7.2. Methodology 152

7.2.1. Sample Preparation.....153
7.2.2. LPGA analysis.....153
7.2.3. SAXS analysis.....155
7.2.4. FE-SEM analysis.....155
7.2.5. Micro-CT Tomography analysis.....158
7.3. Results.....159
7.3.1. Source Rock Characteristics/Nature and Paleoenvironment.....159
7.3.2. LPGA analysis.....162
7.3.3. SAXS analysis.....166
7.3.4. FE-SEM analysis.....168
7.3.5. Micro-CT analysis.....174
7.4. Discussions.....177
7.4.1. Pore System and its Connectivity in the Krol Shale.....177
7.4.2. Comparison between Lesser Himalayan Krol Shale and other Explored Shale Basins.....182
7.4.3. Implications of this Study for Enhanced Gas Recovery with CO2 Sequestration.....184
7.5. Summary.....185
Chapter: 8 Multiscale Characterization of Pore Evolution in Lesser Himalayan Black Shale from Krol Formation under Oxic Thermal Heating: Relevance to Untapped Shale Gas Extraction.....187
8.1. Introduction.....187
8.2. Experimental Procedures.....192
8.2.1. Sample Preparation.....192
8.2.2. Shale Petrography.....193
8.2.3. LPGA analysis.....193
8.2.4. SAXS analysis.....194
8.2.5. FE-SEM analysis.....195

8.2.6. TGA analysis 195
8.2.7. X-ray diffraction (XRD) 196
8.3. Results 197
8.3.1. Petrographic Characterization and TOC analysis 197
8.3.2. TGA analysis 199
8.3.3. XRD analysis 200
8.3.4. FE-SEM analysis 201
8.3.5. N2-LPGA analysis 204
8.3.6. SAXS analysis 208
8.4. Discussions 211
8.4.1. Compositional Variation with Combustion 212
8.4.2. Morphological Variation with Combustion 213
8.4.3. Pore Structural Evolution with Combustion 216
8.5. Summary 220
Chapter: 9 Conclusions and Future Scope 223
9.1. Conclusions 223
9.1.1. Multiscale Weathering-grade Classification of Chandpur Phyllite: Insights from In situ Observation and Laboratory Investigation 223
9.1.2. Impact of Water Saturation on Physico-mechanical Properties of Chandpur Phyllite at Varying Foliation Angles 225
9.1.3. Influence of Specimen Geometry on the Point Load Strength Anisotropy of Phyllite 226
9.1.4. Multiscale Mechanical Characterization of Krol Shale using Brazilian Tensile Strength and Nano-indentation Tests: Implications in Hydrocarbon Recovery and CO_2 Sequestration 227
9.1.5. Pore System Characterization of Untapped Krol Shale Using an Integrated Multi-analytical Approach: Bridging Nano-to Macro Scale Investigation 229

9.1.6. Multiscale Characterization of Pore Evolution in Lesser Himalayan Black Shale from Krol Formation under Oxic Thermal Heating: Relevance to Untapped Shale Gas Extraction 230

9.2. Scope for Future Work 231

References 233

Publications in Referred Journal 259

List of Figures

Figure 1.1. Tectonostratigraphic map of the Himalaya (modified after DeCelles et al., 2001). 4
Figure 1.2. Some of the major Infrastructural projects in the Himalaya. 5
Figure 1.3. Hydrocarbon-bearing shale formations of the Indian Himalaya. 7

Figure 2.1. Geological map of Srinagar area, Uttarakhand, India (after Shekhar et al., 2006). Note: red triangular spots indicate some major engineering practices across the Srinagar area, (**a**) Google image of the tunnel phase of the railway project, and (**b**) Google image of the hydropower project. 15
Figure 2.2. Geological map of the Neoproterozoic-Cambrian Formations of the Lesser Himalayan region, northern India (modified after Singh and Rai, 1983). 17

Figure 3.1. Exposed weathered outcrop of Chandpur Phyllite. 23
Figure 3.2. A schematic diagram representing the two stages of the weathering-grade classification. 24
Figure 3.3. Representative XRD intensity plot for weathering-grades W1–4. 32
Figure 3.4. Progressive deterioration in contact angle values with increasing weathering-grades. 33
Figure 3.5. Mineralogical and textural transformations of Chandpur Phyllite with weathering-grades through petrographic thin section analysis (Note: GB is Grain Boundary and G-G is Grain to Grain). 34
Figure 3.6. Representative FE-SEM photomicrographs of Chandpur Phyllite various weathering-grade samples..... 36
Figure 3.7. Representative surface topography of weathered phyllite. Note: The left side image is the 2D surface topography, the center image is the profile of the topography along the line XX', and the right-side images show the 3D image of the topography at each grade. 38
Figure 3.8. Representative coefficient of friction (CoF) of phyllite with different weathering-grades. 39
Figure 3.9. Wear morphology of a representative weathering-grade sample of phyllite. 40
Figure 3.10. LPGA isotherm curve for different weathering-grade phyllite. 41

Figure 3.11. Pearson correlation matrix showing the relationship among weathering-grades with individual parameters and between the two individual parameters. 44
Figure 3.12. Simple regression analysis results of (**a**) RL vs. weathering-grade, (**b**) CoF vs. weathering-grade, (**c**) contact angle vs. weathering-grade, (**d**) clay content vs. weathering-grade, and (**e**) Ra vs. weathering-grade. 45

Figure 4.1. Schematic of coring at different β. Note: β is the angle between the foliation plane and drilling direction.....61
Figure 4.2. A schematic diagram of specimen preparation followed in this study. 63
Figure 4.3. The Laboratory setup of (**a**) Ultrasonic tester, (**b**) Uniaxial Compressive Strength Tester, (**c**) Brazilian Tensile Strength Tester, (**d**) XRD analysis, and (**e**) FE-SEM analysis. 65
Figure 4.4. Representative XRD pattern of Chandpur Phyllite with accompanying pie chart illustrating mineral quantification. 66
Figure 4.5. FE-SEM microphotographs of Chandpur Phyllite and its representative EDS analysis depicting elemental variations. 67
Figure 4.6. Relationship between β and P-wave velocity under normal and saturation conditions. 68
Figure 4.7. An example of representative stress vs. axial displacement plots for (**a**) dry condition and (**b**) saturation condition. 69
Figure 4.8. Relationship between (**a**) β vs. UCS and (**b**) β vs. BTS under normal and saturation conditions.....70
Figure 4.9. Representative failure modes (**a, b, c,** and **d**) observed in the UCS test and (**e, f, g,** and **h**) observed in the BTS test at 0º, 30º, 60º, and 90º, respectively. 71
Figure 4.10. A bar diagram representing the percentage of failure modes in different ranges of (**a**) UCS and (**b**) BTS. 72
Figure 4.11. Variation of the Brittleness Index (BI) with β for dry and saturated phyllite. 73
Figure 4.12. Illustrates a plot of (**a**) β vs. Elastic modulus and (**b**) β vs. Proneness to rockburst of Chandpur Phyllite under normal and saturation conditions. 75
Figure 4.13. A comparison of the present study with the existing studies with changes in foliation angles. 76
Figure 4.14. The schematic diagram explains the impact of saturation on the phyllite specimen. 79

Figure 4.15. The microphotographs of the failed specimen under UCS at various foliation angles. 80

Figure 5.1. Flow diagram of the PLI test procedure: (**a**) block sample of highly foliated phyllite, (**b**) core drilling at various foliation angles, (**c**) cutting and polishing of cores to prepare specimens of distinct geometries, (**d**) oven drying of prepared specimens, (**e**) representative PLI specimens with different geometries and foliation angles, and (**f**) axial PLI test configuration. 90

Figure 5.2. Petrographic and FE-SEM analysis of Chandpur Phyllite at foliation angles (β) of 0°, 45°, and 90°: (**a**), (**d**), and (**g**) show petrographic images under Plane-Polarized Light (PPL); (**b**), (**e**), and (**h**) show petrographic images under Crossed Nicols (XPL); and (**c**), (**f**), and (**i**) present FE-SEM photomicrographs of the phyllite. 94

Figure 5.3. Graph showing semi-quantitative X-ray diffraction of Chandpur Phyllite. 95

Figure 5.4. (**a**), (**b**), and (**c**) show the $I_{S(50)}$ values at different β for t/d ratios 1, 0.8, and 0.6, while graph (**d**) shows the average, minimum, and maximum values of $I_{S(50)}$ at different t/d ratios, independent of foliation angles. 96

Figure 5.5. Rock failure modes under distinct specimen geometries and foliation angles. 99

Figure 5.6. Bar diagram showing the frequency of specimens failed in various failure modes at t/d ratios of 1, 0.8, and 0.6. 100

Figure 5.7. Representative failure surface of the specimen at (**a**) β = 0° and (**b**) β = 90°. 106

Figure 5.8. Regression analysis using linear fit for valid failure data points for the specimen geometries (t/d): (**a**) 1, (**b**) 0.8, and (**c**) 0.6. 108

Figure 5.9. Shows the best fit curve of the experimental data points across all specimen geometries, plotted in a 3D coordinate system. 109

Figure 6.1. XRD intensity peaks of Krol Shale showing major constituent minerals and their percentage. 118

Figure 6.2. EDX mapping of the Krol Shale showing major elemental composition percentage. 118

Figure 6.3. FTIR spectrum of the Krol Shale for functional group study. 119

Figure 6.4. Petrographic images of the Krol Shale, (**a**) showing vitrinite and mineral matter, (**b**) and (**c**) showing framboidal pyrite and vitrinite, and (**d**) showing amorphous organic matter. 119
Figure 6.5. Schematic representation of the BTS test. 121
Figure 6.6. The schematic representation of the nano-indentation test. 122
Figure 6.7. The schematic representation of a typical nano-indentation curve. 122
Figure 6.8. The schematic representation of the AFM working principle. 124
Figure 6.9. BTS-based load-displacement curve, (**a**) BS1 and (**b**) BS2 samples, of the Krol Shale. 127
Figure 6.10. Characteristic layer-activation failure of the Krol Shale under BTS test. 128
Figure 6.11. Nano-indentation-based load-displacement curve, (**a**) BS1 and (**b**) BS2 samples, of the Krol Shale. 130
Figure 6.12. Typical events observed in the nano-indentation curves of Krol Shale, (**a**) pop-in, (**b**) serial pop-in, (**c**) step-shaped pop-in, and (**d**) elbow event. 130
Figure 6.13. Nano-indentation-based elastic modulus values for the BS1 and BS2 samples of the Krol Shale, (**a**) max, min, and avg values, and (**b**) frequency distribution. 131
Figure 6.14. Nano-indentation-based phase-resolved probability density function of elastic modulus values, (**a**) BS1 and (**b**) BS2 samples, of the Krol Shale. 134
Figure 6.15. Nano-indentation-based spatial distribution mapping, (**a**) BS1 and (**b**) BS2 samples, of the Krol Shale. 137
Figure 6.16. Schematic load-displacement curve, (**a**) BTS and (**b**) nano-indentation, for the brittleness index calculation based on mechanical work under elastic and plastic regions. 139
Figure 6.17. AFM-based representative 2D profile and its corresponding 3D surface topography, (**a**) BS1 and (**b**) BS2 samples, of the Krol Shale. 142
Figure 6.18. AFM-based roughness profile, (**a**) BS1 and (**b**) BS2 samples, of the Krol Shale along line XX'. 143
Figure 6.19. Probability density distributions of (**a**) elastic modulus "E" and (**b**) brittleness index "BI" showing observed micro and macroscale parameters and predicted macroscale parameters. 145

Figure 7.1. Experimental laboratory setup illustrating the adopted methodology. 153

Figure 7.2. Schematic workflow illustrating FE-SEM image analysis and quantitative pore characterization using MATLAB..... 156
Figure 7.3. Van Krevelen diagram showing atomic H/C vs. atomic O/C ratios for the Krol Shale..... 161
Figure 7.4. Petrographic characteristics of the studied shale samples: (**a**) oxidized vitrinite associated with clay minerals; (**b**) amorphous organic matter with pyrite grains and clay minerals; (**c**) oxidized vitrinite interspersed with mineral matter; (**d**) framboidal pyrite grains with amorphous organic matter. [V: vitrinite; C: clay mineral; AOM: amorphous organic matter; P: pyrite; MM: mineral matter]..... 162
Figure 7.5. LPGA isotherms: (**a**) and (**b**) N_2 adsorption-desorption isotherms, and (**c**) and (**d**) CO_2 adsorption isotherms of the representative BS-1 and BS-2 shale samples. 165
Figure 7.6. LPGA PSD: (**a**) and (**b**) N_2 BJH-PSD, and (**c**) and (**d**) N_2 and CO_2 DFT-PSD of the representative BS-1 and BS-2 shale samples. 165
Figure 7.7. 2D SAXS profiles of representative (**a**) BS-1 and (**b**) BS-2 shale samples. 167
Figure 7.8. SAXS scattering profiles of representative (**a**) BS-1 and (**b**) BS-2 shale samples modeled using the PDSP approach. 168
Figure 7.9. SAXS-derived PSD based on the PDSP model for representative shale samples: (**a**) BS-1 and (**b**) BS-2, based on pore volume. 168
Figure 7.10. Photomicrographs illustrating the surface morphology of Krol Shale, such as (**a**) an organic matter pore, (**b**) an intragranular pore, (**c**) a complex and sub-rounded pore, and (**d**) an intergranular and slit-shaped pore. 169
Figure 7.11. Workflow of watershed image segmentation applied to the FE-SEM image of the studied shale: (**a**) original grayscale FE-SEM image, (**b**) binary image generated using Otsu multilevel thresholding, (**c**) depth map showing topographic variation, and (**d**) final watershed-segmented image..... 171
Figure 7.12. Quantitative statistical results derived from FE-SEM image analysis of the shale sample: (**a**) equivalent pore radius, (**b**) pore circularity, (**c**) pore aspect ratio, and (**d**) pore coordination number. 172
Figure 7.13. Throat analysis from FE-SEM image processing: (**a**) throat segmentation derived from the binary segmented image, and (**b**) corresponding throat size distribution. 172
Figure 7.14. Fractal fitting of the data represented on a log-log plot. 173

Figure 7.15. Flowchart illustrating the working principle of the Dragonfly algorithm for micro-CT data analysis. 175
Figure 7.16. Micro-CT-based quantitative analysis of the shale sample showing: (**a**) mean Feret diameter, (**b**) equivalent spherical diameter, and (**c**) pore volume. 176
Figure 7.17. Micro-CT-derived 3D reconstructed profiles of (**a**) connected and (**b**) total pores in the shale sample, along with their few representative orthogonal 2D cross-sections. 176
Figure 7.18. Representative FTIR spectra of the Lesser Himalayan Krol Shale. 179
Figure 7.19. Representative XRD pattern of Lesser Himalayan Krol Shale. 179
Figure 7.20. Total Porosity in the studied shale from SAXS, FE-SEM, and micro-CT analyses. 182
Figure 7.21. Comparison of the characteristic properties: (**a**) TOC, (**b**) vitrinite reflectance, (**c**) kerogen type, (**d**) type of LPGA sorption curve, and (**e**) LPGA fractal dimension, of the untapped Lesser Himalayan Krol Shale with previously explored potential shale basins of India. 183
Figure 7.22. Schematic illustration (**a**) adsorbed/free gas in pores of shale and (**b**) enhanced gas recovery coupled with CO_2 sequestration. 185

Figure 8.1. A schematic representation of the pore attributes in shale. 189
Figure 8.2. A flowchart illustrating the detailed experimental procedure followed in this study. 196
Figure 8.3. Geochemical analysis based on Total organic carbon (TOC) vs. vitrinite reflectance (% VRo) showing thermal maturity of shale. 197
Figure 8.4. Petrographic images of the studied shale samples: (**a**) showing vitrinite grain with oxidation crack, (**b**) vitrodetrinite-a small fragment of vitrinite with mineral matter and AOM, (**c**) rounded vitrinite pach with fine pyrite grains and DOM, (**d**) massive pyrite with fine pyrite grains, (**e**) vitrodetrinite, carbonate mineral and AOM, (**f**) framboidal pyrite, (**g**) vitrinite grain showing alternation due to heat effect, (**h**) vitrinite grain coated with mineral matter, (**i**) vitrinite grain converting into inertinite. [V-Vitrinite; I-Inertinite; P-Pyrite; Py-Framboidal Pyrite; Vh-Heat effect on vitrinite patch; Dom-Dispersed organic matter; Aom-Amorphous organic matter; Vp-Pyrite coating on vitrinite patch; C-Cracks in vitrinite; MM-Mineral Matter]. 199
Figure 8.5. Cumulative mass-loss during combustion using the thermogravimetric curve. 200

Figure 8.6. (**a**) Intensity peaks of different mineral phases during combustion and (**b**) Percentage of dominant mineral phases in a representative sample (Qz: Quartz, Ill: Illite, Mu: Muscovite, Ab: Albite, Py: Pyrite). 201
Figure 8.7. A photomicrograph showing the characteristic features of the shale: (**a**) intra-particle and inter-particle pores, (**b**) organic matter pores, (**c**) complex, rounded, and cylindrical pores, (**d**) slit-shaped pores. 202
Figure 8.8. Representative photomicrographs at combustion temperatures: (**a**) 25 °C, (**b**) 100 °C, (**c**) 400 °C. [A: micro pore, B: micro fracture, C: remnant of organic matter within organic pores after oxic heating]. 203
Figure 8.9. Low-pressure N2 sorption isotherms of Neoproterozoic shale samples subjected to different combustion temperatures: (**a**) 100 °C, (**b**) 200 °C, (**c**) 300 °C, (**d**) 400 °C. 205
Figure 8.10. PSD using the BJH model of the combusted shale samples: (**a**) 100 °C, (**b**) 200 °C, (**c**) 300 °C, (**d**) 400 °C. 207
Figure 8.11. Fractal results showing ln (P_o/P)) vs. ln (Va) of low-pressure N2 sorption for thermally combusted shale: (**a**) 100 °C, (**b**) 200 °C, (**c**) 300 °C, (**d**) 400 °C. 208
Figure 8.12. A PDSP model-based scattering profile of shale subjected to different combustion temperatures. 209
Figure 8.13. Represents the PSD of the combusted shale based on (**a**) pore volume (dV/dlogD) and (**b**) pore area (dA/dlogD) of the SAXS analysis. 210
Figure 8.14. The schematic diagram illustrates the effect of thermal treatment on the structural characteristics of shale, ultimately enhancing gas flow: (1: Zone of free gas within inherent micropores and microfractures, 2: Gas molecules, 3: Zone of adsorbed gas on or near the surface of organic matter, 4: Zone of dissolved gas within organic matter, 5: Thermally induced new pores and microfractures with gas flow). 211
Figure 8.15. A bar plot illustrates the variation of the fractal dimension measured by LPGA and SAXS with combustion temperature. 216
Figure 8.16. A bar plot illustrates the variation in porosity derived from LPGA and SAXS analyses across different temperatures..... 216

List of Tables

Table 1.1. Key findings from various studies on the physico-mechanical properties, geochemical behavior, and hydrocarbon potential of Himalayan rock formations. 8

Table 2.1. Stratigraphic succession of the study area. Reproduced from Shekhar et al. (2006). 14
Table 2.2. Stratigraphic succession of the study area. Reproduced from Kumar et al. (2013). 16

Table 3.1. Weathering-grade classification of rock mass (ISRM, 2015). 24
Table 3.2. Roughness parameters calculated from AFM analysis using standard equations, as adopted from Nilankar et al. (2024b). 28
Table 3.3. Test parameters of the tribology test for CoF and wear measurements. 28
Table 3.4. Characteristics of phyllite with different weathering-grades based on in situ observations. 30
Table 3.5. Relative mineral concentrations across weathering-grades W1–4. 32
Table 3.6. Summary of roughness parameters for each weathering-grade. 38
Table 3.7. Minimum, maximum, average, and standard deviation values of some key parameters. 42
Table 3.8. Paired t-test results obtained by comparing the weathering-grades with individual parameters. 46
Table 3.9. Characteristic behavior of the Chandpur Phyllite with progressive weathering-grade. 52

Table 5.1. Represents the classification of the failure modes in the axial PLI test for anisotropic phyllite. Modified after Khanlari et al. (2015). 97
Table 5.2. Characteristic rock failure modes for each t/d ratio across various foliation angles. 100
Table 5.3. t-test results obtained by comparison of $I_{S(50)}$ values for t/d ratio 0.8 with 1. 102
Table 5.4. t-test results obtained by comparison of $I_{S(50)}$ values for the t/d ratio of 0.6 with the t/d ratio of 1. 102

Table 5.5. t-test result for fitting the regression analysis with t/d ratios of 0.6, 0.8, and 1. 103
Table 5.6. F-test analysis for all three specimen geometries fitting analysis.....103

Table 6.1. Dynamic properties of Krol Shale based on ultrasonic pulse velocity test..120
Table 6.2. BTS and elastic modulus values of the BS1 and BS2 block samples based on the BTS test. 128
Table 6.3. Nano-indentation-based elastic modulus values of the different mineral phases from previous studies. 132
Table 6.4. Phase-wise statistical summary of the elastic modulus for BS1 and BS2 obtained from GMM clustering.....135
Table 6.5. BTS-based brittleness index values for the BS1 and BS2 samples. 140
Table 6.6. Nano-indentation-based brittleness index values for the BS1 and BS2 samples. 140
Table 6.7. AFM-based roughness parameter values of the BS1 and BS2 samples.....143
Table 6.8. Statistical summary between predicted and observed macroscopic parameters. 145

Table 7.1. Ultimate (CHNSO) analysis, vitrinite reflectance, and TOC results of the Lesser Himalayan Krol Shale.....162
Table 7.2. Pore parameters obtained through LPGA analysis. 166
Table 7.3. Summary of pore parameters with their respective ranges and average values derived from multiple FE-SEM image analyses. 174

Table 8.1. Hydrocarbon generation potential and maturity classification scheme after Dow (1977).....198
Table 8.2. PSD of thermally combusted shale analyzed by LPGA and SAXS.....219

List of Abbreviations and Symbols

Abbreviations

AFM	Atomic Force Microscopy
ASTM	American Society for Testing and Materials
BET	Brunauer-Emmett-Teller
BI	Brittleness Index
BJH	Barrett-Joyner-Halenda
BTS	Brazilian Tensile Strength
CA	Contact Angle
CC	Clay Content
CoF	Coefficient of Friction
CW	Completely Weathered
D/Df	Fractal Dimension
DFT	Density Functional Theory
DR	Dubinin-Radushkevich
E/EM	Elastic Modulus
EDS	Energy Dispersive X-ray Spectroscopy
EGR	Enhanced Gas Recovery
EOR	Enhanced Oil Recovery
F	Fresh
FE-SEM	Field Emission Scanning Electron Microscopy
FHH	Frenkel-Halsey-Hill
FTIR	Fourier Transform Infrared Spectroscopy
GPa	Giga Pascal
HW	Highly Weathered
$I_{S(50)}$	Point Load Strength Index
ISRM	International Society for Rock Mechanics
ITSZ	Indus-Tsangpo Suture Zone
IUPAC	International Union of Pure and Applied Chemistry
kN	Kilo Newton
LPGA	Low-Pressure Gas Adsorption

MBT	Main Boundary Thrust
MCT	Main Central Thrust
MFT	Main Frontal Thrust
Micro-CT	Micro-Computed Tomography
mm	Millimetre
MPa	Mega Pascal
MW	Moderately Weathered
Ma	Million Years Ago
NAT	North Almora Thrust
nm	Nanometre
PDSP	Porod-Debye Scattering Profile
PES	Potential Energy of Elastic Strain
PLI	Point Load Index
PSD	Pore Size Distribution
R_a	Mean Roughness
R_{ku}	Kurtosis Coefficient
R_L	Schmidt Rebound Hardness Value
R_q	Root Mean Square Roughness
RS	Residual Soil
R_{sk}	Surface Skewness
SAXS	Small Angle X-ray Scattering
SSA	Specific Surface Area
SSAF(Iv)	Shear Splitting Along Foliation with Invalid Failure
SSAF(V)	Shear Splitting Along Foliation with Valid Failure
SSAF	Shear Splitting Along Foliation
STD	South Tibetan Detachment
SW	Slightly Weathered
t/d ratio	Length/Diameter ratio
TGA	Thermogravimetric Analysis
TOC	Total Organic Carbon
TSAF	Tensile Splitting Along Foliation
TSTM	Tensile Splitting Through Material
UCS	Uniaxial Compressive Strength

VR_o	Vitrinite Reflectance
WV	Wear Volume
XRD	X-ray Diffraction
μm	Micrometer
μN	Micro Newton

Symbols

V_p	P-wave Velocity
V_s	S-wave Velocity
β	Foliation Angle
ν	Poisson's Ratio
ρ	Density

Preface

The Himalaya makes a significant contribution to the growth of the country's economy. The growing infrastructure development and the exploration of natural resources within the highly complex Himalayan terrain require an in-depth characterization of the rock masses. The detailed characterization in terms of physico-mechanical properties, geochemical behavior, morphological parameters, and pore characteristics is critical to understand the behavior of those complex and highly anisotropic formations.

This thesis contains a total of nine Chapters. **Chapter 1** of this thesis outlines the definition of the problem along with a detailed literature survey, followed by the research gaps and the research objectives. Two different rock types, i.e., Chandpur Phyllite and Krol Shale from the Lesser Himalaya, Uttarakhand, have been studied. The Chandpur Phyllite in and around the Srinagar region of Uttarakhand is a dominant lithology where major infrastructure developments are underway, including dams, tunnels, and highways, despite its strong anisotropy and highly fragile nature. The Krol Shale from the Lesser Himalaya has a wide geographical distribution and has a carbonaceous nature, yet this formation remains unexplored. **Chapter 2** represents the selection and collection of rock samples from the study areas. After this, six chapters (**Chapters 3–8)** include the detailed investigations of the proposed objectives, followed by **Chapter 9** on conclusions and future scope.

In **Chapter 3**, an investigation into the multiscale weathering-grade classification of Chandpur Phyllite has been carried out by combining *in situ* observations with laboratory analyses. The results indicate the progressive deterioration of the rock strength as weathering progresses from W1–4. The deterioration of the primary minerals into secondary clay minerals with progressive weathering plays an important role in altering the rock's mechanical behavior. The surface characteristics, including wettability, roughness, and frictional behavior, also change gradually with progressive weathering-grades. This multiscale analysis provides a basis for understanding the weathering phenomena crucial for infrastructure development within Chandpur Phyllite.

In **Chapter 4**, a study on the influence of water saturation on the physico-mechanical behavior of Chandpur Phyllite has been carried out. A combined effect of water saturation and foliation angle (β) has been considered. Although saturation reduces overall rock

strength, it does not affect the failure modes, which are controlled by the micaceous foliations. The U-shaped pattern (initially decreasing and then increasing with β, having a minimum value at β=30° and a maximum at β=0°/90°) of the mechanical parameters under both normal and saturation conditions shows the inherent anisotropic nature of the Chandpur Phyllite. However, the wave velocity does not follow a similar U-shaped pattern, but it decreased with increasing β under both normal and saturated conditions, although values are higher under saturated conditions. The findings of this study are crucial, as the effect of both anisotropy and water saturation should be considered for the design and stability of infrastructures.

In **Chapter 5**, the influence of specimen geometry (ratio of length to diameter, t/d) on the axial Point Load Strength Index ($I_{S(50)}$) of Chandpur Phyllite has been investigated. Specimens with t/d ratios of 1.0, 0.8, and 0.6 across β from 0° to 90° were investigated. The results indicate that for t/d ratios of 0.8 and 1, the $I_{S(50)}$ increases from 0° to 60° and then decreases at higher β (75° and 90°). In contrast, for a t/d ratio of 0.6, $I_{S(50)}$ continuously increases with increasing β. Up to β = 30°, all specimens show valid failure modes along the foliation. However, at higher β (≥ 45°), specimens with t/d ratios of 0.8 and 1 exhibit invalid failure due to uneven stress distribution, while those with a t/d ratio of 0.6 maintain valid failure modes. Statistical validation using the Student's t-test further confirms that the strength indices differ significantly among the geometries, with the t/d ratio of 0.6 showing reliable strength values. Overall, this study provides the role of specimen geometry in point load testing and suggests that a t/d ratio of 0.6 is the most suitable for obtaining accurate strength in phyllite rock masses.

In **Chapter 6**, a study on the multiscale mechanical characterization of the Krol Shale by combining the macroscopic Brazilian Tensile Strength (BTS) test and the microscopic nano-indentation test. The nature of the studied shale indicates that it has strong potential for gas generation, is rich in clay minerals, and was deposited in a marine environment containing terrestrial organic matter. Mechanical parameters indicate low-to-moderate stiffness and a semi-ductile nature, supported by low values of elastic modulus and brittleness index obtained from nano-indentation and BTS tests. Features like pop-in events and elbow events in the load-displacement curve of the nano-indentation test are associated with pores/heterogeneity and phase change during unloading. Nano-indentation tests highlight the microscale mechanical heterogeneity and tectonic deformation mechanism within the Krol Shale, which overall controls its macroscopic

tensile strength. The relatively low BTS values and observed layer-controlled failure along bedding planes further confirm the nature of the shale. Further, a probabilistic distribution approach successfully links microscopic and macroscopic mechanical properties, showing good agreement with experimental results. The findings of this study are very important for assessing the suitability of the Krol Shale for hydraulic fracturing to enhance gas recovery and for long-term CO_2 storage.

In **Chapter 7**, the pore characterization of the Krol Shale using various multi-analytical techniques such as Low-Pressure Gas Adsorption (LPGA), Small Angle X-ray Scattering (SAXS), Field Emission Scanning Electron Microscopy (FE-SEM), and micro-CT has been carried out. This multiscale pore characterization bridges the gap between nano- and macro-scale pores. The geochemical results indicate that the pyrite-rich black Krol Shale contains Type III gas-prone kerogen. This is supported by high vitrinite reflectance (> 1.5 %), absence of liptinite and inertinite, and high sulfur & Total Organic Carbon (TOC) content, indicating strong gas-generation potential. The pore structure mainly consists of irregular, elongated slit- and wedge-shaped pores, as shown by LPGA isotherms and FE-SEM images. Pore size distribution (PSD) indicates the dominance of micro- and mesopores, which overall controls the storage capacity. The fine micropores were identified through LPGA-CO_2 adsorption and mesopores through LPGA-N_2 adsorption and SAXS analysis. Micro-CT analysis suggests that pore connectivity is low to moderate having connected porosity smaller than the total porosity. Micro-CT imaging also reveals the presence of natural microfractures, with most of the connected porosity mainly concentrated along those fracture zones. Overall, this study demonstrates that despite being largely unexplored, the Krol Shale possesses a complex pore network with significant potential for gas storage and flow.

In **Chapter 8**, the study focuses on the evolution of the pore structure of the Krol Shale during combustion to enhance untapped gas extraction. At around 100 °C, pore compactness results from moisture removal, but at higher temperatures (> 100 °C), combustion expands, coalesces, and creates new pores due to thermal heating and organic matter breakdown. This leads to increased surface irregularity, as supported by the LPGA fractal dimension and FE-SEM images. With increasing temperature, pore size distribution also changes, shifting from micro- and mesopores at lower temperatures to larger mesopores and macropores at higher temperatures, with a sharp rise in pore development around 400 °C, confirmed by LPGA and SAXS results. This study shows

the potential of combustion-induced thermal stimulation and suggests that oxic heating can significantly alter shale microstructure, thereby offering a viable technique for shale gas recovery.

The work carried out in this thesis highlights the multiscale approach in characterizing the anisotropic Chandpur Phyllite and Krol Shale from the Lesser Himalayan region of Uttarakhand, India. The findings offer valuable insights into sustainable infrastructure development and strengthening the country's energy security.

Chapter: 1
Introduction

1.1. Definition of the Problem

The Himalaya are one of the youngest and geologically active mountain belts in the world, formed by the convergence of the Indian and Eurasian plates. The collision between the two plates began at ~ 50 million years ago (Ma) and is still ongoing, leading to intense folding, faulting, and active tectonics (Mukherjee, 2013). The Himalayan belt spans across five countries, including India, with ~ 2400 km length. In India, it extends across 11 states and 2 union territories from the northwestern regions of Jammu & Kashmir and Ladakh to the northeastern states of Sikkim and Arunachal Pradesh. The long-term active tectonism in the Himalaya has led to highly heterogeneous, fractured, and complex geological formations. The geology of the Himalaya covers a wide range of lithologies, including sedimentary (shales, slates, limestones, sandstones), metamorphic (phyllites, schists, gneisses, quartzites), and igneous (granites, pegmatites), that have undergone significant deformation and uplift.

The lithological variations and the major fault systems have led to the formation of the following tectonostratigraphic divisions of the Himalaya: i) Sub-Himalaya (outer Himalaya), ii) Lesser Himalaya, iii) Higher Himalaya (Greater Himalayan zone), iv) Tethys Himalaya, and v) The Trans Himalaya (Indus-Tsangpo suture zone, ITSZ) (Figure 1.1). The ITSZ demarcates the possible geological boundary and collision zone between the Indian and Eurasian plates. An overview of the tectonostratigraphic divisions, along with their characteristic lithologies, is mentioned below:

Sub-Himalaya zone

This zone marks the frontal part of the Himalayan Mountain and is confined between the Main Frontal Thrust (MFT) in the south and the Main Boundary Thrust (MBT) in the north (Sharma, 1998; DeCelles et al., 2001). It comprises low altitude hills of 150 - 250 m height, formed by the deposition of weathering and erosion-induced post-collision sediments of the Himalayan front along the active Murree-Siwalik forearc basin. The Siwalik Group comprises a ~ 5000 m thick succession of fluvial conglomerates, sandstones, and siltstones. The rocks in the region are highly deformed, fragile, easily erodible, porous, and are intensely folded.

Lesser Himalayan zone

The Lesser Himalayan zone extends between the MBT in the south and the Main Central Thrust-Vaikrita (MCT-V) in the north. It contains records of marine and shallow sea sediments of the Proterozoic to Cambrian age. This Zone is covered by the Jutogh-Almora Thrust and Chail-Ramgarh Thrust and contains low-grade meta-sedimentary or unmetamorphosed sedimentary rocks (Sharma, 1998; DeCelles et al., 2001; Bose and Mukherjee, 2019). Broadly, the Lesser Himalayan zone was subdivided into the outer, middle, and inner belts, where the outer belt is marked along and near the MBT, and the inner belt lies near the MCT. The outer belt comprises unmetamorphosed sedimentary rocks along with very low-grade meta-sedimentary and metamorphic rocks having highly sheared and brecciated nature. The middle and the inner belts consist of intercalated rocks with medium and high-grade metamorphism and intensely sheared and mylonitized rocks. This zone also comprises high-grade crystalline rocks of the higher Himalaya, which present as a nappe over the Lesser Himalayan zone (Upreti, 1999). The Lesser Himalaya zone consists of a wide variation of rocks, including shales, dolomites,

deformed quartzites, metabasics, undeformed quartzites, foliated and highly anisotropic metamorphic rocks like mica schists, slates, and phyllites.

Higher Himalayan zone

This zone is bounded by the South Tibetan Detachment (STD) in the north and MCT in the south (Burchfiel et al., 1992). It comprises of high-grade metamorphic rocks such as Precambrian crystalline rocks, Cambrian-Ordovician granite/orthogneisses, and the Tertiary leucogranites (Sharma, 1998). Quartzites, garnet-biotite gneisses, biotite-sillimanite gneisses, and, along with migmatites, green-schists and marbles are identified as the dominant rocks in the higher Himalaya sequence (Tandon and Gupta, 2015). The rocks in the vicinity of the MCT zone are highly sheared and thus intensely deformed and mylonitized (Robyr et al., 2002).

Tethys Himalayan zone

The Tethys Himalayan zone stretches between the Indus-Tsangpo Suture Zone (ITSZ) in the north and the STD in the south. It comprises Tethyan sea marine sediments of the late Precambrian to Phanerozoic (Palaeozoic-Mesozoic) Era (Shah, 1991). The rocks in this zone are less metamorphosed (Carosi et al., 1999). The major lithotypes along the region are meta-sandstones, sandstones, phyllites, shales, and crystalline limestones (marbles) (Searle, 1986; DeCelles et al., 2001).

The Trans-Himalayan zone (Indus-Tsangpo Suture Zone, ITSZ)

This zone comprises an ophiolitic sequence which includes obducted slices of the neo-Tethyan oceanic crust, deep-sea trench sediments, subduction and collision-related island arc magmatic rocks, the arc-derived accretionary prism-related sediments, and the

post-collision Kargil molassic sediments. Primarily, the Trans Himalaya comprises gabbro, diorite, granodiorite, tonalite, and granite. The ITSZ consists of a complex association of tectonically imbricated volcanic arcs, ophiolite belts, and sedimentary rocks of sandstones, siltstones, and shales (Jain, 2014).

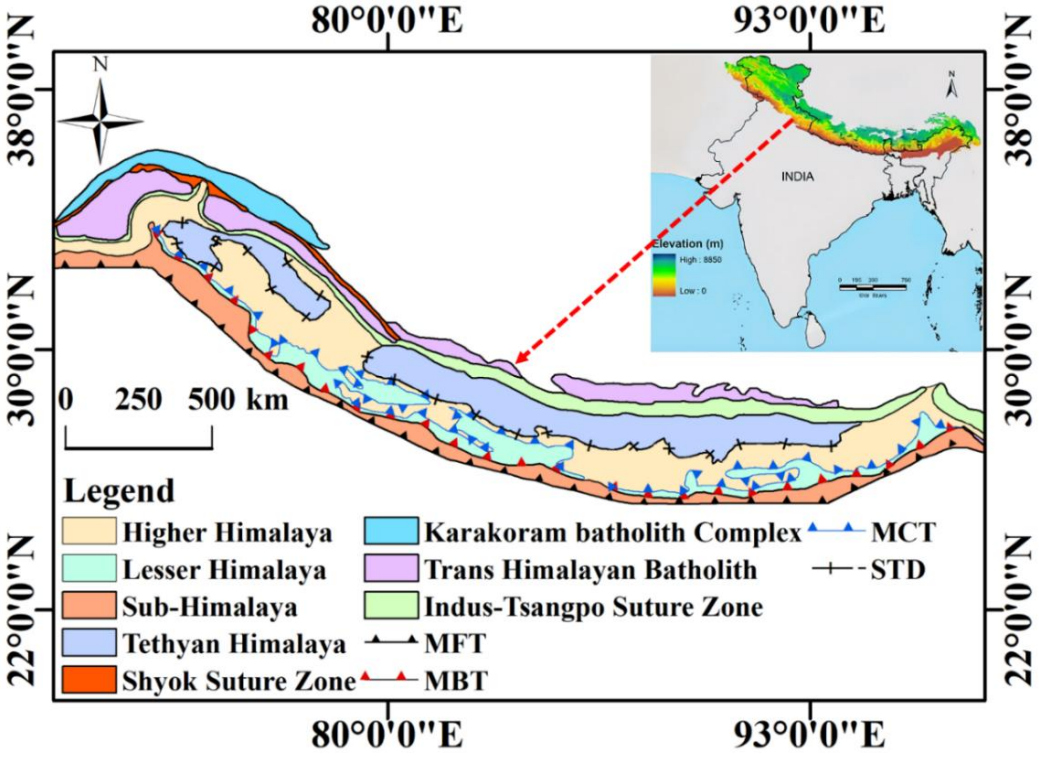

Figure 1.1. *Tectonostratigraphic map of the Himalaya (modified after DeCelles et al., 2001).*

1.2. Importance/Significance of the Himalaya

The Himalayan region in India not only stands out for its geological complexities, but it is also well known for its rapid infrastructure development and natural resources (hydrocarbon potential).

Infrastructure development

The Indian Himalayan region is currently witnessing an unprecedented phase of infrastructure development. Large-scale projects such as highways, all-weather roads,

long tunnels, hydropower dams, and bridges are being developed at a rapid pace across this mountainous terrain. Road widening in the mountains is also underway (Puniya et al., 2026). These projects aim to overcome the natural barriers imposed by rugged topography, steep slopes, and remote accessibility, thereby integrating isolated regions with the nation's mainland. Figure 1.2 shows a few major infrastructural projects across the Himalaya, reflecting the scale and intensity of the development.

However, infrastructure development in the Himalaya is more complex than in stable terrains. The Himalaya, being geologically young and tectonically active, is characterized by highly heterogeneous & anisotropic rock masses. These rock masses exhibit low strength, high deformability, and variable mechanical behavior across different scales, making them vulnerable to landslides, slope failures, and excavation-induced instability. Additionally, factors such as active seismicity and intense weathering due to rainfall further enhance the fragility of the region.

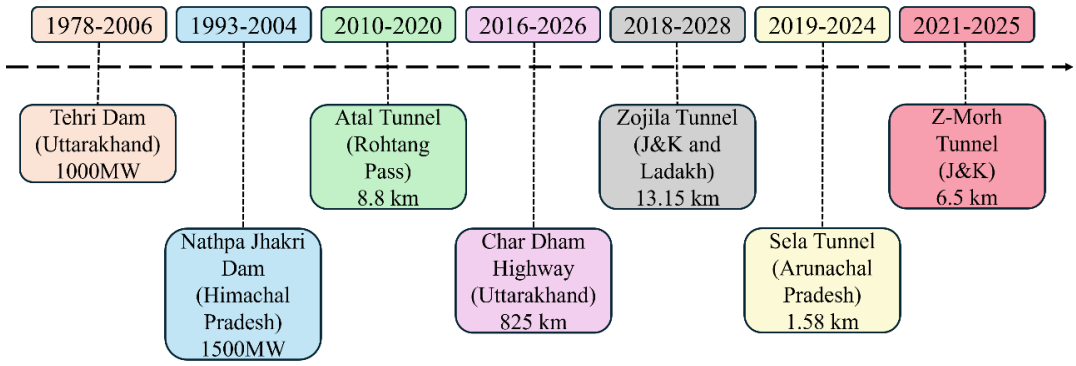

Figure 1.2. *Some of the major Infrastructural projects in the Himalaya.*

Hydrocarbon resources

The exploration of hydrocarbon resources in the Indian Himalayan region represents a new emerging area in energy research, with shale gas gaining significant attention as a potential unconventional resource. Shale gas has gained considerable

attention because of its strong potential and its importance for energy security (Paul et al., 2021; Paul et al., 2025).

In the context of shale gas, the Himalayan region offers several stratigraphic sequences with strong potential for future discovery and development (Bhat, 2019). Therefore, several shale formations across the Himalaya are of particular interest. These include the Permo-Carboniferous Gondwana shales in the eastern Himalaya, as well as the Eocene Subathu shale and the Neoproterozoic-Cambrian Infra-Krol, Krol, & Tal Formation shale in the northwest Himalaya. The Permo-Carboniferous Gondwana shales in the Eastern region exhibit TOC values ranging from 0.3 to 7.3 % (Wahengbam et al., 2025). These Eastern region shales are predominantly Type III kerogen with gas potential, with T_{max} values ranging from 291 to 348 °C. The Eocene Subathu Shale of the NW Himalayan foreland basin exhibits a wide range of TOC content (0.3–42.4 %), with organic matter predominantly composed of Type III, gas-prone kerogen (Hafiz et al., 2022). Thermal maturity indicators, including T_{max} values (486–597 °C) and vitrinite reflectance (% VRo) ranging from 1.16 to 1.65 %, suggest that the Subathu Formation shales have reached the wet to dry gas generation window. Bhattacharya and Chandra (1979) and Raiverman et al. (1984) also confirmed that the Subathu shale demonstrates potential for dry gas generation. While researchers have investigated the Permo-Carboniferous Gondwana shales and the Eocene Subathu shales to assess their hydrocarbon potential and exploration suitability, the Neoproterozoic-Cambrian Infra-Krol, Krol, & Tal Formation shale remains largely untapped.

Although it constitutes an important marine sedimentary sequence in the Lesser Himalaya, the Krol Shale has yet to receive attention from researchers. Mishra and Mukhopadhyay (2012) also stated that the Infra-Krol, Krol, and Tal Formation black carbonaceous shale sequence of the Lesser Himalaya from the north-western region

possesses a well-deposited hydrocarbon potential. The carbonaceous black shale of the Infra-Krol, Krol, and Tal Formations are widely distributed across the NW Himalayan belt, extending from Solan (Himachal Pradesh) in the west to Nainital (Uttarakhand) in the east, with prominent exposures in the Mussoorie and Garhwal regions (Singh et al., 2025c).

The lack of understanding of the Krol Shale represents an important critical research gap in the Himalayan hydrocarbon system. Being a very old (Neoproterozoic) formation, it is likely to have a unique thermal history and organic characteristics, which can provide valuable insights into the region's unconventional energy resource potential. The pie chart shown in Figure 1.3 represents the hydrocarbon-bearing shale formations of the Indian Himalayan region. When viewed from the perspective of hydrocarbon potential, the shale formations in the Himalaya possess numerous challenges for exploration due to the tectonically active region. From the geomechanical point of view, the weak, fractured, and highly anisotropic nature of the potential shale formations may pose serious risks to drilling stability and the effectiveness of hydraulic fracturing operations.

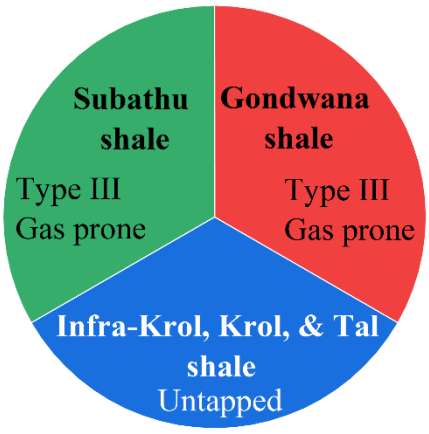

Figure 1.3. *Hydrocarbon-bearing shale formations of the Indian Himalaya.*

In view of both the rapid infrastructure development and the hydrocarbon potential in the Himalayan region, detailed characterization of the rock masses is very important. The rock masses of the Himalayan region are marked by strong heterogeneity from macro to microscales, where variation in mineralogy, fracture density, bedding/foliation orientation, pore parameters, etc., influences the overall geomechanical behavior. Therefore, a detailed characterization is very crucial to understand the true behavior of those complex formations. The lack of which can result in serious environmental consequences. The accurate estimation of the physico-mechanical, geochemical, morphological, and pore characteristic properties of rock masses is crucial for designing and planning safe infrastructure and hydrocarbon exploration. Inadequate knowledge of such properties may lead to slope instability, deformation, foundation failure, and well-bore collapse. Also, for hydrocarbon potential, a sufficient understanding of geochemical behavior and pore characteristics (size, distribution, connectivity, etc) is very important, as insufficient knowledge may lead to poor recovery, fluid loss, and ineffective hydraulic fracturing design. The literature survey in the context of the Indian Himalaya is presented in Table 1.1, which summarizes the contributions of various researchers, highlighting key findings related to physico-mechanical properties, geochemical behavior, and hydrocarbon potential of different rock formations.

Table 1.1. *Key findings from various studies on the physico-mechanical properties, geochemical behavior, and hydrocarbon potential of Himalayan rock formations.*

Author & year	Formations	Key findings
Bhattacharya and Chandra (1979)	Shale (Sub Himalaya)	The Cenozoic Subathu Shale demonstrates significant potential for generating dry gas.
Valdiya (1983)	Several rocks (Lesser Himalaya)	The Lesser Himalayan region is marked by intracrustal thrusts (MBT and MCT), and the rocks of the region have undergone multiple thrusting and shattering.
Raiverman et al. (1984)	Shale (Sub Himalaya)	The Subathu Shale shows strong potential for dry gas generation.
Mehrotra et al. (1991)	Several rocks (Lesser Himalaya)	Rocks in the Lesser Himalaya are soft, weathered, and chemically vulnerable, often containing soluble components. These rocks can lose significant strength

		and deform more when saturated, highlighting the need for long-term geotechnical evaluation.
Ramamurthy et al. (1993)	Phyllite (Lesser Himalaya)	Highly anisotropic phyllite exhibiting a fissile character, with minerals showing a pronounced preferred orientation. Its strength varies with the foliation angle (β).
Shekhar et al. (2006)	Various rocks of the Chandpur Group & the Garhwal Group (Lesser Himalaya)	The rocks of the region date from the Middle-Late Proterozoic to the Early Cambrian. The folds are genetically associated with thrusts and shear zones. Additionally, the stratigraphic succession, structural framework, and deformation patterns show a strong resemblance to those of the upper Vindhyan Supergroup.
Mishra and Mukhopadhyay (2012)	Shale (Sub and Lesser Himalaya)	In the northwestern Himalayan region, the Neoproterozoic-Cambrian Infra-Krol, Krol, and Tal Formation shales of the Lesser Himalaya, along with the Cenozoic Subathu Formation shale of the Sub-Himalaya, constitute well-developed sequences for hydrocarbon potential.
Mani et al. (2014)	Several shales (Sub, Tethys, and Trans Himalaya)	Sixty-seven shale samples, ranging from Proterozoic to Tertiary age, were collected from the Jammu, Kashmir, and Ladakh regions to evaluate their organic richness, kerogen characteristics, and gas generation potential. The Tertiary Subathu shale of Jammu acts as a potential source of gaseous hydrocarbons and shows promising gas potential, whereas the organic matter characteristics of the Proterozoic Sirban shale (Jammu), the Permian-Triassic shales of Kashmir, and the Paleozoic-Mesozoic-Tertiary shales of the Ladakh-Karakoram zones are not encouraging for hydrocarbon generation.
Singh et al. (2015)	Phyllite, slate, orthoquartzite (Lesser Himalaya)	The strength of all three anisotropic rocks varies with β, reaching a minimum at 30° and a maximum at 0°/90°. Additionally, saturated specimens exhibit lower strength compared to dry samples.
Pandey et al. (2018)	Shale (Tethys Himalaya)	Shale from the Spiti and Chikkim Formations in the Tethys Himalaya indicates the presence of methane as both free and fixed hydrocarbons.
Kundu et al. (2018)	Schist (Lesser Himalaya)	The Brazilian tensile strength of saturated schist samples is reduced compared to dry samples. Saturation also shifts the minimum strength to a higher β, with the most pronounced reduction occurring at β = 30°.
Ansari et al. (2021)	Phyllite soil (Lesser Himalaya)	The abundance of phyllosilicate minerals leads to a decrease in the overall strength of the phyllite.
Dey et al. (2022)	Sandstone and Shale (Lesser Himalaya)	The Krol sandstone and shale represent a significant yet largely unexplored component of the Lesser Himalayan Neoproterozoic succession. The pyritic black shale is interpreted to have formed under anoxic marine conditions.
Hafiz et al. (2022)	Subathu shale (Sub Himalaya)	Subathu shale shows a wide range of TOC values (0.3–42.4 wt%), indicating poor to excellent gas generation potential dominated by Type III kerogen. Petrographic analysis further reveals a high proportion of vitrinite.
Singh et al. (2022)	Phyllite, quartzite (Lesser Himalaya)	The relatively low strength is attributed to the abundance of foliations and fractures/microcracks, along with the development of clay minerals.
Ram and Gupta (2024)	Granite (Higher Himalaya)	Under thermal treatment, point load strength decreases exponentially with increasing porosity and damage, and decreasing density, with greater reduction under water cooling than air cooling.
Kaushal et al. (2024)	Gneiss (Lesser Himalaya)	Progressive weathering markedly reduces the mechanical strength of gneiss due to an increase in micro-crack intensity with increasing weathering-grades.

		Simultaneously, primary minerals undergo physical and chemical alterations, transforming into secondary clay minerals.
Wahengbam et al. (2025)	Shale (Lesser Himalaya)	The Permo-Carboniferous Damuda shales of the Gondwana Supergroup, exposed in the Lesser Himalayan region of Sikkim, display total organic carbon (TOC) values ranging from 0.3 to 7.3 %. These shales are dominated by Type III kerogen, indicating gas potential, with Tmax values between 291 and 348 °C.

1.3. Research Gap

Although numerous studies have attempted to characterize Himalayan rocks in terms of their physico-mechanical and geochemical properties, these investigations remain largely fragmented. Given the Himalaya's extreme climatic conditions and active tectonism, a comprehensive, formation-specific characterization is essential rather than relying on dispersed, isolated studies. Therefore, a critical research gap exists in the comprehensive, formation-specific characterization of Himalayan rock formations. This gap becomes particularly critical in the Lesser Himalayan region, where there is significant potential for both infrastructure development and unconventional energy exploration.

The Lesser Himalayan phyllite, particularly of the Chandpur Group, is a dominant rock type for major infrastructure developments, including tunnels, dams, highways, etc. The Phyllite, well known for its strong anisotropy and fragile nature, exhibits strong variation in strength and deformability. Adequate knowledge of the change in the properties (physico-mechanical, chemical, and morphological properties) of such rocks with respect to foliations, chemical weathering, and water saturation becomes very crucial. These variations directly govern the strength, deformability, and failure behavior of the rock mass, thereby influencing the stability and long-term performance of the infrastructure.

In the context of hydrocarbon exploration, while considerable attention has been given to Gondwana and Subathu shales, the Neoproterozoic Krol Shale of the Lesser

Himalaya remains largely unexplored despite its wide spatial distribution and carbonaceous nature. Although existing studies suggest favorable depositional conditions, there is a lack of systematic and comprehensive evaluation of its geochemical properties, including TOC content, kerogen type, and thermal maturity. Additionally, there is a lack of pore-structure characterization, which is critical for gas storage and migration in the Krol Shale. From a geomechanical perspective, the highly anisotropic, fractured, and tectonically disturbed nature of the Himalayan shale formations can pose significant challenges to wellbore stability and hydraulic fracturing efficiency. Such aspects have not been rigorously investigated for the Krol Shale.

Therefore, addressing the research gap for both the Chandpur Phyllite and the Krol Shale is not just an academic need, but is essential for the safe and efficient development of infrastructure and energy resources in the Indian Himalaya.

1.4. Research Objectives

In light of the identified research gaps, the objectives of this doctoral thesis are delineated as follows:

i. A comprehensive investigation of the multiscale weathering-grade classification of Chandpur Phyllite by integrating *in situ* observations with laboratory investigations.
ii. To understand the influence of water saturation on the physico-mechanical behavior of Chandpur Phyllite at different foliation angles (β).
iii. Investigation of the effect of specimen geometry on the point load strength and anisotropy behavior of phyllite.
iv. To perform a multiscale mechanical characterization of Krol Shale using Conventional and Non-conventional analytical techniques.

v. Characterization of the pore system of the Krol Shale using an integrated multiscale analytical method.

vi. Evolution of pore structure in Krol Formation Shale under oxic thermal conditions through multiscale analysis.

Together, these objectives aim to develop a comprehensive and multiscale understanding of both the Chandpur Phyllite and the Krol Shale. This approach will help us address critical research gaps in infrastructure development within the Chandpur Phyllite and in the potential for unconventional hydrocarbon exploration & CO_2 sequestration in the Krol Shale of the Lesser Himalaya.

Chapter: 2
Selection and Collection of Rock Samples

The study area for this thesis is located in Uttarakhand, India, where the Chandpur Group phyllite and the Krol Formation Shale are well exposed and are easily accessible. Both rock units belong to the Lesser Himalayan domain, which is well known for its geological complexity. Geographically, the region lies within an active tectonic belt of the Himalaya, characterized by structural features such as folding, faulting, and thrusting. The area exhibits considerable lithological diversity with varying degrees of deformation, reflecting its prolonged tectonic history.

2.1. Chandpur Phyllite from the Srinagar area, Uttarakhand

The Chandpur Phyllite of Upper Proterozoic age belongs to the Chandpur Group of the Lesser Himalayan region in Uttarakhand. The rock formations in and around the study area fall into two major groups, namely the Chandpur Group and the Garhwal Group, both of Precambrian age (Shekhar et al., 2006). The stratigraphy of the study area is given in Table 2.1. The Chandpur Group comprises Chandpur/Srinagar phyllite, which is associated with the Kilkileshwar metavolcanics. Conversely, Marora Limestone, Koteshwar quartzite (associated with Chamdhar metabasics), and Garhwal slate are the characteristic rocks of the Garhwal Group. An important structure in this area is the NW–SE trending North Almora Thrust (NAT). The studied phyllite is characterized by distinct features such as kink bands, puckers, shiny luster, pronounced shear, and up to 20 cm thick quartz veins (Shekhar et al., 2006).

The study area experiences a subtropical climate, characterized by a mean annual rainfall of 1000–1500 mm, with ~ 80 % of the precipitation occurring between mid-June and mid-September (Sati et al., 2007). Sampling has been carried out at an elevation of ~

560 m above mean sea level from the vicinity of Srinagar city of Garhwal region, Uttarakhand, within the ~ latitude range of 30°08′03″N to 30°13′29″N and longitude range of 78°46′57″E to 78°48′22″E (Figure 2.1).

During sampling, care was taken to collect intact and fresh blocks that were free from any visible signs of weathering, alteration, or fractures to ensure the reliability of laboratory results. These samples were carefully selected to represent the true characteristics of unaltered rock. In contrast, for the study focused on weathering, a detailed *in situ* characterization was carried out before sampling, which included visual inspection and field assessments to classify the weathered rock into appropriate weathering-grades. Based on the classification, representative weathered samples of each grade were collected from the exposed outcrop located along the Rishikesh-Badrinath National Highway in the vicinity of the Alaknanda valley near the Srinagar area of Uttarakhand.

Table 2.1. *Stratigraphic succession of the study area. Reproduced from Shekhar et al. (2006).*

Age	Group	Formations
PRECAMBRIAN	Chandpur	Srinagar Phyllites: Dark green, lustrous rock with localized kink bands and minor folds. It is highly sheared with pronounced sheeny luster. The rock is associated with greenish-grey to dark green metavolcanics (Kilkaleshwar Metavolcanics), which are highly foliated and occur as lensoidal bodies with a gneissose texture.
	Garhwal	Marora Limestone: A bluish-grey, crystalline, medium- to fine-grained limestone notable for its siliceous and ferruginous impurities. The unit is characterized by the development of secondary calcite and dolomite veins that occur both parallel and transverse to the bedding planes. Garhwal Slate: This formation exhibits violet and purple-brown to olive-green colors. It features well-defined secondary surfaces and alternating violet and green ferruginous banding. The slate is highly fissile, readily splitting into thin slabs with smooth, lustrous surfaces. Koteshwar Quartzite: A pinkish to creamish ferruginous quartzite intercalated with violet and grayish-green sheets. Medium- to fine-grained texture. It preserves primary sedimentary structures such as ripple marks and crossbedding. It is associated with the

		Chamdhar Metabasics (massive, grayish-green epidioritic sills), which display marginal foliation and quartz-filled amygdules.

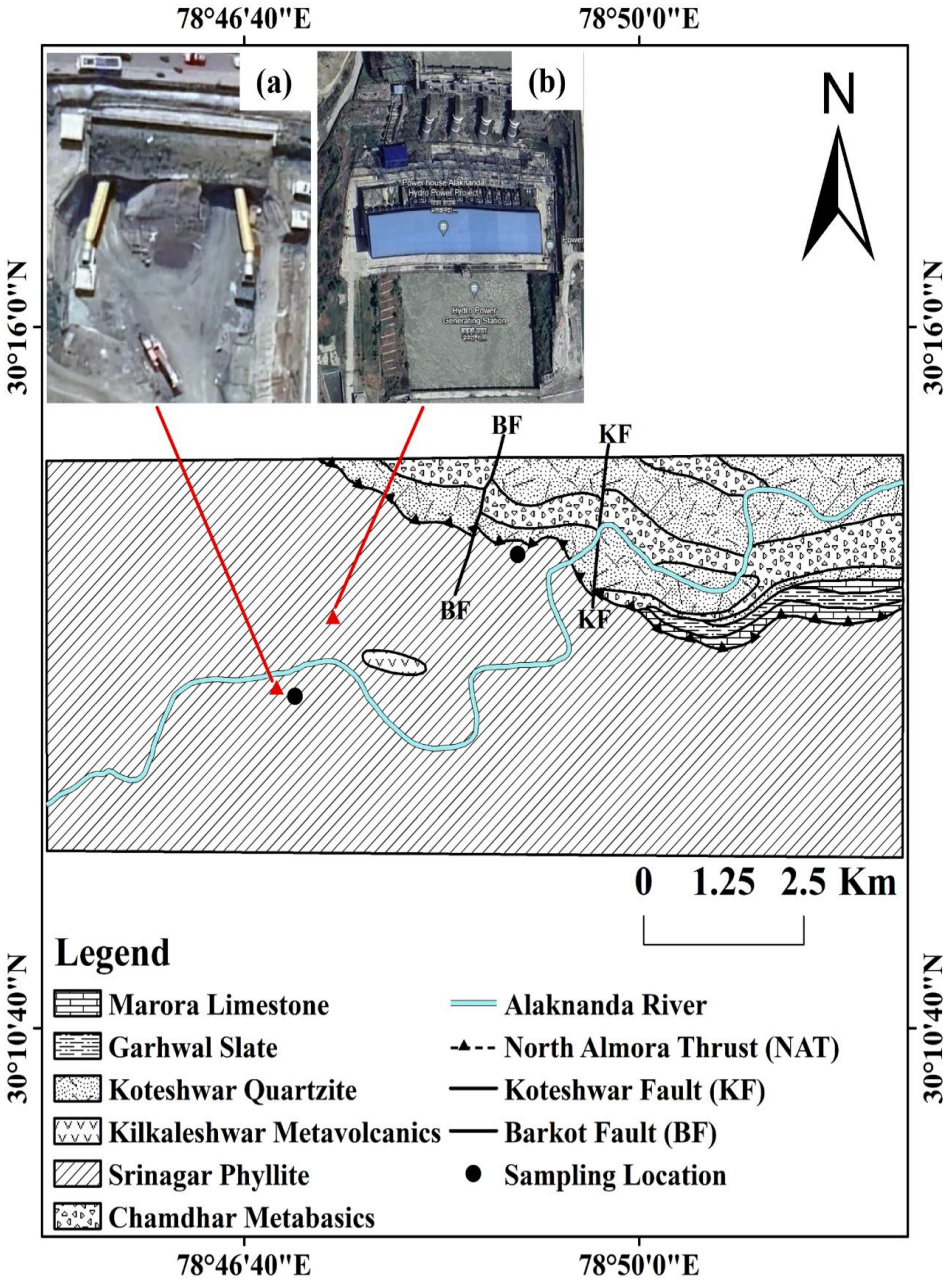

Figure 2.1. *Geological map of Srinagar area, Uttarakhand, India (after Shekhar et al., 2006). Note: red triangular spots indicate some major engineering practices across the Srinagar area,* ***(a)*** *Google image of the tunnel phase of the railway project, and* ***(b)*** *Google image of the hydropower project.*

2.2. Krol Shale from the Kaudiyala area, Uttarakhand

The Krol Shale of Neoproterozoic age belongs to the Krol Formation of the Lesser Himalayan region in Uttarakhand. It is typically black and has an organic-rich nature (Mishra and Mukhopadhyay, 2012). The studied shale samples belong to the Ediacaran Period of the Neoproterozoic Era (Kumar et al., 2013). The stratigraphic succession of the area is shown in Table 2.2. The Krol Formation and Infra-Krol Formation are the main stratigraphic units holding this lithology. This Krol Formation Shale is interbedded (Kaufman et al., 2006). In contrast, the Infra-Krol Formation consists of shale with an upward increase in fine-grained sandstone and siltstone beds towards the Krol Formation (Xiao et al., 2024). The samples of ~ size 18″ * 18″ * 18″ were collected from road cut sites around the Kaudiyala area of the Garhwal region, from the following latitude and longitude: 30°5'38" N and 78°24'54" E Figure 2.2. Attention was given to verify the lithological consistency of the blocks, their stratigraphy, and the presence of any structural discontinuities such as fractures or joints. In addition, the degree of surface weathering and associated alterations were carefully assessed to ensure that the collected material was representative of the fresh, unaltered formation. After thorough investigations of these parameters, sampling was undertaken from the inner section of the road cut, at ~ 100 m from the exposed face.

Table 2.2. *Stratigraphic succession of the study area. Reproduced from Kumar et al. (2013).*

Age	Formation		Dominant lithology
Cambrian	Tal		Quartzite, sandstone, shale, and limestone
Neoproterozoic	Krol	Krol E	Dolomite and limestone
		Krol D	Shale and slate
		Krol C	Dolomite
		Krol B	Shale and slate
		Krol A	Shale and slate
	Infra-Krol & Blaini		Shale, siltstone, slate, and boulder & Shale, limestone, slate, and boulder

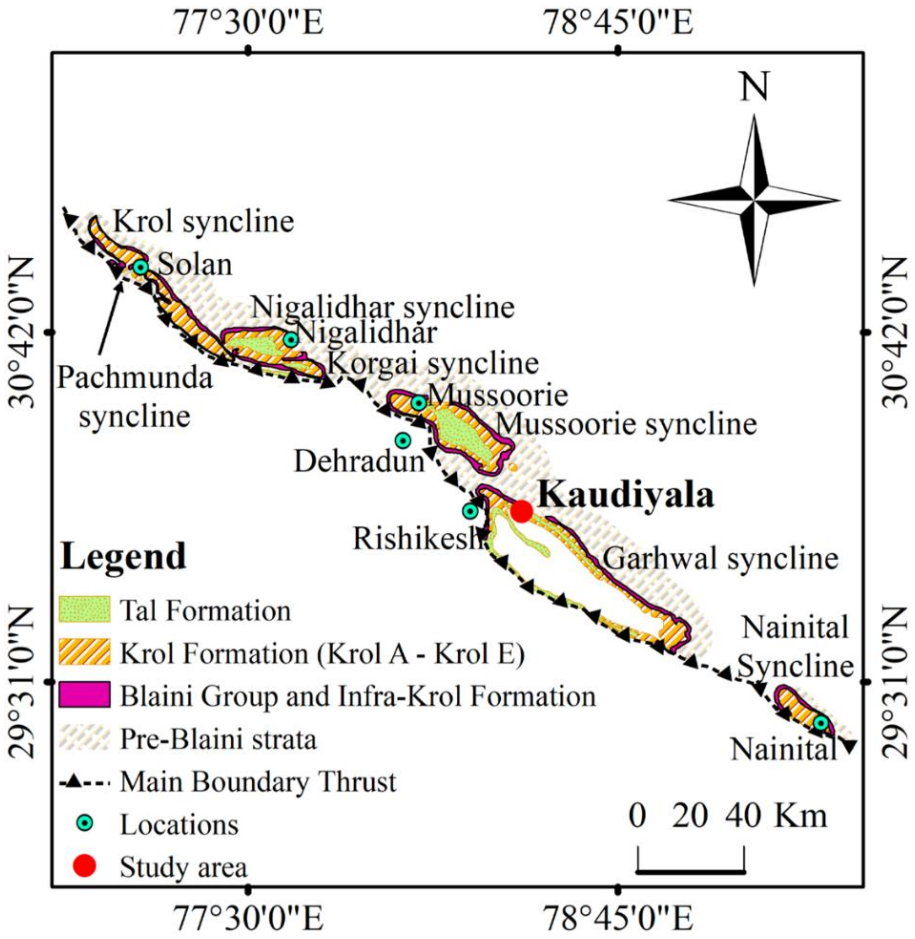

Figure 2.2. *Geological map of the Neoproterozoic-Cambrian Formations of the Lesser Himalayan region, northern India (modified after Singh and Rai, 1983).*

Chapter: 3
Multiscale Weathering-grade Classification of Chandpur Phyllite: Insights from *In situ* Observation and Laboratory Investigation

3.1. Introduction

Weathering is a key geomorphic process that results in physical disintegration and chemical decomposition of the rock (Welivitiya and Hancock, 2024). Weathering brings about substantial changes to rock properties through alteration in geochemical, geomechanical, mineralogical, and petrographic characteristics of rocks. The primary minerals from an unaltered rock transform into secondary or clay minerals during weathering, along with simultaneous modification of the rock's fabric characteristics and development of microfractures/pores (Irfan, 1996; Ram and Basu, 2019a; Luo et al., 2020). Broadly, weathering compromises the structural integrity of the rock masses and affects their performance in geotechnical applications (Gupta and Rao, 1998; Gupta and Rao, 2001; Basu et al., 2009; Hall et al., 2012; Khanlari et al., 2012; Moses et al., 2014; Momeni et al., 2017). Nevertheless, intense weathering of rock masses also possesses slope instability (Viles, 2013; Yee et al., 2023), large-scale mass movements (Lin et al., 2015), as well as the initiation and progression of landslides (Perri et al., 2014; Regmi et al., 2014). Therefore, weathering-grade characterization of rock masses has significant implications in rock engineering, as it helps in assessing rock behavior and defining adequate support for the construction of safe and sustainable structures.

Several researchers worldwide characterized the weathering-grade of rock masses through *in situ* field studies and substantiated the assigned weathering-grades through numerous qualitative and quantitative estimations. However, the six-fold weathering-grade classification scheme, as proposed by the International Society for Rock Mechanics (ISRM, 2015), is the most widely used in routine engineering practices, which closely

aligns with the weathering-grade classification schemes by British Standard BS 5930 (BSI, 1981), Dearman (1995), and Anon (1995). Although the said classification scheme is subjective, this is the primary means of classifying the weathering-grades of rock materials. However, the use of the ranges of physical and/or mechanical properties/indices and microstructural observations with reference to assigned weathering-grades can substantiate the classification and hence can minimize/eliminate the subjectivity. Therefore, identifying and assigning weathering-grades objectively and quantitatively by one or more index tests has obvious advantages and has therefore often been considered in rock engineering research (Martin and Hencher, 1986; Tuğrul, 2004; Basu et al., 2009; Khanlari et al., 2012; Momeni et al., 2017; Ram and Basu, 2019b).

Most research dealing with capturing the gradational changes of rock materials with reference to the degree of decomposition is limited to hard and crystalline rocks such as granite, granitoids, basalt, quartzite, argillite, gneiss, schist, and sandstone, etc., where the degree of alteration of constituent minerals helps in recognizing such gradation (Basu et al., 2009). However, their application to fine-grained and low-grade metamorphic rocks, particularly phyllites, remains scarce, as far as the existing literature is concerned. Marques et al. (2017) and Carvalho et al. (2020) classified the weathering-grade variations of phyllite formations in Australia and Brazil, respectively, following the weathering-grade classification scheme by ISRM (2015).

The conventional weathering-grade classification schemes, which provide a general assessment of degradation, are often subjective and are unable to capture critical microstructural changes. These microstructural changes directly or indirectly control the mechanical response of weathered rock. An overlook of underlying micro- to nanoscale changes, especially in soft and fine-grained rocks, limits the ability of these conventional classification schemes to provide a comprehensive and diagnostic understanding of rock

behavior with weathering. This emphasizes the need for the adoption of a multiscale approach ranging from macroscale to nanoscale to develop a comprehensive understanding of the impact of weathering-grade variations on mineralogical, mechanical, and morphological changes of the rocks.

In this study, Chandpur Phyllite, a soft fine-grained low-grade metamorphic rock from the Lesser Himalayan region, has been investigated. Due to the altitudinal variation, active tectonics, and subtropical climatic conditions, the Himalaya is considered one of the regions with the highest weathering intensity in the world (Chauhan et al., 2004; Kaushal et al., 2024). Mitra et al. (1988) noted that extensive seepage due to the subtropical climatic conditions of the Himalayan region requires a support assessment to ensure the stability and long-term performance of structures. Mehrotra et al. (1991) stated that the Himalayan region is generally characterized by soft, highly weathered lithologies with mineralogical compositions susceptible to chemical weathering processes. They further noted that the progressive strength degradation due to weathering presents a significant challenge for engineers in designing major structures. Mitra (1991) highlighted the impact of weathering on the long-term performance of an underground powerhouse constructed in the weak rock formations of the Lesser Himalayan region.

The current investigation adopts a two-stage, multiscale approach integrating macro-level field assessments with advanced and micro- and nanoscale laboratory investigations. The advanced laboratory techniques include X-ray Diffraction (XRD) analysis, contact angle measurement, Petrographic thin section analysis, Field Emission Scanning Electron Microscopy (FE-SEM) analysis, Atomic Force Microscopy (AFM) analysis, tribology test, and Low-Pressure Gas Adsorption (LPGA) analysis. This integrated approach enables comprehensive insights into the effects of weathering on rock properties.

Although the two-stage weathering-grade classification scheme is a common practice in routine rock engineering applications, incorporation of non-conventional techniques as employed in the present study provides a new approach to substantiate the assigned weathering-grade quantitatively. In particular, the inclusion of tribology (coefficient of friction and wear volume) test, contact angle measurements (wettability), LPGA (surface area and fractal characteristics), and AFM (surface heterogeneity) provides additional information about the physical and inherent characteristics of rock materials. In this study, an attempt has been made to validate whether non-conventional tests would be helpful for fine-grained, loose, and weakly anisotropic rocks such as phyllite, where small grain sizes often limit the effective identification of weathering-induced alterations through conventional testing methods. The non-conventional techniques were not used merely for supplementary testing, but specifically to validate the classified weathering-grades.

3.2. Methodology

The collected samples of the weathered phyllite from a naturally exposed outcrop (Figure 3.1) were transported to the laboratory for further analysis. Care was taken to preserve the weathered specimens during transportation. Due to the absence of unweathered phyllite at the exposure site, the fresh samples were obtained from a nearby location within the study area. Detailed information on the study area, along with the study area map, is provided in Section 2.1 (Chapter 2).

The weathering-grade classification in this study has been performed in two stages (Figure 3.2). In the first stage, macroscale subjective classification of the rock mass is performed through detailed *in situ* investigation of the weathered profile following the International Society for Rock Mechanics (ISRM, 2015) classification scheme, as

summarized in Table 3.1. The current study focuses on the weathering behavior of Chandpur Phyllite within the rock domain (W1–4), rather than the soil domain (W5, 6). The emphasis on weathering-grade study of the rock domain arises from the fact that the major infrastructures within the Chandpur Phyllite of the Lesser Himalaya are confined within the rock masses, making it essential to study the weathering-grades W1–4. The assigned weathering-grades were further substantiated in the second stage, which involves insights from multiscale quantitative and qualitative laboratory investigations such as XRD, contact angle, petrography, SEM, AFM, tribology, and LPGA analysis.

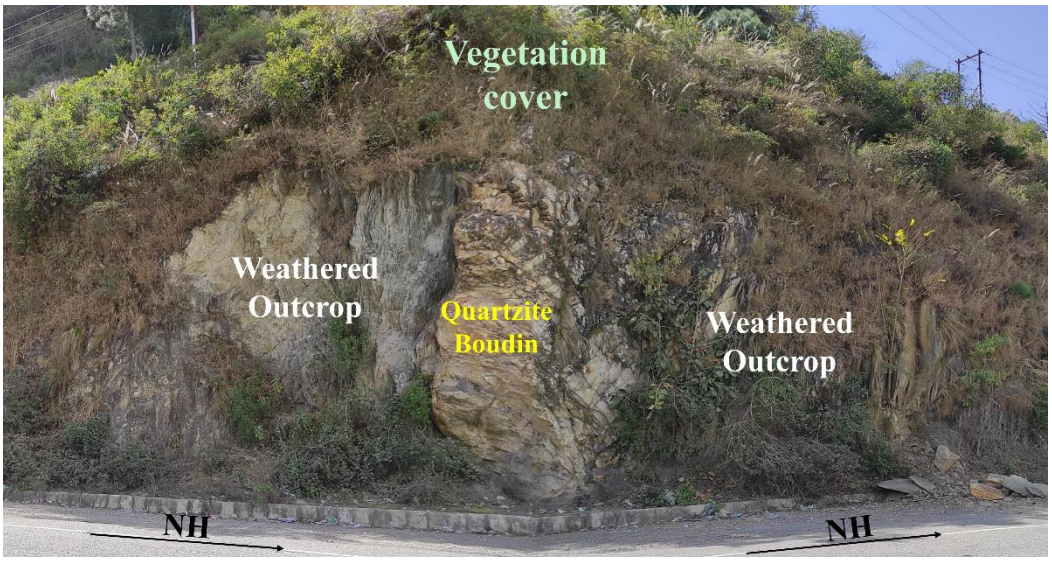

Figure 3.1. *Exposed weathered outcrop of Chandpur Phyllite.*

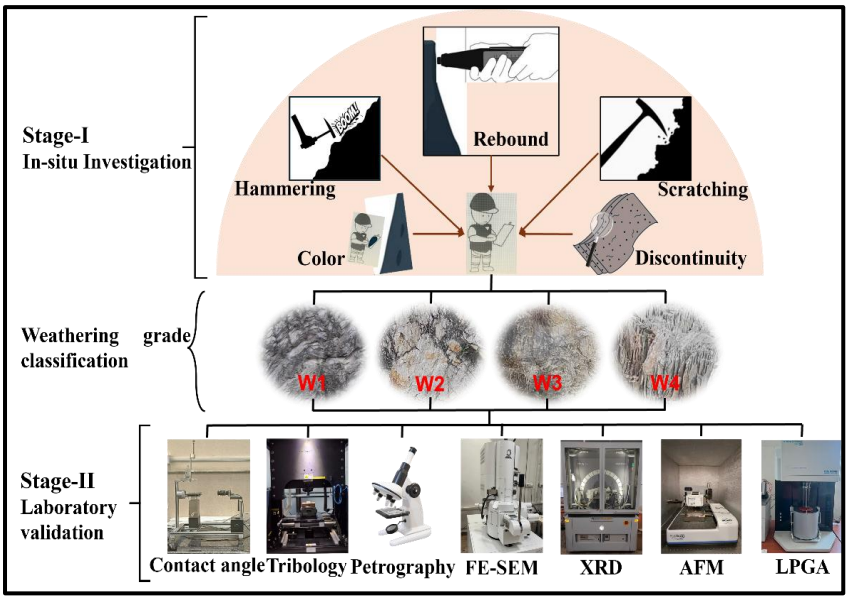

Figure 3.2. *A schematic diagram representing the two stages of the weathering-grade classification.*

Table 3.1. *Weathering-grade classification of rock mass (ISRM, 2015).*

Term	Symbol	Description	Grade
Fresh	F	Rock retains its original color with an unweathered appearance. Its surface is highly resistant to scratching with a geological pick, indicating significant hardness. When struck with a hammer, the rock produces a sharp, ringing sound, which is characteristic of intact and competent material.	W1
Slightly weathered	SW	Discoloration is confined to areas adjacent to joint surfaces, while the primary rock mass retains its original structure. The surface exhibits high hardness, as it is difficult to scratch with the point of a geological pick. When struck with a hammer, the rock emits a clear, ringing sound, indicative of a largely intact and competent material.	W2
Moderately weathered	MW	The rock material exhibits noticeable discoloration, with remnants of the original color appearing intermittently. Despite the color changes, the original mass structure remains well preserved. The surface can be scratched with the point of a geological pick, indicating moderate hardness. When struck with a hammer, the rock produces a dull to intermediate sound, suggesting partial loss of intactness.	W3
Highly weathered	HW	The entire rock material exhibits uniform discoloration, though the original mass structure remains largely intact. The surface resists indentation with the point of a geological pick, indicating moderate hardness. When struck with a hammer, the rock produces a dull sound, reflecting a reduction in material competence due to weathering.	W4
Completely weathered	CW	The rock material is completely discolored and has undergone extensive decomposition to a soil-like state, though the original mass structure remains discernible. The surface resists easy indentation with the point of a geological pick, suggesting residual firmness. When struck with a hammer, the material produces a dull sound, indicative of advanced weathering and significant loss of rock integrity.	W5
Residual soil	RS	The rock material has been entirely transformed into soil, with the original structure completely obliterated. The surface is easily and deeply indented by the point of a geological pick, indicating very low strength. When struck with a hammer, the material produces no sound, reflecting a complete loss of rock competence due to extreme weathering.	W6

3.2.1. In situ classification of Weathering-grades

To classify the weathering-grades, several macroscopic descriptions, including color variations, hammering sound, rebound hammer values, scratching characteristics, and discontinuities of the phyllite outcrop, were carried out in an intact condition. The *in situ* quantitative assessment of weathering-grade variation was also performed using a Silver Schmidt OS8200 L-type rebound hammer to validate the observations. Schmidt's rebound study has gained considerable success in rock weathering and geomorphic studies (Guglielmin et al., 2012). The impact was made horizontally and perpendicularly to the foliation planes. 15 random data points from each recognized weathering-grade stratum were collected in such a way that the distance between two data points was greater than the distance between two plunger diameters. A single impact was applied at each test point, and readings with no visible damage to the rock surface were considered for the investigation. Ten rebound values out of fifteen have been used after eliminating the smaller values, as suggested by ISRM (1978).

3.2.2. Laboratory Investigations of In situ Categorized Weathered Samples

3.2.2.1. X-ray diffraction (XRD) analysis

Compositional variations in the weathered rock samples were examined using X-ray diffraction (XRD) analysis. This analysis was performed on powder samples (100 mesh size) using an Empyrean Panalytical X-ray Diffractometer. This analysis is semi-quantitative because it allows the measurement of relative amounts of crystalline mineral phases rather than absolute concentrations. Each crystalline mineral phase exhibits its unique set of diffraction peaks, such that the intensity of peaks reflects the abundance of the phase in the sample. X-pert HighScore software (version 4023 000 04613, 2020) was used for phase identification and quantification using Rietveld refinement.

3.2.2.2. Contact Angle Measurement

This test was conducted using the Acam-NSC series Goniometer provided by Apex Instruments (India) to analyze the surface wettability of the weathered samples. The setup includes a flat platform, a light to illuminate the drop, and a high-speed camera to capture its images. The setup used in this study has a range from 0° to 180°, with a precision of ± 0.05°. The syringe holding the water as a test sample was infused at the rate of ~ 0.0012 ml min^{-1} onto the weathered surface (perpendicular to foliation) of phyllite. The water droplet emerged from the syringe as a pendant drop on the solid rock surface (10mm * 10mm * 5mm) and was further recorded by the high-speed camera.

3.2.2.3. Petrographic analysis

A thin-section analysis using petrographic examination was conducted to support and validate the classification of weathering-grades in the phyllite samples. Representative rock specimens from each weathering-grade were carefully selected and processed into a standard thin section slide of dimensions 25 mm * 75 mm * 2 mm. Subsequently, they were analyzed under the petrological microscope to get insight into microstructural changes due to the progressive weathering-grades.

3.2.2.4. FE-SEM analysis

The surface morphology of the weathered samples was examined using photomicrographs captured from solid 5 mm thick chip samples using a JEOL JSM-7900F FE-SEM microscope. A focused electron beam generated from the field emission gun results in high-resolution images of the sample surface. Examining small features like grain disintegration, surface evenness, surface etching, microfractures, etc., has

served as a crucial tool for understanding the progressive deterioration of mineral grains and textures with weathering-grades.

3.2.2.5. AFM analysis

It is an advanced 3D imaging technique used to characterize the structures quantitatively as well as qualitatively. The structural measurements are based on the physical forces between the cantilever and the surface. The cantilever consists of a fine tip made from hard materials, connected to an electronic system that detects its deflections as it scans across the sample surface, allowing precise measurement of surface topography, including heights and depths. Imaging was performed in a contact mode (preferred for rough samples) using a Bruker DM FASTSCAN3-SYS system equipped with a SCANASYST-PIT-V2 cantilever tip. From each weathering-grade, a chip sample with the dimensions of ~ 15 mm * 15 mm * 2 mm was prepared for the analysis. Further, three different regions within the sample were scanned with a scan area of 5 µm * 5 µm. The acquired images were analyzed using the Gwyddion software (version 2.65.20240419, 2024), which is an open-source software to statistically evaluate the surface and morphological features of the weathered samples.

Various roughness parameters derived from the AFM images (Table 3.2), such as mean roughness (R_a), surface skewness (R_{sk}), root mean square roughness (R_q), and kurtosis coefficient (R_{ku}), were calculated and proved effective in assessing the evolution of surface roughness with increasing weathering-grade.

Table 3.2. *Roughness parameters calculated from AFM analysis using standard equations, as adopted from Nilankar et al. (2024b).*

Parameters	Description	Measure	Eq. no.
R_a	R_a represents the arithmetic average of the absolute deviations of surface height values from the mean plane	$R_a = \frac{1}{n}\sum_{i=1}^{n}\lvert Z_i\rvert$ Here, Z_i: surface height at position i relative to the mean plane, and n represents the total number of data points in the image grid.	Eq.3.1
R_q	R_q is defined as the square root of the average of the squared height deviations from the mean data plane	$R_q = \sqrt{\frac{\sum Z_i^2}{n}}$	Eq.3.2
R_{sk}	R_{sk} shows the asymmetry of the surface height distribution relative to the mean plane	$R_{sk} = \frac{1}{nR_q^3}\sum_{i=1}^{n} Z_i^3$	Eq.3.3
R_{ku}	R_{ku} describes the sharpness or flatness of the surface height distribution relative to the mean plane	$R_{ku} = \frac{1}{nR_q^4}\sum_{i=1}^{n} Z_i^4$	Eq.3.4

3.2.2.6. Tribology Test

To calculate the Coefficient of Friction (CoF) of weathered phyllite, a well-polished thin film sample of dimensions 15 mm * 15 mm * 5 mm for each weathering-grade was prepared. The prepared samples were subjected to a tribology test using the MFT 5000 Tribometer with High Frequency Reciprocating Module (HFRR). In this module, a ceramic ball slides against a thin film of rock with a stroke of 1 mm at a high frequency. The test parameters used in this analysis are mentioned in Table 3.3. In addition to calculating the CoF, the wear track morphology was analyzed using a Lambda profilometer equipped with a 20x optical objective lens to quantitatively assess the wear volume of the samples.

Table 3.3. *Test parameters of the tribology test for CoF and wear measurements.*

Samples: Phyllite	
Normal force 10N	Wear ring diameter 5mm
Speed 100 rpm	Wear ball diameter 6mm

Test duration 10 min	Frequency 50 Hz

3.2.2.7. LPGA analysis

Mineral disintegration during weathering often leads to the formation of voids and microcracks, enabling LPGA analysis highly suitable for the study of adsorption behavior. To investigate this, LPGA analysis was performed on the powder samples of 100 mesh size in the presence of nitrogen (N_2) gas through a MicrotracBEL BELSORP Max II Brunauer-Emmett-Teller (BET) analyzer. Although N_2 adsorbate does not represent the natural environmental conditions experienced by the rock, it provides an effective means for comparing the relative changes in adsorption across various weathering-grades.

3.3. Results

3.3.1. Stage 1: In situ Weathering-grade Classification

The *in situ* field investigation was performed on the exposed weathered outcrops of phyllites in the study area following the ISRM (2015) (Table 3.1). The characteristics of phyllite with different weathering-grades are shown in Table 3.4. The W1 samples show a grayish-silver tone with well-developed and tightly spaced discontinuities (foliation planes). For this weathering-grade, fractures are not prominent in hand-specimens, but their extent is well pronounced on a larger scale in the field. As weathering progressed, discoloration became pronounced, and discontinuities widen. The color transition progresses from a grayish-silver (W1) to a light gray (W2), then to a light- to medium grayish brown (W3), and finally to a warm grayish brown (W4). Discontinuity (foliation) widened progressively with advancing weathering-grades, reaching its maximum expansion in W4 samples, where openings were notably dramatic compared to lower grades. Beyond widening, weathering also degraded the inherent structural features of foliations, i.e., small-scale minor folds (puckers). To assess the progressive degradation

of rock strength across weathering-grades, the resistance to scratching was evaluated using the sharp pick end of the geological hammer. W1 and 2 samples exhibit high resistance, with shallow scratches (< 1 mm). W3 samples are easily scratched up to 1–2 mm depth, while the W4 samples displayed negligible cohesion, having scratches greater than 3 mm depth.

For quantitative validation, the above observations were correlated with the *in situ* rebound hardness value (R_L) and measured density values. The rebound value data shown in Table 3.4 across varying weathering-grades (W1–4) reveal a consistent decline in surface hardness and strength characteristics with increasing degrees of weathering.

Table 3.4. *Characteristics of phyllite with different weathering-grades based on in situ observations.*

Characteristics	**Weathering-grades**			
	W1	**W2**	**W3**	**W4**
Surface appearance				
Description	Hard and intact	Hard, slight alteration	Moderately stiff	Soft and friable
Color	Grayish silver	Light gray	Light-medium grayish brown	Warm grayish brown
Discontinuity (foliations)	Well-developed and tightly spaced	Well-developed and slightly tight spacing	Indistinct and loose	Degraded and widely expanded
Scratching	High resistance, shallow (< 1 mm) depth	High resistance, shallow (< 1 mm) depth	Easily scratched up to 1–2 mm depth	Negligible cohesion, scratches > 3 mm in depth
Range of rebound values	41–50	40–46	25–31	13–20
Average rebound values	46	43	29	16
Avg. Density	2.64	2.62	2.52	2.28

3.3.2. Stage 2: Validation of In situ Weathering-grades using Multiscale Analysis

3.3.2.1. XRD analysis

XRD analysis of the phyllite samples indicates a mineralogical composition primarily comprising quartz, mica (muscovite and biotite), feldspar (microcline), chlorite,

and clay (kaolinite, sepiolite, and smectite) minerals. Comparative evaluation of the diffraction patterns for the weathered samples (Figure 3.3) reveals notable mineralogical transformations with progressive weathering. In particular, the intensity of diffraction peaks corresponding to mica and chlorite reduces significantly in the W4 samples, signifying substantial mineral degradation. Conversely, diffraction peaks associated with clay minerals become more pronounced in the weathered samples, indicating the formation or enrichment of the clay minerals. The dominance of clay minerals, along with the degradation of mica and chlorite, indicates the influence of both chemical alteration and physical disintegration during the weathering process. Relative quantification, performed via Rietveld refinement using X-pert HighScore software (version 4023 000 04613, 2020), supports these observations. As presented in Table 3.5, the relative concentrations of quartz and feldspar remain largely invariant across weathering-grades, while mica and chlorite contents decrease significantly by 50.4 % and 27.52 %, respectively, accompanied by a progressive increase in clay mineral abundance by 56.25 % in the W4 sample compared to W1.

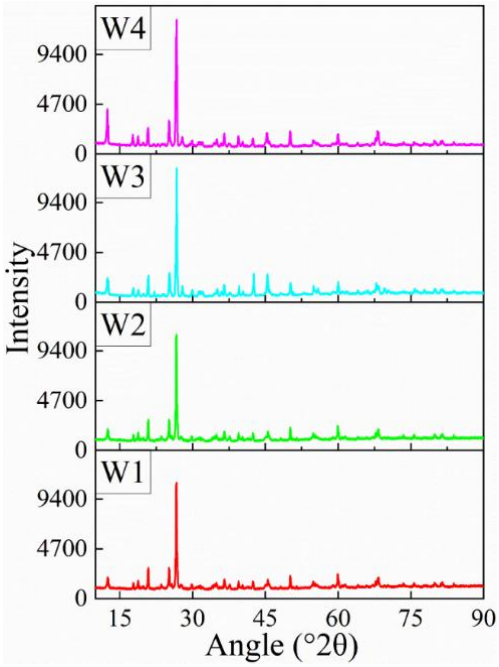

Figure 3.3. *Representative XRD intensity plot for weathering-grades W1–4.*

Table 3.5. *Relative mineral concentrations across weathering-grades W1–4.*

Phase	2θ (°)	Quantity (%)			
		W1	W2	W3	W4
Quartz	26.6	12.98	12.96	12.92	12.63
Mica (muscovite and biotite)	26.6 and 26.8	38.01	35.23	28.98	18.85
Feldspar (microcline)	27.4	4.98	4.98	4.92	4.62
Chlorite	18.6	5.85	5.57	5.01	4.24
Clay (kaolinite, sepiolite, and smectite)	12.3, 28, and 18	38.18	41.26	48.17	59.66
Weighted total		100	100	100	100

3.3.2.2. Wettability measurement

The wettability of samples across all weathering-grades was measured through contact angle measurement using deionized water to assess the affinity of water molecules towards the phyllite matrix. W1 sample exhibited the highest contact angle (45.12º), indicating a relatively less reactive surface (Figure 3.4). Whereas, at higher weathering-grades, the contact angle value is observed to decrease with the measured values of 38.9º, 30.92º, and 25.86º for W2–4 samples, respectively, reflecting the higher affinity towards water and enhanced surface wettability.

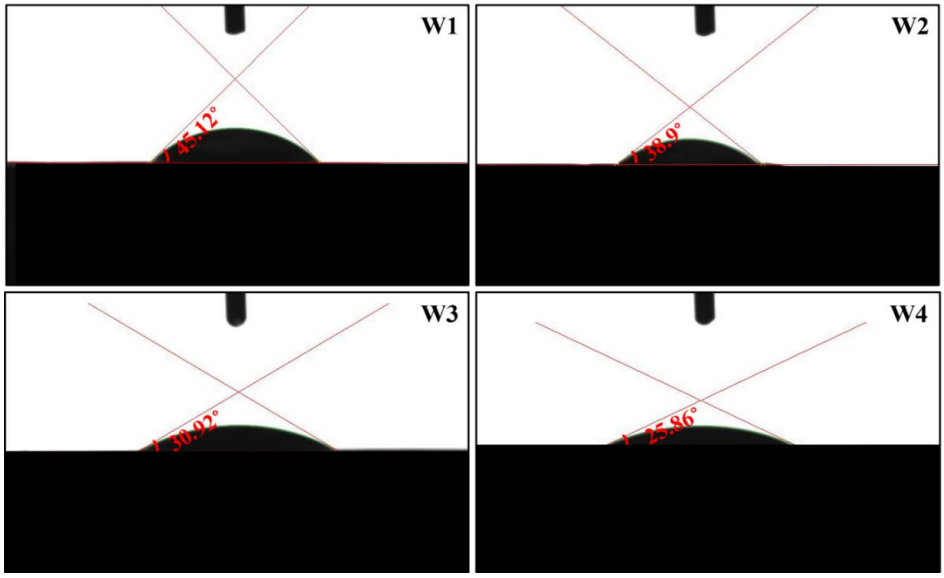

Figure 3.4. *Progressive deterioration in contact angle values with increasing weathering-grades.*

3.3.2.3. Petrographic analysis

The petrographic analysis under a petrographic microscope was performed on thin sections prepared from the weathered samples, as shown in Figure 3.5. The W1 sample exhibits well-defined mineral grains showing minimal signs of alteration. The image further highlights the primary mineral phases, including muscovite (Mus), biotite (Bt), and quartz (Qtz), each displaying its characteristic optical properties.

The microfractures observed in mineral grains are indicative of metamorphism. Grain boundaries (GB) and grain-to-grain (G-G) contacts appear sharp and continuous, reflecting an unaltered framework. In contrast, the W4 sample displays significant mineralogical and textural degradation. Furthermore, the petrographic image of W4 illustrates a pronounced breakdown of the original mineral matrix. Grain boundaries become irregular, and G-G contacts are notably loose, indicative of loss of cohesion due to mineral disintegration. Additionally, the widespread presence of secondary weathering products (probably clay-rich materials) was observed. This transformation from W1–4

reflects the combined effects of physical and chemical weathering, which alter mica, feldspar, and chlorite. Structurally weak clay mineral phases in the most weathered samples.

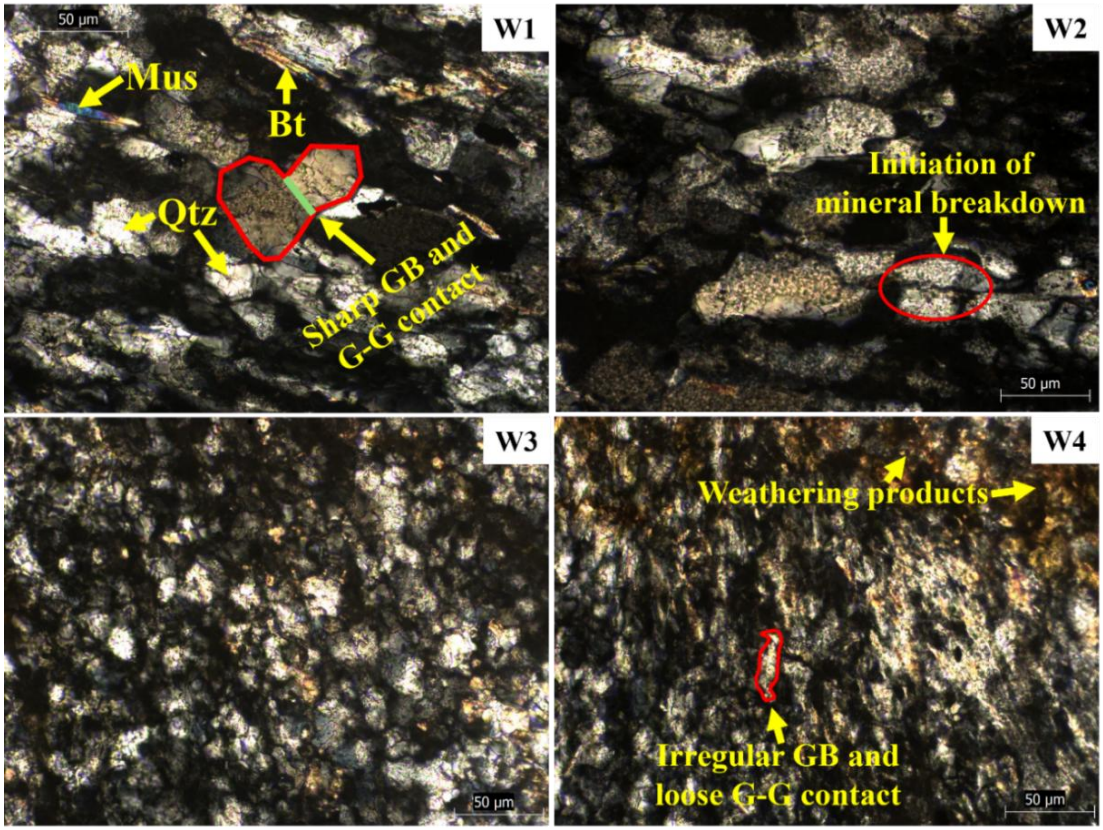

Figure 3.5. *Mineralogical and textural transformations of Chandpur Phyllite with weathering-grades through petrographic thin section analysis (Note: GB is Grain Boundary and G-G is Grain to Grain).*

3.3.2.4. FE-SEM analysis

The FE-SEM analysis demonstrates a clear and progressive transformation of microstructural characteristics. For each weathering-grade, multiple specimens were examined, and > 15 photomicrographs were acquired from different regions of the sample surface and at varying magnifications ranging from x200 to x10000. The images were collected from spatially distinct areas to ensure that local heterogeneity associated with

mineral distribution, microfractures, and weathering features is adequately captured. The representative photomicrograph of each weathering-grade is shown in Figure 3.6.

The images at x1000 magnification were selected as they provide an optimal balance between field of view and microstructural detail, enabling better visualization of weathering-induced features over a relatively larger surface area compared to higher magnifications. The surface morphology of the W1 sample appears smooth, with well-defined, closely packed micaceous foliations. The integrity of the characteristic features of the phyllite, such as platy structure, alignment of the micaceous minerals, and small-scale minor folds (puckers), are well preserved within the fresh sample. As the weathering progressed to W2, the roughness within the sample slightly increased. However, the general fabric, such as micaceous foliations, remained preserved. In the case of W3 phyllite, the surface in the photomicrographs appeared to be highly deteriorated with significant pores and fractures. The characteristic foliations are indistinct. The surface appears to be more rough, with a higher degree of fragmentation and disaggregation of mineral grains. The disaggregation of mineral grains was likely caused by the combined effect of physical and chemical weathering, resulting in the breakdown of phyllosilicate structures. Notably, a few clay minerals were also observed within the photomicrographs, suggesting mineral alteration and secondary mineral formation. In the W4 sample, the FE-SEM image shows a heavily altered surface dominated by clay minerals. The original foliation is almost entirely damaged, and the rock matrix appears to be smoothed due to the accumulation of fine clay particles within the asperities.

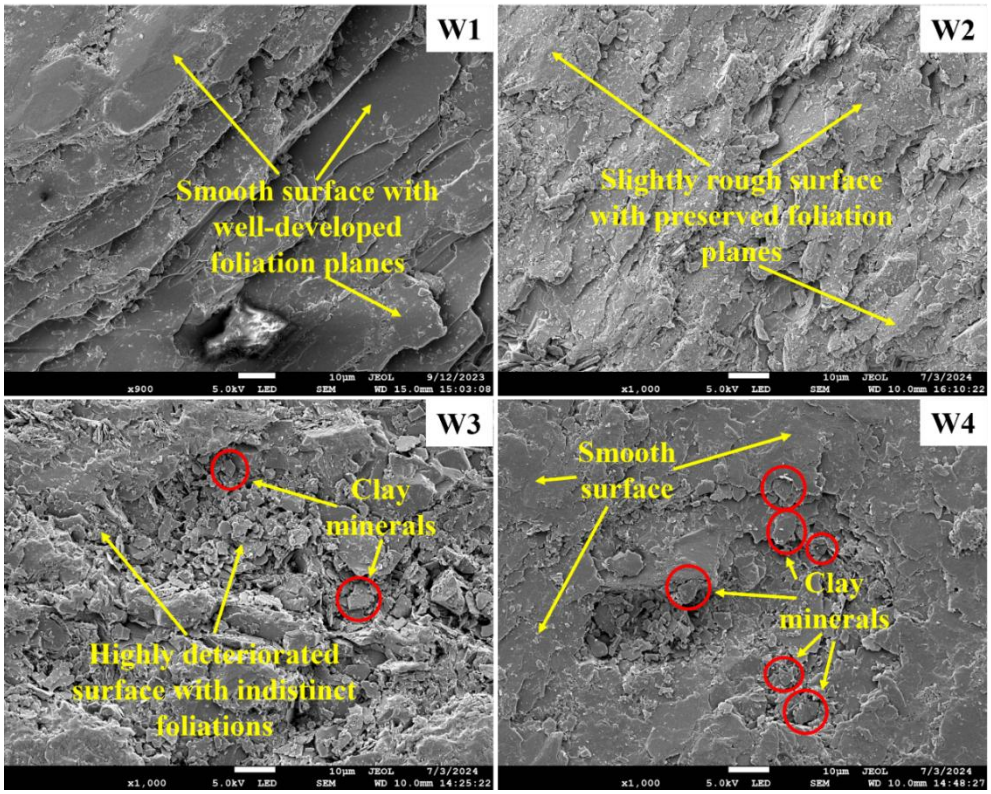

Figure 3.6. *Representative FE-SEM photomicrographs of Chandpur Phyllite various weathering-grade samples.*

3.3.2.5. Roughness Parameters determination using AFM analysis

For AFM analysis, at each weathering-grade, multiple scans have been carried out between 1 µm * 1 µm and 5 µm * 5 µm. Among these, the 5 µm scan size images were selected for the presentation as a representative of the weathering-grade because they cover the larger surface area and give a better representation of the surface heterogeneity. In contrast, the 1 µm scan size images capture highly localized features and are more sensitive to small-scale variations.

Phyllite samples across varying weathering-grades (W1–4) reveal a distinct evolution in surface topography and roughness characteristics, as shown in Figure 3.7 and Table 3.6. These indicate progressive mineral degradation and secondary phase formation. The W1 sample exhibits a relatively smooth surface topography, with a R_a of 36.17 nm and R_q of 45.69 nm. Its near-zero R_{sk} of -0.13 and very low R_{ku} of 0.1 indicate

a mildly asymmetric surface dominated by shallow valleys and minimal topographic extremes. As weathering advances to W2 and 3, there is a substantial increase in surface irregularity. W2 shows a marked rise in roughness (R_a = 113.49 nm; R_q = 131.91 nm), with a more negative R_{sk} of -0.25, suggesting a surface topography increasingly characterized by depressions or voids, possibly due to selective mineral dissolution. Its R_{ku} of 1.06 reflects a slight increase in the sharpness of these features. W3 presents the highest roughness values (R_a = 118.55 nm; R_q = 141.27 nm), continuing the trend of negative R_{sk} of -0.28 and slightly higher R_{ku} of 1.08, indicating further modification of surface topography due to mineral disintegration. Interestingly, in the W4 sample, both roughness values decrease notably (R_a = 40.67 nm; R_q = 51.79 nm), with an even more negative R_{sk} of -0.30 and a R_{ku} value of 0.58.

This suggests the surface has become more homogenized due to the accumulation or infilling of weathering byproducts such as clays. The corresponding 3D AFM images verify this quantitative interpretation, with W1 and 4 exhibiting smoother, less textured surfaces, whereas W2 and 3 display greater peak-valley heights and more heterogeneous topographies. These trends collectively indicate that surface roughness peaks at intermediate weathering stages (W2 and 3) and then diminishes in the later stage (W4), likely due to smoothing via clay deposition and mineral transformation.

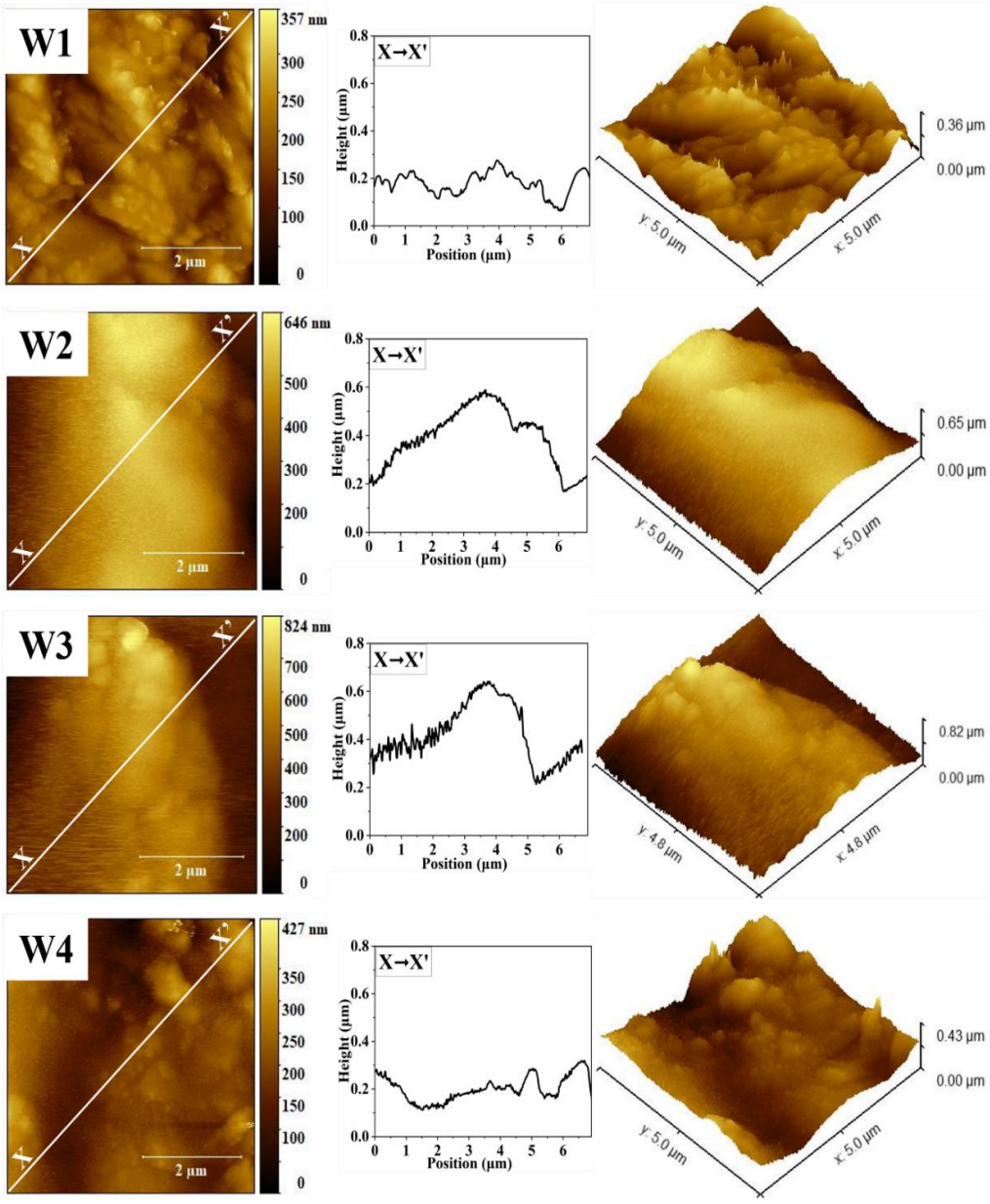

Figure 3.7. *Representative surface topography of weathered phyllite. Note: The left side image is the 2D surface topography, the center image is the profile of the topography along the line XX', and the right-side images show the 3D image of the topography at each grade.*

Table 3.6. *Summary of roughness parameters for each weathering-grade.*

Weathering-grade	Roughness parameters			
	Avg. R_a (nm)	Avg. R_q (nm)	Avg. R_{sk}	Avg. R_{ku}
W1	36.17	45.69	-0.13	0.1
W2	113.49	131.91	-0.25	1.06
W3	118.55	141.27	-0.28	1.08
W4	40.67	51.79	-0.3	0.58

3.3.2.6. Coefficient of Friction (CoF) and Wear Volume

Phyllite samples of varying weathering-grades, subjected to high-frequency reciprocating tribology tests to evaluate their frictional response, are shown in Figure 3.8. The CoF did not follow a consistent increasing or decreasing pattern with weathering-grades but instead showed a non-linear (fluctuating) trend. The CoF exhibits a decreasing trend from W1–2, followed by an increasing trend up to W3, and subsequently decreased again through W4. The W1 sample exhibited the highest CoF value of ~ 0.0708, whereas the W4 sample recorded the lowest value at around 0.0327. Intermediate weathering-grades showed fluctuating CoF values, with W2 averaging 0.0435 and W3 increasing to 0.0641. The minimum, maximum, average, and standard deviation values of the CoF for different weathering-grades are shown in Table 3.7. Several factors, including contact area, surface asperity characteristics, intrinsic material properties, and many others, influence CoF. As a result, the relationship obtained between increased weathering-grade and CoF is non-linear, depending on several parameters.

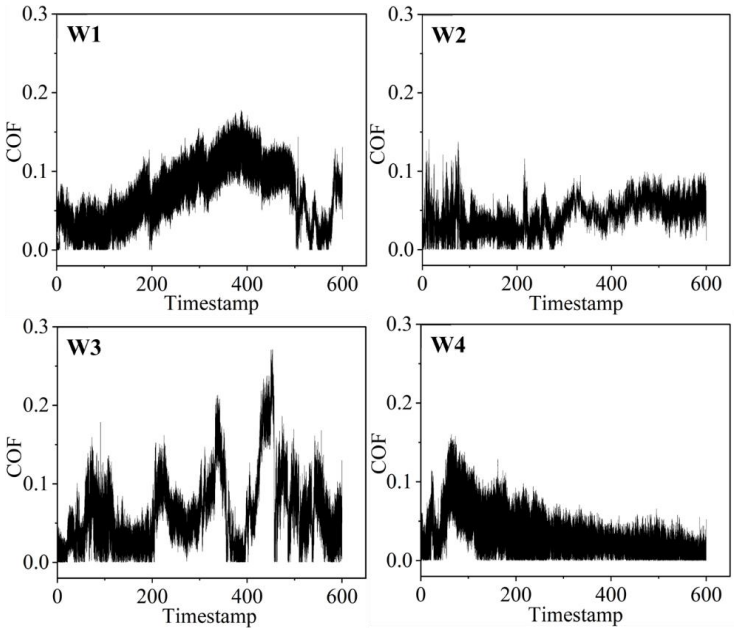

Figure 3.8. *Representative coefficient of friction (CoF) of phyllite with different weathering-grades.*

The wear morphology, as examined through a Lambda profilometer with a 20x optical lens, revealed significant differences across the different weathering-grades (Figure 3.9). A consistent increase in wear volume was observed with increasing weathering-grades. W1 samples display shallow grooves and minimal surface damage, corresponding to a wear volume of ~ 0.003 mm^3 and a maximum wear depth of around 22 µm, indicating limited material removal. W2 samples showed an increased wear volume of 0.006 mm^3 and a maximum wear depth of ~ 46 µm, reflecting greater surface degradation. In contrast, W3 and 4 samples exhibit more pronounced wear scars with well-developed groove patterns. Both W3 and 4 samples recorded a wear volume of ~ 0.009 mm^3 and a maximum wear depth of about 48 µm, suggesting enhanced material removal due to progressive weathering of the rock matrix.

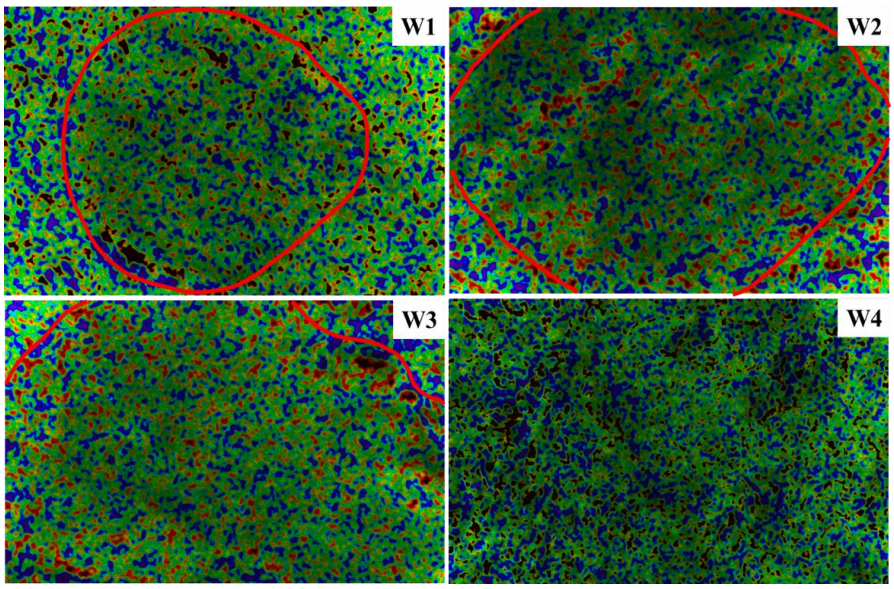

Figure 3.9. *Wear morphology of a representative weathering-grade sample of phyllite.*

3.3.2.7. LPGA analysis

The N_2-based LPGA analysis in this study demonstrated itself to be a robust method for understanding the nanoscale alterations induced by weathering. The

adsorption-desorption isotherms, as depicted in Figure 3.10, exhibit a progressive increase in the volume of gas adsorbed within the pores/microfractures with increasing weathering-grade. This reflects an enhanced surface area and new pore/microfracture development with weathering due to mineral breakdown and structural alterations. The Brunauer-Emmett-Teller (BET) model-based surface area shows a significant increase from 1.0032 $m^2 g^{-1}$ in W1 and 2, to 1.2805 $m^2 g^{-1}$ and 1.4132 $m^2 g^{-1}$ in W3 and 4 samples. This highlights the surface development with progressive weathering-grades. The increased surface area at a higher weathering-grade suggests the mineral disintegration and generation of microfractures. The average pore width obtained from the BJH (Barrett-Joyner-Halenda) model also shows a similar trend, having a value of 12.102 nm in the W1 and 2 samples, increasing to 16.14 nm and 19.04 nm in the W3 and 4 samples.

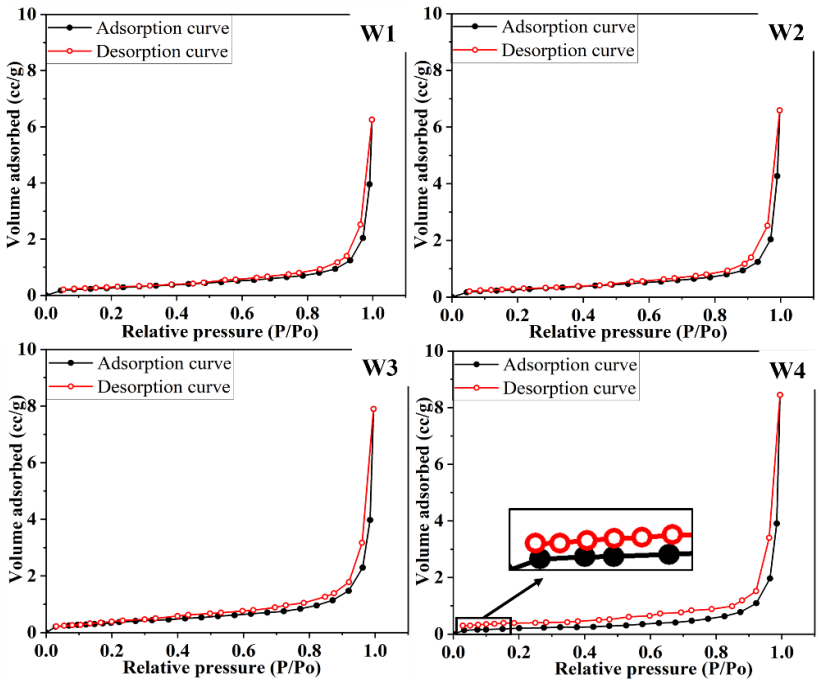

Figure 3.10. *LPGA isotherm curve for different weathering-grade phyllite.*

Table 3.7. *Minimum, maximum, average, and standard deviation values of some key parameters.*

Parameters	WG	Min.	Max.	Avg.	Std.
RL	W1	41	50	46	3.15
	W2	40	46	43	2.12
	W3	25	31	29	1.69
	W4	13	20	16	2.39
Ra	W1	29.18 nm	44.39 nm	36.17 nm	5.38 nm
	W2	110.12 nm	116.82 nm	113.49 nm	2.14 nm
	W3	114.13 nm	128.58 nm	118.55 nm	5.34 nm
	W4	33.12 nm	21.12 nm	40.67 nm	6.1 nm
CoF	W1	1.07E-6	0.29	0.07	0.04
	W2	2.34E-7	0.14	0.04	0.02
	W3	3.02E-6	0.37	0.06	0.05
	W4	1.01E-7	0.22	0.03	0.03
CA	W1	40º	61.86º	45.12º	8.39º
	W2	34.17º	41.98º	38.9º	2.59º
	W3	27.63º	33.01º	30.92º	1.87º
	W4	20.72º	28.19º	25.86º	2.81º

Note: R_L: Rebound value, R_a: Mean roughness, CoF: Coefficient of friction, and CA: Contact angle.

3.4. Discussions

3.4.1. Quantitative Investigation

Quantitative assessments were conducted using Pearson correlation (between weathering-grades and individual parameters, as well as between the two individual parameters), regression analysis (between weathering-grades and individual parameters), and paired t-tests (between weathering-grades and individual parameters). The following subsections provide detailed information on the statistical investigation of assigned weathering-grades and key indicator parameters.

3.4.1.1. Pearson Correlation Matrix

The Pearson correlation coefficient (r), as shown in Figure 3.11, ranges from -1 to +1, where +1 indicates a strong positive correlation, -1 a strong negative correlation, and 0 signifies no correlation. Weathering-grade shows a strong positive correlation with clay content (r = +0.97), wear volume (r = +0.94), and surface area (r = +0.95), suggesting enhanced mineral alteration, surface development, and particle disintegration with

increasing weathering intensity. Conversely, weathering-grade shows a strong negative correlation with rebound value ($r = -0.97$), contact angle ($r = -1.00$), and density ($r = -0.92$), indicating mechanical weakening, increased surface hydrophilicity, and reduced compactness. Other variables, such as roughness parameters (mean roughness, RMS roughness, surface skewness, and kurtosis coefficient), coefficient of friction, and fractal dimension, show a moderate correlation with the weathering-grade.

Overall, the relative sensitivity analysis indicates that clay content, wear volume, surface area, rebound value, contact angle, and density are highly sensitive indicators of weathering progression, whereas other variables are moderately sensitive indicators of weathering progression. The Pearson correlation coefficients among the variables were also evaluated. Density and rebound value indicate a strong positive correlation ($r = +0.97$). Clay content has a strong negative correlation with both density and rebound value ($r = -0.99$), indicating its significance in mechanical degradation. Contact angle shows a strong positive correlation with rebound value ($r = +0.97$) and a strong negative correlation with clay content ($r = -0.95$), suggesting the influence of mechanical degradation and mineralogical alteration on surface wettability. Mean roughness and RMS roughness are strongly correlated ($r = +1.00$) with each other, but with other variables, they mostly show moderate to weak correlations.

The coefficient of friction, which is one of the important variables, shows a moderate correlation with density, rebound value, and clay content, indicating that the frictional behavior of the material is not dependent on a single parameter. The surface area and the wear volume have been observed to have a strong positive correlation with clay content ($r = +0.96$ and $r = +0.84$) and a negative correlation with rebound value and density. The fractal dimension, which indicates complexity, has a moderate correlation with rebound value ($r = +0.63$), density ($r = +0.79$), and clay content ($r = -0.70$).

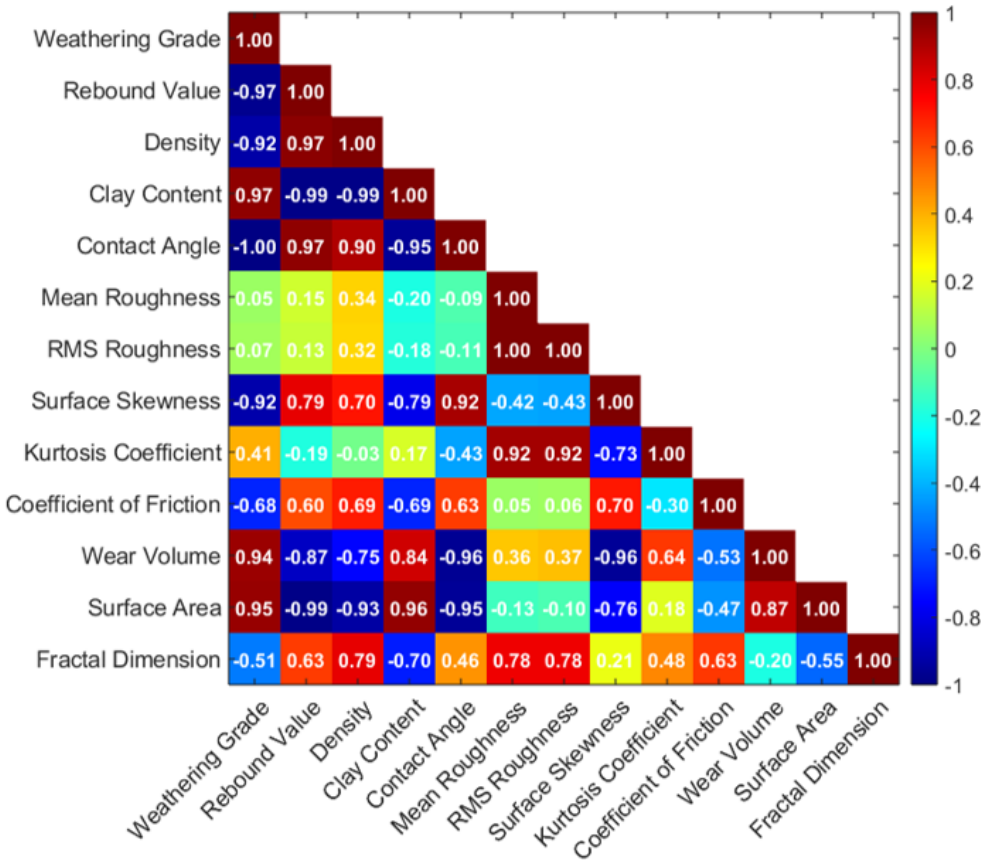

Figure 3.11. *Pearson correlation matrix showing the relationship among weathering-grades with individual parameters and between the two individual parameters.*

.

3.4.1.2. Regression analysis

To establish the regression equation, a regression model was developed by considering the weathering-grade as an independent variable and the individual parameters as dependent variables of the weathering-grade (Figure 3.12). The regression equation between the two experimental parameters was not developed because one individual parameter depends on several other parameters.

The regression analysis between weathering-grade and experimental parameters shows a systematic trend. The rebound number and the contact angle exhibit a strong decreasing non-linear trend with increasing weathering-grade, with $R^2 = 0.99$, indicating

high reliability. This inverse relationship is consistent with the strong negative correlation observed during the Pearson correlation analysis.

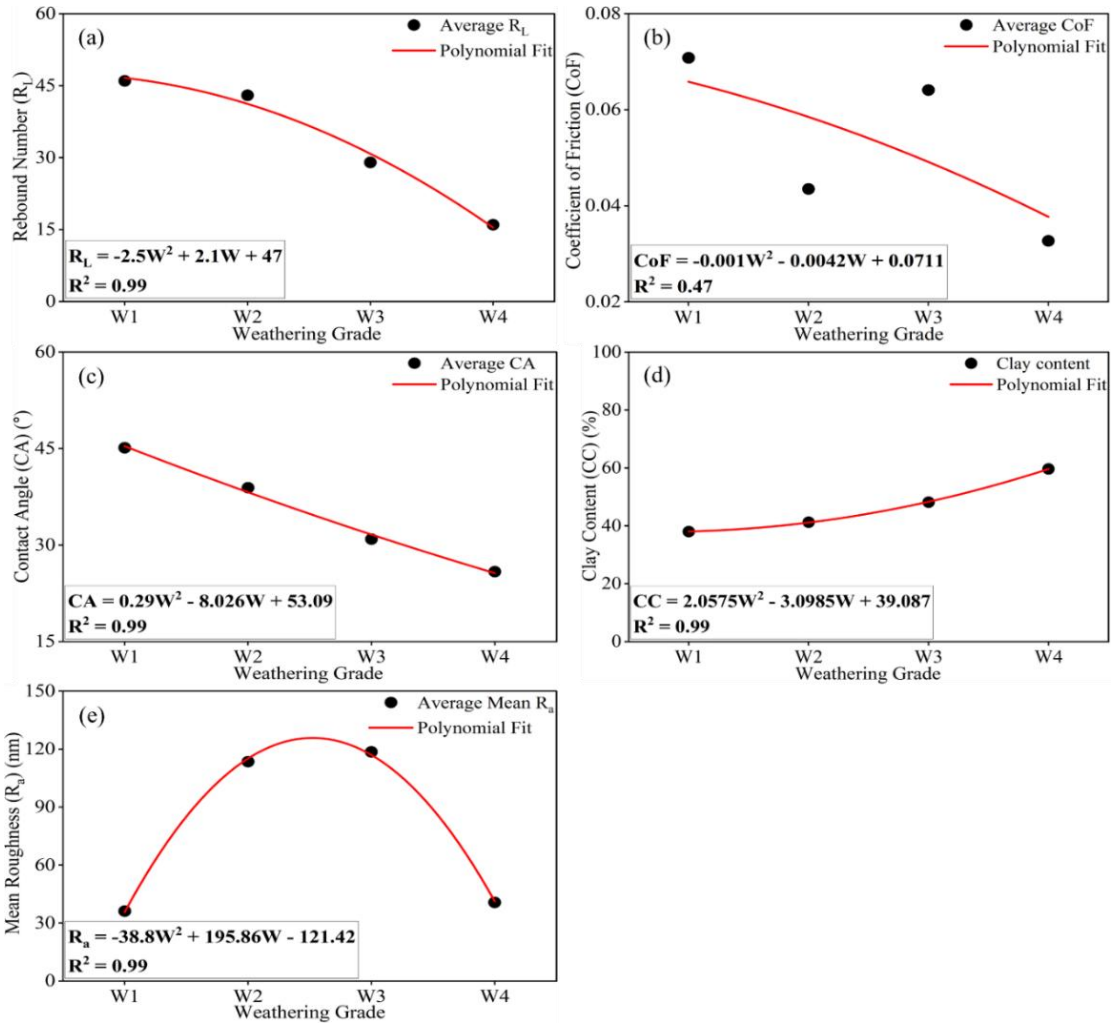

Figure 3.12. *Simple regression analysis results of (**a**) RL vs. weathering-grade, (**b**) CoF vs. weathering-grade, (**c**) contact angle vs. weathering-grade, (**d**) clay content vs. weathering-grade, and (**e**) Ra vs. weathering-grade.*

In contrast, clay content shows a strong increasing non-linear trend with weathering-grade, with $R^2 = 0.99$, and aligns closely with a strong positive Pearson correlation analysis. The coefficient of friction shows highly scattered values with a non-monotonic (initially decreasing, then increasing, and again decreasing with increasing weathering-grades) trend and a low coefficient of determination ($R^2 = 0.47$), indicating

low reliability. The mean roughness also shows a non-monotonic (initially increasing and then decreasing with increasing weathering-grades) trend, with a strong R^2 = 0.99. Although the regression fit is strong, the Pearson correlation of mean roughness with weathering-grade is moderate. This indicates that roughness does not change linearly as weathering progresses.

3.4.1.3. Paired t-test

To assess the significant difference between the two groups (weathering-grade and key parameters), paired *t*-test analysis has been carried out. It is an important statistical method to evaluate the mean differences between two groups and can help to determine if the weathering has a significant impact on rock mass properties. The calculated *p*-value from the paired t-test has been compared against the significance level (0.05) to determine whether the observed differences are statistically significant. As shown in Table 3.8, the paired *t*-test results confirm statistically significant changes with weathering progression, as their *p*-values are below the significance level. Overall, the paired *t*-test results confirm that rebound value, clay content, wettability, surface roughness, and tribological properties are all significantly influenced as weathering progressed in Chandpur Phyllite.

Table 3.8. *Paired t-test results obtained by comparing the weathering-grades with individual parameters.*

Parameters	*p*-value
R_L	0.026
CC	0.002
CA	0.007
R_a	0.045
CoF	0.033
WV	0.031

Note: CC: Clay content and WV: Wear volume.

3.4.2. Qualitative Interpretation

The *in situ* evaluation of weathering-grades of phyllites exhibits a change in color from greyish-silver tone in the unweathered state (W1) to greyish-brown color at W4. This could mostly be attributed to oxidation of iron-rich minerals like biotite and chlorite, which, during weathering, produce a warm greyish-brown tint to rock materials. The increased discontinuity spacing is also prominent with increasing weathering-grade of rock masses, with higher spacing being mostly pronounced at W4. Measured density and rebound hammer values were used to quantitatively substantiate the assigned weathering-grades, and the values infer a substantial drop in rock properties at W3 and 4 (Table 3.4), which is attributed to weathering-induced microstructural changes. The decreasing rebound value with progressive weathering-grade is shown in the regression analysis (Figure 3.12a).

The *in situ* assigned weathering-grades were validated through a comprehensive multi-scale laboratory investigation approach, viz., petrography, SEM, XRD, LPGA, tribology test, AFM-based roughness measurements, and wettability test via contact-angle analysis. The phyllite primarily comprises quartz, mica (muscovite and biotite), feldspar (microcline), chlorite, and clay minerals (kaolinite, sepiolite, and smectite). Although the mineral composition was similar across the weathering-grades, notable variations were recorded in the intensity of mineral peaks, particularly for clay minerals such as kaolinite, which displays a marked increase in intensity in the W4 phyllite (Figure 3.3). The regression analysis (Figure 3.12d) indicate that clay content continuously increase as weathering progress. The intensity peaks and relative mineral compositions suggest that primary minerals, e.g., quartz, mica, feldspar, and chlorite, degrade through combined physical and chemical weathering, forming secondary clay minerals (Kaushal et al., 2024). However, quartz displays almost no degradation, feldspar shows moderate

degradation, while both mica and chlorite reveal significant weathering (Table 3.5). Micas, particularly biotites, are highly prone to weathering due to the release of interlayer K^+ ions and Fe^{2+} oxidation, which leads to their conversion to clay minerals (Egli et al., 2001). Marques and Williams (2015) and Marques et al. (2017) studied the weathering-grade classification of Bunya phyllite and noted the predominance of kaolin group clay minerals with increasing weathered grades. The progressive mineralogical alteration provides the physicochemical basis for the mechanical weakening of the Chandpur Phyllite, as the primary load-bearing minerals transform into weaker, less resistant clay minerals. Weathering-induced alteration promotes structural instability and reduces overall intergranular bond strength (Basu et al., 2009; Khanlari et al., 2012).

The petrographic study reveals that W1 phyllite exhibits sharp well-developed grain boundaries, whereas advanced weathering produces secondary clay minerals with disrupted grain boundaries. Petrographic observations confirm that primary muscovite, biotite, and quartz in W1 are replaced by distorted grains and secondary clay minerals as weathering products in W4 (Figure 3.5). The disruption of the grain boundaries and replacement of primary crystalline minerals by clay minerals often facilitate the initiation and propagation of microcracks, therefore directly linking to microstructural alteration and overall strength reduction. The findings of this study are consistent with standard mineral weathering behavior, where quartz and K-micas like muscovite are amongst the most resistant phases, whereas biotite readily degrades to clays (Wilson, 2004). Biotite is also observed to transform into kaolinite clay during weathering, a transformation that is similarly noted in the current investigation. Wu et al. (2023) studied the weathering of phyllite from Lushan Mountains and reported a marked reduction in primary mineral contents (mica and feldspar) and strength, and an increase in clay minerals. Staining of the minerals from Fe-rich halos provides visible evidence of rock weathering. This iron

staining observed in the microscopic thin section of the weathered samples validates the *in situ* observation, showing a transition from light-medium grayish-brown color in W3 samples to warm grayish-brown color in W4 samples.

SEM photomicrographs (Figure 3.6) of fresh phyllite reveal well-preserved platy/flaky micaceous foliations (Singh et al., 2025b). With progressive weathering (W2–3), surface roughness increased significantly, accompanied by intense fracturing and grain disintegration in W3 (Figure 3.6). Irfan (1996) states that weathering alters mineral arrangements by generating microfractures and voids. Makumbi and Jackson (1977) and Vicent (1983) state that mineral disintegration and significant cracks/pores development in the weathered samples are due to the decomposition of silica-bearing minerals. With progression to W4, the rock surface essentially smoothens due to clay coating as secondary clays fill voids and fractures. The original foliation alters entirely (Figure 3.6). The void-filled surface with the clay matrix experiences reduced frictional resistance and mechanical strength. This progression from W1–4 matches the mineralogical evolution, showing the breakdown of minerals like mica/chlorite and their conversion into clay minerals.

The application of contact angle analysis in weathering-grade classification remains relatively unexplored, yet it offers a promising indirect measure of weathering intensity through quantification of surface wettability. As weathering progresses, phyllite surfaces exhibit markedly higher wettability, reflecting a systematic shift toward greater hydrophilicity (Figure 3.4). The reduction in contact angle values with increasing weathering-grades (regression analysis in Figure 3.12c) indicates a shift towards a more hydrophilic nature. The progressive shift towards hydrophilicity accelerates the chemical weathering processes by promoting the fluid-rock interaction. This behavior is primarily attributed to the formation of hydroxyl-rich clay minerals, particularly kaolinite generated

through hydrolysis and oxidation of K^-, Mg^-, and Fe^-bearing minerals such as feldspar, mica, and chlorite. The increase in clay content, combined with microstructural breakdown and the resulting expansion of specific surface area, absorbs more water and thus lowers the contact angle. Carvalho et al. (2020) also observed a significant water adsorption capacity in weathered phyllites due to the enhancement of clay minerals with progressive weathering-grade. Consequently, the progressive decrease in contact angle provides a sensitive indicator of both mineralogical alteration and microstructural degradation associated with higher weathering-grades.

The adsorption behavior of the weathered samples was further verified through LPGA analysis (Figure 3.10), where increasing pore surface area and absorbed volume with increasing weathering-grades align well with the observation by Navarre-Sitchler et al. (2013). The pore-scale changes with progressive weathering-grade promote fluid accessibility, thereby leading to weakening of the rock mass. An increase in adsorbed volume also signifies the hydrophilic nature of the material as weathering intensifies, likely due to the formation of secondary clay minerals and weathering products. The progressive development of secondary clay minerals with increasing weathering is evident in the W4 isotherm, which exhibits an open adsorption-desorption hysteresis loop at low relative pressures. The lack of closure in the adsorption-desorption hysteresis loop at low relative pressure is commonly associated with the presence of porous clay, whose swelling behavior impedes the closure of pores during desorption (Chen et al., 2015; Singh et al., 2025c).

Surface topography through AFM analysis and tribological results reflect changes due to weathering in the form of roughness and CoF. The AFM-derived roughness (R_a and R_q) increases from W1 to a maximum at W3, then unexpectedly drops at W4 (Figure 3.7). This pattern suggests that initial weathering produces a highly irregular surface,

whereas extensive clay precipitation at W4 fills in asperities and homogenizes the texture. The unexpected drop in roughness at W4 likely reflects the lubricity due to the filling action of secondary clay minerals. The non-monotonic trend of the mean roughness (Ra) with weathering-grade is also shown in Figure 3.12e. Indeed, the skewness and kurtosis trends also suggest that intermediate weathering stages create uneven peaks and valleys, while heavy clay coverage at W4 yields a more uniform, smoother surface. The same has also been substantiated in FE-SEM analysis.

In addition to surface roughness, variations in pore structural roughness of the weathered samples were carried out using the fractal dimension derived from LPGA analysis. The results were found to be consistent with the surface roughness trends observed through AFM. The fractal dimension (D), which theoretically ranges between 2 and 3, serves as an indicator where 'D' values ~ 3 suggest increased roughness and irregularity. In this study, the fractal dimension values were found to be 2.449 for W1, 2.471 for W2, 2.486 for W3, and 2.385 for W4. In tribological testing, W1 phyllite exhibited the highest friction coefficient and lowest wear, whereas the most weathered sample (W4) had very low friction and the largest wear volume (Figures 3.8 and 3.9). Clay minerals have a very low frictional coefficient compared to other minerals like quartz and feldspar, and therefore, frictional strength decreases linearly with increasing clay content (Takahashi et al., 2007). In our case, the high CoF of W1 reflects a fresh foliation with interlocking grains, whereas the low CoF of W4 reflects a slippery clay coating. While the wear volume consistently increased with the weathering-grade subjected to weakening of rock material, the CoF follow a non-linear trend, initially decreasing from W1–2, followed by increasing from W2–3, and subsequently decreasing from W3–4. The higher CoF in the W3 sample than that of W2 is mainly due to increased surface roughness (Reeves, 1985). Higher asperities due to a rough surface increase CoF.

The dominance of soft, clay-rich material over surface roughness is less within the W3 sample, resulting in more friction than that for W2, but is less than the smoother, clay-dominated W4 sample. The regression analysis trend of the CoF with weathering-grade is shown in Figure 3.12b. The wear volumes for the W3 and 4 phyllites are almost identical, having a maximum value of 0.009 mm^3. As weathering progressed, it promoted mineralogical modifications, leading to the transformation of primary minerals (mainly mica and chlorite) into fine clay phases (Baldermann et al., 2021), which act as low-friction mineral constituents, and consequently led to high wear volume.

The comprehensive analysis of weathering-induced changes in phyllite across *in situ* and multiscale lab analysis reveals a progressive transformation driven by both physical and chemical weathering processes. Collectively, these results underscore the interconnected nature of mineralogical alteration, surface property evolution, and mechanical weakening during weathering. The multiscale approach adopted in this study not only validates the *in situ* weathering-grade classification but also provides a basis for understanding the degradation behavior of phyllite under natural weathering conditions. Table 3.9 summarizes the characteristic behavior of the Chandpur Phyllite with progressive weathering-grade.

Table 3.9. *Characteristic behavior of the Chandpur Phyllite with progressive weathering-grade.*

WG	Characteristic behavior
W1	Fresh Chandpur Phyllite is characterized by a grayish-silver, stiff, and compact rock mass with closely spaced foliation and high intact strength. It exhibits the highest rebound value, low surface roughness, negligible wear, and high density, indicating an unweathered state.
W2	Slightly weathered Chandpur Phyllite exhibits a light gray base with localized rusty-brown staining and increased surface roughness. Despite minor physicochemical alterations (reduced contact angle and a slight decrease in density), the rock retains high mechanical integrity.
W3	Moderately weathered Chandpur Phyllite exhibits light to medium grayish-brown coloration with earthy texture, increased foliation spacing, and reduced mechanical strength. Surface roughness and wear volume increase, accompanied by a significant reduction in density. Elevated specific surface area and fractal dimension indicate enhanced microcrack development and structural complexity.
W4	Highly weathered Chandpur Phyllite represents an advanced weathering stage with warm grayish-brown, soil-like disintegration and loss of primary rock fabric. Mechanical strength is minimal, with widely spaced foliation and easy fragmentation. Although surface roughness decreases due to

	material breakdown and mineralogical changes, high specific surface area and reduced density reflect intense alteration.

This study addresses a long-standing gap in understanding the weathering behavior in weak and fine-grained rock masses such as phyllite. The conventional techniques that aimed at minimizing the subjectivity in qualitative weathering-grade classification have been found to be highly effective for coarse-grained rocks, where mineralogical and textural changes are prominent and can be easily identified. However, their applicability becomes limited for fine-grained rocks, as weathering-induced alterations are often indistinct and difficult to identify using standard procedures.

To overcome this issue, the present study adopted an integrated approach by incorporating non-conventional techniques along with the conventional ones, which have demonstrated significant effectiveness in validating and supporting the initially assigned weathering-grades. The non-conventional techniques in this study have provided additional quantitative and micro-scale insights into surface, mechanical, and mineralogical changes, thereby improving the reliability of the proposed weathering-grade classification for the fine-grained, weak, and foliated Chandpur Phyllite from the Himalayan region. This integrated methodology not only enables the accurate weathering-grade classification of Chandpur Phyllite but also establishes critical links between mineralogical changes (change in clay content and hydrophilicity) and mechanical behavior (change in friction, rebound value, and wear).

The evaluation of the weathering-grade of rock materials is one of the important aspects in rock engineering, as it affects the engineering structures built at or near the Earth's surface. The weathering of soft rocks is one of the primary causes of slope failure and shallow landslides in hilly areas. Individual failures within weathered rock masses occur at very shallow depths and tend to recur over time. Therefore, understanding the

nature of weathering is an important step in predicting the occurrence of slope failure and landslides, including their timing, style, and extent (Goel and Mitra, 2015). Borrelli et al. (2007) have compared the weathering-grade with slope stability for plutonic and metamorphic rocks of medium to high grade and inferred that the percentage of landslide area included in W2 and 3 is small (~ 1 %), while the percentage of landslide areas in W4 is ~ 24 %. Deere and Deere (1989) highlighted the variation in RQD with the degree of weathering. According to them, fresh and slightly weathered rock ought to be used in the RQD count; moderately weathered rock should be included with caution regarding its soundness; and highly weathered rock must not be included. Hack and Price (1997) presented the variation in rock properties with the degree of weathering. They indicated that the intact rock strength deteriorates up to 65% while the spacing of discontinuities increases by 37 % from W1–4. Santi (2006) briefly discussed engineering behavior/properties related to weathering-grades and defined excavability, tunnel support, and rock properties based on variation in weathering-grade. Moreover, weathering-grade and its weightages are also incorporated in the rock mass rating (RMR) system by Bieniawski (1989).

Therefore, weathering-grade evaluation of rock masses is duly needed in the Himalaya, which are not only seismo-tectonically active but also a weather-sensitive zone (Mehrotra et al., 1991). The rock formations composed of phyllites in the Lesser Himalaya are often encountered with slope instabilities and require substantial attention in terms of identification and assigning weathering-grades before any kind of rock engineering practices. This study provides some non-conventional approaches for classifying rock weathering in phyllites, which could be useful in preparatory geotechnical investigations for building safe and sustainable structures on or within the rock masses.

The current study is limited to a single lithology (Chandpur Phyllite) from a single study area. However, the proposed methodology is not restricted to this specific case. The same methodology can be extended on different lithologies from different geographical regions and to varying environmental conditions. However, the applicability of the proposed methodological approach is highly significant for fine-grained rocks, e.g., shales, slates, and siltstones, where similar challenges in identifying weathering-grades are commonly encountered.

3.5. Summary

Weathering brings about substantial changes to rock properties. However, the magnitude of alteration is strongly influenced by mineral content and the rock's inherent texture. Although the weathering-grade classification scheme has attracted substantial attention over the years, its application to soft and fine-grained rocks, particularly phyllites, remains scarce as far as existing literature is concerned. This study presents an integrated two-stage methodology for weathering-grade classification of Chandpur Phyllite from the Lesser Himalaya, combining *in situ* assessments with unconventional multiscale laboratory validation. The field observations have been performed following the six-fold weathering-grade classification scheme, based on discoloration, discontinuity spacing, scratch resistance, hammering, and rebound hardness, through which rock weathering-grades from W1–4 were assigned. This subjective classification was further substantiated by integrating multiscale lab analyses, including XRD, contact angle, petrography, FE-SEM, AFM, tribology, and LPGA techniques, to get a comprehensive insight into the effects of weathering on rock microstructure and surface morphological parameters. The results imply that, as weathering-grade increases from W1–4, hydrophilicity and wear volume increase, while surface roughness and coefficient of

friction exhibit notable variation. This integrated approach enables systematic investigation of weathering-grades in rock masses. It provides a comprehensive understanding of the effects of weathering-grades on mineralogical, mechanical, and morphological changes to the rock's inherent characteristics. Such a study is very crucial, particularly within the complex and geologically sensitive Himalayan terrains and humid subtropical climatic zones.

Chapter: 4
Impact of Water Saturation on Physico-mechanical Properties of Chandpur Phyllite at Varying Foliation Angles

4.1. Introduction

Assessment of the physico-mechanical properties of rocks is considered an important aspect of rock engineering. The inherent characteristics of rocks are defined through the physical properties, whereas the mechanical characterization of rocks predicts the stress-strain behavior, which helps to understand the actual behavior of rocks during construction and the long-term sustainability of structures made within the rock masses (Bieniawski, 1974; Hoek and Brown, 1980). In rock engineering, anisotropic rocks have always gained significant attention from researchers due to their critical and complex behavior. The anisotropy leads to the directional variability towards various physio-mechanical and hydraulic properties. This effect further amplifies when combined with water saturation. Thus, site characterization of anisotropic rock masses, in terms of evaluation of their physico-mechanical properties in water-saturated conditions is significantly important as it helps in determining the type and application of support systems for various engineering structures, boreholes, cut slopes, and underground excavation projects (Tavallali and Vervoort, 2010; Ozturk and Nasif, 2013; ISRM, 2014; Kundu et al., 2018).

Singh et al. (1989) first brought the concept of "*type of anisotropy*" and "*anisotropy ratio*" to quantify rock anisotropy. They stated that, to be considered in the anisotropic category, rock behavior should follow various curve patterns such as U-type, Shoulder type, and Undulatory types. To quantify rock anisotropy, they put forward the concept of the '*anisotropy ratio*' which was defined as the ratio of "*maximum strength to minimum strength*" or the ratio of "*strength at β = 90° to the minimum strength at β other than 90°*" i.e., σ90°/σmin (β is the anisotropy angle between weakness plane and loading

direction). In addition, Liu et al. (2023a) introduced a new "type of anisotropy" curve which was intermediate between the "*U*" type and "shoulder" type i.e., the "U-shoulder" type. They stated that, if the rock type has been highly anisotropic, then the characteristic curve should be a "*U-shoulder*" shape.

In past decades, many scientists investigated the influence of anisotropic angles on mechanical, hydraulic, and seismic behavior, and they reported that, in general, these properties significantly vary with the direction of loading for rocks containing anisotropic structures (Agliardi et al., 2014). He and Afolagboye (2018) examined the consequence of weak lamination planes on the mechanical properties of shale using the Brazilian Tensile Strength (BTS) test. They reported that shale exhibits strong failure strength perpendicular to the lamination plane, whereas it exhibits weak strength parallel to the lamination plane. Singh et al. (2015) examined data from > 1140 triaxial tests conducted globally on transversely isotropic rocks such as slate, orthoquartzite, and phyllites. They proposed a non-linear method for determining the triaxial strength. The study of the engineering behavior of anisotropic rocks becomes even more critical under water saturated condition.

Water is widely known as the most prevalent and challenging factor for engineers triggering numerous geotechnical disasters (Zhang and Sheng, 2018; Zhu et al., 2024). Li et al. (2019a) proposed that water saturation significantly alters rock strength along with the composition and internal microstructure. Weakening strength after water saturation may trigger several engineering complications, such as slope instability, tunnel rock damage, etc. (Iverson, 2000; Bian et al., 2019). Water seepage within soft/layered anisotropic rocks is frequently encountered in nature. Thus, it represents a significant challenge to the long-term stability of foundations within soft rocks due to unfavorable effects on the physico-mechanical properties, which induce shear fracture under

anisotropic stress conditions (Azhar et al., 2020). Kundu et al. (2018) performed the Brazilian tests on Himalayan schistose rocks and demonstrated that the saturation leads to shifting in the minimum strength towards a higher foliation angle (β). At β = 30°, the rock softens the most. Kundu et al. (2018) also inferred that, unlike tensile or mixed mode rock failure modes in dry rocks, layer activation failure mode becomes conspicuous in saturated samples as water reduces the frictional strength between the planes of weakness and facilitates the sliding.

As one of the youngest mountain chain in the world, the Himalaya constitute varied rock types and have undergone intense deformation in the geological past. Therefore, these rocks are highly deformed and are anisotropic. The Lesser Himalaya comprises meta-sedimentary rocks like phyllites, a type of weak-soft anisotropic rock that exhibits a significant level of anisotropy due to foliation planes and is intrinsically friable. These rocks become vulnerable to failure during the rainy seasons as the rainwater enhances the pore pressure along the foliation planes. A few studies have been conducted over the past few decades to comprehend the physico-mechanical behavior of phyllite. For example, the engineering behavior of three different phyllites collected from the Himalaya region has been investigated under different foliation angles (β) by Ramamurthy et al. (1993) and proposed various types of anisotropic curves.

To comprehend the impact of foliation angle (β) on the mechanical properties and rockburst proneness, SI et al. (2021) conducted a Uniaxial Compressive Strength (UCS) test on phyllite. Their findings revealed “U” type anisotropy for peak stress, peak strain, potential energy of elastic strain, and cumulative acoustic emission counts. As β increase from 0° to 90°, the failure modes shift from shear slip failure along the weak bedding plane to tensile splitting one along the bedding plane. For Rockburst proneness, SI et al. (2021) followed the classification proposed by Wang and Park (2001), who categorized

proneness to rockburst into five categories based on the Potential Energy of Elastic Strain (PES): such as (*i*) PES = 50 kJ m^{-3} indicated very low rockburst hazard, (*ii*) 50 < PES = 100 kJ m^{-3} indicated to low rockburst hazard, (*iii*) 100 < PES =150 kJ m^{-3} indicated moderate rockburst hazard, (*iv*) 150 < PES = 200 kJ m^{-3} indicate high rockburst hazard and (*v*) PES > 200 kJ m^{-3} indicated very high rockburst hazard. Duan et al. (2023) studied phyllite specimens subjected to triaxial compressions with cyclic loading and gas permeability. The aim was to comprehend the directional impact on gas permeability coefficient, peak stress, failure mode, and energy evolution. The study revealed that deformation parameters and stress parameters exhibited U-shaped anisotropy. Hu et al. (2016) and Xu et al. (2018) delved into the anisotropic mechanical behavior of phyllite. Their studies involved triaxial compression tests conducted under varying orientations of the foliation plane and different moisture content. Ansari et al. (2021) and Singh et al. (2022) studied the mineralogy of phyllite specimens from Lesser Himalaya, and they reported that the presence of micaceous minerals can often contribute to a reduction in the strength of the rock.

In recent years, the construction of significant engineering projects, including dams, tunnels, and caverns, has mainly taken place in phyllite formations in the Himalayan region. However, based on the existing literature on phyllite, the impact of saturation on physico-mechanical behavior does not get much attention over time. Moreover, limited studies on the anisotropic behavior of such formations suggest scarcity, especially when considering the effect of water saturation, leading to frequent large-scale deformations and infrastructure failures.

In line with the above discussion, this study comprehensively examined the influence of water saturation on the physico-mechanical properties of phyllites at different foliation angles. Physical properties such as P-wave velocity and mechanical

properties such as UCS, BTS, Elastic Modulus (EM), Brittleness Index (BI), and PES were estimated. The FE-SEM analysis was also performed to substantiate the role of water and foliation planes on the failure behavior of phyllite. This investigation provides a reference for constructing various engineering structures on or within rock masses composed of phyllites, ensuring stability and preventing failure.

4.2. Methodology

After the collection of fresh samples from the study area mentioned in Section 2.1 (Chapter 2), they were transported to the lab. Subsequently, specimens for different tests were prepared, and laboratory tests were performed. Detailed descriptions of the procedures are outlined in the following subsections:

4.2.1. Specimen Preparation

As illustrated in Figure 4.1, the rock cores of 50mm diameter were drilled from the collected blocks at various foliation angles "β" (angle between foliation plane and drilling direction) of 0°, 30°, 60°, and 90°. Subsequently, the drilled cores were cut into different dimensions for UCS tests with an aspect ratio of L:D=2/1 and BTS with an aspect ratio of L:D=1/2, following ASTM standards (ASTM, 2001).

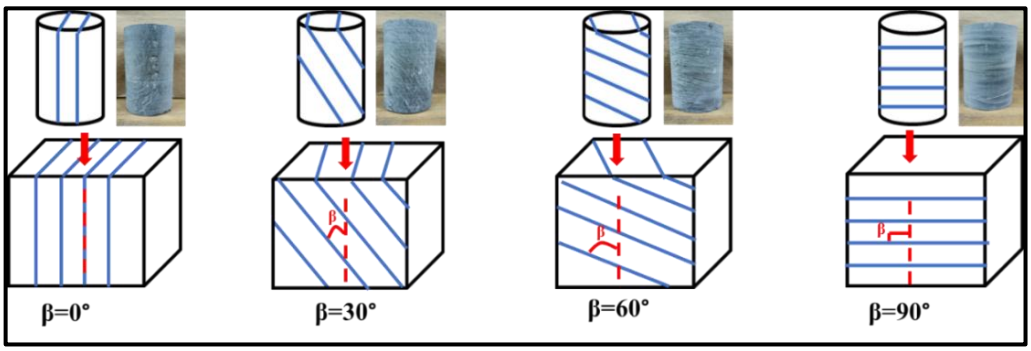

Figure 4.1. *Schematic of coring at different β. Note: β is the angle between the foliation plane and drilling direction.*

Total 64 specimens (32 for each mechanical parameter) were meticulously prepared. The end surfaces of these specimens were carefully polished and ground to ensure the maximum uniformity of applied stress. The tests were categorized into two groups: normal condition and saturation condition. In each group, 4 specimens were prepared and tested at different foliation angles 0°, 30°, 60°, and 90°.

To comprehend phyllite's chemical and morphological properties, analyses were conducted using X-ray diffraction (XRD) and Field Emission Scanning Electron Microscopy (FE-SEM). For XRD analysis, powder specimens were precisely prepared, ensuring a particle size < 44 μm through crushing and sieving processes. In contrast, FE-SEM analysis aimed to elucidate surface morphology, grain size, and texture. For this analysis, chip specimens ranging from 2 to 4 mm were carefully prepared, each exhibiting different foliation angles. Figure 4.2 represents the schematic diagram of the specimen preparation for various tests. Before subjecting the specimens to testing in both normal and saturation conditions, they were first oven-dried at 105 °C in a hot air oven for 4 hours. After reaching room temperature (27 °C), half of the specimens were immersed in distilled water for 21 days to ensure thorough saturation. Distilled water was used to minimize the impact of chemical reactions between minerals and water.

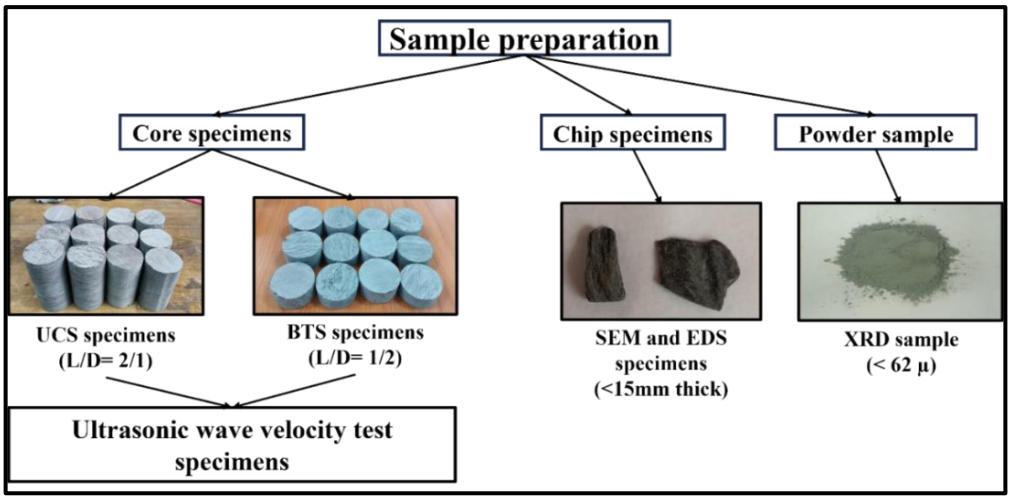

Figure 4.2. *A schematic diagram of specimen preparation followed in this study.*

4.2.2. Experimental Test and Procedures

Phyllite specimens with varying foliation angles under normal and saturation conditions underwent laboratory investigation to comprehend their physical, chemical, mechanical, and morphological characteristics. An example of the experimental setup is illustrated in Figure 4.3.

As shown in Figure 4.3a, P-wave velocities inside phyllites were measured using a Pundit PL-200 ultrasonic pulse velocity test instrument. The wave velocities were measured using 250 kHz transducers. Both transducers, i.e., emitter and receiver, were placed along the length of the core specimens, and the place of contact between the transducer and the specimen was made smooth to avoid the attenuation of the wave (as per ISRM, 2007).

The UCS for normal and saturated specimens at various foliation angles was evaluated in the laboratory using an automatic compression testing machine manufactured by HEICO (Figure 4.3b) to measure the load at the time of failure and further it was calculated using Eq. 4.1 (ISRM, 2007).

$$\mathrm{UCS} = \frac{\mathrm{F}}{\mathrm{A}} \qquad \text{Eq.4.1}$$

Here, UCS: Uniaxial Compressive Strength (MPa), F: failure load (kN), and A: cross-section area of the specimen (mm^2).

BTS is another crucial strength test that measures the tensile strength of rock indirectly. To assess the tensile strength of the rock, the BTS test shown in Figure 4.3c was performed using a Brazilian test setup designed by Intellitest. A core specimen with a 50 mm diameter was positioned in the Brazilian set up and subjected to compression until failure. After the specimen failed, the tensile strength was calculated using Eq. 4.2 (ISRM, 2007).

$$BTS = \frac{2P}{\pi DL} \quad \text{Eq.4.2}$$

Here, BTS: Brazilian tensile strength (MPa), P: peak load (kN), D: diameter (mm), and L: thickness (mm).

The rock's behavior is not only influenced by its physical and mechanical properties but also by its chemical composition and surface morphology (Mishra and Ram, 2024). To assess the mineral phases through XRD analysis, a semi-quantitative compositional analysis technique was employed. The Empyrean Panalytical X-ray diffractometer served as the instrument for this analysis (Figure 4.3d). The technique involves directing a monochromatic X-ray beam onto the powdered rock specimen to identify various mineral phases within the specimen. Morphology along with elemental studies through FE-SEM analysis was conducted using the JEOL JSM-7900F FE-SEM instrument (Figure 4.3e). FE-SEM analysis, as described by Kwiecińska et al. (2019), allows for the identification of surface morphology, texture, structure, fracture behavior, and grain size of the specimen, whereas EDS gives elemental composition, grain size variations, and depositional nature in soil or rock (Avşar et al., 2015).

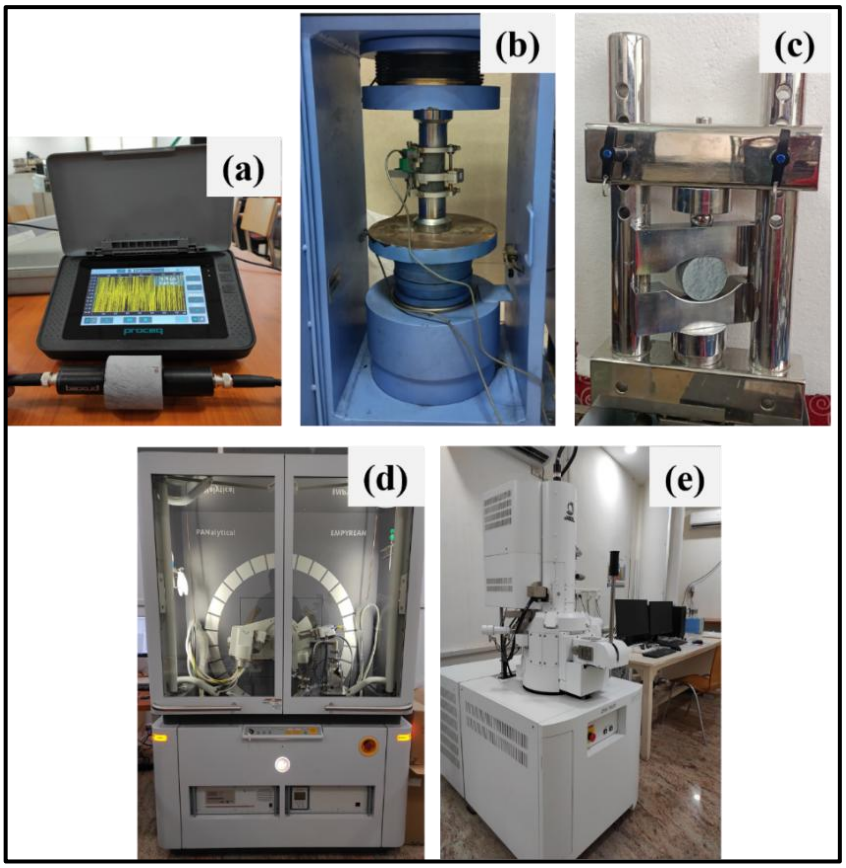

Figure 4.3. *The Laboratory setup of* ***(a)*** *Ultrasonic tester,* ***(b)*** *Uniaxial Compressive Strength Tester,* ***(c)*** *Brazilian Tensile Strength Tester,* ***(d)*** *XRD analysis, and* ***(e)*** *FE-SEM analysis.*

4.3. Results

The various lab tests were performed and the data were analyzed to evaluate the changes in the physico-mechanical properties. Besides, chemical composition and morphological changes were also analyzed. The detailed analyses of the changes and the outcome of the tests are summarized in the following sub-sections.

4.3.1. XRD characteristics and FE-SEM analysis of the Chandpur Phyllite

The general composition of Chandpur Phyllite is characterized by the presence of micaceous minerals, quartz, feldspar, and a few accessory minerals resulting from the metamorphism of shale and slate. A semi-quantitative XRD analysis was conducted on the powder specimens to understand the chemical behavior. The semi-quantitative XRD analysis (Figure 4.4) reveal that the Chandpur Phyllite in the Srinagar area was notably

enriched in micaceous minerals including Muscovite (2θ = 26.58) and Illite (2θ = 19.8) along with Quartz (2θ = 26.6) and Feldspar (2θ = 27.89). Quantitatively, the Chandpur Phyllite analyzed in this study contains ~ 55.6 % quartz, 24.9 % muscovite, 15.1 % illite, and 4.4 % albite.

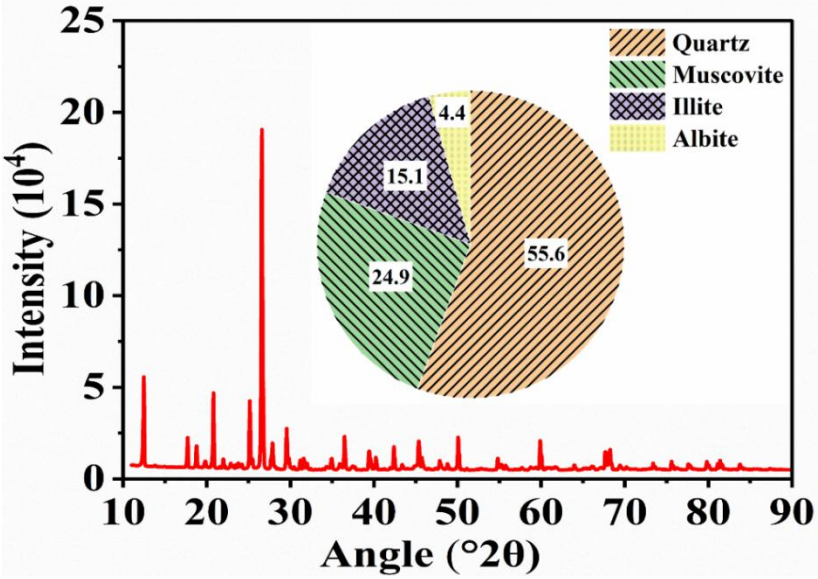

Figure 4.4. *Representative XRD pattern of Chandpur Phyllite with accompanying pie chart illustrating mineral quantification.*

Figures 4.5a, c reveal that the surface morphology of phyllite is shaped by well-developed foliation planes, which arise from the alignment of platy minerals during metamorphism and/or deformation. Figure 4.5a shows the dominance of numerous foliation planes of micaceous minerals at a lower foliation angle (0–30°). In contrast, at a higher foliation angle (60–90°), Figure 4.5c shows the presence of rock matrix (mostly quartz) along with the foliation planes responsible for the behavior of the rock. The elemental studies using EDS analysis depicted in Figures 4.5b, d reveal elevated concentrations of Si and Al in phyllites, accompanied by notable amounts of K, Fe, and Mg. The higher concentration of Mg and Fe in the surface mapping of the microphotographs and the elemental peaks of phyllite at a lower foliation angle indicated

that numerous foliation planes are enriched of the micaceous mineral “Illite” having composition $(K,H_3O)(Al,Mg,Fe)_2(Si,Al)_4O_{10}[(OH)_2\cdot(H_2O)]$. The increased “Si” concentration at a higher foliation angle suggested quartz's presence between the foliation which is responsible for the physico-mechanical behavioral changes. These characteristic properties (XRD, FE-SEM, and EDS) served as a medium for developing a correlative relation with the physico-mechanical properties of foliated phyllite.

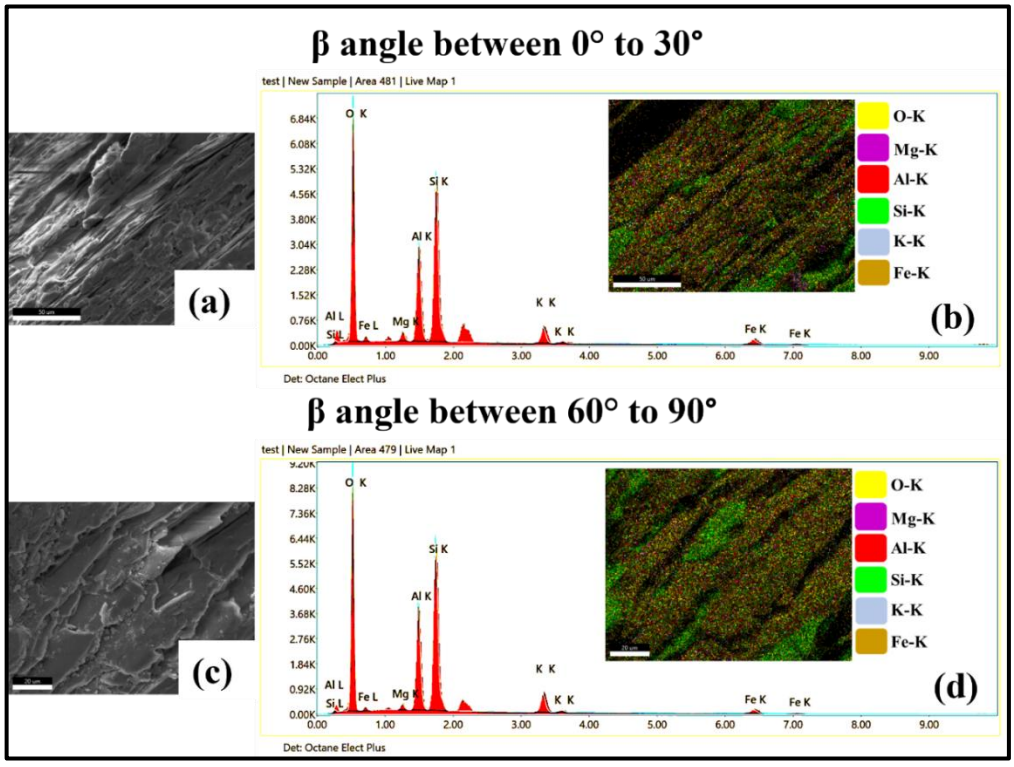

Figure 4.5. *FE-SEM microphotographs of Chandpur Phyllite and its representative EDS analysis depicting elemental variations.*

4.3.2. Variation in Ultrasonic P-wave Velocities with Foliation Angle

The ultrasonic P-wave velocities of specimens before and after saturation were measured, and the data are illustrated in Figure 4.6. Under normal and saturation conditions, wave velocities exhibit a declining trend as the β increased. However, the magnitude of body wave velocity under saturated conditions was slightly higher than that under normal conditions. The observed increase in the magnitude of P-wave velocity

under saturated conditions is attributed to the fact that water is relatively denser compared to air or gas. The average bulk density value of 2.886 g cc^{-1} for saturated specimens and 2.856 g cc^{-1} for dry specimens was calculated using Archimedes Principle.

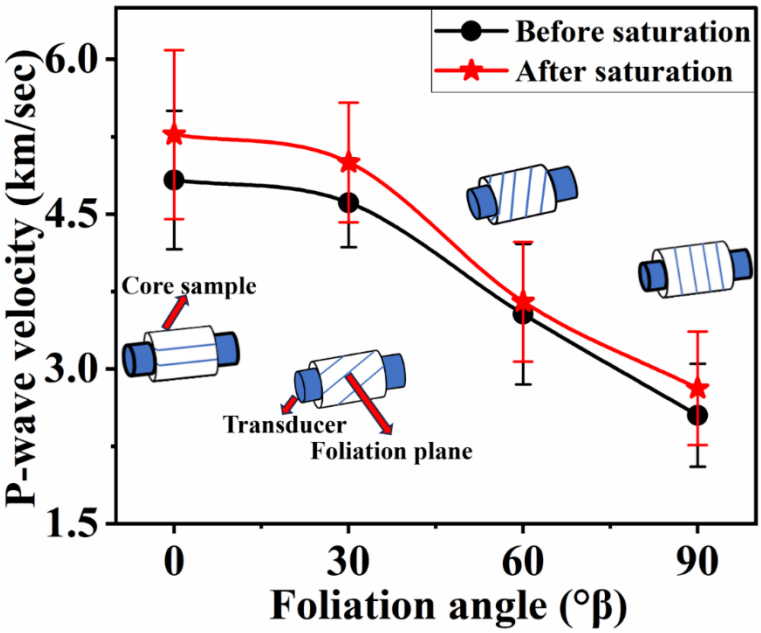

Figure 4.6. *Relationship between β and P-wave velocity under normal and saturation conditions.*

The maximum average P-wave velocities of 4825 m sec^{-1} and 5274 m sec^{-1} were observed parallel (β = 0°) to the foliation plane under dry and saturation conditions. Conversely, the minimum average P-wave velocities of 2549 m sec^{-1} and 2811 m sec^{-1} were observed perpendicular (β = 90°) to the foliation plane under dry and saturation conditions. The primary factor contributing to the influence of the foliation plane on wave velocity is that, as the foliation angle increases from 0 to 90°, the waves encounter a greater number of foliation planes, leading to increased dissipation of wave energy, and ultimately this process results in a weakening of wave velocity.

4.3.3. Strength and Deformation Behavior with Foliation Angle

In the current study, the deformation behavior of phyllite as shown in Figure 4.7 was examined using the Stress *vs.* axial displacement curve of the UCS test subjected to various foliation angles.

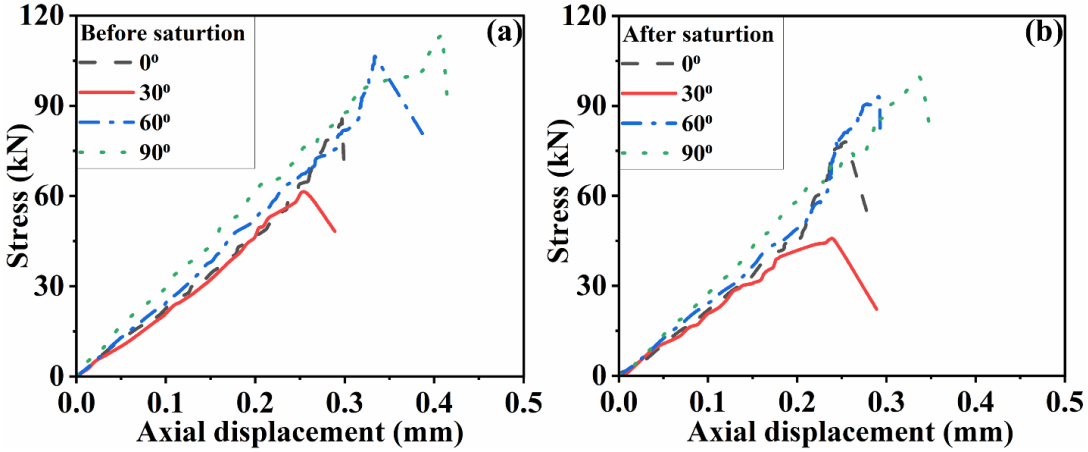

Figure 4.7. *An example of representative stress vs. axial displacement plots for* ***(a)*** *dry condition and* ***(b)*** *saturation condition.*

Stress *vs.* axial displacement/strain curves reveal a consistent trend of increasing axial strain with rising stress under both normal and saturated conditions. The phyllite specimens exhibited maximum stress and strain at β = 90°, while specimens with a β = 30° exhibited minimum stress and strain under dry and saturation conditions. However, the magnitude of stress *vs.* strain was lower under saturation conditions at each foliation angle.

Based on the amount of stress at the time of failure, Figure 4.8 represents the UCS and BTS of the phyllite with foliation angles. In general, both UCS and BTS demonstrated a consistent trend with the foliation angle under normal and saturation conditions. This pattern was characterized by an initial decrease followed by a continuous increase as the foliation angle rose. Under both normal and saturation conditions, this study revealed a minimum average UCS value of 26.29 MPa and 20.14 MPa at β = 30° and a maximum

average UCS value of 61.57 MPa and 55.19 MPa at β = 90°. Similarly, for BTS, the minimum average value was 7.63 MPa and 6.4 MPa at 30°, and the maximum average BTS value was 15.36 MPa and 13.37 MPa at 90° under normal and saturation conditions, respectively. Both BTS and UCS of phyllite under normal and saturation conditions demonstrate a "U-shoulder" type anisotropy, signifying the directional dependency of the rock's strength and representing the qualitative approach for the study of the anisotropic rock. Specifically, such a type of curve was characteristic of highly anisotropic rock (Liu et al., 2023a) with the material's strength reaching its maximum value at β = 0°/90° and minimum value when β was between 20 and 40°.

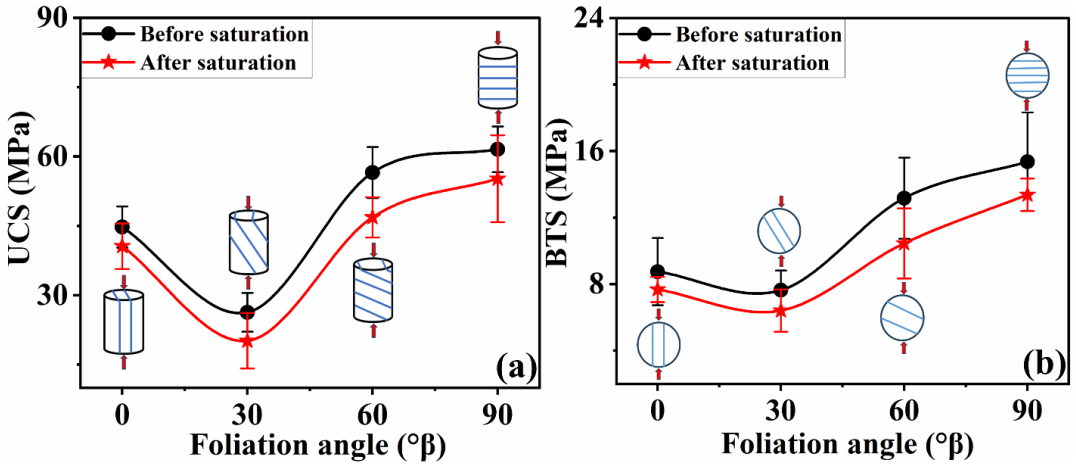

Figure 4.8. *Relationship between* ***(a)*** *β vs. UCS and* ***(b)*** *β vs. BTS under normal and saturation conditions.*

The strength anisotropy ratio is crucial for assessing the mechanical behavior of rocks under different loading conditions. For UCS, the strength anisotropic ratio of Chandpur Phyllite under dry and saturation conditions was 2.34 and 2.74. Similarly, for BTS, the values under dry and saturation conditions were 2.01 and 2.08, respectively. The anisotropy ratio for the saturated specimens was greater than that for the dry ones.

4.3.4. Rock Failure Modes under UCS and BTS at Different Foliation Angles

Failure modes have been studied to comprehend the impact of the foliation angle on phyllite's failure behavior. Figure 4.9 illustrates the failure mode of Chandpur Phyllite concerning the foliation angle under UCS and BTS. The failure mode of Chandpur Phyllite under UCS was classified into shear failure across foliation at β = 0°, shear failure along foliation at β = 30°, and multiple shear failures across foliation at β = 60 and 90°.

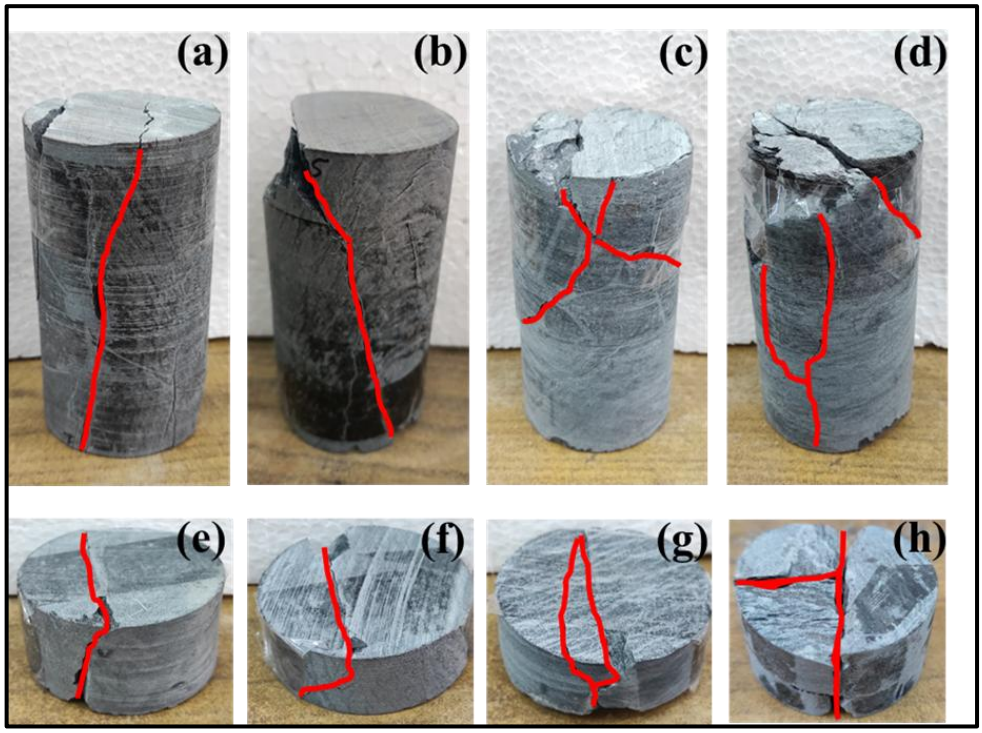

Figure 4.9. *Representative failure modes (**a, b, c,** and **d**) observed in the UCS test and (**e, f, g,** and **h**) observed in the BTS test at 0º, 30º, 60º, and 90º, respectively.*

For BTS, failure modes were structured into non-central failure at 0° and 30°, central + non-central failure at 60°, and central + layer activation failures at a 90° foliation angle. Further, Figure 4.10 represents the percentage of specific failure modes at different ranges of UCS and BTS using a bar diagram. In Figure 4.10a for UCS, the values ranging between 15–30 MPa show only “shear along” failure to be more likely occur. This failure mode was characterized by a foliation angle of 30°. For the 30–45 MPa range, “shear

across" failure and the "multiple shears across" failure were found. The shear across failure was characterized to be found at β = 0° angle, whereas multiple shears across failure were the characteristic failure for higher foliation angles, i.e., β = 60 and 90°. At a higher UCS range ≥ 45 MPa, there was a dominancy of "multiple shears across" failure with few "shear across" failure modes. Similarly, the failure mode under BTS is presented in Figure 4.10b. The values ranging between 5–10 MPa showed the dominancy of "non-central" failure, the characteristic failure mode occurring at the foliation angle of 0° and 30°. For the 10–15 MPa range, the "central + non-central" failure mode was dominated along with the "central + layer activation" failure mode, whereas for BTS ranging ≥ 15 MPa, "central + layer activation" failure was more likely to occur. These failure modes (central + non-central and central + layer activation) were the characteristic BTS failure modes of higher β, i.e., 60° and 90°. Although the water saturation altered the strength of phyllite, its effect on the failure mode was found insignificant. Rather, the examined failure modes corresponded to the orientation of the foliation planes.

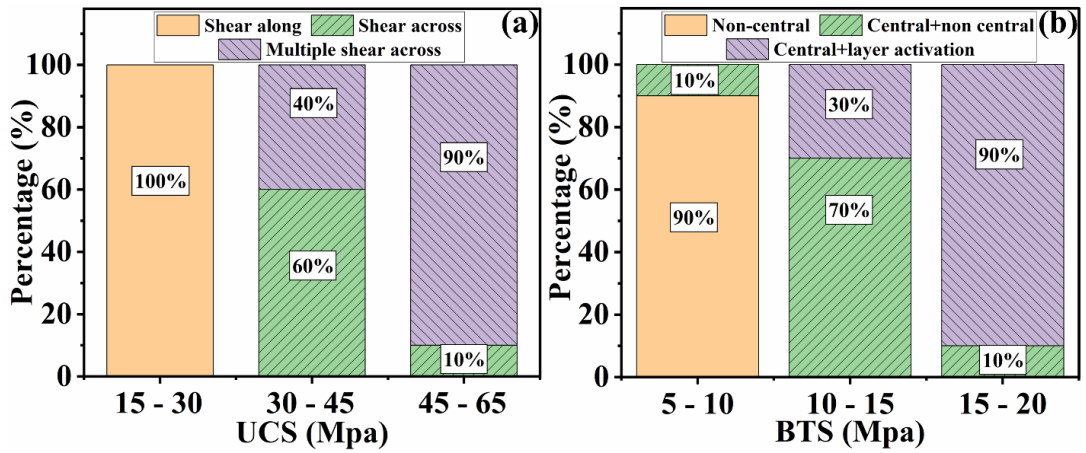

Figure 4.10. *A bar diagram representing the percentage of failure modes in different ranges of* ***(a)*** *UCS and* ***(b)*** *BTS.*

4.3.5. Brittleness Index, Elastic Modulus, and Proneness to Rockburst

The current study determines the BI, EM, and Proneness to Rockburst using criteria derived from the strength tests. Figure 4.11 illustrates the graphical representation of the BI with a foliation angle. BI plays a pivotal role in evaluating the brittleness of rock formations and is defined as the property of the material to break with almost negligible ductile deformation (Bates and Jackson, 1984). According to the classification proposed by Altindag (2010) based on Eq. 4.3, phyllite specimens under dry state exhibited characteristics of "moderate brittle" at β = 0° and 30°, "brittle" at β = 60°, and "very brittle" at β = 90°. While for the saturated specimens, phyllite exhibited characteristic “moderate brittle” at β = 0°, “low brittle” at β = 30°, and “brittle” at β = 60° and 90°, respectively.

$$BI = \sqrt{\frac{(UCS * BTS)}{2}} \qquad \text{Eq.4.3}$$

Here, BI: Brittleness Index, UCS: Uniaxial Compressive Strength, and BTS: Brazilian tensile strength.

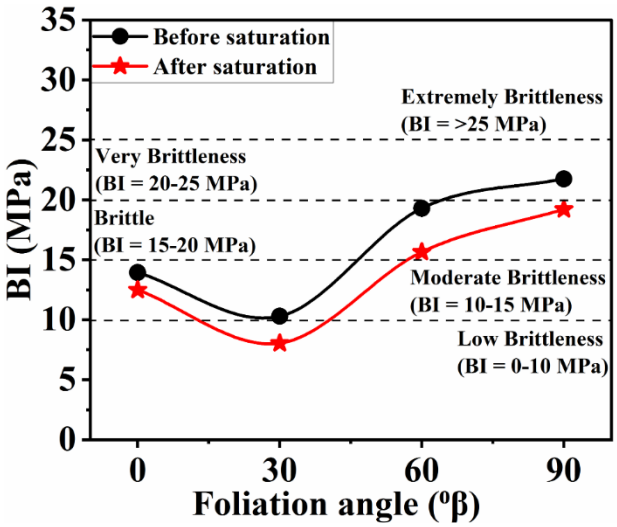

Figure 4.11. *Variation of the Brittleness Index (BI) with β for dry and saturated phyllite.*

The EM, a measure of stiffness and resistance to deformation, was determined by analyzing the slope of the stress-strain curve of UCS. The formula for calculating EM from a stress-strain curve is stated in Eq. 4.4.

$$EM = \frac{\Delta\sigma}{\Delta\varepsilon} \quad \text{Eq.4.4}$$

Here, EM: elastic modulus, σ: stress, and ε: strain.

The results in Figure 4.12a revealed that the lowest average EM of 12.04 GPa under dry and 10.79 GPa under saturation conditions was obtained at β = 30°. In comparison, the highest average EM of 15.26 GPa under dry and 15.02 GPa under saturation conditions was observed at β = 90°. At β = 30°, specimens subjected to the UCS test exhibited a higher susceptibility to slippage along the foliation plane compared to the 90° foliation angle, where foliation planes were perpendicular to the loading direction. This leads to a comparatively greater axial deformation at β = 30° than at β = 90°. The intensity of slippage is further enhanced with saturation, resulting in reduced EM.

Proneness to rockburst is another important indirect parameter in rock engineering to assess the risk during rockburst disasters. Rockburst is a highly significant dynamic geological disaster, leading to an instantaneous release of elastic strain energy stored in rock (Gong et al., 2020). Proneness to rockburst was determined by calculating the PES using Eq. 4.5 (Gong et al., 2020).

$$PES = \frac{\sigma_c^2}{2EM} \quad \text{Eq.4.5}$$

Here, PES: potential energy of elastic strain, σ_c: peak stress of rock specimen under UCS, and EM: elastic modulus under UCS.

Figure 4.12b shows the graph between PES *vs.* β under normal and saturation conditions. The trend of the PES under the dry state was similar to that of the UCS, BTS, BI, and EM, with maximum PES values at β = 90° and minimum at β = 30°. Whereas for

saturated specimens, the maximum PES value is at β = 60° and the minimum value was at β = 30°. Therefore, the phyllite specimens under normal and saturation conditions exhibited very high rockburst hazards at β = 0°, 60°, and 90°, while at β = 30°, they exhibited very low to low and moderate rockburst hazards (Wang and Park, 2001).

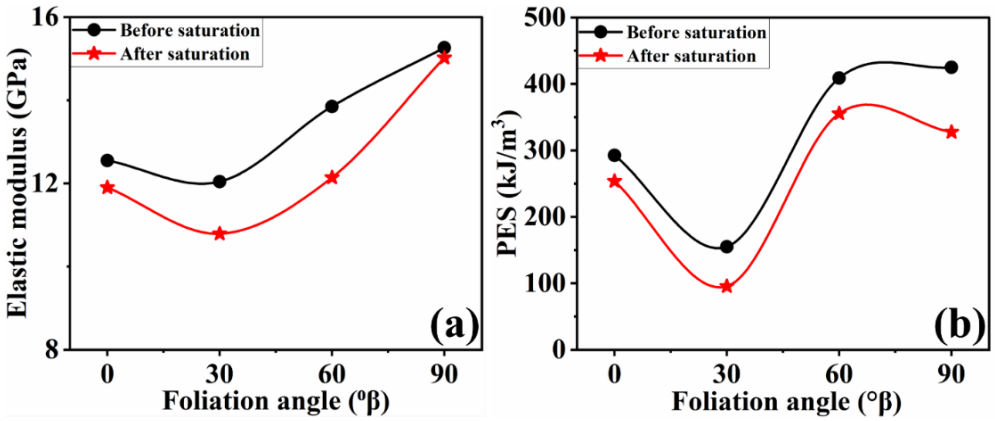

Figure 4.12. *Illustrates a plot of* ***(a)*** *β vs. Elastic modulus and* ***(b)*** *β vs. Proneness to rockburst of Chandpur Phyllite under normal and saturation conditions.*

4.4. Comparison of the Present Study with Existing Literature

Phyllite specimens with well-developed foliations are widely found across the globe. These foliations significantly control the mechanical behavior of the phyllite at the micro and macro levels. Numerous engineering practices may often lead to geotechnical complications due to inadequate knowledge of phyllite's physico-mechanical behavior with the orientation of foliation planes. Area to area/project to project, the properties of phyllite significantly vary due to the inherent directional anisotropy. Therefore, to gain a deeper understanding of the behavior of phyllite, a comparative study of the properties investigated with the previous findings was essential. Figure 4.13 shows a comparative plot of UCS, BTS, wave velocity, EM, and PES with foliation angles.

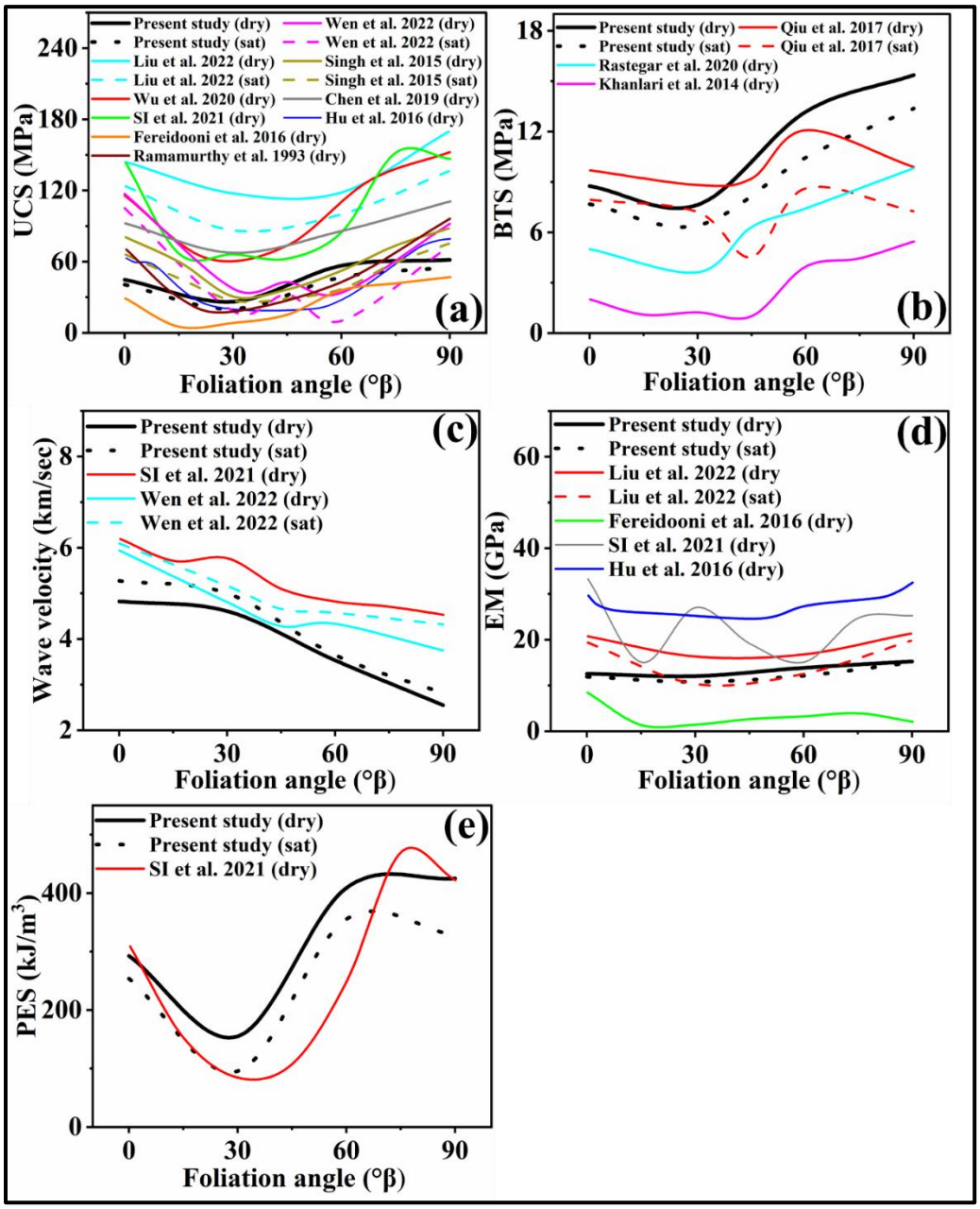

Figure 4.13. *A comparison of the present study with the existing studies with changes in foliation angles.*

From Figure 4.13, it was observed that the trend of the present study was almost like the previous findings. The trend of UCS, BTS, EM, and PES in the present study with optimum value at β = 0°/90° and minimum value at an intermediate angle (between β = 20–40°) coincided with the previous ones. In comparison, the trend of wave velocity in the present study and the previous findings showed a decreasing trend with increasing

foliation angle. However, the variation in the magnitude was significant, and in some cases, a few dissimilarities in the trend were also observed in this comparative analysis, which might be attributed to the inherent directional anisotropy due to differences in mineralogical composition, metamorphic grade/degree of metamorphism, mineral alignment, etc.

4.5. Discussions

Studying the directional dependency of phyllite characteristics in a rock engineering environment requires accurate planning and consideration. Ignorance of such inherent directional anisotropy may often lead to erroneous results. In addition to its physical and mechanical properties, phyllite's behavior is often controlled by mineralogy and surface morphology with direction. XRD investigation revealed platy/flaky micaceous minerals as major contributors influencing the physico-mechanical properties of Chandpur Phyllite. Ansari et al. (2021) and Singh et al. (2022) also reported the presence of similar micaceous minerals within phyllites from the Lesser Himalaya. EDS analysis further confirmed the mineralogy-based on elements such as Si, Al, K, Fe, and Mg. The arrangement of platy/flaky minerals in a well-defined foliation plane is observed in the photomicrographs obtained from FE-SEM examinations (Figure 4.5). This emphasizes the importance of orientation in influencing attributes such as phyllite's strength and failure behavior. The FE-SEM microphotographs clearly illustrate the distinct and well-developed foliations characteristic of phyllite, as Shekhar et al. (2006) described. Hence, it is imperative to analyze the arrangement and distribution of minerals and determine the precise minerals found in the phyllite to anticipate their response to various directional stresses.

The P-wave velocity was determined under normal and saturation conditions with reference to foliation planes. The orientation of foliations on the wave velocity of phyllite

is significant, with maximum velocity measured parallel to the foliations (β = 0°) and minimum velocity measured perpendicular to the foliations (β = 90°). Studies by SI et al. (2021) and Wen et al. (2022) observed similar foliation effects on phyllite's wave velocity. They reported that increasing the foliation angle resulted in lower wave velocities, attributed to increased resistance due to heightened reflection and refraction of waves through the increasing number of foliation planes within the path, leading to wave energy dissipation. Considering the effect of water saturation, the trend in wave velocity with changes in the foliation plane remains the same as in dry specimens; however, the magnitude of wave velocities increase. This is because water is denser than air, resulting in higher overall density in saturated specimens compared to dry ones, thus enhancing wave velocity. Wen et al. (2022) also observed this phenomenon, noting that phyllite's water-absorbing ability increases the specimen's density when saturated, leading to higher wave velocities than that of the dry specimens.

The mechanical response to the foliation plane under dry and saturated conditions significantly affects geotechnical complications within phyllite formations. Despite being a low-porosity rock, phyllite is known for its water-absorbing ability, as water generally percolates along the foliations. Therefore, the combined effect of saturation and foliation on the mechanical properties of phyllite is crucial for safety and stability. The deformation using a stress-strain curve for UCS indicated a consistent trend of increasing axial strain with rising stress under both dry and saturated conditions, with a smaller magnitude for the saturated specimens compared to the dry ones. The observed maximum stress and its corresponding strain at β = 90° and the minimum stress and its corresponding strain at β = 30° were due to the alignment of the foliation planes and the interaction between the foliation planes and the rock matrices with the applied stress. The directional dependency of stress and its strain on phyllite is very important in estimating its deformational

behavior. Chen et al. (2019) investigated the stress-strain relationship of phyllite with varying orientations and reported similar findings. The UCS and BTS of phyllite under dry and saturated states were found to have a "U-shoulder" shaped anisotropy curve (Figure 4.8), indicating high anisotropy and directional dependency of strength, with a maximum value at $\beta = 0°/90°$ and a minimum at $\beta = 30°$. However, the strength magnitude for the saturated specimens was lower. This could be possible because of the following reasons: (*a*) a reduction in internal friction between mineral grains or foliation planes, influencing the internal structure of the rock and rendering it more prone to sliding or deformation along foliation planes; (*b*) the presence of pore water pressure causing an overall reduction in strength; and (*c*) a decline in the surface energy of the rock, consequently affecting its cohesive nature and bond strength (Cai et al., 2019; Wen et al., 2022) (Figure 4.14).

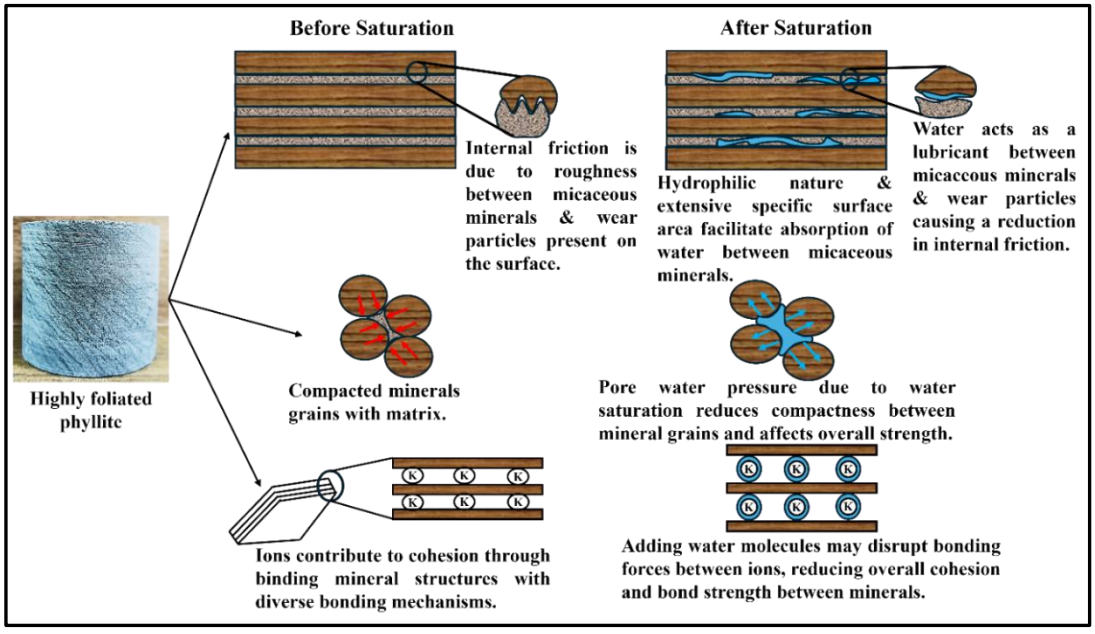

Figure 4.14. *The schematic diagram explains the impact of saturation on the phyllite specimen.*

As shown in Figure 4.15, the specimens exhibited minimum strength at β = 30° foliation plane with smooth failure surfaces and negligible broken fragments, whereas, in the case of maximum strength at β = 90°, the specimens mostly failed with rough failure surfaces and broken fragments. Li et al. (2021) stated that rough and jagged surfaces were indicative of greater strength due to large adsorption of energy during failure whereas, in contrast slightly rough and flat failure surfaces indicated lower strength.

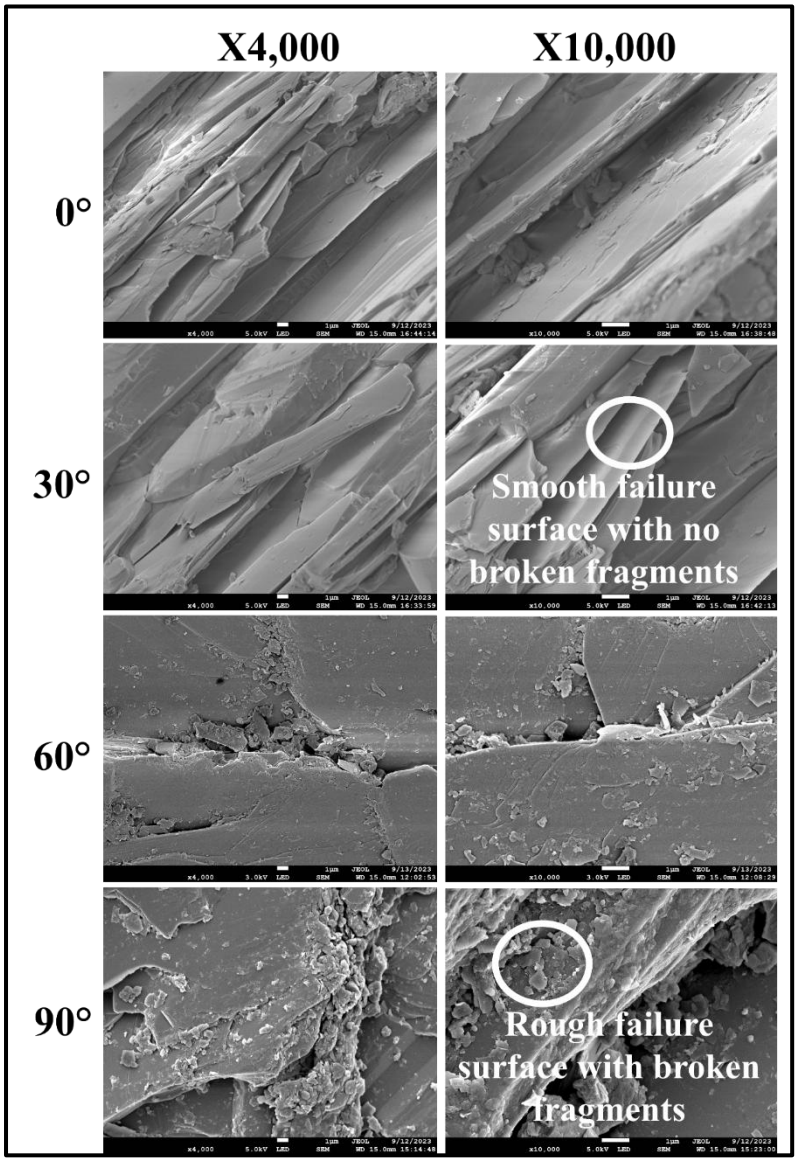

Figure 4.15. *The microphotographs of the failed specimen under UCS at various foliation angles.*

The impact of the rock matrix found between the foliation planes was insignificant at β = 30°; however, at β = 90°, the rock matrix between the foliation planes enhanced cohesiveness and withstands higher levels of stress before failing. As per SI et al. (2021), the strength of cementation within phyllite is significantly weaker between foliation planes than within rock particles. Moreover, this analysis also indicates that the failure at β = 0° was affected by both weak planes and the rock matrix, leading to a strength that was higher than at β = 30° but lower than at β = 60 and 90° (Ramamurthi et al., 1993; Singh et al., 2015).

Failure modes under different loading conditions provide valuable insights into the structural integrity and stability of geological formations. The orientation of the foliation planes significantly influences the failure of the specimen. The strength of UCS and BTS can be directly correlated with the failure modes. As in Figure 4.9, the lower strength corresponds to the smooth failure pattern with failure along the foliation or non-central, whereas higher strength corresponds to the rough and jagged failure pattern with failure across the foliation or central. This could be possible because the foliations within phyllite composed of micaceous minerals have a lower strength as compared to the rock matrix of quartz present between the foliations. Thus, for failure along the foliation, the rock mass follows the path of weak foliations and fails at a very low strength value, while in the case of failure across the foliation, the rock matrices come into play, which induce cohesion and result in high strength value.

In addition to strengths and failure modes, BI, EM, and PES are essential to predict rock behavior under various conditions. These parameters are crucial for ensuring safety and optimizing design in engineering and geological projects. All three parameters shown in Figures 4.11 and 4.12 exhibit a "U-shoulder" shaped anisotropy curve, like the UCS and BTS curves, indicating directional dependency. Fereidooni et al. (2016) and Liu et al.

(2022a) examined the EM of dry and saturated phyllite. They reported an almost similar trend with foliation planes. The trend of the PES curve observed by SI et al. (2021) for dry specimens was almost identical to that of the present study, except at β = 30°, where an increase in value was observed. This change can be attributed to the anisotropic behavior of phyllite due to variations in mineralogy and bond strength. SI et al. (2021) studied the PES of phyllite and found that the values initially decreased, then increased, and finally slightly decreased with an increase in foliation angle. These all-indirect parameters are crucial in defining the mechanical behavior and fracture characteristics of phyllite, with an emphasis on the foliation angle.

4.6. Summary

The effect of water saturation in the Himalayan rocks is a critical factor influencing the physico-mechanical properties of rocks. Typically, the anisotropic and fragile rock formations are vulnerable to it, as it may directly/indirectly cause directional variation of rock's physico-mechanical properties. One such notable formation is phyllite, within which numerous geotechnical engineering projects are ongoing or have been completed. This study aimed to assess the impact of water saturation on the physico-mechanical properties of highly foliated Chandpur Phyllite at varying foliation angles. The findings revealed a decreasing trend in P-wave velocity with increasing foliation angles, with higher values observed in saturated specimens. Mechanical properties exhibited a "U-shoulder" type anisotropic curve with the foliation angle, reaching minimum values at β = 30° and maximum values at β = 90°. Although the overall trend of the mechanical properties remained consistent with the foliation angle, their values were significantly influenced by saturation. At the microscopic level, the failure surface of the specimen having β = 30° displayed a smooth surface with negligible broken

fragments indicating reduced cohesion and lower strength with failure along foliation, regardless of saturation. In contrast, specimens at $\beta = 90°$ exhibited a rough/jagged surface with numerous broken fragments suggesting increased cohesion and higher strength with failure across foliation. The mineralogical analysis further highlighted the role of well-developed micaceous minerals in the form of foliation planes with the rock matrix present between them, influencing the directional behavior of phyllite.

Chapter: 5
Influence of Specimen Geometry on the Point Load Strength Anisotropy of Phyllite

5.1. Introduction

Rock masses often exhibit anisotropism due to the existence of bedding planes, foliation/lineation, and joint planes. These planes of weakness within the rock masses can be inherent or induced. The inherent anisotropy is developed in the rock during rock formation, arising from bedding planes, foliations, and schistosity. The induced anisotropy results from a differential force field leading to the development of joints, fractures, shear planes, and faults (Zeng et al., 2008). Consequently, these weak planes often govern the mechanical behaviors of the anisotropic rocks, and they usually vary depending upon the orientation of the weak planes with reference to loading directions (Ramamurthy et al., 1993; Sun et al., 2022; Liu et al., 2023b; Singh et al., 2025b). Therefore, a detailed investigation of anisotropic strength variations is a key concern in rock engineering for developing safe and sustainable infrastructure on or within the rock masses.

Uniaxial Compressive Strength (UCS) tests have been routinely performed to characterize the rock masses for rock engineering projects (Cargill and Shakoor, 1990). Although the UCS test is highly reliable, it requires quality machined core specimens with a Length/Diameter (t/d) ratio of 2:1 to 2.5:1, and both end faces of the core should be parallel to each other. However, obtaining a core with such specifications is difficult in many instances, particularly in weak, bedded, and anisotropic rocks, where the specimen tends to split/break along the weak planes/discontinuities/foliations. Therefore, determining strength indirectly using the index test methods, like Point Load Index (PLI) tests, has always been attractive. The advantage of these tests is that they can be performed on core specimens of smaller t/d ratios of 1:1 (t/d ratio may vary within 0.3–1

as per the ISRM standard) or on irregular lump specimens. Thus, it will not require extensive specimen preparation and costly test set up, unlike uniaxial compression tests. Because of its usefulness and effectiveness in predicting rock strength, the Point Load Index (PLI) is also utilized in the rock mass rating (RMR) classification system proposed by Bieniawski (1989), which is a commonly used method for rock engineering applications.

To date, the implication of point load strength ($I_{S(50)}$) for the estimation of UCS for different isotropic rocks, e.g., basalt, quartzite, limestone, sandstone, granite, etc. has been evaluated by Bieniawski (1975), Singh and Singh (1993), Fener et al. (2005), Basu and Aydin (2006), Sahin et al. (2020), Xue et al. (2020), Bhowmik et al. (2022), Garrido et al. (2022), Jamshidi (2022), Akbay (2023), Akbay (2024), Jamshidi and Sousa (2024), and Wang et al. (2024a) and many of them have established well-defined empirical equations between $I_{S(50)}$ and UCS for several hard and crystalline rocks.

In contrast, the existing literature infers that the point load strength of anisotropic rocks has not been explored adequately. Broch and Franklin (1972) and Forster (1983) found that anisotropic rock specimens loaded parallel to bedding experienced minimum and highly scattered values of point load strength. In contrast, the specimens loaded perpendicular to bedding exhibit maximum and less scattered values. On the other hand, UCS of bedded/foliated rocks studied by a few authors (Ramamurthy et al., 1993; Karakul et al., 2010) found that minimum strength became conspicuous when specimens were loaded at $\beta = 30°$ to bedding, while the maximum strength was obtained when specimens were loaded perpendicular to foliation ($\beta = 90°$).

Few researchers, like Greminger (1982) and Basu and Kamran (2010), attempted to validate UCS from $I_{S(50)}$ of anisotropic rocks with weak planes at various angles to the loading direction. Greminger (1982) was successful in finding an efficient correlation for

a gneiss sample. Basu and Kamran (2010) established a significant correlation between UCS and $I_{S(50)}$ for schist rock, and recommended that the $Is_{(50)}$ values that occurred with invalid failure modes of the specimen be avoided along weakness planes. The correlation between UCS and $I_{S(50)}$ for gneiss at $\beta = 0$, 45, and 90° with the direction of loading was studied by Xue et al. (2022). They found that for specimens with $\beta = 45°$ inclined anisotropy, the relation between UCS and $I_{S(50)}$ exhibits weak correlation, and while specimens with vertical anisotropy exhibit no significant correlation between UCS and $I_{S(50)}$ was evident.

PLI tests can be performed both diametrically and axially on core specimens. Saroglou and Tsiambaos (2006) estimated the $I_{S(50)}$ for schist and gneiss using a diametral test, while Khanlari et al. (2014b) evaluated the axial $I_{S(50)}$ of various metamorphic rocks, including sillimanite garnet hornfelses, phyllites, slates, staurolite andalusite schists, and andalusite garnet hornfelses at seven different β values. Rastegar et al. (2020) examined the variation of $Is_{(50)}$ at different β magnitudes concerning the loading axis for diametral and axial PLI tests of phyllite specimens. The strength behavior, anisotropic ratio/index (ratio of maximum to minimum strength or the ratio of strength in the strongest to weakest direction), and rock failure mode of weathered shale were studied using the PLI test at different anisotropy angles with loading direction by Abbas and Mohamed (2022). Bieniawski (1975) stated that the diametral test is the simplest and most convenient form of the PLI test. Although diametral tests provide a quicker and more reliable result for isotropic rocks, researchers such as Forster (1983), Mishra and Basu (2012), and Khanlari et al. (2014a) postulated that the axial PLI test should be preferred for bedded or foliated anisotropic rocks, as it could be useful to estimate the strength anisotropy of these rocks.

Despite significant advancements in rock mechanics testing, a critical gap remains in assessing the reliability of the PLI for predicting UCS, especially in anisotropic rocks,

where structural variability can strongly influence test outcomes and rendering prediction inaccurate (Jamshidi and Sousa, 2024). In many instances, it has been observed that the anisotropic rock specimens fail at a very early stage of loading with an invalid failure mode, representing the failure modes to be invalid (Basu and Kamran, 2010; Basu et al., 2013).

Nevertheless, although the reference core diameter of 50 mm is widely regarded as reliable for indexing the strength of both isotropic and anisotropic rocks, specimen geometry, particularly the length (t) to diameter (d) ratio (t/d), remains a critical consideration. This issue is particularly significant for anisotropic rocks, where inappropriate geometry selection can yield erroneous strength index values. In the previous study by Read et al. (1980), the specimens with a geometry ratio (i.e., t/d ratio) of 1.1 were observed to be either rotated between the platens or failed at the edges, producing inconsistent results in axial point load testing. In contrast, a ratio of 0.65 yields consistent outcomes and thus is recommended this value as the site standard. Similarly, Saroglou and Tsiambaos (2006), through axial PLI tests on gneiss and schist with t/d ratios ranging from 0.25 to 1.5, comprehended that a t/d ratio < 0.7 will be ideal, as a higher t/d ratio causes invalid failure modes.

Forster (1983) also recommended that a t/d ratio between 0.5 to 1.0 will be ideal for isotropic rocks, e.g., dolerites, greenstones, and sandstones, while emphasizing that a t/d ratio below 0.7 is preferable for laminated or anisotropic rocks. However, Forster (1983) further indicated that specimens having a very small t/d ratio may induce error in estimating the $Is_{(50)}$, and also the effects of anisotropy on strength will either diminish or be minimized. Consistent with these concerns, ISRM (2015) further indicated that results obtained from small rock specimens should not be directly applied to address rock engineering problems.

Although the t/d ratio is a crucial concern, only limited studies have systematically examined its effect on $I_{S(50)}$ in anisotropic rocks, highlighting the necessity for further research to improve the robustness and reliability of PLI-based strength evaluation. Following the aforementioned discussion three distinct t/d ratios of 1, 0.8, and 0.6 were optimally chosen and specimens were prepared across seven distinct β angles of 0°, 15°, 30°, 45°, 60°, 75°, and 90° to investigate the effect of specimen geometry on the anisotropy in point load strength characterization with reference to Srinagar/Chandpur Phyllite. To ensure the reliability of the experimental results, a multivariable regression-based mathematical modeling approach with statistical validation was employed. Furthermore, based on this regression analysis, empirical equations were developed between $I_{S(50)}$ and its influencing parameters (β and t/d). In addition, Student's *t*-test and *F*-test were also performed to understand the statistical significance of the difference in the dataset across specimen geometries.

5.2. Methodology

Block samples of fresh phyllite with a highly foliated nature were collected from the study area mentioned in Section 2.1 (Chapter 2).

5.2.1. Preparation of the Test Specimens

The NX size, i.e., 54 mm diameter, rock cores were drilled from the collected phyllite blocks using a core drilling machine. The core specimens were retrieved at different β = 0, 15, 30, 45, 60, 75, and 90°. Obtaining core specimens with the desired anisotropic angle and length proved to be the most challenging aspect of this experimental investigation, largely due to the low success rate of core survival. Although the desired foliation angles of the specimens have been specified with respect to the coring direction, there is a possibility of slight deviation from the specified orientation by a few degrees.

This is due to the ambiguity of foliation planes on the specimen's surface, which leads to challenges in accurately identifying the orientation angle. Moreover, the undulating/wavy nature of the foliation planes in phyllite presents challenges in accurately determining the foliation angles. Thus, a deviation in β of ± 3° was considered.

After drilling the cores at desired angles, specimens with three different length/diameter (t/d) ratios of 0.6, 0.8, and 1 were prepared using a core cutting apparatus. Thus, a total of 12 specimens (four in each t/d ratio) at each anisotropic angle, summing to a total of 84 core specimens, were prepared for the axial PLI test in this investigation (Figure 5.1).

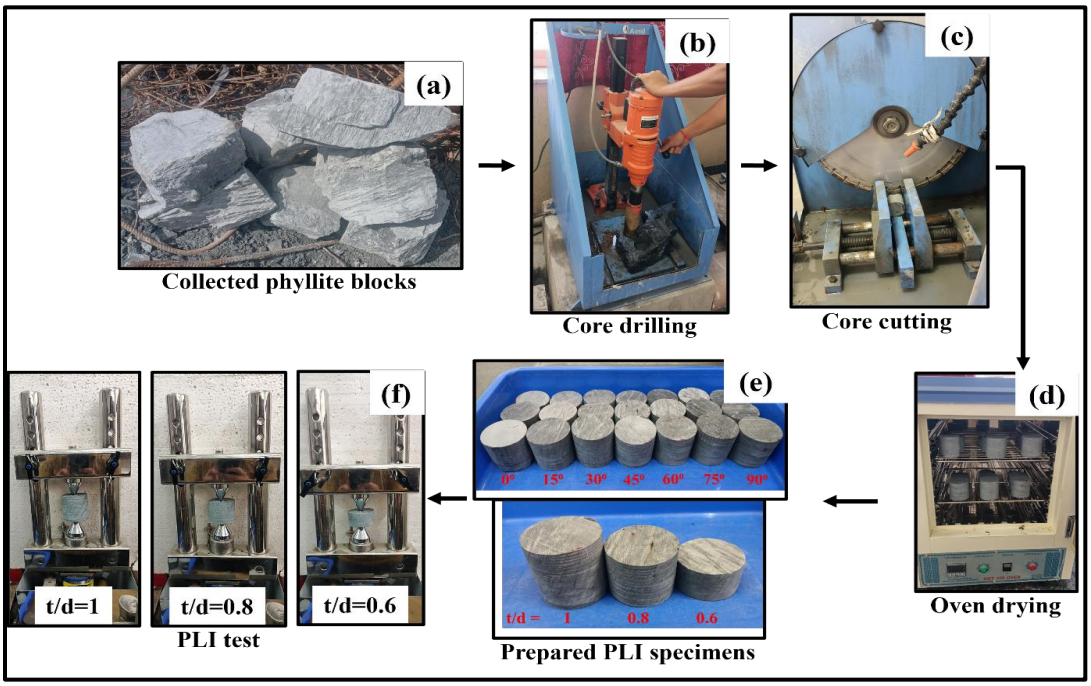

Figure 5.1. *Flow diagram of the PLI test procedure: (**a**) block sample of highly foliated phyllite, (**b**) core drilling at various foliation angles, (**c**) cutting and polishing of cores to prepare specimens of distinct geometries, (**d**) oven drying of prepared specimens, (**e**) representative PLI specimens with different geometries and foliation angles, and (**f**) axial PLI test configuration.*

5.2.2. PLI test

The axial PLI tests were performed using an Intellitest© point load test apparatus of 100 kN capacity. The test necessitates the rock specimens to be placed between two conical platens with precise geometry and hardness. This arrangement causes the specimen to fail with the development of one or more extensional planes along the loading line. The $I_{S(50)}$ of the specimens was determined using the following Eqs. (ISRM, 2007)

$$I_S = \frac{P}{D_e^2} \quad \text{Eq.5.1}$$

$$D_e^2 = \sqrt{\frac{4*A}{\pi}} \quad \text{Eq.5.2}$$

$$I_{S(50)} = F * I_s \quad \text{Eq.5.3}$$

Here, I_S: uncorrected point load strength index, $I_{S(50)}$: corrected point load strength index, P: Peak load at the time of failure, D_e: equivalent specimen diameter, A: area obtained by multiplying width (W) into Depth or height (D) of the specimens (i.e. A = W * D) and F: is size correction factor equivalent to a reference dimension of 50 mm and is estimated using Eq. 5.4 (ISRM, 2007).

$$F = (D_e/50)^{0.45} \quad \text{Eq.5.4}$$

5.2.3. Mathematical analyses

5.2.3.1. Hypothesis Test

The independent Student's t-test is an important statistical tool that assesses whether there is a significant difference between the means of two independent groups. This can help determine if the specimen geometry has a significant effect on the strength index of anisotropic rocks. It provides insights into whether observed differences are statistically significant, contributing to evidence-based inference about the geometry of anisotropic rocks. It is based on the distribution of differences between mean values of groups under the null hypothesis and considers the variability within each group. The null

hypothesis assumes no difference among the groups, whereas we have executed a right-tailed test, suggesting a significant difference in means. In the present analysis, a t-test was applied to compare the difference in strength between specimens with a t/d ratio of 1 and those with ratios of 0.8 and 0.6, respectively. The test includes comparisons for each β individually and as well as for all β combined. Further, a t-test has also been used to evaluate the statistical significance of the coefficients in the model.

In the first case, the following formula has been used:

$$t_{calc} = \frac{x_1 - x_2}{\sqrt{\frac{s_1^2}{n_1} + \frac{s_2^2}{n_2}}} \quad \text{Eq.5.5}$$

Here, t_{calc}: calculated t-value, $\overline{x}_1$ and $\overline{x}_2$ are the means of the first and second group of specimen sizes 'n_1' and 'n_2' having standard deviations 'S_1' and 'S_2', respectively.

The degree of freedom for this t-test is calculated using the following formula:

$$df = \frac{\left(\frac{s_1^2}{n_1} + \frac{s_2^2}{n_2}\right)^2}{\frac{\left(\frac{s_1^2}{n_1}\right)^2}{n_1 - 1} + \frac{\left(\frac{s_2^2}{n_2}\right)^2}{n_2 - 1}} \quad \text{Eq.5.6}$$

For the other part, we use the formula:

$$t_{statistic} = \frac{\hat{a}}{SE(\hat{a})} \quad \text{Eq.5.7}$$

Here, â: estimated coefficient and SE (â): standard error of the estimated coefficient.

In addition, an F-test was applied to validate the overall significance of the model. It assesses the degree to which the predictor is significantly related to the dependent variable. The F-statistics are evaluated as

$$\text{F-statistic} = \frac{Mean\ Square\ Regression}{Mean\ Square\ Error} \quad \text{Eq.5.8}$$

In all the tests, a 95 % confidence level is chosen compared to a 5 % significance level. The $p - values$ represent the probability of obtaining the observed results, or more extreme results if the null hypothesis is true. A small $p - value$ (typically less than a

chosen significance level, 0.05) indicates that the observed difference is unlikely to have occurred by chance alone, providing evidence to reject the null hypothesis. On the other hand, a larger $p-value$ indicates that the difference observed is not statistically significant, and there is not enough evidence to reject the null hypothesis.

5.2.3.2. Generalized Empirical Equation Development

The least squares method of linear regression was employed using Python to validate and develop empirical equations between $I_{S(50)}$ and various influencing parameters. This method minimizes the sum of the squared differences between the observed values and those predicted by the linear model, thereby identifying statistically optimal and robust empirical equations between $I_{S(50)}$ and β for different t/d ratios. For the specimens with t/d ratios of 1.0 and 0.8, a selective data fitting approach was used where empirical formulas were derived using only the valid failure data points. Additionally, multi-variable linear regression was performed using Python's statistical libraries on all valid failure data points to develop a combined empirical equation that incorporates the effect of both β and t/d ratio on $I_{S(50)}$. This combined approach resulted in a single predictive equation capable of estimating $I_{S(50)}$ across specimens with different t/d ratios and β, also including the potential interaction between β and t/d ratio.

5.3. Results

5.3.1. Characterization of Phyllite

Characterizations such as petrography, Field Emission Scanning Electron Microscopy (FE-SEM), and X-ray diffraction (XRD) analysis were conducted before the PLI test. These characterizations served as an important tool in understanding the mineral alignment, grain orientation, and mineralogical composition, which significantly influence the mechanical behavior. Petrographic thin section and FE-SEM analyses

conducted at three distinct β (0°, 45°, and 90°) showed well-developed foliations with matrix embedded between them (Figure 5.2). These foliations are the result of the alignment of flaky micaceous minerals developed during metamorphism. Petrographic observations further confirm the presence of quartz and other mineral grains oriented parallel to the foliation, typically situated between micaceous layers, forming a distinct mineralogical matrix. The elongation and deformation of mineral grains observed in thin sections indicate the induced pressure-temperature regime during low-grade metamorphism. The presence of micaceous minerals has been further varied using semi-quantitative X-ray diffraction analysis (Figure 5.3). Based on the Rietveld refinement technique using XRD data, it is evident that the Chandpur Phyllites mostly contain 45.6 % muscovite, 40.7 % quartz, with minor proportions of illite, albite, and ilmenite.

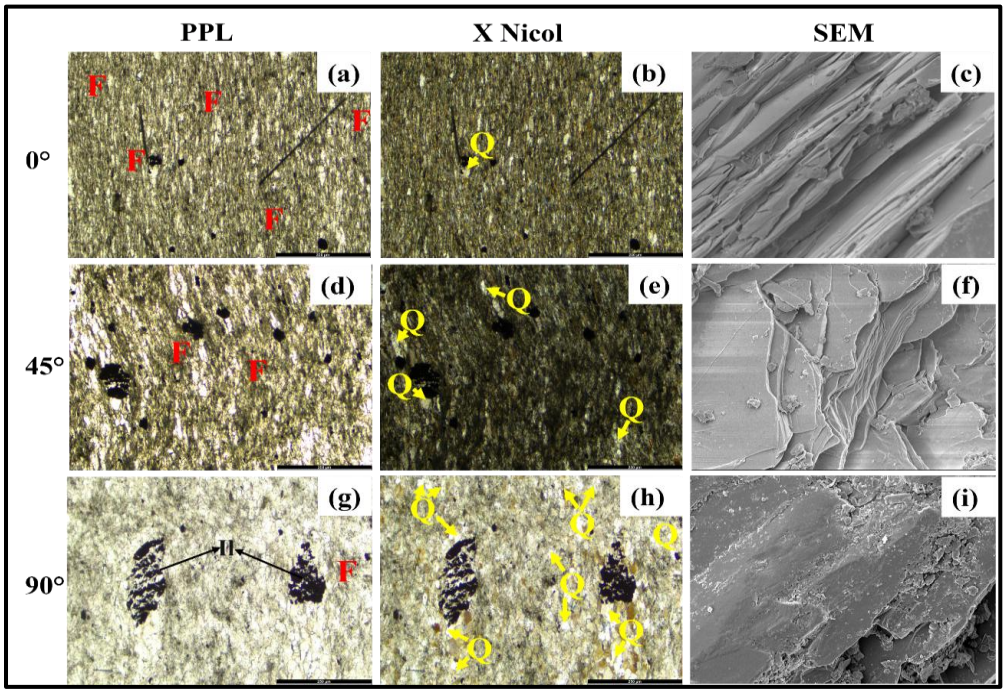

Figure 5.2. *Petrographic and FE-SEM analysis of Chandpur Phyllite at foliation angles (β) of 0°, 45°, and 90°: (**a**), (**d**), and (**g**) show petrographic images under Plane-Polarized Light (PPL); (**b**), (**e**), and (**h**) show petrographic images under Crossed Nicols (XPL); and (**c**), (**f**), and (**i**) present FE-SEM photomicrographs of the phyllite.*

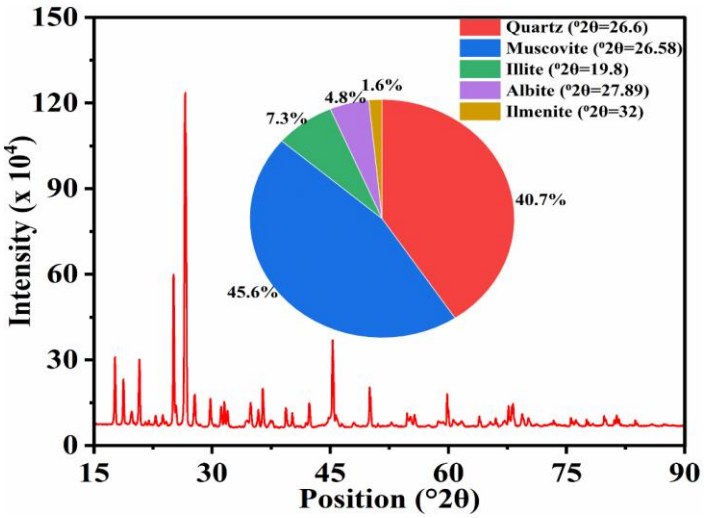

Figure 5.3. *Graph showing semi-quantitative X-ray diffraction of Chandpur Phyllite.*

5.3.2. Effect of t/d ratios on Axial PLI test

The $I_{S(50)}$ was calculated at varying β of 0°, 15°, 30°, 45°, 60°, 75°, and 90° for t/d = 1, 0.8, and 0.6 (Figure 5.4). It has been observed that in cases t/d = 1 and 0.8, the point load strength of phyllites increases gradually with increasing β from 0° to 60° followed by a decrease at angles 75° and 90° (Figures 5.4a, b). At t/d =1, the minimum and maximum point load strengths were estimated as 0.11 MPa (at β=0°) and 5.23 MPa (at β=60°), respectively. For t/d =0.8, these values were calculated as 1.01 MPa (at β= 0°) and 6.32 MPa (at β=60°), respectively. In contrast, for t/d = 0.6, the point load strength of phyllites showed a continuous increase with an increasing angle from 0° to 90° (Figure 5.4c), with a minimum value of 1.61 MPa at β = 0° and a maximum value of 7.01 MPa at β = 90°. The minimum, maximum, and average $I_{S(50)}$ values for each t/d ratio, independent of β, are shown in Figure 5.4d.

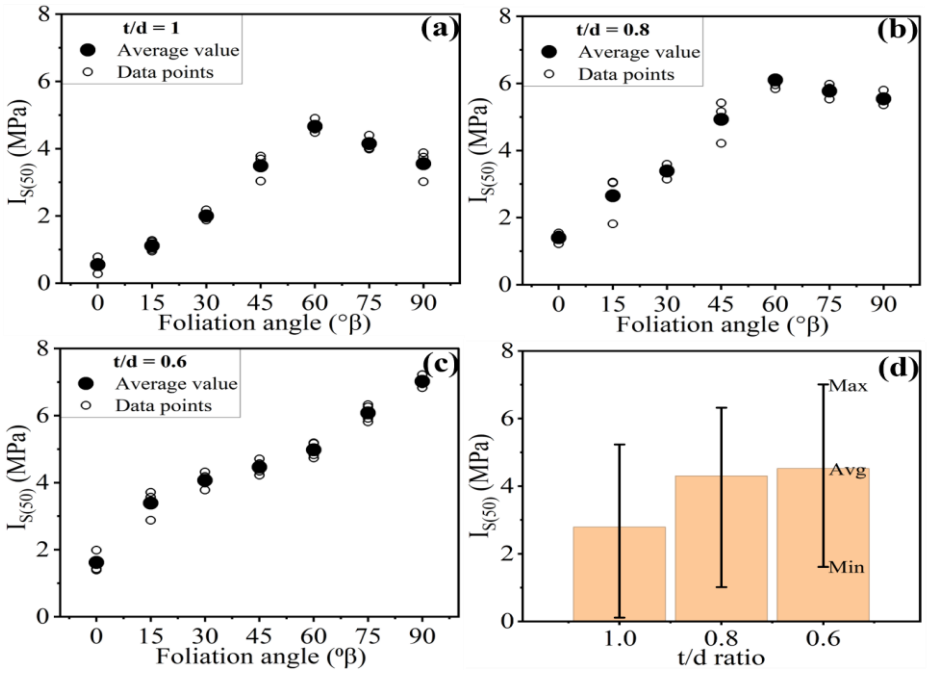

Figure 5.4. *(**a**), (**b**), and (**c**) show the $I_{S(50)}$ values at different β for t/d ratios 1, 0.8, and 0.6, while graph (**d**) shows the average, minimum, and maximum values of $I_{S(50)}$ at different t/d ratios, independent of foliation angles.*

The strength anisotropy ratio ($I_{a(50)}$), i.e., the ratio of $I_{S(50)}$ calculated in the strongest and weakest direction ($I_{S(50)\,max}/I_{S(50)min}$), has also been calculated for specimens to characterize the anisotropic rocks. The values were determined to be 8.47, 4.42, and 4.33 for the t/d ratios of 1, 0.8, and 0.6. As per the ISRM (1985) classification scheme of anisotropy ratio for $I_{S(50)}$, Chandpur Phyllite grades into very highly anisotropic with very strongly developed foliations.

5.3.3. Rock Failure Modes with varying β and t/d ratios

Failure of rock masses is a major concern in rock engineering practices. Therefore, understanding the rock failure modes under different stress conditions is crucial for recognizing the suitability of support design (Bhowmick et al., 2022).

The rock failure modes of Chandpur Phyllite were analysed across the β for t/d= 1, 0.8, and 0.6, following Basu et al. (2013) and Khanlari et al. (2015). In case of

anisotropic rock masses, the nature of failure could broadly be identified as (*i*) along the foliation, in which the failure plane passes parallel to the foliation plane, and (*ii*) through material, in which the failure plane passes across the foliation plane as well as the rock matrix. Based on the failure mechanism of tensile or shear in nature, these two failure categories can be subdivided into three failure modes to address the role of anisotropy. They are (*i*) Tensile splitting along foliation (TSAF); (*ii*) Shear splitting along foliation (SSAF), and (*iii*) Tensile splitting through material (TSTM). The SSAF failure mode has been further categorized as (*i*) SSAF(V) for the valid failure in cases when the failure plane of shear splitting along foliation passes through the loading points, and **(ii)** SSAF(Iv) for the invalid failure, when the failure plane of shear splitting along foliation is unable to pass through the loading points, and chipping of small fragments occurs. A generalized schematic representation of observed failure modes under axial PLI test for Chandpur Phyllite is shown in Table 5.1, whereas the failed specimens and schematics of characteristic rock failure modes for each t/d ratios across various foliation angles are shown in Figure 5.5 and Table 5.2.

Table 5.1. *Represents the classification of the failure modes in the axial PLI test for anisotropic phyllite. Modified after Khanlari et al. (2015).*

Nature of failure	Failure mode	Schematic representation
Along foliation (AF)	Tensile splitting along foliation (TSAF)	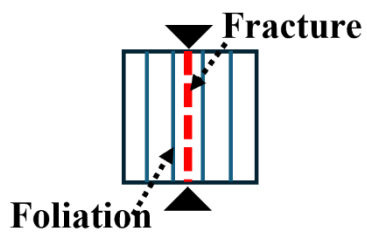

	Shear splitting along foliation (SSAF)	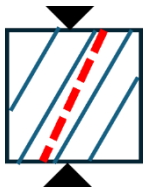 SSAF(V) [Valid failure]	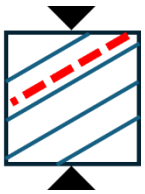 SSAF(Iv) [Invalid failure]
Through material (TM)	Tensile splitting through material (TSTM)		

At low foliation angles (β = 0–15°), irrespective of specimen geometry, the valid failure was obtained with the TSAF failure mode. With increasing β (30–45°), the dominant mode transitioned to SSAF for specimens with t/d ratios of 1.0 and 0.8, indicating shear-driven splitting along inclined foliation planes. In contrast, specimens with a lower t/d ratio of 0.6 exhibited TSTM failure mode at the same β range, reflecting a shift from foliation-controlled failure to combined (matrix and foliation-controlled) failure. However, in the case of t/d ratio 1, at a β of 30°, the failure mode remained TSAF, underscoring the role of geometry in controlling the failure behavior. At higher foliation angles (β = 60–90°), TSTM failure mode became dominant with valid failure in thinner specimens (t/d = 0.6), whereas thicker specimens (t/d = 1.0 and 0.8) primarily failed with SSAF(Iv) failure mode, reflecting continued influence of foliation planes. Broadly, at a specimen geometry of t/d ratio= 1, 43 % of the specimens manifested by the TSAF failure mode, whereas only 28 % of specimens with t/d ratios of 0.8 and 0.6 possessed this behavior. In contrast, SSAF (Iv) failures dominated at higher thickness ratios, accounting for 57 % of specimens at both t/d = 1.0 and 0.8. Conversely, at t/d ratio= 0.6, TSTM became the prevailing mechanism, observed in 72 % of specimens (Figure 5.6).

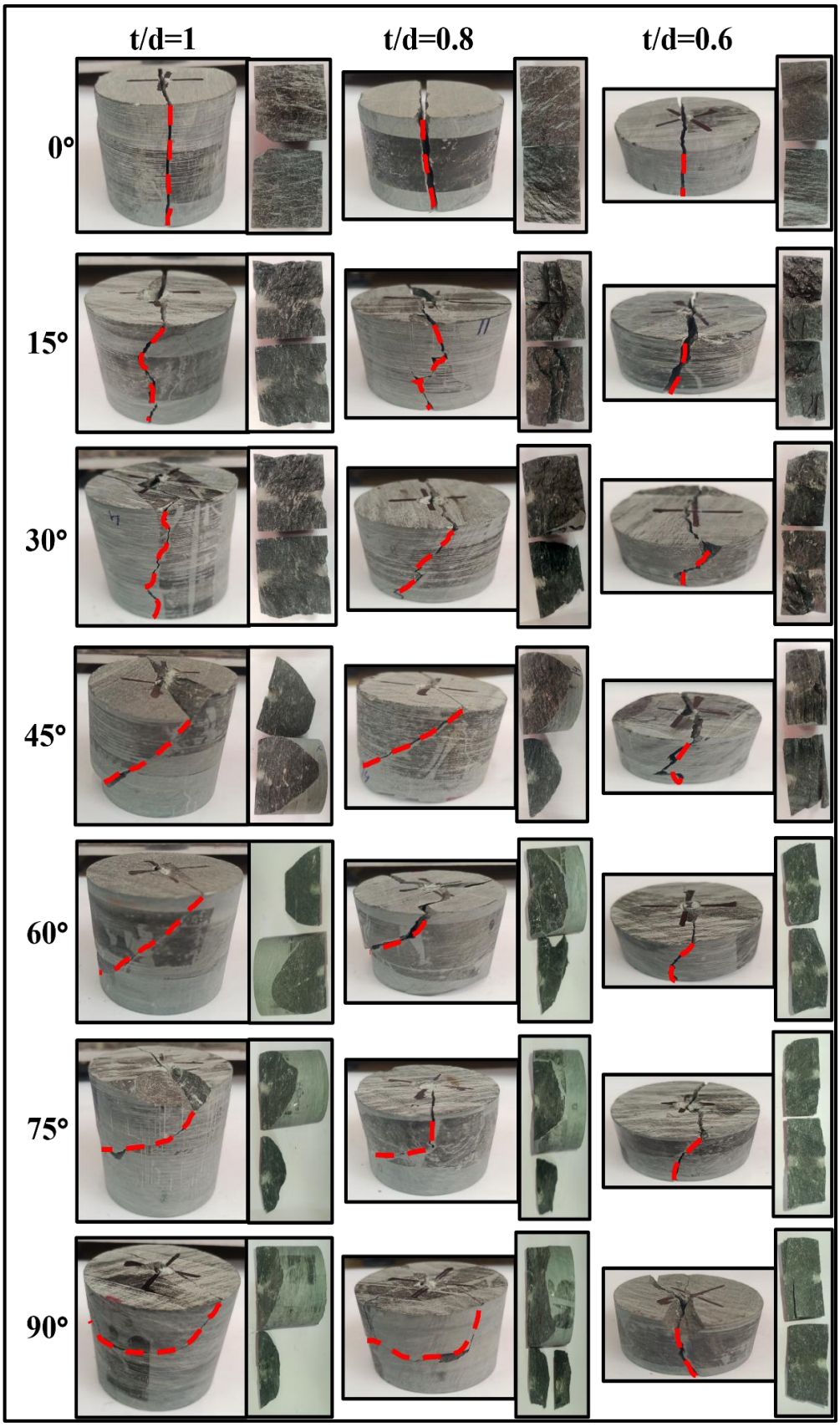

Figure 5.5. *Rock failure modes under distinct specimen geometries and foliation angles.*

Table 5.2. *Characteristic rock failure modes for each t/d ratio across various foliation angles.*

(°β)	t/d = 1		t/d = 0.8		t/d = 0.6	
	Schematic	**Failure mode**	**Schematic**	**Failure mode**	**Schematic**	**Failure mode**
0		TSAF		TSAF	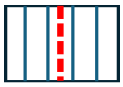	TSAF
15	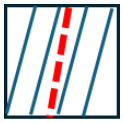	TSAF	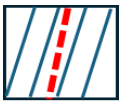	TSAF	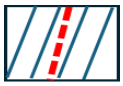	TSAF
30	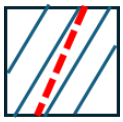	TSAF	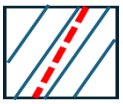	SSAF(V)	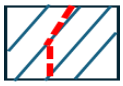	TSTM
45	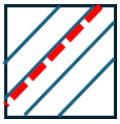	SSAF(Iv)	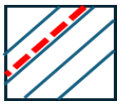	SSAF(Iv)	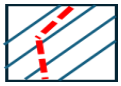	TSTM
60	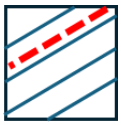	SSAF(Iv)	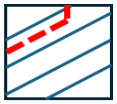	SSAF(Iv)	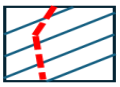	TSTM
75		SSAF(Iv)	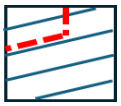	SSAF(Iv)	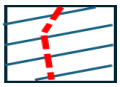	TSTM
90		SSAF(Iv)		SSAF(Iv)		TSTM

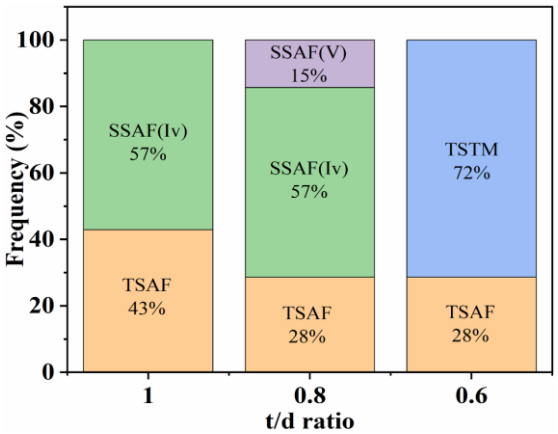

Figure 5.6. *Bar diagram showing the frequency of specimens failed in various failure modes at t/d ratios of 1, 0.8, and 0.6.*

5.3.4. Student's t-test and F-test

A two-specimen independent t-test is a statistical method used to compare two independent groups to identify if there is significant statistical evidence that their population means differ significantly, assuming the samples are mutually independent. Further, this comparison identifies the appropriate specimen geometry for better indexing the strength and knowing the strength anisotropy ratio of anisotropic rock. R-software (Version 4.2.2, 2022) has been used to perform the Student's t-test analysis in this study. Table 5.3 presents the t-test results obtained by comparing the $I_{S(50)}$ values of the specimen geometry of 0.8 with 1 for each foliation angle. A 95 % confidence interval for the difference in the means for each of the β values is presented in Table 5.3. It indicates the range within which the true difference in the axial $I_{S(50)}$ is expected to fall with 95 % confidence. Since this is a one-tailed test, the interval extends to infinity on the upper end, reflecting that the test is only considering values greater than a certain threshold. The $p-values$ for each of the angles in Table 5.3 indicate that the corresponding t-calculated values lie in the rejection region, and thus, the null hypothesis is rejected. It means that the difference in the strength index is claimed. Therefore, anisotropic phyllite with a t/d = 0.8 has a better strength index than that for a t/d = 1.

A similar procedure was carried out to compare $I_{S(50)}$ values of the t/d = 0.6 with the t/d = 1 for each β angle. The results obtained in this case are listed in Table 5.4. Based on the aforementioned arguments, the null hypothesis is rejected, indicating a difference in the strength index. As discussed in Section 5.3.2, specimens with t/d = 0.6 are found to exhibit a superior strength index compared to other geometries.

Table 5.3. *t-test results obtained by comparison of $I_{S(50)}$ values for t/d ratio 0.8 with 1.*

(°β)	t_{cal}	$p-value$	95 % CI (for difference)
0°	6.5702	0.0004492	(0.5866834, Inf)
15°	5.1251	0.005138	(0.8957747, Inf)
30°	12.185	2.067e-05	(1.171868, Inf)
45°	4.7278	0.002458	(0.8450648, Inf)
60°	7.3084	0.000646	(1.060823, Inf)
75°	11.418	1.441e-05	(1.323117, Inf)
90°	8.1949	0.0001442	(1.450759, Inf)
combined	3.4147	0.0006153	(0.7491523, Inf)

The fitting of the regression model to the $I_{S(50)}$ values of all considered specimen geometries has also been verified using both the t-test and the F-test. For specimen geometries 0.6, 0.8, and 1, a simple linear regression model was used, where fitting was done only for valid failure data points. Consequently, the t-test and the F-test have been applied accordingly. The t-value was used to test the hypothesis that a particular coefficient is statistically significant against the null hypothesis, which assumes no effect on the dependent variable. The results are presented in Table 5.5. Since the $p-value$ is smaller than the threshold limit, the null hypothesis is rejected, and we conclude the coefficients to be statistically significant for all specimen geometries. Further, the F-statistic was used to test the overall significance of the model. It compares the given model to a model that is independent of the predictor, with the latter serving as the null hypothesis. The results of the F-test have been presented in Table 5.6. Since the $p-value$ is very small in all cases, the null hypothesis is rejected, and the resulting parameters significantly improve the model's fit. The models are thus considered statistically significant.

Table 5.4. *t-test results obtained by comparison of $I_{S(50)}$ values for the t/d ratio of 0.6 with the t/d ratio of 1.*

(°β)	t_{cal}	$p-value$	95 % CI (for difference)
0°	6.2035	0.000531	(0.7319941, Inf)
15°	11.475	0.0001365	(1.858361, Inf)
30°	15.303	1.72e-05	(1.789215, Inf)

45°	4.843	0.002125	(0.571174, Inf)
60°	2.1468	0.03925	(0.02662957, Inf)
75°	12.24	1.605e-05	(1.616881, Inf)
90°	16.731	2.951e-05	(3.027633, Inf)
combined	4.0558	8.195e-05	(1.014927, Inf)

Table 5.5. *t-test result for fitting the regression analysis with t/d ratios of 0.6, 0.8, and 1.*

Geometry	Coefficient	Estimate	Std. Error	$t_{statistic}$	$p-value$
0.6	Intercept	1.7662	0.2034	8.685	3.67e-09
	Sine Slope	4.4780	0.2876	15.569	1.07e-14
0.8	Intercept	1.4753	0.1749	8.433	7.40e-06
	Sine Slope	4.0378	0.5382	7.503	2.06e-05
1	Intercept	0.4874	0.0863	5.646	0.000214
	Sine Slope	2.8962	0.2655	10.905	7.15e-07

Table 5.6. *F-test analysis for all three specimen geometries fitting analysis.*

Geometry (t/d ratio)	$F_{statistic}$	$p-value$
0.6	242.4	1.075e-14
0.8	56.29	2.056e-05
1	118.9	7.146e-07

5.4. Discussions

PLI testing not only provides an effective means of assessing rock strength but also yields valuable insights into potential failure modes under tensile stress regimes. However, to obtain reliable test results, typically for anisotropic rocks like phyllites, the specimen geometry must be optimally selected to ensure that the influence of anisotropy is adequately captured. Accordingly, this study evaluates the effects of specimen geometry (i.e., t/d ratio) on the point load strength of phyllites at different β. Subsequently, mathematical modeling and statistical analysis have been performed in order to validate the specimen geometry effect on axial PLI of anisotropic rock.

For t/d ratios of 0.8 and 1, the $I_{S(50)}$ increases with the increase in β within the range of $0° \leq \beta \leq 60°$, followed by a decrease in strength at β = 75 and 90° (Figures 5.4a, b). This could mostly be attributed to stress distribution and microstructural attributes of the rock. Phyllites mostly comprise quartz and micaceous minerals, with well-developed foliations consisting of micaceous minerals, while quartz and other mineral grains

oriented parallel to the foliation, typically situated between micaceous layers, forming a distinct mineralogical matrix (Figure 5.2). For t/d ratios of 0.8 and 1, the increase in $I_{S(50)}$ with $\beta = 0° \leq \beta \leq 60°$ implies that the failure mechanism progressively shifts from being predominantly foliation-controlled to a combined influence of both foliation and matrix strength, thereby providing higher resistance to failure.

However, at higher $\beta = 75$ and 90°, premature chipping along foliation planes was observed under relatively low applied stress. This localized failure does not represent the true axial point load strength of the rock at higher β in the case of t/d ratios of 0.8 and 1. This highlights the importance of specimen geometry in axial PLI test of anisotropic rock, as phyllite specimens with higher t/d ratios (1.0 and 0.8) are more susceptible to premature chipping under low stress. Åkesson et al. (2003) inferred that the foliation planes formed by the accumulation of micaceous grains could act as large flaws and might control the propagation of cracks during the failure. Li et al. (2001) indicated that micaceous minerals undergo plastic deformation under stress, leading to the generation of local tensile stress at the periphery of harder minerals. Thus, the microcracks induced around the micaceous minerals facilitate crack propagation at lower stress levels (Mishra and Ram, 2024; Ram and Gupta, 2024).

In contrast, for a t/d ratio of 0.6, the smaller geometry facilitates more uniform stress distribution across the loading axis as well as along the foliation planes and rock matrix at different orientations. It leads to a gradual increase in $I_{S(50)}$ with increasing β from 0 to 90° (Figure 5.4c). Similar observations of the increase in axial point load strength with the increasing β for anisotropic rocks have been reported by Behrestaghi et al. (1996), Khanlari et al. (2014b), and SI et al. (2021), who stated that cementation strength significantly influences the rock properties, which are notably lower along the foliation planes as compared to the rock matrix.

The rock failure modes of the investigated phyllites at different t/d ratios and β values have also been assessed. The lower angles, i.e., up to β = 30° (Figure 5.5), are mostly characterized by failure along the foliation planes with failure occurring throughout the specimen. This could be attributed to the alignment of foliation planes parallel or nearly parallel to the loading axis, along which the induced tensile stress concentration facilitates tensile splitting. Moreover, since the stress distribution along the foliation planes mostly controls the mechanical behavior at lower β, it typically exhibits lower strength across all t/d ratios.

However, an increase in β > 30° leads to substantial variation in failure modes. The t/d ratios of 1 and 0.8 mostly possess shear splitting along the foliation. This could be attributed to increased shear stress and a decrease in normal stress along the foliation planes with the increase in angle between the loading axis and foliation planes. This causes a clear shift from tensile splitting along foliation to shear splitting along foliation mode. However, such failure modes cannot propagate throughout the material and hence are considered invalid rock failure modes in PLI tests (Basu and Kamran, 2010; Basu et al., 2013). In contrast, the smaller t/d ratio of 0.6 facilitates tensile splitting through the material across the β = 30° ≤ β ≤ 90°. This is mostly because the smaller thickness favors the formation of a more uniform tensile stress field between the two conical loading platens. This reduces the probability of shear localization along the foliations, thereby governing the generation of cracks at the central part of the specimen and facilitating propagation throughout the material, regardless of foliation orientation, making them a valid failure mode.

Thus, the failure mode and possible uniform tensile stress throughout the specimen also substantiate the increase in strength with increasing β. The failure/rupture surface also provides critical insight into the rock's strength and mechanical response.

The rough and jagged failure surface observed in specimens tested at higher foliation angles is indicative of greater strength, with the large absorption of energy during failure. In contrast, at smaller β, the failure surface appears slightly smoother and flatter, indicating lower strength (Figure 5.7). Similar observations on fracture surface morphology with the strength of anisotropic rock material have also been reported by Li et al. (2021).

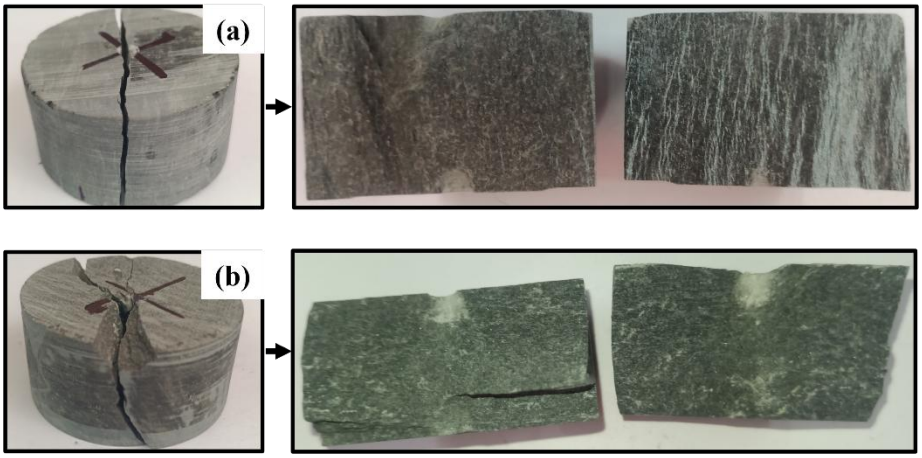

Figure 5.7. *Representative failure surface of the specimen at* ***(a)*** *β = 0° and* ***(b)*** *β = 90°.*

The independent Student's t-test performed in this study has proven to be an effective method in examining the differences between the means of two independent groups. The results suggest a significant difference between the selected specimen geometries, indicating that specimens with a t/d ratio of 0.6 or 0.8 exhibit a relatively better strength index than those with a t/d = 1. Further, based on the 95 % confidence level analysis, the difference in strength between specimen geometries with a t/d ratio of 1 and 0.6 was significantly larger compared to the difference between geometries with a t/d ratio of 1 and 0.8. Also, the t-test analysis performed on the coefficients of the empirical equations of different specimen geometries was found to be highly significant, indicating that the models effectively explain the variation in the data.

The specimen geometry plays a critical role in determining the $I_{S(50)}$ of anisotropic rocks. Based on the multiple observations, i.e., experimental observations and statistical analysis used in this investigation, it is recommended to use a smaller specimen geometry (t/d ≈ 0.6) for accurate estimation of $I_{S(50)}$ in case of anisotropic phyllite rock masses. Some previous researchers also suggested improving the test practice by including specimens with smaller t/d ratios within a range of 0.60–0.70 for anisotropic rocks (Read et al., 1980; Forster, 1983; Saroglou and Tsiambaos, 2006), and this study provides complete validation for such recommendations through combined experimental and mathematical analysis.

5.4.1. Generalized Empirical Relation between t/d ratio and β

Empirical relationships between the sine of the β and $I_{S(50)}$ were developed for each t/d ratio using the valid failure mode data point through the regression analysis using linear fit (Figure 5.8). The empirical equations between t/d ratios of 1.0, 0.8, and 0.6 with $I_{S(50)}$ are presented in Eqs. 5.9, 5.10, and 5.11, respectively.

$$I_{S(50)} = 2.8962\ sin\ (\beta)\ + 0.4874 \quad \text{Eq.5.9}$$

$$I_{S(50)} = 4.0378\ sin\ (\beta)\ + 1.4753 \quad \text{Eq.5.10}$$

$$I_{S(50)} = 4.4780\ sin\ (\beta)\ + 1.7662 \quad \text{Eq.5.11}$$

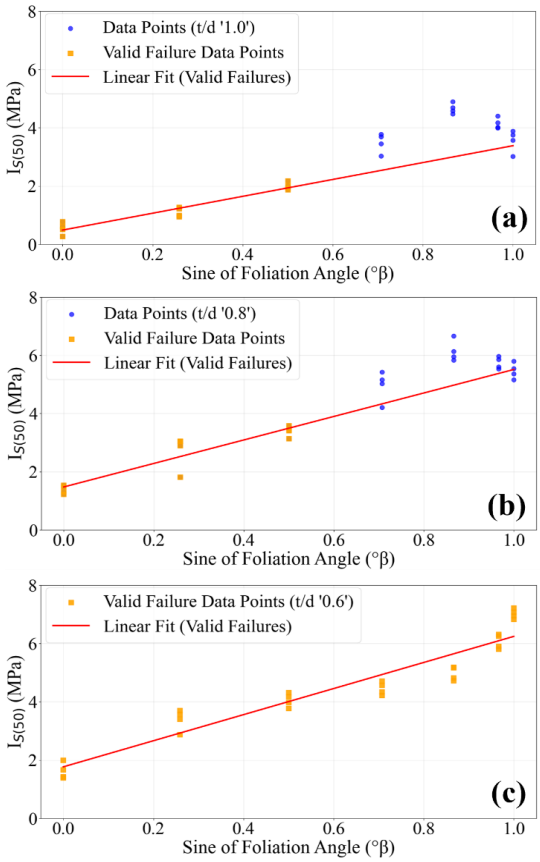

Figure 5.8. *Regression analysis using linear fit for valid failure data points for the specimen geometries (t/d):* ***(a)*** *1,* ***(b)*** *0.8, and* ***(c)*** *0.6.*

Moreover, a combined empirical equation incorporating both β and t/d effects was further developed using multivariable linear regression on valid failure data points to generalize the prediction of $I_{S\,(50)}$ across all t/d ratios and β. Figure 5.9 shows the best-fit curve of the experimental data points (valid and invalid) across all specimen geometries, plotted in a 3D space. In this model, dataset preparation involved merging valid failure data from all three specimen geometries to develop the combined empirical equation while maintaining consistency with individual formula fitting approaches.

$$I_{S(50)} = 6.1818\ sin\ (\beta) - 3.3433\left(\frac{t}{d}\right) - 3.1126\ sin\ (\beta)\ \left(\frac{t}{d}\right) + 3.9371 \qquad \text{Eq.5.12}$$

This generalized empirical equation revealed the complex interactions between β and the t/d through the negative interaction term (-3.1126 sin(β) (t/d)). This indicates that geometry (t/d of sample) effects become increasingly important at higher foliation angles.

This mathematical model provides theoretical support for the experimental findings regarding stress distribution challenges in larger specimens at higher β values. The combined model provides a single, generalizable predictive equation for $I_{S(50)}$, applicable across a range of β and t/d values, a major advancement over the geometry-specific linear fit models, which were limited to only three values of t/d. This flexibility is critical in practical scenarios, where specimen geometry and β may vary. Moreover, the combined empirical equation analysis, utilizing only valid failure data points, shows the importance of data quality in empirical modelling for anisotropic rocks. The high improvement in combined equation performance ($R^2 = 0.94$) after removing invalid failures validates the experimental observation that specimen geometry directly influences failure behavior. This approach accurately estimates the $I_{S(50)}$ across different specimen geometries.

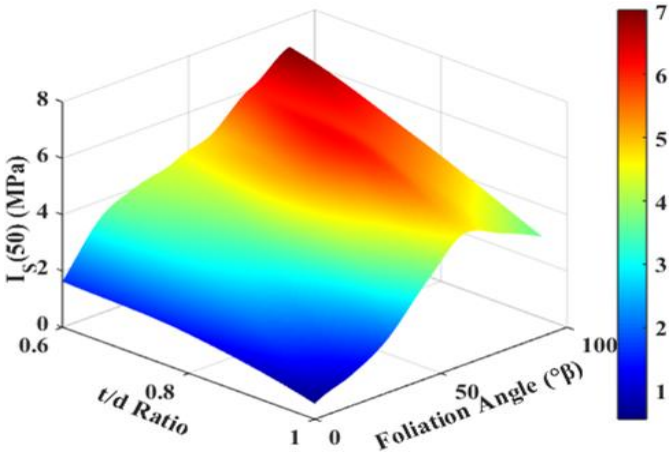

Figure 5.9. *Shows the best fit curve of the experimental data points across all specimen geometries, plotted in a 3D coordinate system.*

5.5. Summary

The PLI test has always been attractive in the indirect determination of rock strength. Unlike uniaxial compression tests, this test becomes even more important for the anisotropic rocks as it does not require extensive specimen preparation and costly test setup. Although the PLI test is important to assess the strength of isotropic rocks, its

applicability to anisotropic rocks remains inadequately evaluated. This is primarily due to challenges in achieving the accurate specimen geometry (t/d ratio), resulting in inaccurate strength measurements and invalid failure modes. Addressing this issue, an experimental investigation has been carried out to investigate the effects of specimen geometry (t/d ratio) on the $I_{S(50)}$ value of the Srinagar/Chandpur Phyllite for different β values using an axial PLI test. The results indicate that geometry has a significant impact on the strength and failure mode of phyllite.

More specifically, specimens with t/d ratios of 1.0 and 0.8 exhibited increasing strength as the β increases up to 60°; thereafter, strength declined with further increases in β. For these two geometries, valid failure modes occurred only up to β = 30°; beyond that, failure became invalid with larger β. In contrast, specimens with t/d = 0.6 shows a continuous increase in strength from β = 0 to 90°, consistently exhibiting valid failure modes across the entire β. The mathematical analyses (empirical modelling, statistical validation, and Student's t-test & F-test) further validate the experimental results. The experimental results and statistical validations demonstrate that a specimen having t/d ≈ 0.6 is a preferred geometry for PLI testing of anisotropic phyllite rock masses. Additionally, a combined empirical equation incorporating both β and t/d was developed. The negative interaction of the equation reveals that geometry effects become increasingly critical at higher foliation angles. This experimental investigation with analytical validation is crucial for understanding the effect of specimen geometry (t/d ratio) in axial PLI testing of anisotropic rocks. It is also important for the design, analysis, and safety evaluation of engineering structures in complex geological formations where anisotropy plays a significant role.

Chapter: 6
Multiscale Mechanical Characterization of Krol Shale using Brazilian Tensile Strength and Nano-indentation Tests: Implications in Hydrocarbon Recovery and CO_2 Sequestration

6.1. Introduction

Globally, shale formations are recognized as promising oil/gas reservoirs and a major sink for long-term CO_2 storage (Paul et al., 2025). Over the past decade, due to its importance as a hydrocarbon reservoir and as a promising CO_2 storage formation, shale has attracted considerable attention in India and elsewhere. Due to its unique pore system, characterized by extremely low permeability, complex mineralogy, and nanoscale pores, extensive research has primarily focused on its pore structure, adsorption behavior, and fluid-flow mechanisms. However, despite considerable attention, minimal focus has been given to the mechanical behavior of shale. This research gap is very crucial for the success of both CO_2 sequestration and hydrocarbon exploration, which is primarily governed by stress evolution and the deformation behavior of the shale formation.

Given that shale is heterogeneous, inherently anisotropic, and stress-sensitive, its mechanical response is equally important to understand. Graham et al. (2021) stated that the mechanical response of shale is of critical importance for engineering and energy applications, such as oil/gas production and CO_2 storage, and these applications rely most on the accurate estimation of shale's mechanical properties. In particular, the mechanical properties of the shale directly control the fracture initiation and propagation, which are critical for enhancing hydrocarbon production and CO_2 storage applications.

Oil/gas production requires hydraulic fracturing or thermal stimulation, for which mechanical parameters such as elastic modulus, hardness, strength, roughness, and brittleness are crucial. For CO_2 storage in depleted oil/gas reservoirs, assessing its mechanical behavior is important for ensuring long-term storage, as reservoir depletion

often induces overburden compaction (Obradors-Prats et al., 2017). Furthermore, changes in the stress field during CO_2 injection can modify fracture networks, making mechanical characterization essential for evaluating the risk of leakage. In combined CO_2-Enhanced Gas Recovery (CO_2-EGR) sequestration, where CO_2 is injected into the shale formation to enhance methane recovery while storing CO_2, the mechanical parameters become vital for maintaining stability and overall reservoir integrity. The mechanical properties of shale vary significantly across different origins due to its highly heterogeneous nature (Liu et al., 2021a). Therefore, a lack of understanding of the mechanical properties of individual shale formations often leads to numerous safety accidents, such as borehole collapse and wall instability, along with uncontrolled fracture propagation that may reduce the CO_2 storage capacity and hydrocarbon recovery.

At the macroscopic level, conventional analytical techniques, e.g., uniaxial or triaxial compression tests and indirect tensile tests, are used to obtain mechanical parameters of rocks (Kumar et al., 2017). From the perspective of shale formations, during hydraulic fracturing or thermal stimulation for hydrocarbon production and CO_2 storage, the formation generally induces tensile failure as the primary fracture (Feng et al., 2020). Such tensile stress-induced failure creates fracture for hydrocarbon flow and also affects the capacity during CO_2 injection. Li and Wong (2013) stated that tensile strength is the primary indicator of strength, deformability, and bearing capacity for shale formation. Therefore, during both hydrocarbon production and CO_2 storage, the tensile strength test of shale becomes a key parameter for designing effective and safe rock-engineering practices (Erarslan et al., 2012). Accurate estimation of tensile strength is important to predict fracture limitation, which is important for reliable geomechanical models used in reservoir stimulation and CO_2 storage capacity assessment. Mahanta et al. (2018) investigated the Jhiri shale from the Damoh district of Madhya Pradesh and

reported that its tensile strength is highly sensitive to changes in strain rate. The tensile strengths of thermally treated shales from the Jharia, Wardha, and Raniganj coalfields of the Gondwana Supergroup has been reported in previous studies (Srinivasan et al., 2020; Vishal et al., 2022; Nilankar et al., 2024a). Despite numerous shale formations in India with potential for oil and gas recovery and CO_2 storage, only a few have been evaluated for tensile strength and associated mechanical parameters, viz. hardness, elastic modulus, and brittleness. This is particularly important because tensile strength governs the initiation and growth of hydraulic fractures during hydrocarbon extraction and limits fracture propagation under injection-induced stresses during CO_2 sequestration. However, such evaluation remains limited due to the challenges associated with conventional mechanical testing of shale: (*a*) the requirement of a large quantity of rock to prepare test samples, and (*b*) the inherent bedding planes, which make coring or extracting suitable samples extremely difficult (Fan et al., 2019). Kumar et al. (2012) also highlighted that technical and economic challenges in core recovery restrict the use of conventional geomechanical tests.

The mechanical response of the rock is not only controlled at the macroscopic level, but microscopic properties also significantly control the mechanical behavior (Bobko and Ulm, 2008). The investigation of microscopic mechanical behavior is particularly critical for shale, where abundant micropores (nanoscale) not only host hydrocarbons but also serve as potential sites for CO_2 storage. At this scale, the way mineral matter, organic content, pore structures, etc., interact, governs local deformation, swelling, and shrinkage during CO_2 injection. Manjunath and Jha (2019) stated that conventional (macroscopic) analysis cannot explain the complexities encountered during hydraulic fracturing because it does not account for the microscopic heterogeneity of shale.

Therefore, in response to this, recent researchers have introduced an unconventional nano-indentation technique to characterize the micromechanical properties of shale (Shi et al., 2019; Lu et al., 2020; Kong et al., 2021; Du et al., 2022; Wang et al., 2022; Yang et al., 2024; Han et al., 2025; Pei et al., 2025; Li et al., 2026). The nano-indentation technique uses a diamond indenter of known geometry and mechanical properties, which is pressed onto the sample surface under a load of millinewton range (Schuh, 2006). In this technique, indentation depth is a key factor because variations in indentation depth probe different material volumes, resulting in varying mechanical responses (Yang et al., 2020). In the context of Indian shales, research on their micromechanical properties using nano-indentation is extremely limited. Based on an extensive review of the available literature, only a few studies have reported nano-indentation characterization of Indian shale formations (Manjunath and Jha, 2019; Chowdhury et al., 2025). They have assessed mechanical parameters, including the elastic modulus and hardness of the mineral phases present in the samples.

Although both macroscopic tensile-strength tests and microscopic nano-indentation tests are important for understanding the multiscale mechanical behavior of shale, a significant research gap exists, especially in the context of Indian shale. A conventional tensile strength test provides essential parameters, such as elastic modulus and tensile strength, that control fracture initiation or propagation during hydraulic fracturing for hydrocarbon extraction and CO_2 storage. In contrast, the unconventional nano-indentation technique captures mechanical heterogeneity by determining the elastic moduli, hardness, and stiffness of distinct mineral phases, as well as organic matter and clay, which strongly influence nanoscale pore-size deformation.

Therefore, the main purpose of this study is to adopt an integrated approach combining a macroscopic tensile strength test with a microscopic nano-indentation test

to address the multiscale mechanical response of the untapped Krol Shale from the Lesser Himalaya, Uttarakhand. In addition to the multiscale mechanical parameters, surface topography was analyzed using Atomic Force Microscopy (AFM). The topographic studies provide valuable insights into surface morphology in terms of roughness, fractal, maximum height, etc. The surface characteristics influence the fracture roughness and adsorption behavior of the shale, thereby linking mechanical behavior with hydrocarbon productivity and CO_2 storage efficiency.

The outcomes of this integrated study will collectively strengthen the basis for designing efficient strategies for efficient hydrocarbon recovery and long-term CO_2 sequestration within the Lesser Himalaya Krol Shale formation.

6.2. Sample Preparation and Nature of Krol Shale

Two block samples of Krol Shale from the study area mentioned in Section 2.2 (Chapter 2) were used in this study. The spacing between two sampling locations was ~ 200 m, ensuring that the collected blocks represent distinct yet comparable sections of the Krol formation. The purpose of selecting two blocks from the spacing of 200 m is to capture the inherent heterogeneity of the shale. Since shales are highly heterogeneous and anisotropic, their properties vary significantly within short distances. Collecting two blocks (BS1 and BS2) from a spacing of ~ 200 m enables to have a more reliable representation of the overall mechanical behavior of the formation.

6.2.1. Sample Preparation

To assess tensile strength, rock cores 50 mm in diameter were drilled perpendicular to the bedding. Once drilled, the cores were cut to a preferred length-to-diameter (t/d) ratio of 0.5, in accordance with American Society for Testing and Materials

(ASTM) standards (ASTM, 2001). A total of 20 specimens (10 from each block) were prepared. The end surfaces of the specimens were further polished to ensure uniformity in the applied stress. For the nano-indentation test, a 25 mm diameter core was drilled from each block in a direction perpendicular to the bedding. The surface (perpendicular to bedding) intended for indentation was further embedded in epoxy resin. The use of resin is important, as it provides a stable, supportive base that prevents damage and chipping to the sample during indentation. For surface topography, chip specimens were extracted from each block parallel to the bedding, with imaging performed perpendicular to the bedding. For AFM imaging, a chip of ~ 15 mm * 15 mm * 3 mm was prepared. The imaging surface was well polished to prevent probe damage and provide reliable nanoscale imaging. Before imaging, the prepared specimens were thoroughly washed with acetone to remove loose matter or surface contaminants.

6.2.2. Nature of the Krol Shale

Since both the studied shale blocks (BS1 and BS2) have lithological similarity and originated from the same formation i.e., Neoproterozoic Krol Formation, the results shown in this section reflect the overall nature of the Krol Shale rather than being specific to either BS1 or BS2 individually.

Mineralogical analysis was carried out through X-ray diffraction (XRD) analysis on powdered samples (particle size < 75 μm) using an Empyrean panalytical XRD apparatus. The results indicate that the Krol Shale contains a dominant proportion of clay minerals, mainly illite, along with other major minerals such as quartz, muscovite, albite, and pyrite (Figure 6.1). Based on bulk mineralogy and possible elements within shale, elemental mapping was conducted on chip specimen (~ 5 mm) using energy-dispersive X-ray spectroscopy (EDX) analysis through JEOL JSM-7900F field emission scanning

electron microscope (FE-SEM). The elemental composition of the mapped area, as shown in Figure 6.2, is as follows: C 24.4 %, O 45.7 %, Na 0.8 %, Mg 0.6 %, Al 3.7 %, Si 20.3 %, S 1.6 %, K 1.6 %, and Fe 1.3 %.

The functional group study of the Krol Shale was carried out on powder samples (particle size < 75 μm) using Nicolet iS20 Fourier Transform Infrared Spectroscopy (FTIR). Within the FTIR absorbance spectrum (Figure 6.3), which ranges from 400 cm^{-1} to 4000 cm^{-1}, functional groups corresponding to clay minerals (O-H), organic matter (C-H), and silicates (Si-O) were identified. Absorbance spectra bands 3700–3500 cm^{-1}, 3000–2800 cm^{-1}, and 1200–800 cm^{-1} represent O-H, C-H, and Si-O functional groups. The maturity level of the Krol Shale was investigated using petrographic studies (Figure 6.4). A significant proportion of vitrinite in petrographic images, with its reflectance value of 1.5 to 2, suggests the potential for hydrocarbon gas generation. The presence of framboidal pyrite in petrographic images indicates deposition under anoxic marine conditions, whereas the amorphous humic organic matter suggests its terrestrial origin. Therefore, the Krol Shale is of a marine depositional setting containing terrestrial-derived organic matter.

In addition to the geochemical and petrographic studies, an ultrasonic wave-velocity test was performed on core specimens using Pundit PL-200 ultrasonic pulse velocity test instrument with 250 kHz transducers to evaluate the dynamic properties of Krol Shale, including elastic modulus and Poisson's ratio (Table 6.1). The dynamic properties indicate that the Krol Shale is low-to-moderately stiff and semi-ductile. Overall, the Krol Shale is a clay-rich, semi-ductile formation deposited in a marine environment, containing terrestrial organic matter and showing the potential for gas generation.

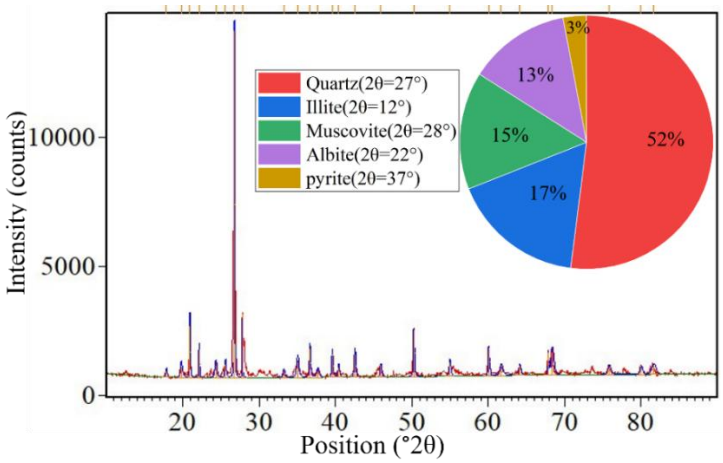

Figure 6.1. *XRD intensity peaks of Krol Shale showing major constituent minerals and their percentage.*

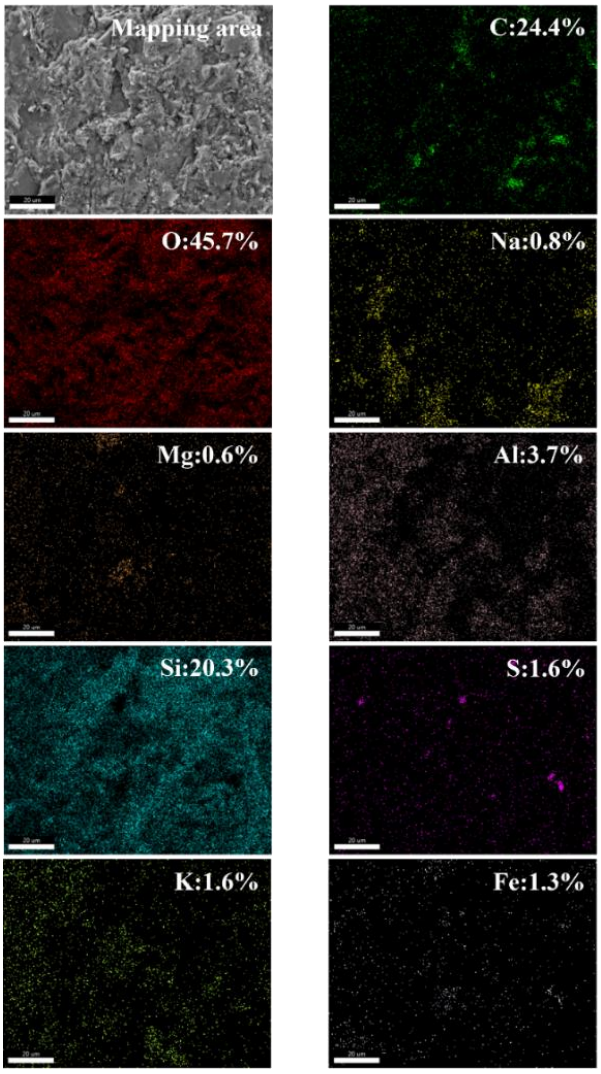

Figure 6.2. *EDX mapping of the Krol Shale showing major elemental composition percentage.*

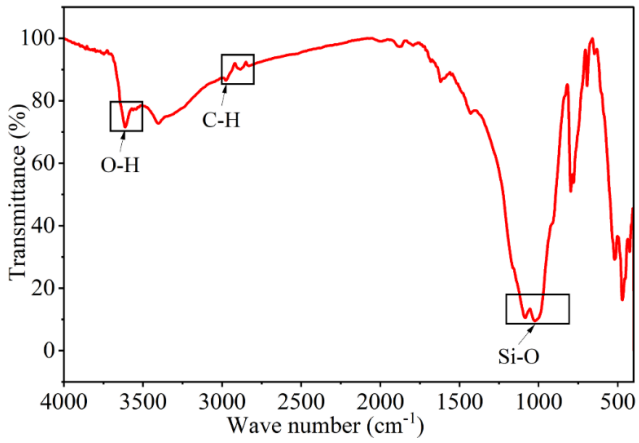

Figure 6.3. *FTIR spectrum of the Krol Shale for functional group study.*

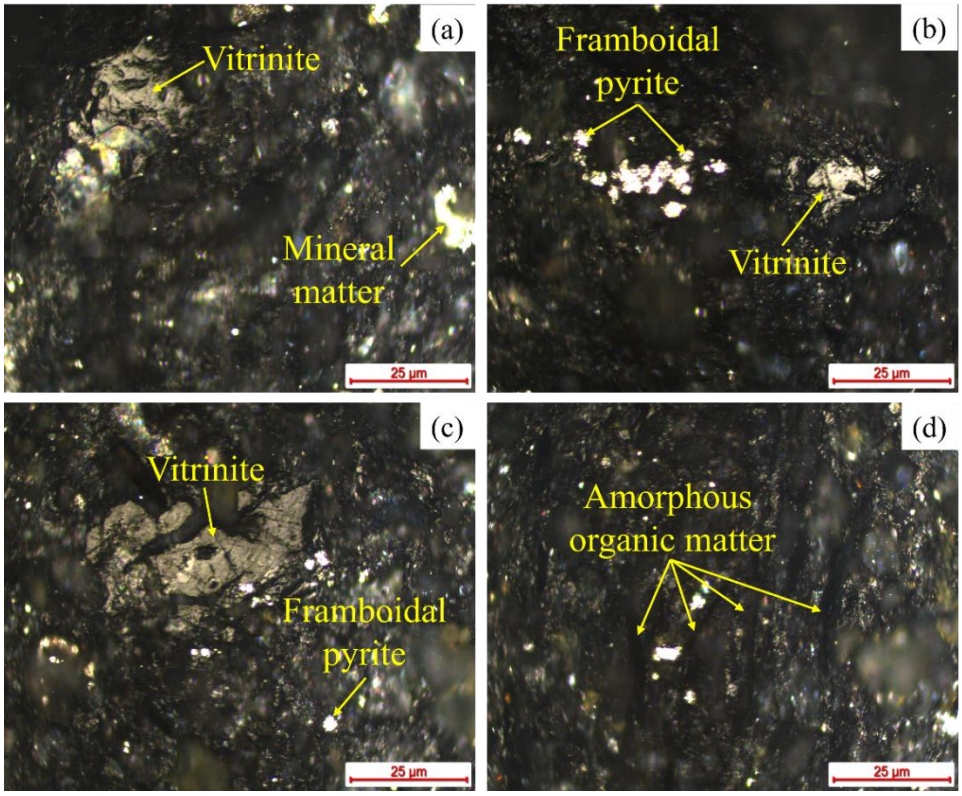

Figure 6.4. *Petrographic images of the Krol Shale,* ***(a)*** *showing vitrinite and mineral matter,* ***(b)*** *and* ***(c)*** *showing framboidal pyrite and vitrinite, and* ***(d)*** *showing amorphous organic matter.*

Table 6.1. *Dynamic properties of Krol Shale based on ultrasonic pulse velocity test.*

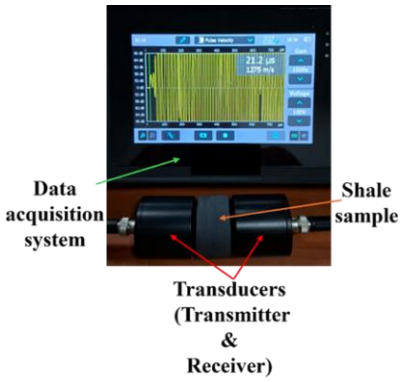

Sample	V_P (m s^{-1})	V_S (m s^{-1})	ρ (kg m^{-3})	E_d (GPa)	ν
BS1	2452	1380	~2457	11.76	0.27
	2388	1420		11.55	0.26
	2532	1465		13.04	0.25
	2539	1402		12.37	0.28
	2419	1356		11.48	0.27
BS2	2685	1562		13.48	0.29
	2680	1550		14.74	0.25
	2608	1490		13.72	0.26
	2550	1402		12.39	0.28
	2589	1492		13.68	0.25

Note: V_P is P-wave, V_S is S-wave, ρ is density, E_d is dynamic elastic modulus, and ν is the dynamic Poisson ratio.

6.3. Laboratory investigation

6.3.1. Brazilian Tensile Strength (BTS) Test

The BTS test is an indirect method for measuring rock tensile strength. To obtain tensile strength, the BTS test setup shown in Figure 6.5 was used. In this set up, a cylindrical core specimen (drilled perpendicular to the bedding) was loaded in diametral compression. The loading was applied in such a way that the bedding plane of the sample was positioned in a vertical direction, thereby inducing tensile stresses across the bedding plane (perpendicular to bedding). The test procedure was conducted in accordance with the International Society of Rock Mechanics (ISRM) standard (ISRM, 2007). Load and corresponding displacement data were continuously recorded for each specimen. After the specimen failed, the BTS was calculated using Eq. 6.1 (ISRM, 2007).

$$BTS = \frac{2P}{\pi DL} \qquad \text{Eq.6.1}$$

Here, P: peak load at which the specimen failed (kN), D: diameter of the specimen (mm), and L: thickness of the specimen (mm).

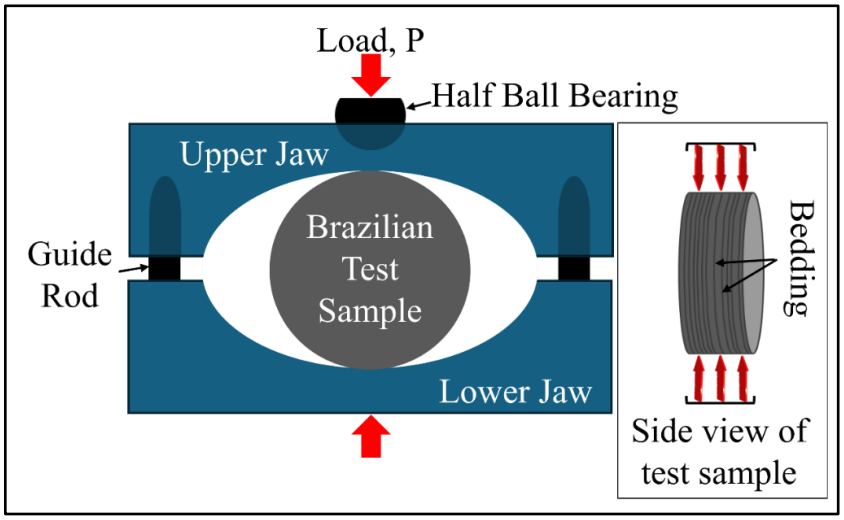

Figure 6.5. *Schematic representation of the BTS test.*

6.3.2. Nano-indentation Test

This technique measures the material's micromechanical properties by pressing a hard indenter tip onto its surface under controlled loading conditions. The quasi-static Triboindenter (TI 950, Hysitron Inc., USA) test apparatus was used for indentation, housed in the nano-indentation and nano-tribology lab of the central research facility at IIT Kharagpur. For the indentation, a triangular pyramidal diamond Berkovich indenter tip (TI0039, Hysitron Inc.) of known geometry (total included angle: 142.3° and tip radius: 100 nm) and mechanical properties [Elastic modulus (E_i): 1140 GPa and Poisson's ratio (ν_i): 0.07] was used. The test was conducted at room temperature in load-controlled mode, applying forces between 5 mN and 300 mN with a resolution better than 1 nN. A total of 14 indentation points were tested for each sample. The complete methodology and the operating principle have been based on the Oliver and Pharr model (Oliver and Pharr, 1992). The schematic of the nano-indentation test is shown in Figure 6.6.

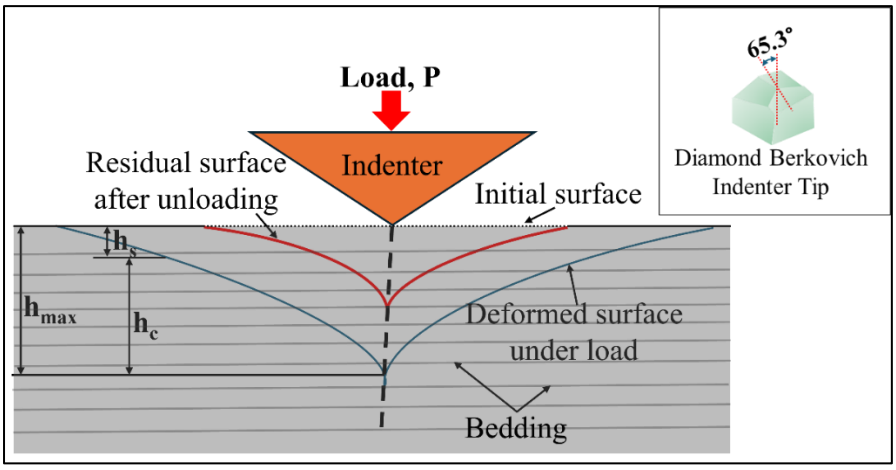

Figure 6.6. *The schematic representation of the nano-indentation test.*

The load (P) *vs.* displacement (h) curve was generated, consisting of three different stages: (1) loading, (2) holding, and (3) unloading. The schematic of a typical nano-indentation curve is shown in Figure 6.7. The loading stage involves both elastic and plastic deformation, while the unloading stage, corresponding to recovery mode, involves only elastic deformation. Accordingly, the area under the loading curve represents the total work 'W_t', while the area under the unloading curve corresponds to the elastic work 'W_e'. Therefore, the area enclosed between the loading and unloading curves defines the plastic work 'W_p', calculated as: $W_p = (W_t - W_e)$.

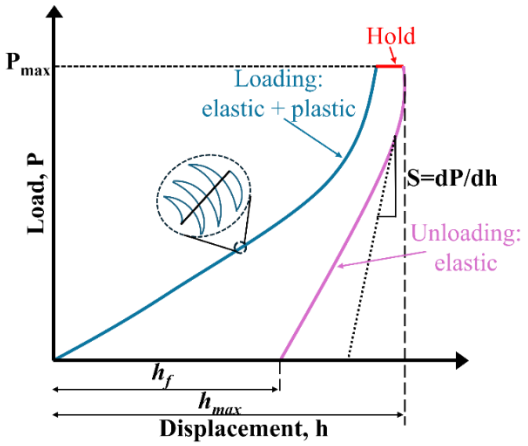

Figure 6.7. *The schematic representation of a typical nano-indentation curve.*

The mechanical parameters were obtained using the resultant load-displacement curve following the Oliver and Pharr model:

$$S = \frac{dP}{dh} = \frac{2\sqrt{A_c}}{\sqrt{\pi}} * E_r \quad \text{Eq.6.2}$$

$$H = \frac{P_{max}}{A_c} \quad \text{Eq.6.3}$$

Here, $S = \frac{dP}{dh}$: initial unloading slope of the load-displacement curve and corresponds to the stiffness of the material, A_c: contact area of the indenter on the sample surface ($A_c = 24.5h_c^2$, where h_c is the contact depth), E_r: reduced elastic modulus, H: hardness of the material, and P_{max}: peak indentation load.

Moreover, the reduced modulus from the indentation test accounts for the elastic responses of both the specimen and the indenter (Oliver and Pharr, 1992). Therefore, using the reduced modulus along with Poisson's ratio of the material, the elastic modulus of the material can be determined as follows:

$$\frac{1}{E_r} = \frac{(1-\nu^2)}{E} + \frac{(1-\nu_i^2)}{E_i} \quad \text{Eq.6.4}$$

Here, ν_i and ν are the Poisson's ratios of the indenter and the indented material, while E_i and E are the elastic modulus of the indenter and the indented material.

6.3.3. AFM analysis

The mechanical response of any material is strongly governed by its surface topography. Characterization of roughness parameters, fractal dimensions, maximum height, etc., from surface topography analysis provides a basic understanding of the material's mechanical response. The AFM analysis was conducted using a Bruker DM FASTSCAN3-SYS atomic force microscope in contact operating mode. The AFM technique uses a nanometer-scale tip mounted on a cantilever to physically interact with

the sample's surface. As the tip scans across the surface, an atomic-scale force (e.g., van der Waals force) between the tip and the sample surface deflects the cantilever. Such deflections are measured using a laser-induced photodiode system to reconstruct a 3D topographic image of the surface. The schematic of the AFM working phenomena is shown in Figure 6.8.

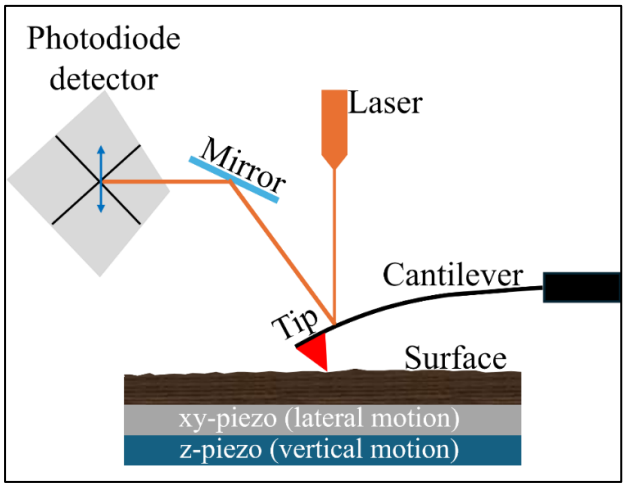

Figure 6.8. *The schematic representation of the AFM working principle.*

6.4. Results and Discussions

6.4.1. Macroscale Mechanical Characteristics using the BTS Test

The tensile strength of shale reservoirs containing natural joints and fractures is a critical parameter for predicting fracture initiation during hydraulic fracturing and for designing safe and efficient engineering operations. During hydrocarbon extraction, the tensile strength determines when and how hydraulic fractures form and grow, which is important for enhancing permeability, while during CO_2 sequestration, it plays a key role in limiting fracture growth under injection-induced stresses.

To evaluate the macroscale mechanical response of the studied shale under tensile stress, BTS tests were performed by applying the external load along the bedding planes of the samples, such that the tensile stress was applied across the bedding. In this study,

each shale specimen was carefully oriented so that the tensile stress acted across the bedding planes. This configuration minimizes the influence of bedding-controlled anisotropy and allows a more representative assessment of the intrinsic tensile strength. Such a configuration of the specimen during the BTS test is highly relevant for subsurface engineering applications, where stress reorientation during hydrocarbon extraction or CO_2 injection may lead to fractures independent of bedding planes. A similar experimental approach was also adopted by Chong et al. (1984) for Devonian oil shale and by Li et al. (2017) for organic-rich gas shale, in which the tensile stress was applied across the bedding planes. They reported that the testing orientation was intentionally selected to minimize the influence of anisotropy.

The load *vs.* displacement curve of the tested sub-samples from BS1 and BS2 is shown in Figure 6.9. Most of the sub-samples exhibit a low-to-moderately stiff, semi-ductile nature under tensile stress conditions. The distinct quasi-linear portion of the curve reflects the shale's low-to-moderate stiffness, whereas the gradual reduction in load beyond the peak indicates its semi-ductile behavior. Such behavior is commonly observed in shales, where deformation is governed by the interaction between brittle mineral phases (e.g., quartz) and weaker organic matter and clay-rich constituents. In fact, the overall mechanical response of shale is controlled by the combined influence of soft organic matter, clay minerals, and brittle mineral components (Wild and Amann, 2018; Weijermars et al., 2020).

The mineralogical control on the mechanical response is significant in determining the fracture complexity and fluid conductivity for hydrocarbon recovery, as well as in understanding whether fractures may close or heal over time during CO_2 storage. Li et al. (2022a) further emphasized that shale brittleness depends on the relative proportions of brittle minerals, such as quartz, and ductile phases, such as clay minerals.

Quantitatively, the BTS values for the BS1 sample range from 3.56 MPa to 7.49 MPa, with an average of 5.16 MPa. In contrast, the BS2 sample shows a wider variation, with BTS values between 2.52 MPa and 10.81 MPa and an average of 5.92 MPa (Table 6.2).

The macroscopic failure characteristics further shed light on the overall heterogeneous nature of the Krol Shale during the BTS test. Most samples showed layer-activation failure, with fractures moving along the bedding planes (Figure 6.10). This type of failure is associated with the shale's low-to-moderate stiffness. According to Basu et al. (2013), such failures occur when compression induces tensile stresses that activate bedding or foliation planes, releasing strain energy earlier than in central or non-central failures. Nilankar et al. (2024a) documented layer-activation failure occurring in combination with central and non-central fracture modes. The layer-activation failure mode suggests that although the tensile stress was applied across the bedding planes, once the tensile stress during loading exceeds the interlayer bond strength, the inherent weakness associated with the bedding planes of the shale sample becomes activated (Basu et al., 2013; Nilankar et al., 2024a). Variations in the interlayer bond strength may lead to significant differences in the overall tensile strength of the shale. Some specimens may exhibit early activation of the weaker planes, while few may sustain higher loads before failure. This variability in fracture behavior contributes to the significant scatter in the observed tensile strength values, highlighting the heterogeneous nature of Krol Shale.

Besides direct experimental analysis, the elastic modulus of the Krol Shale was also calculated indirectly from the slope of the linear elastic region of the load-displacement curve. From the linear region of the curve, two points corresponding to σ_1, ε_1 and σ_2, ε_2 were obtained. Eq. 6.5 has been used to calculate the elastic modulus (Singh et al., 2025b).

$$E = \frac{\Delta\sigma}{\Delta\varepsilon} = \frac{\sigma_2 - \sigma_1}{\varepsilon_2 - \varepsilon_1} \qquad \text{Eq.6.5}$$

Here, E: elastic modulus, Δσ: change in stress between the two selected points, and Δε: corresponding change in strain.

The elastic modulus is an important parameter that characterizes the stiffness of a material and its resistance to elastic deformation (Singh et al., 2025b). The average elastic modulus values are 6.64 GPa for the BS1 samples and 8.29 GPa for the BS2 samples. Although there is no standard range of elastic modulus to directly classify material stiffness based on stress-strain curves, the comparison with previously reported values for other shale formations in the literature indicates that the Krol Shale exhibits relatively low-to-moderate stiffness, with a semi-ductile nature. Previous studies by Gao et al. (2017) and Guo et al. (2023) estimated shale elastic moduli from load-displacement curves, reporting average values of 16.12 GPa and 25.5 GPa, respectively. In comparison, the lower values obtained for the Krol Shale indicate relatively low-to-moderate stiffness and support the semi-ductile behavior observed in the tensile tests.

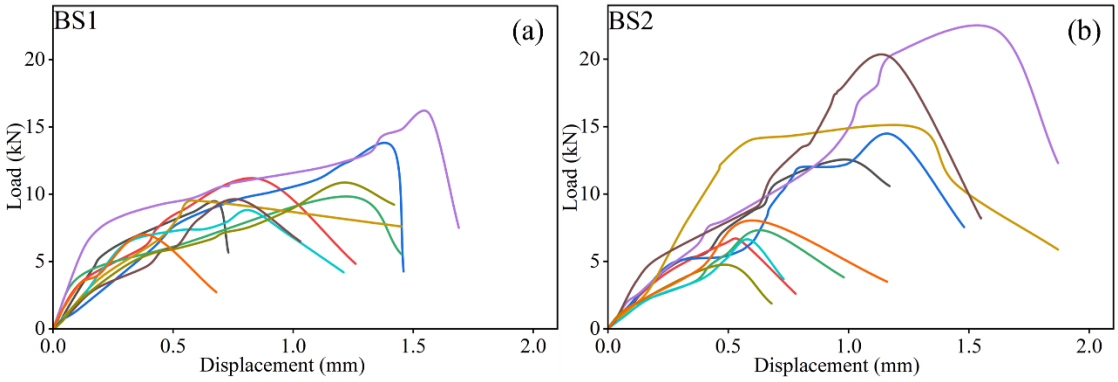

Figure 6.9. *BTS-based load-displacement curve, **(a)** BS1 and **(b)** BS2 samples, of the Krol Shale.*

Table 6.2. *BTS and elastic modulus values of the BS1 and BS2 block samples based on the BTS test.*

Sample	P (kN)	BTS (MPa)	E (GPa)	Sample	P (kN)	BTS (MPa)	E (GPa)
BS1.1	9.33	5.16	4.17	BS2.1	12.55	6.94	8.81
BS1.2	11.08	5.87	2.58	BS2.2	6.55	3.20	6.28
BS1.3	13.33	6.52	3.29	BS2.3	14.33	6.75	9.35
BS1.4	9.83	4.81	7.69	BS2.4	7.28	3.31	3.58
BS1.5	15.9	7.49	7.22	BS2.5	22.1	10.81	12.29
BS1.6	9.53	5.05	11.45	BS2.6	14.94	7.92	14.61
BS1.7	8.8	4.87	5.66	BS2.7	6.6	3.65	5.90
BS1.8	9.58	4.51	7.36	BS2.8	19.94	10.15	14.51
BS1.9	10.86	5.76	5.18	BS2.9	4.75	2.52	3.00
BS1.10	6.99	3.56	11.83	BS2.10	8.03	3.93	4.53

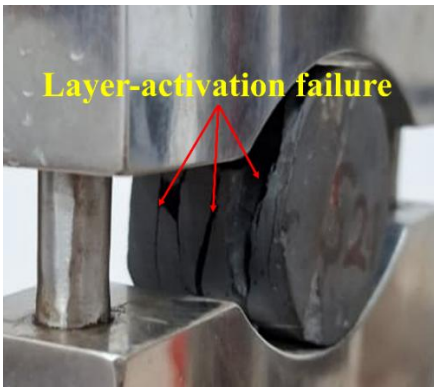

Figure 6.10. *Characteristic layer-activation failure of the Krol Shale under BTS test.*

6.4.2. Microscale Mechanical Characteristics using Nano-indentation Test

6.4.2.1. Load-vs.-Displacement Curve

The load-displacement curve from the nano-indentation tests of BS1 and BS2 samples is presented in Figure 6.11. For sample BS1 with peak load (P) ~7997 μN, the displacement ranges from 1081 nm to 4841 nm, while for BS2 with P_{max} ~7997 μN, the displacement ranges from 693 nm to 4972 nm. Although the number of indentation points is limited for the BS1 and BS2 samples, the results obtained have proven highly effective in representing the micromechanical behavior of the Krol Shale.

Microscale mechanical characterization is very crucial, where small-scale or local deformation directly influences the fluid transport pathways and CO_2 storage efficiency.

In the load-*vs.*-displacement curve, the typical events such as “pop-in” and “elbow” represent the deformation mechanisms at the microlevel. The representative pop-in and elbow event is shown in Figure 6.12. The pop-in event, characterized by a sudden jump in displacement at loading, has been observed in both samples. This event is attributed to the fact that, during indentation, the tip initiates cracks or probes micro/nano pores and microfractures, thereby increasing the displacement very sharply (Li et al., 2019b; Pohl, 2019; Wang et al., 2022).

From the reservoir perspective, the pop-in events providing evidence of microcrack initiation and pore presence are important for improving permeability during hydrocarbon recovery and for identifying possible pathways for CO_2 adsorption and migration. Pop-ins also indicate the shape of the pores present within the sample (Liu et al., 2021b). For example, if the indenter tip probes the slit-shaped pores, which are very thin and sheet-like in one dimension, a small creep deformation occurs due to the sudden release of pressure from the indenter tip (Figure 6.12a). In irregularly shaped (U-shaped) pores, the indenter tip experiences two or more successive pressure releases, resulting in serial pop-in events (Figure 6.12b). While the globular/pyriform pores might undergo prolonged creep deformation during loading, resulting in step-shaped pop-in events (Figure 6.12c). The observed pore geometries are closely linked to gas storage behavior, where slit-shaped pores support adsorption-dominated gas storage (Singh et al., 2026). Irregular and globular pores help improve fluid flow and CO_2 injection capacity.

In addition to the pop-in, the elbow event (Figure 6.12d) occurs when the indenter tip encounters a phase transformation during unloading (Kong et al., 2021). During the elbow event, the pressure beneath the indenter may exceed the critical limit, and therefore, the material is expected to expand during the slow transformation into the amorphous phase (Domnich et al., 2000). Such microscale phase transformation may reflect the

stress-induced alteration in the mineral structures, which can affect the long-term mechanical stability of the formation during CO_2 injection.

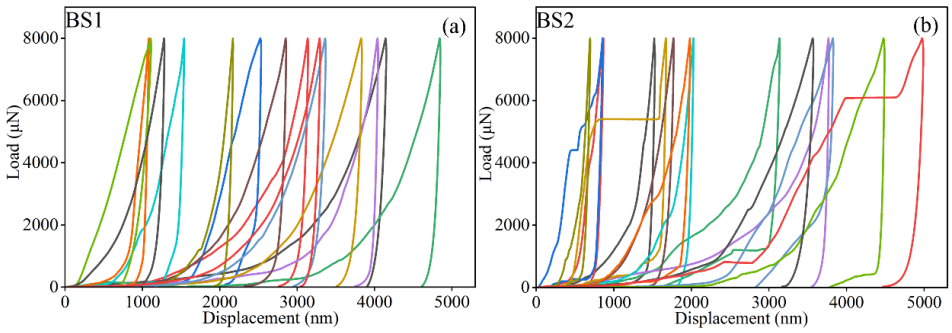

Figure 6.11. *Nano-indentation-based load-displacement curve, (**a**) BS1 and (**b**) BS2 samples, of the Krol Shale.*

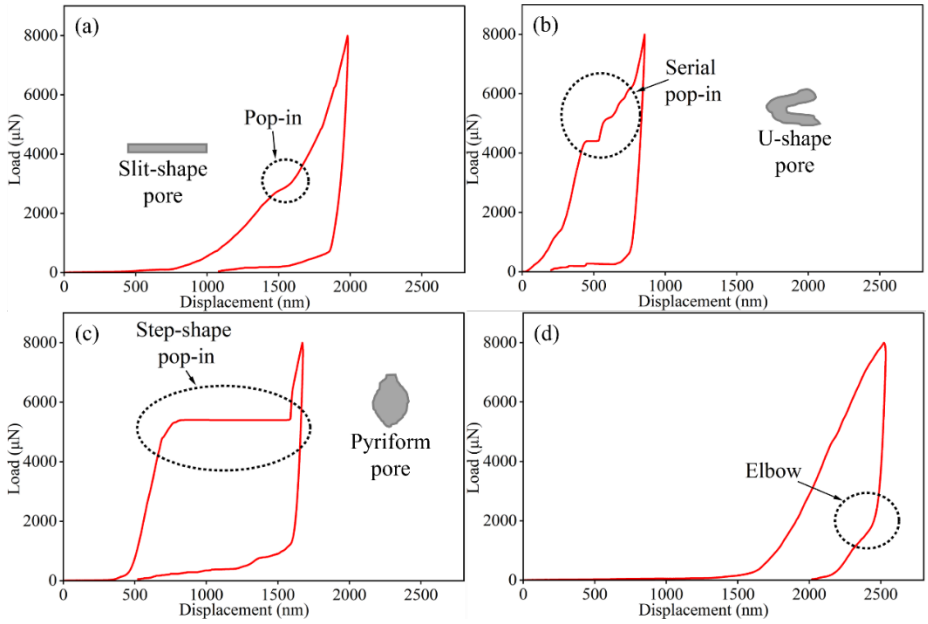

Figure 6.12. *Typical events observed in the nano-indentation curves of Krol Shale, (**a**) pop-in, (**b**) serial pop-in, (**c**) step-shaped pop-in, and (**d**) elbow event.*

Based on the indentation results, the mechanical properties, such as the elastic modulus, were examined to gain a better understanding of how Krol Shale behaves mechanically. Elastic modulus is a critical parameter that strongly influences hydraulic fracture propagation (Gao et al., 2025). Chowdhury et al. (2025), in their nano-indentation

study of the Raniganj Shale, primarily focused on elastic modulus to characterize the mechanical behavior of the material. As shown in Figure 6.13a, sample BS1 exhibits an average elastic modulus of 8.5 GPa, ranging from a minimum of 3.62 GPa to a maximum of 25.17 GPa. In contrast, sample BS2 shows a higher average elastic modulus of 13.17 GPa, with values varying between 1.47 GPa and 38.45 GPa. The significant variation in the elastic modulus values within the BS1 and BS2 samples indicates the mechanical heterogeneity of the Krol Shale. This heterogeneity in mechanical properties plays an important role in controlling fluid flow pathways, fracture complexity, and localized deformation, which are important for efficient hydrocarbon recovery and for achieving uniform CO_2 distribution during storage. In the frequency distribution shown in Figure 6.13b, the dominant occurrence of elastic modulus values in the 0–10 GPa range is generally attributable to the presence of soft constituents in both samples. In addition, the influence of long-term tectonic disturbances should also be considered, which may have contributed to the observed reduction in elastic modulus of the studied Krol Shale in comparison to other shale formations. Khadka et al. (2025) stated that post-depositional Himalayan tectonics dynamically alter the rock matrix through microcrack development.

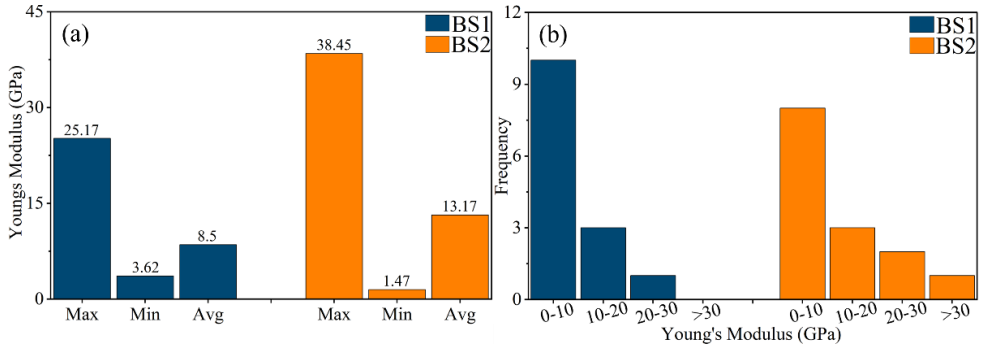

Figure 6.13. *Nano-indentation-based elastic modulus values for the BS1 and BS2 samples of the Krol Shale, (**a**) max, min, and avg values, and (**b**) frequency distribution.*

However, it is assumed that during the nano-indentation tests, an individual indentation point reflects the mechanical behavior of a specific mineral phase, rather than the overall mechanical behavior of the shale. Mechanically, shales are highly heterogeneous in nature, consisting of different phases/components such as organic matter, clay content, and other minerals (Li et al., 2018). These phases exhibit significant differences in their mechanical behavior. The elastic modulus values of the different phases present in shale, as reported in previous studies, are summarized in Table 6.3. As a result, the direct interpretation of the nano-indentation-derived elastic modulus from the average values can be unreliable and may often lead to a misleading interpretation. Therefore, analysis using statistical approaches is crucial for identifying the distinct mechanical phases.

Table 6.3. *Nano-indentation-based elastic modulus values of the different mineral phases from previous studies.*

Organic matter	Clay	Mica	Feldspar	Quartz	Pyrite
2.0–8.7 GPa (Shukla et al., 2013) and 3.4–9.7 GPa (Wang et al., 2022)	18.5–29.4 GPa (Zhao et al., 2019) and 20.4–25.9 GPa (Bennett et al., 2015)	52 GPa (Zhang et al., 2009)	75–85 GPa (Yang et al., 2020)	87.2 GPa (Zhao et al., 2019) and 74.7–78.5 GPa (Goodarzi et al., 2017)	> 130 GPa (Zhao et al., 2019)

Note: GPa is the giga pascal

6.4.2.2. Statistical analysis

Statistical analyses were carried out in Python using deterministic numerical algorithms. No manual adjustment, post-processing, or subjective data selection was applied. A deconvolution technique has been used to statistically separate the distinct phases. Phase identification has been carried out using an elastic modulus (E) as the single clustering variable. Phase separation is important to understand how organic matter, clay minerals, and brittle minerals contribute differently to the mechanical behavior of the

formation during hydraulic fracturing phenomena and CO_2 injection. The multivariable clustering based on other nano-indentation-derived mechanical parameters (such as hardness and stiffness) was not performed in this study, as it requires a reliable estimation of covariance structures, which is difficult for limited datasets and may result in numerical instability. The statistical clustering deconvolution on the dataset was performed by assuming a Gaussian distribution (i.e., Gaussian Mixture Model, GMM) to be the best fit. GMM is commonly applied to heterogeneous rocks like shale, in which the mechanical properties of individual phases do not exhibit constant values (Wang et al., 2025a). For both the samples, BS1 and BS2, the GMM distribution of the elastic modulus was modelled with three phases based on Eq. 6.6. Such a probabilistic distribution approach gives a more realistic view of subsurface heterogeneity.

$$p(E) = \sum_{k=1}^{3} \pi_k N(E \mid \mu_k, \sigma_k^2) \quad \text{Eq.6.6}$$

Here, $p(E)$: probability density function (PDF) of elastic modulus E, π_k: mixing coefficient of k^{th} phase, $N(E \mid \mu_k, \sigma_k^2)$: Gaussian distribution, μ_k: mean elastic modulus of k^{th} phase, σ_k^2: variance of the k^{th} phase, and k = 1, 2, 3 correspond to phase 1, phase 2, and phase 3.

The phase-resolved probability density function of elastic modulus for BS1 and BS2 is shown in Figure 6.14. It represents the fitted normal distribution of the elastic modulus for individual phases, based on Gaussian mixture deconvolution. In cases where the phase contained only a single indentation point, the standard deviation was undefined. To prevent numerical instability of the corresponding probability density function and to ensure meaningful interpretation for such cases, an effective standard deviation was assigned. This effective standard deviation was introduced to stabilize the graphical representation of phase-resolved probability density functions and does not influence

phase assignment or phase fractions. The formula for the effective standard deviation is as follows:

$$\sigma_{eff} = 0.05\mu \quad \text{Eq.6.7}$$

Here, σ_{eff}: effective standard deviation and μ: mean elastic modulus of the phase.

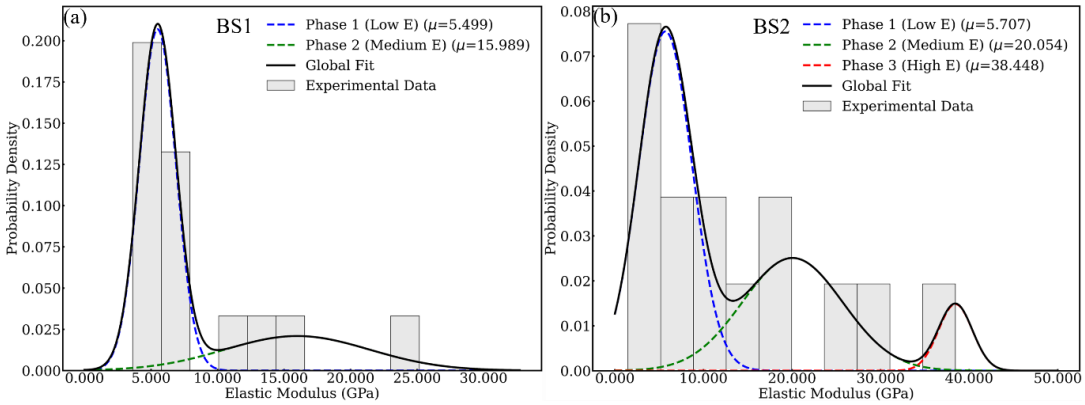

Figure 6.14. *Nano-indentation-based phase-resolved probability density function of elastic modulus values, (**a**) BS1 and (**b**) BS2 samples, of the Krol Shale.*

The phase-wise statistical summary of the elastic modulus for the BS1 and BS2 samples is shown in Table 6.4, computed directly from the clustered datasets without any additional filtering. As per Table 6.4, the elastic modulus of sample BS1 has been categorized into two phases, i.e., phase 1 and 2, while the elastic modulus of sample BS2 has been categorized into three phases 1–3. Although a three-component Gaussian Mixture Model (GMM) was fitted for both samples, in the case of BS1, one component converged to a negligible mixture weight during the elastic modulus optimization and therefore did not represent a statistically meaningful phase, resulting in two effective phases. Phase 1 corresponds to the lowest elastic modulus. Phase 2 has an average modulus value higher than that of phase 1 but lower than that of phase 3. Phase 3 corresponds to the highest elastic modulus value. Based on the previously reported studies shown in Table 6.3, phase 1, with mean elastic modulus values of 5.50 GPa and 5.71 GPa

for the BS1 and BS2 samples, falls within the range of elastic modulus values for organic matter. Phase 2, with mean values of 15.99 GPa and 20.05 GPa for the BS1 and BS2 samples, falls within the range of elastic moduli for clay minerals. Phase 3, with a mean elastic modulus of 38.45 GPa observed in the BS2 sample, represents a composite phase, i.e., a combination of various mineral phases. This phase-wise study of the elastic modulus is very useful in the context of hydrocarbon recovery and CO_2 storage, as the organic matter phases with low elastic modulus primarily control the gas adsorption and storage capacity (Bakshi and Vishal, 2021). In contrast, the clay-rich phases influence the ductility, while brittle mineral phases control the fracture growth and structural stability.

Table 6.4. *Phase-wise statistical summary of the elastic modulus for BS1 and BS2 obtained from GMM clustering.*

Sample	Phase 1			Phase 2			Phase 3		
	Fraction (%)	Mean (GPa)	Std. (GPa)	Fraction (%)	Mean (GPa)	Std. (GPa)	Fraction (%)	Mean (GPa)	Std. (GPa)
BS1	71.4	5.50	1.45	28.6	15.99	6.29	–	–	–
BS2	57.1	5.71	3.23	35.7	20.05	6.35	7.1	38.45	–

Although XRD analysis of the Krol Shale (Figure 6.1) confirms the presence of brittle minerals such as quartz, feldspar, pyrite, and muscovite, which typically exhibit high elastic modulus values (Table 6.3), the nano-indentation results show predominantly lower elastic modulus values, largely corresponding to organic matter and clay minerals. This is mainly due to long-term tectonic deformation, which has significantly influenced the microstructure of the Neoproterozoic Krol Shale, leading to a reduction of the overall elastic modulus. Therefore, the obtained statistical clusters might be also representative of effective mechanical phases rather than pure mineralogical phases. Unlike other shale formations investigated globally through nano-indentation studies that have not undergone tectonic deformation, the Krol Shale in the Lesser Himalayan region has

undergone a prolonged tectonic history. Valdiya (1983) stated that the Lesser Himalayan region is marked by the intracrustal Main Boundary Thrust (MBT) and the Main Central Thrust (MCT) with multiple thrusting and strong shattering. Dey et al. (2022) also confirmed that the Neoproterozoic Krol Group is a part of a tectonically deformed succession. Tectonism has introduced widespread microcracks and has also weakened intergranular bonds within the Krol Shale, which can provide easy pathways for hydrocarbon migration and CO_2 injection, but the imprint of the tectonism may also lead to a reduction in the long-term storage capacity. Therefore, the micromechanical behavior of the constituent phases in the Krol Shale may differ significantly from the phases reported in the undeformed shales.

The spatial distribution mapping was also employed to examine the distribution of the micromechanical heterogeneity during nano-indentation measurements (Figure 6.15). The purpose of the spatial mapping was to understand how the elastic modulus varies across the indented surface. Such mapping enables the identification of the constituent phases and provides information about the skeletal framework of the indented surface (Liu et al., 2021b). For both the samples, BS1 and BS2, the indentation points were mapped onto a two-dimensional grid based on their acquisition order and the maximum experimental spacing of 100 μm between adjacent indentation points. No spatial optimization or rearrangement was applied to present the inherent heterogeneity of the studied shale. Most of the regions in the spatial map of BS1 and BS2 samples are enclosed by low-modulus areas with purple-blue colors, while the higher modulus regions with yellow-green colors are localized in the form of patches. Although the BS2 sample exhibits a higher elastic modulus than BS1, the overall distribution is still dominated by the low-modulus region.

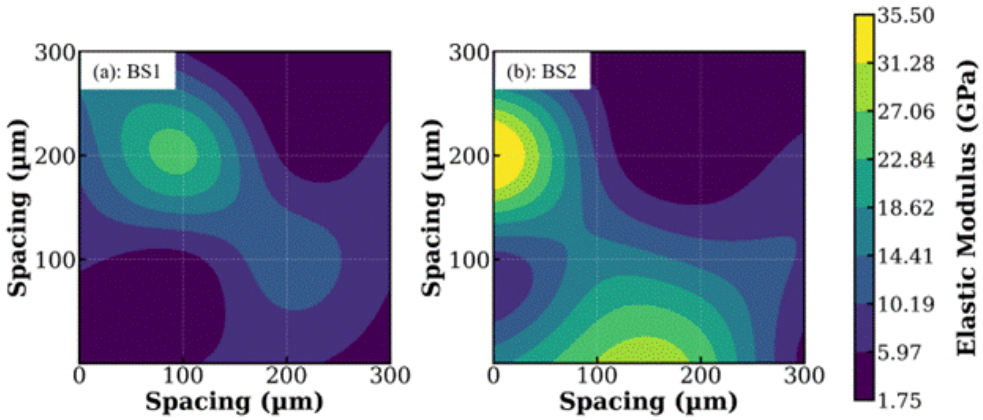

Figure 6.15. *Nano-indentation-based spatial distribution mapping,* ***(a)*** *BS1 and* ***(b)*** *BS2 samples, of the Krol Shale.*

6.4.3. Determination of Multiscale Brittleness Index (BI) based on Load vs. Displacement Curve

Brittleness is a key parameter for characterizing unconventional shale reservoirs in the context of hydraulic fracturing (Jarvie et al., 2007; Zhang et al., 2016). Ductile reservoirs tend to heal hydraulic-induced fractures, whereas brittle reservoirs are more likely to respond favourably to hydraulic fracturing, thereby enhancing fracturing efficiency (Jin et al., 2014). Numerous BIs have been proposed worldwide based on different parameters, but those obtained from the stress-strain (Load-displacement) curve give the most insightful reflection of rock behavior (Meng et al., 2021). The load-displacement curves from BTS and nano-indentation tests on the Krol Shale were analyzed to decompose the mechanical work into elastic and plastic components, enabling energy-based quantification of brittleness. During nano-indentation tests, both the loading and unloading curves were recorded directly; during the BTS tests, only the loading curves were recorded, as unloading was not captured due to sample failure at peak load. Since only the loading curve was available for brittleness evaluation in the BTS tests, the unloading curve was estimated using the tangent method, with a straight elastic line drawn from the peak stress point, assuming elastic recovery during unloading. In this method, an initial linear region from the loading curve was selected to draw a tangent. Parallel to

this tangent, an unloading line was drawn from the peak stress point. This method is most widely used in literature to obtain unloading curves when experimental data are unavailable. Meng et al. (2021) also showed a similar method for estimating the unloading curve.

After the following, the BI calculations were performed directly in Python, without any curve fitting or smoothing. The mechanical work was calculated by integrating the area under the curve using Simpson's rule, which provides higher accuracy. For the BTS load-displacement curve (Figure 6.16a), the area enclosed by ABC corresponds to recoverable elastic work (W_e), the area enclosed by OAC corresponds to irreversible plastic work (W_p), and the area enclosed by OABC corresponds to total mechanical work (W_t). Similarly, for the nano-indentation load-displacement curve (Figure 6.16b), the area enclosed by BCD corresponds to recoverable elastic work (W_e), the area enclosed by OABD corresponds to irreversible plastic work (W_p), and the area enclosed by OABCD corresponds to total mechanical work (W_t). The following energy components were calculated:

$$W_t = \int_{loading} F(\delta) d\delta \quad \text{Eq.6.8}$$

$$W_e = \left| \int_{unloading} F(\delta) d\delta \right| \quad \text{Eq.6.9}$$

$$W_p = W_t - W_e \quad \text{Eq.6.10}$$

Here, W_t: total mechanical work, W_e: recoverable elastic work, W_p: irreversible plastic work, F: applied load, and δ: displacement corresponding to the applied load.

After the calculation of the energy components, the dimensionless BI for the BTS (Table 6.5) and nano-indentation (Table 6.6) test was calculated using the following formula:

$$BI = \frac{W_e}{W_t} \quad \text{Eq.6.11}$$

The BI calculated using the above formula ranges from 0 to 1, where values ~ 0 indicate ductile behavior, and those ~ 1 indicate brittle behavior of the material. Overall, the BI from both tests indicates the low brittle/semi-ductile characteristics of the Krol Shale. However, the macroscopic BTS-based BI of both samples has an average value slightly higher than the microscopic nano-indentation-based BI. For the BS1 and BS2 samples, the average BI values derived from the BTS tests are 0.38 and 0.42, whereas from the nano-indentation tests, the average BI values correspond to 0.13 and 0.17. Although a few BTS samples exhibit higher BI values (> 0.5), the nano-indentation result shows that all samples have BI values lower than 0.5. The BI from the BTS test is representative of the large specimen, which includes the effect of large-scale features, such as bedding (for shale), mineral distribution, etc. These macroscopic features can sometimes locally increase the stress concentration within the sample, thereby explaining the higher BI values in some BTS samples. In contrast, the uniformity in the nano-indentation results can be attributed to the fact that this technique captures the mechanical behavior of the rock's constituent mineral phases, rather than accounting for the effects of large-scale features.

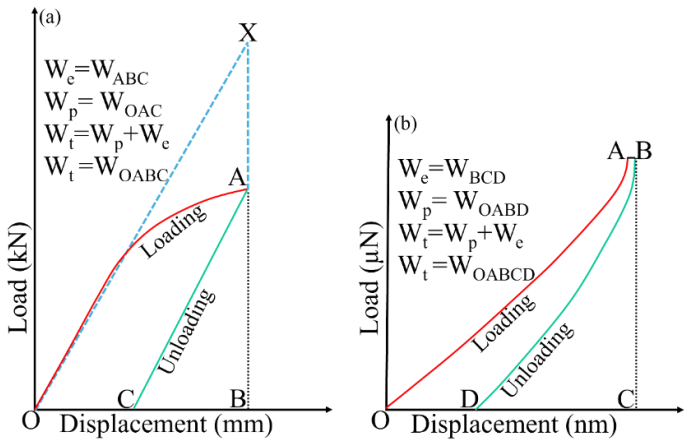

Figure 6.16. *Schematic load-displacement curve, **(a)** BTS and **(b)** nano-indentation, for the brittleness index calculation based on mechanical work under elastic and plastic regions.*

Table 6.5. *BTS-based brittleness index values for the BS1 and BS2 samples.*

Sample	W (Joule, J)			BI	Sample	W (Joule, J)			BI
	W_e	W_p	W_t			W_e	W_p	W_t	
BS1.1	1.40	2.83	4.23	0.33	BS2.1	2.81	4.33	7.14	0.39
BS1.2	1.98	3.99	5.97	0.33	BS2.2	1.09	1.11	2.21	0.50
BS1.3	5.14	6.36	11.50	0.45	BS2.3	1.71	7.58	9.30	0.18
BS1.4	1.45	9.48	10.93	0.13	BS2.4	1.23	1.15	2.38	0.52
BS1.5	2.66	13.73	16.39	0.16	BS2.5	4.58	15.68	20.26	0.23
BS1.6	2.10	0.67	2.77	0.76	BS2.6	2.43	11.67	14.10	0.17
BS1.7	1.58	3.18	4.76	0.33	BS2.7	1.49	0.38	1.87	0.80
BS1.8	2.08	1.88	3.96	0.52	BS2.8	4.10	8.28	12.38	0.33
BS1.9	2.70	4.85	7.55	0.36	BS2.9	0.42	0.90	1.32	0.32
BS1.10	0.69	0.90	1.59	0.43	BS2.10	1.87	0.51	2.38	0.79

Table 6.6. *Nano-indentation-based brittleness index values for the BS1 and BS2 samples.*

Sample	W (Femtojoule, fJ)			BI	Sample	W (Femtojoule, fJ)			BI
	W_e	W_p	W_t			W_e	W_p	W_t	
BS1.1	410896.09	5159425.65	5570321.75	0.07	BS2.1	279947.21	1710233.63	1990180.85	0.14
BS1.2	423627.32	4059431.66	4483058.98	0.09	BS2.2	337895.05	1106287.08	1444182.14	0.23
BS1.3	519843.01	3023371.12	3543214.13	0.15	BS2.3	462267.27	2473669.81	2935937.08	0.16
BS1.4	335192.14	4494885.02	4830077.16	0.07	BS2.4	1502845.92	3237626.23	4740472.16	0.32
BS1.5	251651.50	3596260.18	3847911.69	0.07	BS2.5	229629.97	4959300.26	5188930.24	0.04
BS1.6	410864.48	4319527.90	4730392.38	0.09	BS2.6	706608.11	5251429.68	5958037.80	0.12
BS1.7	514077.32	2148946.21	2663023.53	0.19	BS2.7	315258.24	1787589.35	2102847.60	0.15
BS1.8	424616.87	3684678.57	4109295.44	0.10	BS2.8	430351.20	1939561.70	2369912.91	0.18
BS1.9	315318.09	1506592.54	1821910.64	0.17	BS2.9	316374.52	696812.30	1013186.83	0.31
BS1.10	305865.92	989005.57	1294871.49	0.24	BS2.10	560512.69	2556924.61	3117437.31	0.18
BS1.11	484158.47	3613690.17	4097848.64	0.12	BS2.11	1543004.07	3511533.05	5054537.13	0.31
BS1.12	873045.69	2671782.82	3544828.52	0.25	BS2.12	294094.68	5122497.97	5416592.66	0.05
BS1.13	418118.76	2488815.68	2906934.45	0.14	BS2.13	570991.71	4634381.25	5205372.97	0.11
BS1.14	346303.17	3888071.38	4234374.56	0.08	BS2.14	485021.83	10507804.34	10992826.17	0.04

6.4.4. Surface Heterogeneity using AFM

AFM provides high-resolution images to study the mechanical behavior of materials. In this study, several regions of each sample were scanned over an area of 1 µm * 1 µm. The images were processed and analyzed using the open-source software Gwyddion (version 2.65.20240419, 2024). It is important to note that the AFM analysis was performed only to characterize the surface heterogeneity and topographical complexities of the studied shale, rather than providing the mechanical parameters. The roughness parameters, surface height, and fractal values obtained from the AFM analysis

are very useful for understanding the stress concentration sites and crack initiation zones at the microscale. The shale surface shows strong topographic variation. Figure 6.17 presents the 2D height profiles and 3D surface images of samples BS1 and BS2. Both samples display frequent height changes, with maximum heights of 249.5 nm (BS1) and 391 nm (BS2). These variations appear as sharp peaks and valleys. Similar results were also reported by Tian et al. (2021), who observed stronger surface undulations in shale compared to igneous rocks.

Quantitative surface roughness parameters, including mean roughness (Ra), root mean square roughness (Rq), and surface skewness (Rsk), were obtained from the AFM images. The mean roughness (Ra) measures overall surface irregularity by averaging the absolute height variations from the mean plane. The root mean square roughness (Rq) represents the standard deviation of surface heights and is calculated from the squared deviations from the mean plane. Surface skewness (Rsk) describes the asymmetry of the height distribution relative to the mean plane. The roughness profile along line XX' (Figure 6.17), along with the corresponding values for BS1 and BS2, is shown in Figure 6.18 and Table 6.7. The Ra and Rq values for both samples indicate a high density of surface asperities and strong irregularity. During hydrocarbon recovery and CO_2 storage, higher surface roughness plays a crucial role by increasing the effective surface area.

From a mechanical point of view, such roughness creates microscale stress concentration sites that can initiate microcracks under loading. Tian et al. (2022) showed that shale has a rougher surface than granite and limestone. Nilankar et al. (2024a) observed temperature-induced mechanical degradation in Raniganj shale, while an AFM-based study on the same shale by Nilankar et al. (2024b) reported a systematic increase in surface roughness, with Ra and Rq increasing from 12.45 nm and 15.57 nm at room

temperature to 35.94 nm and 43.08 nm at 400 °C, respectively. Therefore, surface roughness parameters are important indicators of mechanical behavior.

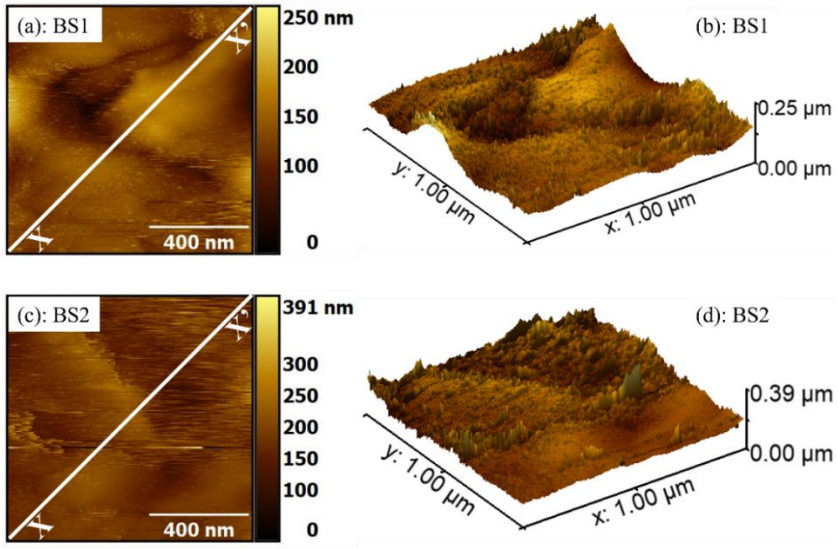

Figure 6.17. *AFM-based representative 2D profile and its corresponding 3D surface topography, (**a**) BS1 and (**b**) BS2 samples, of the Krol Shale.*

The R_{sk} values further describe the height distribution. BS1 shows negative skewness, indicating valley-dominated surfaces. BS2 shows positive skewness, indicating peak-dominated surfaces. The occurrence of both positive and negative skewness within the same Krol Shale suggests mixed surface features, as valley-dominated areas tend to promote fluid adsorption, whereas peak-dominated areas improve fluid connectivity and movement. In addition, the fractal dimensions of 2.53 for BS1 and 2.73 for BS2 indicate a highly rough and complex surface. The fractal dimension measures surface complexity, with values ranging from 2 for a smooth surface to 3 for a very rough and complex surface. Overall, the highly heterogeneous and rough surface morphology of the Krol Shale plays an important role in enhancing hydrocarbon storage and recovery by increasing surface area and providing sites for fracture initiation, while also affecting CO_2 adsorption, injectivity, and storability.

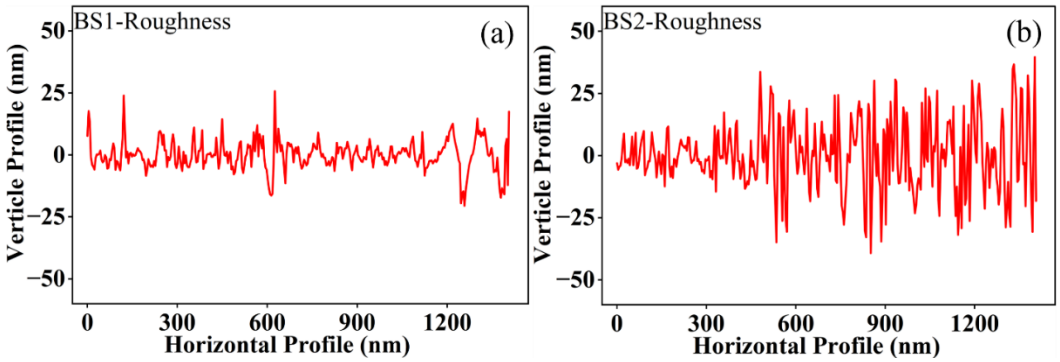

Figure 6.18. *AFM-based roughness profile, (**a**) BS1 and (**b**) BS2 samples, of the Krol Shale along line XX'.*

Table 6.7. *AFM-based roughness parameter values of the BS1 and BS2 samples.*

Parameter	Formula	Eq. no.	Value
R_a	$R_a = \frac{1}{n}\sum_{i=1}^{n}\lvert Z_i\rvert$	Eq.6.12	BS1: 18.70 nm BS2: 21.72 nm
R_q	$R_q = \sqrt{\frac{\sum Z_i^2}{n}}$	Eq.6.13	BS1: 24.97 nm BS2: 28.45 nm
R_{sk}	$R_{sk} = \frac{1}{nR_q^3}\sum_{i=1}^{n} Z_i^3$	Eq.6.14	BS1: -0.18 BS2: 0.25

Note: n is the total number of data points in the image grid, and Z_i is the surface height at position i relative to the mean plane.

6.5. Integration of Multiscale Elastic Modulus and Brittleness Index

An integrated approach was used in this study by combining macroscopic and microscopic parameters for elastic modulus (E) and brittleness index (BI). This approach provides a consistent framework for understanding the mechanical behavior of Krol Shale in the context of stability and hydrocarbon exploration. Multiscale effects play a critical role in governing deformation, fracture initiation, and fluid flow in shale. At the macroscopic scale, the mechanical response is primarily controlled by features such as bedding planes, anisotropy, and pre-existing fractures or natural joints (Hoek and Brown, 1997). In contrast, microscopic response is governed by localized stress concentrations,

mineralogical composition, and microstructural heterogeneity (Bobko and Ulm, 2008). Variations at this scale, such as grain-scale stiffness contrast and microcracks, strongly influence the initiation of failure. Both macroscopic BTS testing and microscopic nano-indentation analysis are effective in characterizing the shale. The results indicate that Krol Shale exhibits low-to-moderate stiffness and semi-ductile mechanical behavior. This semi-ductile nature arises from the combined effects of microcrack interaction, mineral heterogeneity, and progressive energy dissipation during deformation (Brace et al., 1966). Multiscale integration is important because reservoir behavior during hydraulic fracturing and CO_2 injection depends on the combined mechanical response across different scales, from individual mineral phases to large-scale structures. For the integration, a statistical approach based on numerical modelling in Python was implemented. The objective of this approach was not to create a direct one-to-one relationship between individual data points. This is because such pairing is not physically meaningful across scales. Instead, the relationship was developed at the distribution level.

Since shale is highly heterogeneous and the number of measurements differs between scales, a probabilistic distribution approach (Figure 6.19) was adopted. In this approach, both BI and E datasets were treated as statistical representations of the same material across different scales. Macroscopic parameters were predicted using this approach, which is particularly useful because obtaining large, intact shale samples for lab testing is often difficult. The microscopic data were first modelled using the Gumbel extreme value distribution. This distribution model was used because it captures extreme responses within the material associated with localized stress, mineralogical changes, and microstructural heterogeneity, which controls the overall failure of rock masses.

The modelled microscopic distribution was then upscaled to the macroscopic-scale response using a scaling factor (λ), defined as the ratio of the mean macroscopic

value to the mean microscopic value. This factor provides a direct measure of how mechanical properties evolve across scales. As shown in Table 6.8, $\lambda = 2.72$ for BI indicates amplification from the micro to the macro scale. This amplification can be attributed to the interaction and coalescence of microcracks and structural discontinuities, which enhance brittleness at macroscopic scales (Wong and Baud, 2012). In contrast, $\lambda = 0.72$ for E indicates a reduction in stiffness at the macroscopic scale. This reduction is due to the presence of fractures, bedding planes, and defects, which reduce the effective stiffness of the rock mass at the macroscopic scale.

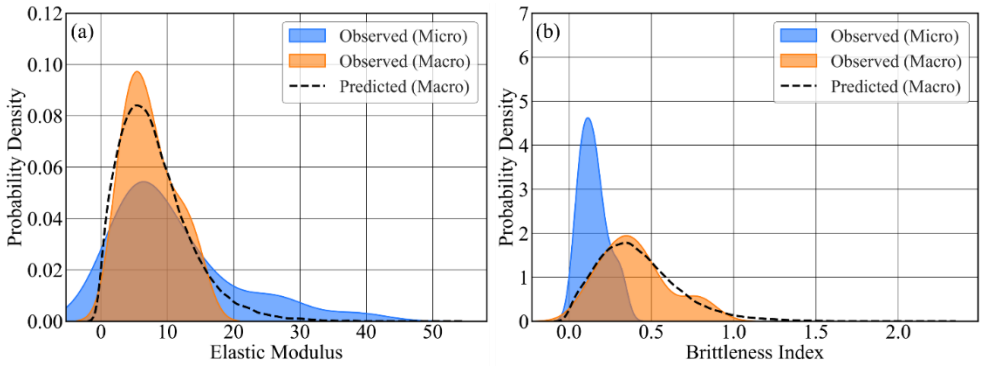

Figure 6.19. *Probability density distributions of* ***(a)*** *elastic modulus "E" and* ***(b)*** *brittleness index "BI" showing observed micro and macroscale parameters and predicted macroscale parameters.*

Table 6.8. *Statistical summary between predicted and observed macroscopic parameters.*

Statistical values	BI	E
Scaling factor (λ)	2.72	0.72
Kolmogorov-Smirnov (KS) statistic	0.14	0.13
p-value	0.77	0.84
Coefficient of determination (R^2)	0.91	0.83

To account for additional variability introduced during scale transition, a controlled stochastic variability approach was introduced using Gaussian noise and lognormal multiplicative factors. Such stochastic approaches ensure that the predicted macroscopic parameters include the effect of large-scale heterogeneity and are not

unrealistic. This stochastic approach is important for a realistic representation of the reservoir heterogeneity, which has a strong effect on uncertainties in the efficiency of the hydrocarbon recovery and the behavior of the stored CO_2 over time.

After that, the predicted macroscopic values were generated from the microscopic data, and the agreement between the predicted and observed macroscopic values was further evaluated using multiple statistical metrics, namely the Kolmogorov-Smirnov (KS) statistic, p-value, and coefficient of determination (R^2). The KS statistic measures the maximum difference between predicted and observed distributions. The low KS values (0.14 for BI and 0.13 for E, Table 6.8) indicate strong agreement between the two distributions. However, the KS statistics alone are not sufficient, and therefore, the p-value associated with the KS test is also considered. The p-value provides a statistical measure of whether the predicted and observed values are from the same distribution.

The associated p-values (0.77 for BI and 0.84 for E) suggest no statistically significant difference between the predicted and observed datasets, supporting the validity of the proposed micro- to macroscale integration. Furthermore, the R^2 values (0.91 for BI and 0.83 for E), obtained through quantile-based comparison, demonstrate a strong correlation between predicted and observed macroscopic behavior. Such strong agreement shows the reliability of the proposed integration approach for estimating macroscale mechanical parameters from the microscale data, which is particularly useful for remote shale reservoirs, especially in the Himalayan region. The agreement between predicted and observed distributions is also evident in Figure 6.19, where the predicted curves closely follow the observed macroscopic curve for both E and BI.

The combined interpretation of statistical metrics and graphical comparison indicates that the predicted macroscopic parameters are consistent with experimental observations. Therefore, the proposed multiscale integration approach provides a reliable

and physically meaningful linkage between microscopic and macroscopic mechanical behavior, which is important for improving hydraulic fracturing in hydrocarbon reservoirs and for ensuring safe, efficient, and long-term CO_2 storage in shale formation.

6.6. Summary

Multiscale mechanical characterization of organic-rich shale is crucial for designing effective and safe rock-engineering practices during hydrocarbon exploration and for long-term CO_2 sequestration. This study employed a conventional macroscopic BTS test and a non-conventional microscopic nano-indentation test to understand the multiscale mechanical behavior of untapped Krol Shale from the Lesser Himalaya. The studied shale with hydrocarbon gas potential exhibits significant mechanical heterogeneity influenced by its prolonged tectonic history, including multiple thrusting events and intense fracturing. Results indicate consistently low elastic (E) modulus values across scales, suggesting low-to-moderate stiffness and a semi-ductile nature. Despite the presence of brittle mineral phases such as quartz and feldspar, nano-indentation results predominantly reflect lower modulus values associated with clay minerals and organic matter, indicating substantial microstructural alteration due to prolonged tectonic history. Brittleness index (BI) values derived from both BTS and nano-indentation load-displacement curves consistently indicate semi-ductile behavior. Additionally, AFM analysis reveals pronounced surface heterogeneity, characterized by high roughness and dense asperity distributions, which may act as localized stress concentrators and facilitate microcrack initiation. To bridge the gap between scales, multiscale integration was carried out using a probabilistic distributional approach, in which microscopic BI and E data were modeled with a Gumbel extreme-value distribution and upscaled to the macroscopic level using a scaling factor. The predicted macroscopic BI and E show strong agreement with

experimental results, confirming the robustness of the integration approach. This multiscale mechanical characterization and integration approach offers important implications for the safe and effective hydrocarbon gas recovery, as well as for ensuring the long-term reliability of CO_2 storage in shale formation.

Chapter: 7
Pore System Characterization of Untapped Krol Shale Using an Integrated Multi-analytical Approach: Bridging Nano- to Macroscale Investigation

7.1. Introduction

Unconventional shale gas reservoirs have emerged as a major focus of global research owing to the progressive decline of conventional hydrocarbon resources (Clarkson et al., 2013). Initially developed in the United States during the last century, shale gas exploration subsequently expanded to China, Australia, and India, thereby stimulating significant research activity in recent decades (Vishal et al., 2019). As an unconventional energy source, shale gas is recognized as a potential contributor to energy security and greenhouse gas mitigation, while also being seen as capable of meeting future global energy demand (Wang and Li, 2016).

Despite these prospects, large-scale exploitation of shale gas remains constrained by the inherent complexity of shale pore systems. The principal challenge in assessing shale gas storage and transport lies in deciphering the pore architecture, which fundamentally governs reservoir capacity, fluid flow, and production performance (Kuila and Prasad, 2013). Critical pore attributes, including size distribution, porosity, geometry, and connectivity, serve as proxies for adsorption capacity and flow behavior (Vishal et al., 2019). Relative to conventional reservoirs, shale is characterized by nanometer-scale pore throats, low porosity (≤ 10 %), and ultra-low permeability in the nano-darcy range. Its pore structure comprises both nanoscale intergranular and intragranular pores, as well as microscale pores (Curtis et al., 2012). A robust understanding of pore characteristics is critical for sweet-spot identification. However, accurate pore characterization remains hindered by the pronounced heterogeneity and anisotropy inherent to shale formations.

To address this challenge, extensive research has focused on characterizing pore systems in shale formations to improve gas recovery. These methods are generally classified into imaging, fluid-injection, and non-fluid/radiation techniques (Wang et al., 2024b). Imaging tools, such as Field Emission Scanning Electron Microscopy (FE-SEM) and Atomic Force Microscopy (AFM), allow for direct observation of pore morphology. Fluid-injection techniques, including Low-Pressure Gas Adsorption (LPGA), Mercury Intrusion Capillary Porosimetry (MICP), and Nuclear Magnetic Resonance (NMR), together with scattering and tomography methods such as Small Angle X-ray Scattering (SAXS) and micro-CT, provide quantitative data on pore size, surface area, and connectivity. Applications of these methods, FE-SEM (Li et al., 2022a), AFM (Chen et al., 2021), LPGA (Liu et al., 2018), MICP (Mastalerz et al., 2021), NMR (Liu et al., 2020b), SAXS (Liu et al., 2022b), and micro-CT (Garum et al., 2020), have built a multiscale understanding of shale pore networks. Together, they capture PSD, porosity, volume, connectivity, and morphology.

In India, shale gas has received significant attention due to its role in energy security and its large potential across several sedimentary basins (Paul et al., 2021). Major prospective basins include Cambay, Cauvery, Damodar, Mahanadi, and Krishna-Godavari (K-G) basin, which together hold an estimated 584 Trillion Cubic Feet (TCF) of risked gas in place and 96 TCF of technically recoverable resources (Kuuskraa et al., 2013). Research has therefore focused on pore network characterization to assess shale gas recovery and CO_2 sequestration. Anand et al. (2023) reported sorption and morphological features of Cambay shales, suggesting potential for enhanced recovery, whereas Kumar et al. (2018) observed limited microporosity in Cambay Shales, suggesting limited reservoir potential.

Studies of Damodar and Jharia Basin shales have revealed heterogeneous pore types and strong links between pore characteristics and storage capacity (Bakshi et al., 2018). Kumar et al. (2024) found higher micropore volumes in Korba shales than in Raniganj shales, while Chandra et al. (2020b) observed a decline in micropore volume with depth in Ib Valley shales. Chandra et al. (2020a) also confirmed variations in pore accessibility in Raniganj shale using SAXS/SANS. Ghosh et al. (2025) reported that clay minerals dominate mesopore development, whereas organic matter controls micropore development in Mand-Raigarh shales. Rani et al. (2020) emphasized the role of PSD in methane storage and CO_2 sequestration in Damodar and K-G shales. Bal et al. (2024) reported complex pore accessibility in the Raghampuram shales of the K-G basin. In addition, thermal studies demonstrate that elevated temperatures promote the maturation of organic matter and induce micro-fracturing, thereby modifying pore morphology and connectivity (Nilankar et al., 2024a, b).

Despite these advances, existing investigations reveal that most pore network studies in India remain concentrated within a limited number of prospective basins. Singh et al. (2025c) highlighted that many shale formations across the country remain inadequately explored, despite their considerable potential to host substantial gas reserves. Among these underexplored regions, the Himalayan domain emerges as a frontier for hydrocarbon exploration, presenting multiple stratigraphic sequences with substantial promise for future prospecting and development (Bhat, 2019). In the NW Himalayan region, the Infra-Krol, Krol, and Tal Formation black carbonaceous shale from the Neoproterozoic-Cambrian sedimentary sequence of the Lesser Himalaya and the Subathu Formation shale from the Cenozoic sequence of the Sub-Himalaya form a well-deposited sequence with hydrocarbon potential (Mishra and Mukhopadhyay, 2012). While the Cenozoic Subathu Shale has demonstrated significant potential for generating

dry gas (Bhattacharya and Chandra, 1979; Raiverman et al., 1984; Hafiz et al., 2022), investigations of the Neoproterozoic shales remain almost absent. The Infra-Krol, Krol, and Tal Formation shales exhibit a widespread occurrence across the northwestern Himalayan belt, extending from Solan in Himachal Pradesh (West) to Nainital in Uttarakhand (East), with exposures around Mussoorie and Garhwal. To advance towards such unexplored shale formations, a comprehensive understanding of the pore network system is crucial for controlling the storage and flow behavior of hydrocarbons.

Therefore, this study focuses on the Neoproterozoic Krol Formation black shale from the Kaudiyala area of the Lesser Himalayan Garhwal region, Uttarakhand. Following confirmation of hydrocarbon gas generation, the shale samples were subsequently subjected to comprehensive pore characterization. An integrated approach employing imaging, fluid-injection, and non-fluid-injection techniques, including FE-SEM, LPGA-N_2/CO_2 sorption, SAXS, and micro-CT analyses, was undertaken to characterize the pore attributes of this underexplored formation. This comprehensive pore characterization investigation not only provides critical insights into shale gas recovery in the Himalayan region but also establishes a robust foundation for evaluating the feasibility of CO_2 sequestration. The findings from this study will highlight the dual role of the investigated shale formations, serving both as potential reservoirs for hydrocarbon generation and as viable geological sinks for CO_2 storage.

7.2. Methodology

The block samples BS-1 and BS-2 of the Krol Shale were used in this study, collected from the study area mentioned in Section 2.2 of Chapter 2.

7.2.1. Sample Preparation

For FE-SEM analysis, a total of 10 specimens were prepared from both block samples in the form of a thin film/chip, each ~ 5 mm thick. For LPGA N_2/CO_2 and SAXS analyses, powder samples with a particle size of 75 µm were prepared from each block, resulting in a total of 10 samples for these analyses. For micro-CT analysis, cylindrical specimens with a diameter of 35 mm were prepared from each block. The methodology, with experimental setup, is shown in Figure 7.1. Before conducting the experimental investigations, the prepared specimens were placed in an oven at 105 °C for 12 hr to remove moisture and ensure homogeneity.

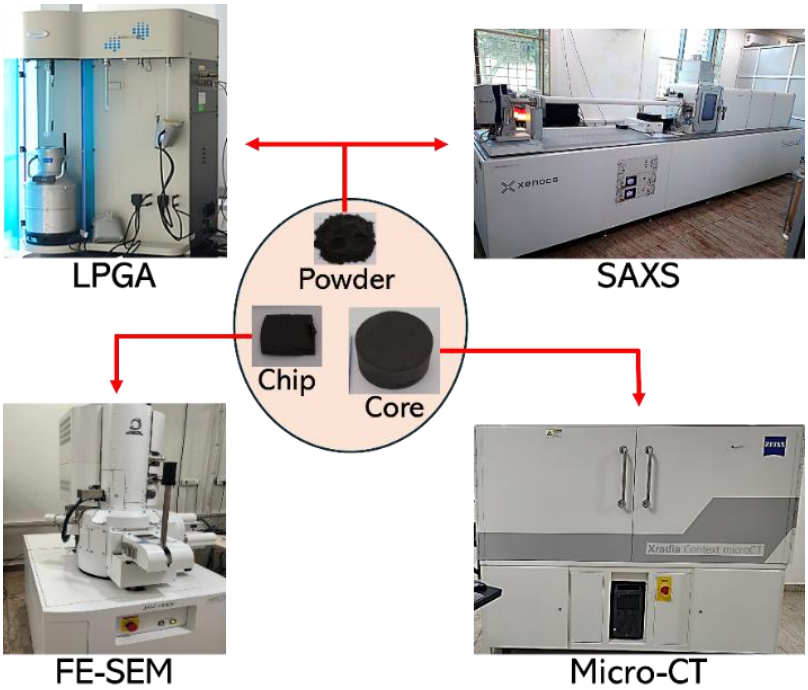

Figure 7.1. *Experimental laboratory setup illustrating the adopted methodology.*

7.2.2. LPGA analysis

The combined N_2 and CO_2 sorption through LPGA analysis is a useful tool to characterize shale, especially at the micro-and mesoscales. A 2–3 g powder sample having a particle size less than 75 microns was analyzed in a Quantachrome Autosorb iQ single

station physisorption analyzer available at the Indian Institute of Technology, Bombay. Before analysis, all samples were subjected to degassing under vacuum at room temperature for 12 hr in an oxic environment to eliminate inherent moisture and volatile components from the pore spaces. Degassing ensures enhanced pore accessibility during the sorption process (Chandra et al., 2022). N_2 at -196 °C (77K) characterizes meso and macropores along with a few micropores of shale, while CO_2 at 0 °C (273K) critically accesses only micropores. Because of its strong affinity towards organic matter and strong quadrupolar nature, CO_2 has the potential to access fine micropores in shale (Hazra et al., 2020). In contrast, N_2, which possesses a weak quadrupole nature in comparison to CO_2, interacts weakly with fine micropores, making it more effective in probing pores larger than 1.3 nm.

Therefore, the combined N_2 and CO_2 sorption enabled a comprehensive characterization of the pore system by covering a wide range of pore sizes in the studied shale. The sorption isotherm consists of two branches, the adsorption isotherm and the desorption isotherm. The adsorption isotherms represent the volume of adsorbate adsorbed within the porous material with an increase in relative pressure. The desorption isotherms record the volume of desorbate desorbed from the porous material with decreasing relative pressure. The relative pressure (P/P_0), where P is the vapor pressure and P_0 is the saturation pressure of the adsorbate gas, ranged from 0.01 to 0.99 for N_2-LPGA and from 0.005 to 0.03 for CO_2-LPGA. For N_2-LPGA, both adsorption and desorption isotherms were recorded, whereas for CO_2-LPGA, only the adsorption branch was considered, since CO_2 does not readily desorb from the adsorbent surface without external energy. The recorded isotherms were subsequently analyzed using Quantachrome AsiQWin software to determine the surface area, pore volume, PSD, and fractal characteristics.

7.2.3. SAXS analysis

SAXS was performed using XENOCS, Xuess 3.0 HR apparatus available at the Central Instrumentation Facility (CIF), Rajiv Gandhi Institute of Petroleum Technology, Jais. This technique has proven to be highly effective in characterizing the nanoscale pores within shale and coal (Radlinski et al., 2004). Compared to gas adsorption or imaging techniques, this technique is well-suited for characterizing both accessible and inaccessible pores. For analysis, a 0.1–1 g powder sample with a particle size of less than 75 microns was packed using Kapton tape and mounted on the sample holder. The distance between the sample and the detector was ~ 1.5 m. For measurements, a 30 W copper X-ray source was used in conjunction with a Pilatus 300K 1M hybrid pixel detector, equipped with single photon counting capability.

According to Eq. 7.1, the raw data is recorded in the form of scattering intensity I(Q) as a function of the scattering wave vector Q (Chandra et al., 2020a).

$$Q = \frac{4\pi \sin(\theta)}{\lambda} \qquad \text{Eq.7.1}$$

Here, θ: half of the scattering angle and λ: X-ray wavelength.

In this experiment, the accessible Q range was between 0.0001 and 0.181 $Å^{-1}$. Data processing, including background correction and noise removal, was performed using XSACT software. Subsequently, pore attributes were computed with MATSAS, an open-source MATLAB-based code.

7.2.4. FE-SEM analysis

The surface morphology of the studied shale was assessed using a JEOL JSM-7900F FE-SEM analyzer available at the Central Instrumentation Facility (CIF), Rajiv Gandhi Institute of Petroleum Technology, Jais. This technique is highly efficient in

visualizing the pore characteristics of shale, and when combined with a statistical approach, it provides a quantitative characterization of the pore system (Fredrich et al., 1995). For this analysis, a dried thin chip specimen was coated with a gold layer to improve conductivity and subsequently mounted on the sample holder for imaging under the electron beam. The imaging was carried out at an operating voltage of 5 keV with a working distance of ~ 10 mm.

Once the high-resolution FE-SEM images of the shale samples were acquired, quantitative image analysis was performed using MATLAB to obtain pore parameters, including porosity, PSD, coordination number, fractal dimension, and tortuosity. The workflow for image analysis, from image acquisition and processing to segmentation and extraction of quantitative pore characteristics, is shown in Figure 7.2.

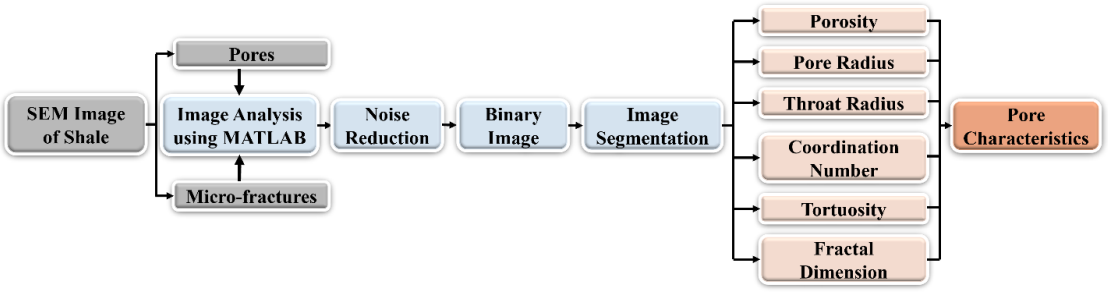

Figure 7.2. *Schematic workflow illustrating FE-SEM image analysis and quantitative pore characterization using MATLAB.*

At a known spatial resolution (µm/pixel for each image), each grayscale FE-SEM image, with darker regions corresponding to voids/pores and brighter regions representing the mineral matrix, was imported. To classify different intensity levels, the Otsu multi-level threshold method was adopted (Otsu, 1975). By using the Otsu multi-level threshold method on the greyscale FE-SEM image, the darkest regions can be detected, allowing the image to be segmented so that each segment has the lowest possible

variation in intensity (Rabbani and Salehi, 2017). The grayscale image was quantized into N intensity levels (here N = 8), which reduces noise sensitivity and enhances pore-matrix contrast. The binary segmentation was carried out to distinguish the pore spaces from the solid matrix, with pixels corresponding to pores assigned a value of 1, while pixels corresponding to the matrix were assigned a value of 0. Furthermore, in the binary segmented image, the watershed algorithm was used to label the segmented pore spaces with different random colors (Rabbani and Ayatollahi, 2015). The watershed image segmentation algorithm is widely used in the field of image processing, which works on the principle of water flooding in a watershed and catchment basin system, where unique regions are defined by connected pixel values and delineated by well-defined boundaries (Beucher, 1992).

Pore parameters such as equivalent pore radius, porosity, circularity, aspect ratio, and coordination number were calculated using the watershed image segmentation method of Otsu-binarized FE-SEM images, while for throat radius calculation, only Otsu-binarized FE-SEM images were used. For the fractal dimension, the Differential Box Counting (DBC) method was applied to Otsu-binarized FE-SEM images. This DBC method works on the reticular cell counting approach, where any box containing at least one sample of the gray-level intensity surface is considered a countable box and is one of the most widely applied techniques for estimating the fractal dimension of 2D images (Liu et al., 2014).

The following mathematical formulations were employed to compute each parameter:

$$r = \sqrt{\frac{A_{pore}}{\pi}} \qquad \text{Eq.7.2}$$

Here, r: equivalent pore radius (μm) and A_{pore}: pore area (μm^2), obtained by multiplying the number of pixels in the pore by pixel area.

$$\phi = \frac{A_{pore}}{A_{total}}$$ Eq.7.3

Here, ϕ: 2D porosity and A_{total}: total image area (μm^2), obtained by multiplying the total number of pixels by pixel area.

$$C = \frac{4\pi A_{pore}}{P^2}$$ Eq.7.4

Here, C: circularity and P: perimeter of the pore.

$$AR = \frac{L_{major}}{L_{minor}}$$ Eq.7.5

Here AR: aspect ratio, L_{major}: length of the major axis of the pore (μm), and L_{minor}: length of the minor axis of the pore (μm).

$$CN_i = \sum_{j=1}^{n} C_{ij}$$ Eq.7.6

Here, CN_i: coordination number of pore i, C_{ij} will be 1 if pore i is connected to pore j, otherwise it will be 0, and n: total number of neighboring pores.

$$r_{throat} = \sqrt{\frac{A_{throat}}{\pi}}$$ Eq.7.7

Here, r_{throat}: pore throat radius (μm) and A_{throat}: throat cross-sectional area (μm^2) obtained from binary segmentation.

$$N_\varepsilon \propto \varepsilon^{-D}$$ Eq.7.8

$$D = \lim_{\varepsilon \to 0} \frac{\log N_\varepsilon}{\log\left(\frac{1}{\varepsilon}\right)}$$ Eq.7.9

Here D: Fractal Dimension, N_ε: number of boxes of size ε.

7.2.5. Micro-CT Tomography analysis

X-ray micro-CT has proven to be the best non-invasive and non-destructive technique to characterize the complex pore structure. This technique facilitates 3D visualization and quantitative characterization of multiphase systems, thereby enabling the identification and analysis of internal features having a size of order 100 μm (Tiwari

et al., 2013). The analysis was performed using a ZEISS Xradia Context Micro-CT system available at the Indian Institute of Petroleum & Energy, Visakhapatnam. The instrument is equipped with a 160 kV/10 W X-ray tube with a maximum voxel size of 0.5 μm to obtain a high-resolution 3D spatial image. During the scanning process, the sample-to-source and sample-to-detector distances were maintained at 25 mm and 450 mm, respectively, and remained constant throughout the scanning process. This arrangement enabled the detectability range of pixel size 7.88 μm. The sample was carefully mounted on a 360° rotating stage and incrementally rotated, with each step exposed to X-rays for 0.5 s. During the single revolution, a total of ~ 2401 projections were acquired under an operating condition of 100 kV voltage and 7 W power.

7.3. Results

7.3.1. Source Rock Characteristics/Nature and Paleoenvironment

The Neoproterozoic pyritic black shale from the Krol Formation (Lesser Himalaya) was evaluated through combined geochemical and petrographic analyses for the hydrocarbon generation and kerogen type. The Atomic H/C *vs.* O/C plot (Figure 7.3) indicates that the shales are dominated by Type III kerogen, which is primarily gas-prone. The H/C ratios (0.7–1.4) and O/C ratios (0.65–0.80) mostly fall within the Type III field on the Van Krevelen diagram, suggesting a terrestrial (humic) organic origin with significant oxidation or relatively high maturity. Because the type of organic matter strongly affects kerogen classification and hydrocarbon generation, petrographic maceral analysis was performed under both white and UV light. The results show that the samples mainly contain oxidized vitrinite, with very little inertinite and the absence of flourishing liptinite (Figure 7.4). The predominance of vitrinite indicates that the kerogen is primarily Type III. The measured range of vitrinite reflectance (% VRo) suggests that the organic

matter has reached the post-oil or gas maturity stage. The absence of liptinite macerals and the presence of highly reflective vitrinite (% VRo > 1.5 %) further confirm a high level of thermal maturity. Petrographically, the elevated reflectance values and vitrinite features suggest that organic matter has undergone significant alteration, likely due to strong oxidation during deposition and/or advanced catagenesis (Hutton, 1995). Geochemical studies by Singh et al. (2025c), which included Total Organic Carbon (TOC) analysis and petrographic observations of the Krol Shale, support these findings. Their TOC versus % VRo cross plot and petrographic images indicate that the shale lies within the gas generation window. Microscopic analysis also revealed an abundance of mineral matter, including clay minerals and notable amounts of pyrite (Figures 7.4a–d). The very high total sulfur content (> 10 wt %) reported in Table 7.1, together with the abundance of framboidal and disseminated microscopic pyrite (Figure 7.4d), indicates deposition under anoxic conditions. Such environments favor sulfur enrichment and pyrite preservation. However, the organic matter in these shales was likely dominated by terrestrial humic material, which is inherently low in hydrogen. This interpretation is supported by the presence of amorphous humic organic matter (Figures 7.4b, d) and the absence of liptinitic components.

The combined analysis of total sulfur (TS), TOC, and their ratio (TOC/TS) is a well-established approach for distinguishing marine from non-marine depositional settings under varying redox conditions (Wei and Algeo, 2020). Typically, marine sediments deposited under reducing conditions contain high sulfur (> 2 wt %) and moderate TOC (> 1 %), whereas well-oxygenated freshwater environments exhibit much lower sulfur (< 1 wt %) and higher TOC (> 10 %) values (Wei and Algeo, 2020). Based on these parameters, the Krol Formation Shale can be interpreted as predominantly marine-influenced facies, where terrestrially derived organic matter accumulated under

reducing marine conditions. This interpretation is consistent with Auden (1934) earlier observation that the Krol sediments were deposited in a shallow marine environment.

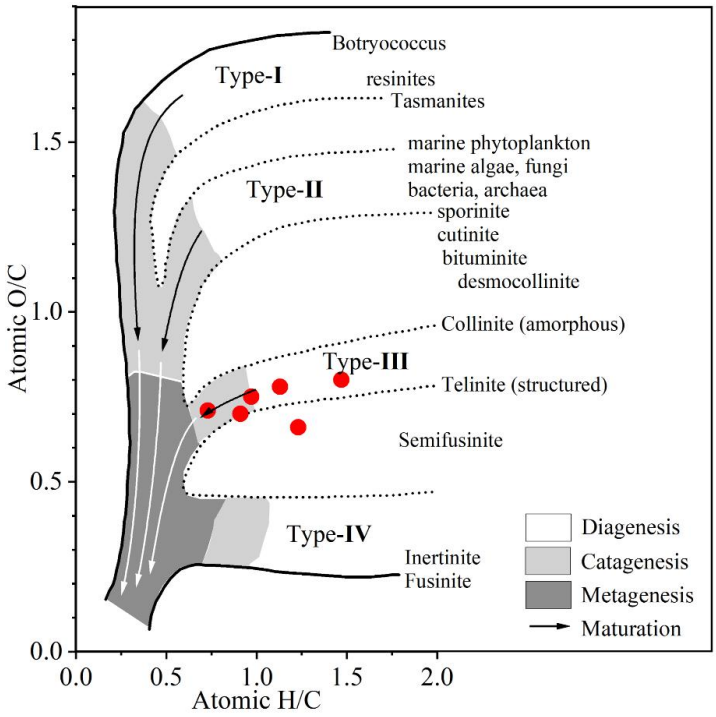

Figure 7.3. *Van Krevelen diagram showing atomic H/C vs. atomic O/C ratios for the Krol Shale.*

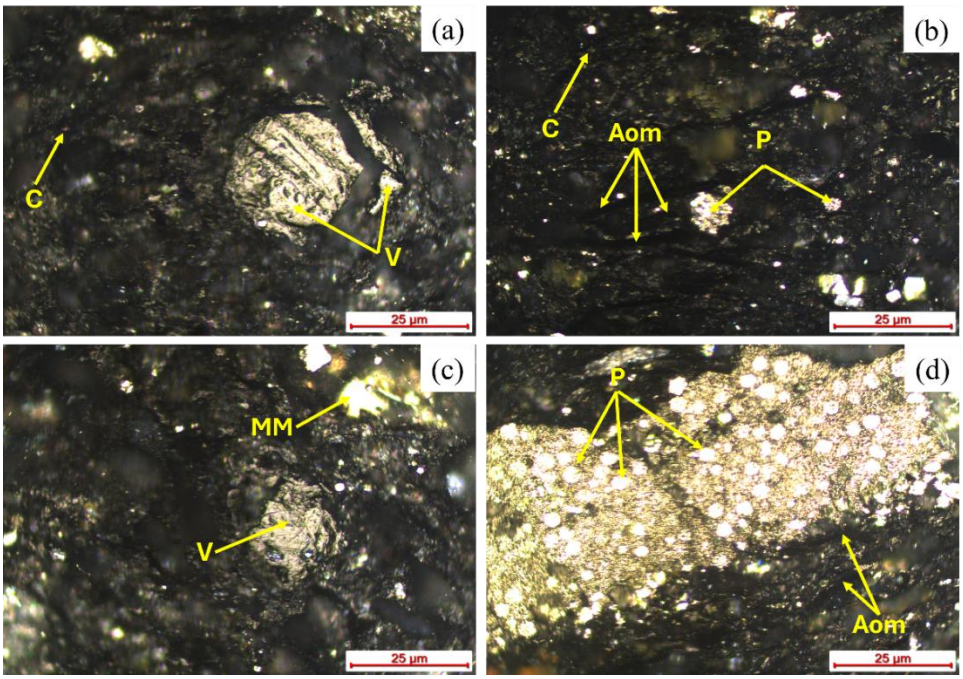

Figure 7.4. *Petrographic characteristics of the studied shale samples: (**a**) oxidized vitrinite associated with clay minerals; (**b**) amorphous organic matter with pyrite grains and clay minerals; (**c**) oxidized vitrinite interspersed with mineral matter; (**d**) framboidal pyrite grains with amorphous organic matter. [V: vitrinite; C: clay mineral; AOM: amorphous organic matter; P: pyrite; MM: mineral matter].*

Table 7.1. *Ultimate (CHNSO) analysis, vitrinite reflectance, and TOC results of the Lesser Himalayan Krol Shale.*

Sample ID	In wt %, daf					H/C	O/C	% VR_o	TOC (wt %)
	C	H	S	N	O				
BS-1.1	42.01	2.61	10.58	5.15	39.65	0.73	0.71	1.51	2.74
BS-1.2	42.08	2.55	10.53	5.54	39.3	0.91	0.7	1.97	4.39
BS-1.3	42.18	2.13	11.09	2.77	41.83	0.97	0.75	1.96	4.67
BS-2.1	42.1	2.15	11.19	2.77	41.79	1.13	0.78	1.93	4.62
BS-2.2	43.79	3.16	11.69	3	38.35	1.23	0.66	2.04	5.56
BS-2.3	41.33	1.98	10.55	2.23	43.91	1.47	0.80	1.94	2.77

7.3.2. LPGA analysis

The LPGA analyses of N_2 and CO_2 provide valuable insights into the pore structure of the studied shale samples. The adsorption-desorption isotherm shapes and corresponding hysteresis loops, as classified by the International Union of Pure and Applied Chemistry (IUPAC), are essential indicators of pore geometry and sorption mechanisms. According to the IUPAC classification (Kuila and Prasad, 2013), adsorption

isotherms are divided into six types (Type I–VI), while hysteresis loops are categorized into four types (H1–4). Based on this classification, the N_2 adsorption-desorption isotherms for samples BS-1 and BS-2 (Figures 7.5a, b) exhibit a typical Type IIB pattern (Rouquerol et al., 1998). This type is preferred over Type IV because it lacks a plateau and instead displays a continuous steep slope at high relative pressures (P/Po). The observed hysteresis corresponds to a Type H3 loop, indicating the presence of slit-shaped pores at higher relative pressures and wedge-shaped pores at lower pressures (Thommes et al., 2015). The hysteresis loop morphology, therefore, provides indirect evidence of the pore shape and connectivity. In addition to N_2-LPGA, CO_2-LPGA analysis was performed to characterize the micro- and ultra-microporous domains. CO_2 adsorption is highly effective in detecting micropores (Hu et al., 2024). The CO_2 adsorption isotherms for samples BS-1 and BS-2 (Figure 7.5c, d) display a Type I isotherm, characterized by a concave curvature toward the P/Po axis, confirming the dominance of microporous structures.

For the N_2 adsorption, the specific surface area was calculated using the DFT and Brunauer-Emmett-Teller (BET) models. Although N_2 adsorption is well-suited for meso- and macropores, it can also probe micropores, but with limited capability. Accordingly, the DFT model, which is more appropriate for evaluating micropore surface area, was used alongside the BET model, which is better suited for assessing meso and macropore surface areas. Wei et al. (2016) suggested the suitability of the DFT model for micropore surface area analysis and the BET model for meso and macropore surface area analysis. The N_2-DFT surface areas for the shale samples BS-1 and BS-2 are 4.97 $m^2\ g^{-1}$ and 3.1 $m^2\ g^{-1}$, while the N_2-BET surface areas for the shale samples BS-1 and BS-2 are 3.51 $m^2\ g^{-1}$and 3.24 $m^2\ g^{-1}$, respectively (Table 7.2). For the CO_2 adsorption isotherms, the micropore surface area was determined using the DFT and Dubinin-Radushkevich (DR)

model. The CO_2-DFT surface areas for samples BS-1 and BS-2 are 28.04 $m^2\ g^{-1}$ and 27.93 $m^2\ g^{-1}$, while the CO_2-DR surface areas for samples BS-1 and BS-2 are 27.06 $m^2\ g^{-1}$ and 26.98 $m^2\ g^{-1}$, respectively (Table 7.2). These results indicate that the studied shales are dominantly microporous, with CO_2 adsorption contributing significantly more to surface area than N_2 adsorption.

The PSD from N_2 adsorption was evaluated using the BJH and DFT models, both applied to the adsorption isotherm. The BJH model can estimate pore sizes up to ~ 100 nm, whereas the DFT model provides more accurate results for smaller mesopores (2–35 nm) by considering adsorbate-adsorbent interactions. Together, these models reveal a bimodal to multimodal pore distribution (Figure 7.6). The BJH-derived PSD curves show an increasing trend within the mesopore range, with average pore widths of 4.61 nm for BS-1 and 3.21 nm for BS-2, and a total pore volume of 0.009 cc g^{-1} (Figures 7.6a, b). Both samples exhibit bimodal distributions, with dominant peaks in the finer mesopore range (2–10 nm) and secondary peaks near the meso-macropore boundary (40–60 nm). The DFT-based PSD for N_2 (Figures 7.6c, d) displays a multimodal pattern with several peaks between 2 and 30 nm. Common peaks appear at 4, 13, 24, and 29 nm for both samples, while BS-2 shows an additional peak at 3 nm. The DFT curves also indicate a gradual increase in pore volume with pore width, with average pore width of 1.29 nm for BS-1 and 1.54 nm for BS-2, and a pore volume of 0.008 cc g^{-1}. The CO_2-derived PSD, also analyzed using the DFT model, shows a multimodal distribution dominated by ultra micropores (Figures 7.6c, d). Major peaks occur between 0.2 and 1 nm, notably at 0.3, 0.5, 0.6, and 0.8 nm. The average pore width is 0.35 nm for BS-1 and 0.46 nm for BS-2, with a pore volume of 0.008 cc g^{-1}.

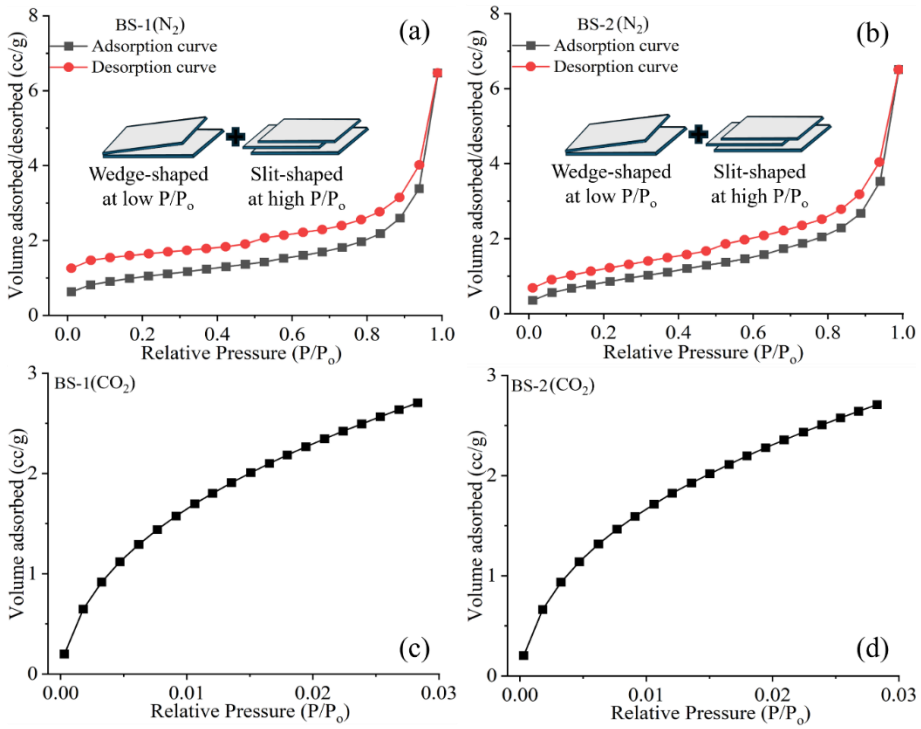

Figure 7.5. *LPGA isotherms: (**a**) and (**b**) N_2 adsorption-desorption isotherms, and (**c**) and (**d**) CO_2 adsorption isotherms of the representative BS-1 and BS-2 shale samples.*

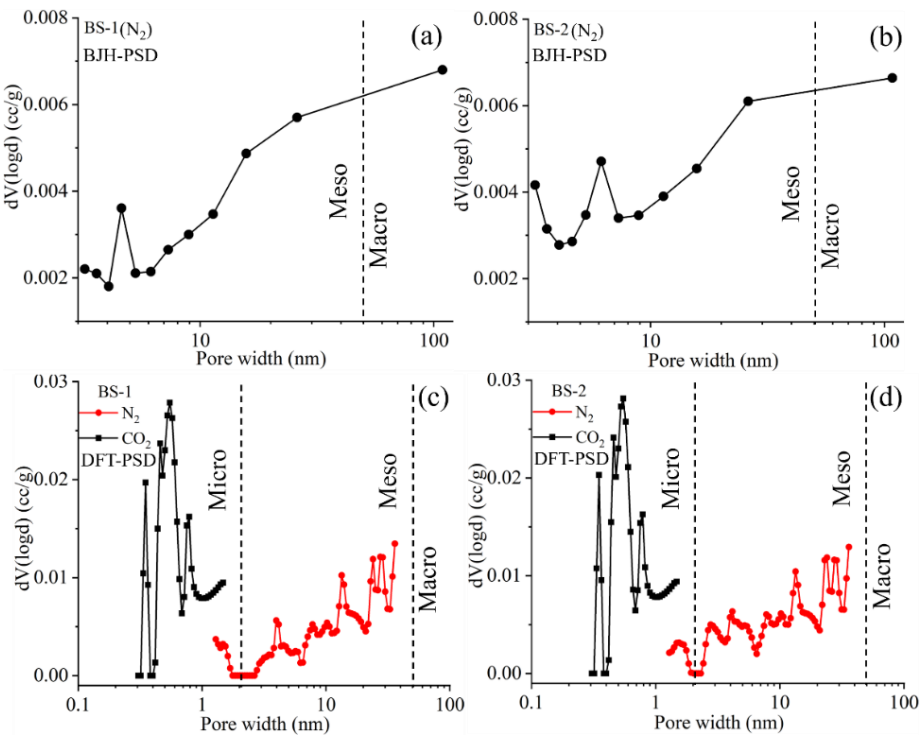

Figure 7.6. *LPGA PSD: (**a**) and (**b**) N_2 BJH-PSD, and (**c**) and (**d**) N_2 and CO_2 DFT-PSD of the representative BS-1 and BS-2 shale samples.*

Additionally, the irregularity and complexity of the pore structure were also evaluated using the fractal dimension derived from the Frenkel-Halsey-Hill (FHH) model. The calculated fractal dimensions of BS-1 (2.49) and BS-2 (2.55) suggest an intermediate level of structural complexity. Generally, higher fractal values indicate rougher and more irregular pore surfaces, while lower values reflect smoother and more uniform structures.

Table 7.2. *Pore parameters obtained through LPGA analysis.*

Parameters		BS-1	BS-2
N_2 adsorption	DFT surface area	4.97 $m^2 g^{-1}$	3.1$m^2 g^{-1}$
	BET surface area	3.51 $m^2 g^{-1}$	3.24 $m^2 g^{-1}$
	BJH pore volume	0.009 cc g^{-1}	0.009 cc g^{-1}
	BJH average pore width	4.61 nm	3.21 nm
	DFT pore volume	0.008 cc g^{-1}	0.008 cc g^{-1}
	DFT average pore width	1.29 nm	1.54 nm
	FHH fractal dimension	2.49	2.55
CO_2 adsorption	DFT surface area	28.04 $m^2 g^{-1}$	27.93 $m^2 g^{-1}$
	DR surface area	27.06 $m^2 g^{-1}$	26.98 $m^2 g^{-1}$
	DFT pore volume	0.008 cc g^{-1}	0.008 cc g^{-1}
	DFT average pore width	0.35 nm	0.46 nm

7.3.3. SAXS analysis

SAXS is a powerful technique for characterizing porous materials, capable of detecting both accessible and inaccessible pores across a wide size range. In this method, a monochromatic X-ray beam interacts with the shale powder and scatters due to differences in electron density between the solid matrix and pore spaces. The 2D SAXS patterns of the BS-1 and BS-2 shale samples exhibit isotropic scattering, with intensity uniformly distributed in all directions (Figure 7.7). Both samples display a bright central scattering region, with intensity gradually decreasing outward in concentric rings.

The pore structures were quantified using MATSAS, an open-source MATLAB-based code. The scattering data were plotted as a log-log curve of the scattering vector (Q) versus intensity (I(Q)) following the PDSP model (Figure 7.8). The linear trend in the

log-log plots (Figures 7.8a, b) indicates that both BS-1 and BS-2 follow a power-law relationship ($I(Q) \propto Q^{-D}$), where *D* is the fractal dimension. Such behavior suggests a fractal nature of the samples. When this power-law trend extends over at least one decade of Q, the scattering material is considered fractal in nature (Radlinski et al., 1999). The observed fractal nature reflects the inherent structural complexity of the shale pore system (Bahadur et al., 2015). The fractal dimension values, 2.373 for BS-1 and 2.368 for BS-2, indicate a moderate level of structural complexity in both samples.

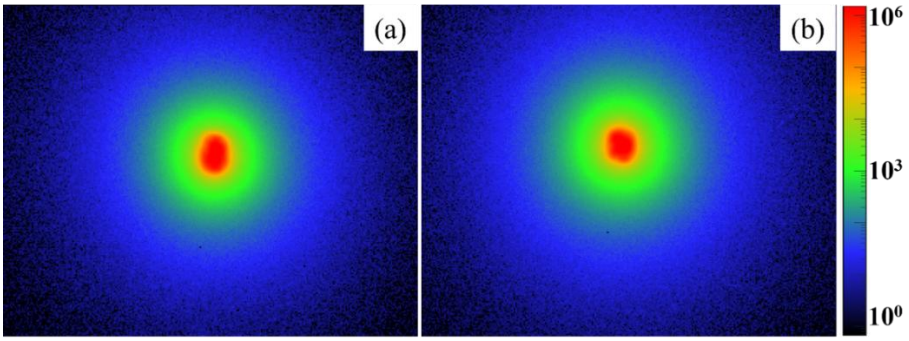

Figure 7.7. *2D SAXS profiles of representative (**a**) BS-1 and (**b**) BS-2 shale samples.*

The PDSP model-based PSD was further calculated in terms of logarithmic differential pore volume. The PDSP model is particularly suitable for PSD estimation in randomly oriented scattering systems such as shale (Chandra et al., 2022). The PSD curves of BS-1 and BS-2 indicate that both samples are predominantly composed of mesopores. The pore volume distribution shows a gradual increase with pore width in both samples (Figures 7.9a, b). In sample BS-1, the total pore volume is 4.003 cc g^{-1}, comprising 2.381 cc g^{-1} of mesopores and 1.622 cc g^{-1} of macropores. Similarly, in BS-2, the total pore volume is 4.109 cc g^{-1}, with 2.532 cc g^{-1} of mesopores and 1.577 cc g^{-1} of macropores. The sharp rise near the meso-macropore transition boundary reflects the presence of larger, interconnected pores.

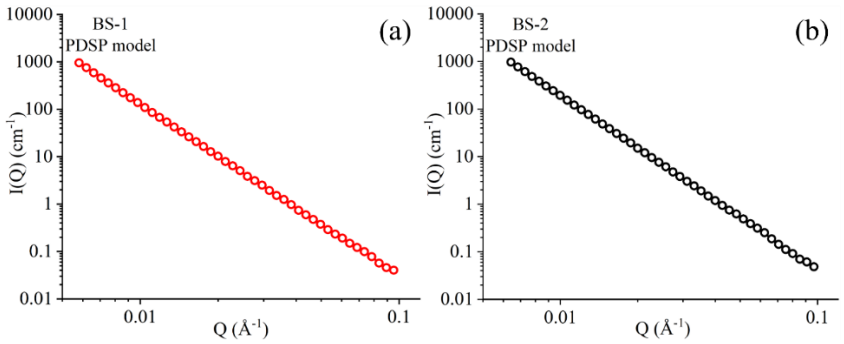

Figure 7.8. *SAXS scattering profiles of representative* ***(a)*** *BS-1 and* ***(b)*** *BS-2 shale samples modeled using the PDSP approach.*

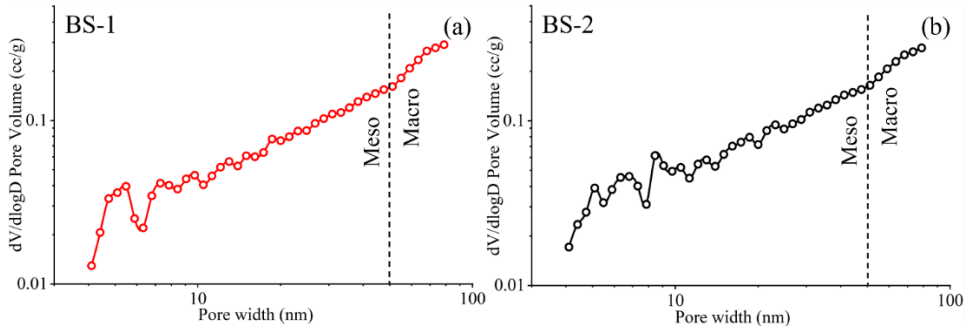

Figure 7.9. *SAXS-derived PSD based on the PDSP model for representative shale samples:* ***(a)*** *BS-1 and* ***(b)*** *BS-2, based on pore volume.*

7.3.4. FE-SEM analysis

The photomicrographs of the Krol Shale reveal a highly heterogeneous microstructure (Figure 7.10). Bright regions represent the mineral matrix, while dark regions indicate pore spaces. Numerous nanoscale interparticle, intraparticle, and organic matter pores are observed, along with a few micron-scale fractures. Organic matter pores are mostly isolated and globular, forming a sharp contrast with the surrounding minerals. Intergranular pores occur between grains, whereas intragranular pores are enclosed within individual grains. These pore types are classified according to the Loucks matrix-related pore classification scheme (Loucks et al., 2012). Abundant organic matter pores (Figure 7.10a) likely play a key role in controlling the gas storage potential. Additionally, various

pore shapes, such as intergranular (Figure 7.10b), complex (Figure 7.10c), and slit-shaped pores (Figure 7.10d), have been identified. These pore geometries strongly influence the fluid flow behavior within the rock.

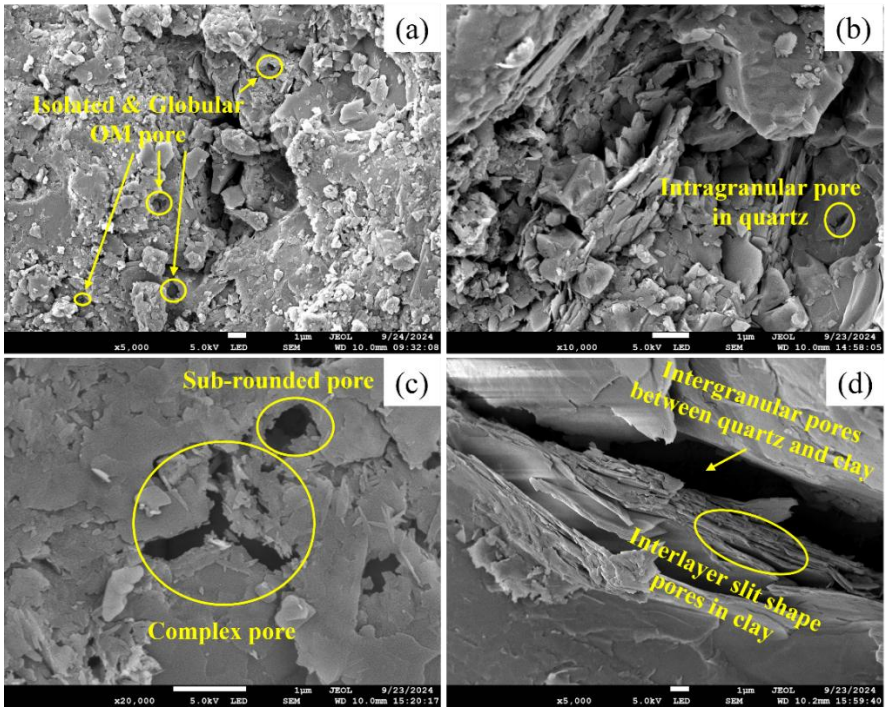

Figure 7.10. *Photomicrographs illustrating the surface morphology of Krol Shale, such as (**a**) an organic matter pore, (**b**) an intragranular pore, (**c**) a complex and sub-rounded pore, and (**d**) an intergranular and slit-shaped pore.*

7.3.4.1. Pore System Characterization using Quantitative Image Analysis

The 2D FE-SEM photomicrograph provides a quantitative assessment of pore parameters, offering a representative view of the sample's 3D structure. The open-source MATLAB-based image processing algorithm exhibits better efficiency compared to conventional software, which typically requires manual parameter tuning. Such manual intervention can lead to inconsistencies between images, whereas the MATLAB-based approach ensures consistent and reliable analysis. Additionally, errors in selecting optimal parameters during image acquisition may introduce noise and degrade image quality (Buades et al., 2005). Building upon this, watershed image segmentation was performed following Otsu's multilevel threshold binarization of the original FE-SEM image (Figure

7.11). The grayscale FE-SEM image (Figure 7.11a) was initially converted into a binary segmented image (Figure 7.11b), with pores represented in black and the matrix in white. Binarization of the grayscale image is a prerequisite for segmentation, and the Otsu method was employed to automatically determine the optimal threshold values. Subsequently, a depth map (Figure 7.11c) was generated from the binarized image to represent topographic variations in pixel intensity. This serves as the foundation for watershed segmentation. The application of the watershed algorithm to the depth map is to delineate distinct boundaries, resulting in the final pore space segmentation (Figure 7.11d). The segmented pores are displayed in varying color intensities, facilitating differentiation between shallow, deep, isolated, and interconnected pore structures.

Following image binarization and watershed segmentation of the shale sample, a quantitative statistical analysis was conducted to characterize the pore network. The evaluated parameters include PSD, circularity, aspect ratio, and coordination number (Table 7.3), which collectively govern hydrocarbon storage and transport behavior within the shale matrix.

The PSD, expressed in terms of equivalent pore radius (Figure 7.12a), ranges from 20 nm to 230 nm, with the majority of pores < 50 nm (Table 7.3). The frequency decreases sharply with increasing pore size, indicating a dominance of nanopores. The pore circularity histogram (Figure 7.12b) describes the degree to which pore geometries deviate from a perfect circle, where a circularity value of 1 denotes a perfectly circular pore. Most pores exhibit low circularity values (< 0.3), suggesting irregular and elongated shapes. The aspect ratio (Figure 7.12c), defined as the ratio of the minor (shorter) axis to the major (longer) axis, ranges between 0.15 and 0.25 (Table 7.3), further confirming the prevalence of elongated pore structures. The pore connectivity was evaluated using the pore coordination number (Figure 7.12d), defined as the maximum number of pores

directly connected to a given pore within the network. The results indicate that most pores exhibit coordination numbers between 2 and 3, reflecting a low to moderate degree of connectivity (Table 7.3). A higher coordination number corresponds to an increased number of interconnected flow paths, which enhances the potential for fluid migration through the pore network.

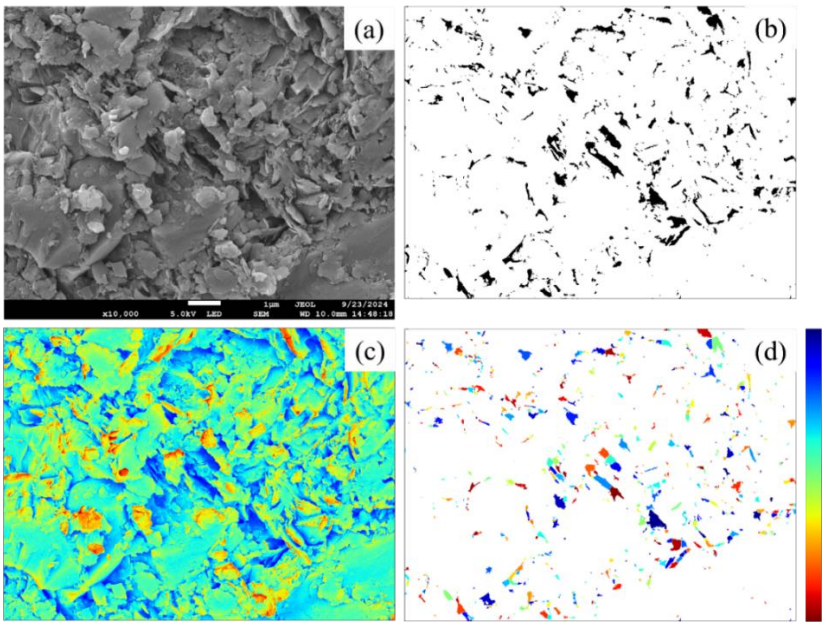

Figure 7.11. *Workflow of watershed image segmentation applied to the FE-SEM image of the studied shale: (**a**) original grayscale FE-SEM image, (**b**) binary image generated using Otsu multilevel thresholding, (**c**) depth map showing topographic variation, and (**d**) final watershed-segmented image.*

The throat size distribution, expressed in terms of throat radius (Figure 7.13), represents a key pore structural parameter, as throats act as narrow constrictions or pathways connecting adjacent pore bodies. In this study, throats are defined as the interconnecting channels between neighboring pores that control fluid transmission within the pore network. The throat radius was determined from the Otsu multilevel threshold binary segmented image (Figure 7.13a). For the analyzed shale sample, throat radii range from 10 nm to 250 nm (Table 7.3), with the majority of values below 50 nm.

The frequency decreases sharply with increasing throat size (Figure 7.13b), indicating the dominance of fine, nanometer-scale constrictions that may significantly influence permeability and capillary behavior.

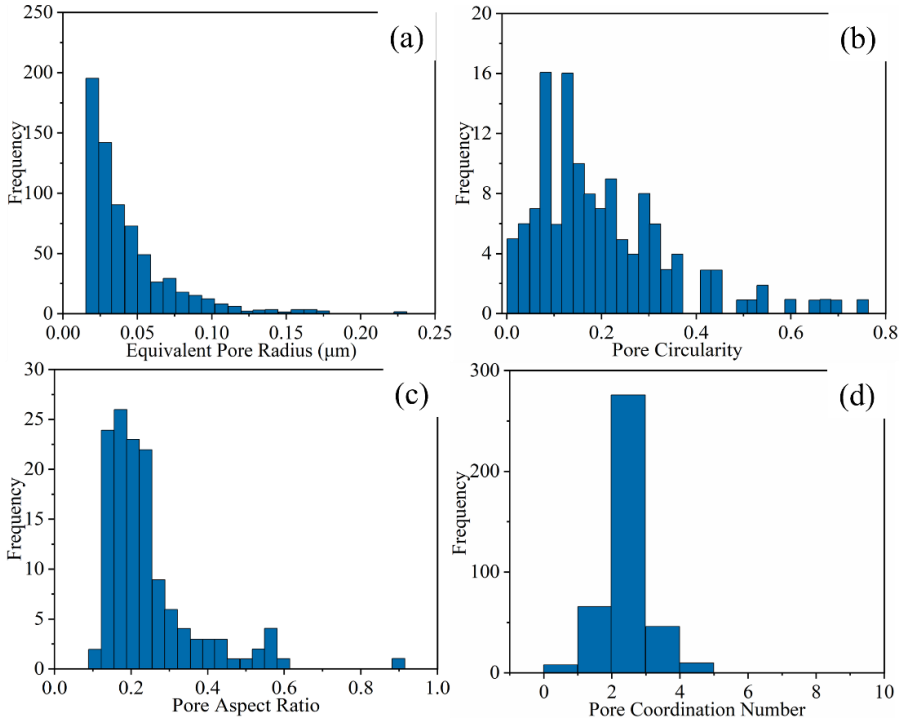

Figure 7.12. *Quantitative statistical results derived from FE-SEM image analysis of the shale sample: (**a**) equivalent pore radius, (**b**) pore circularity, (**c**) pore aspect ratio, and (**d**) pore coordination number.*

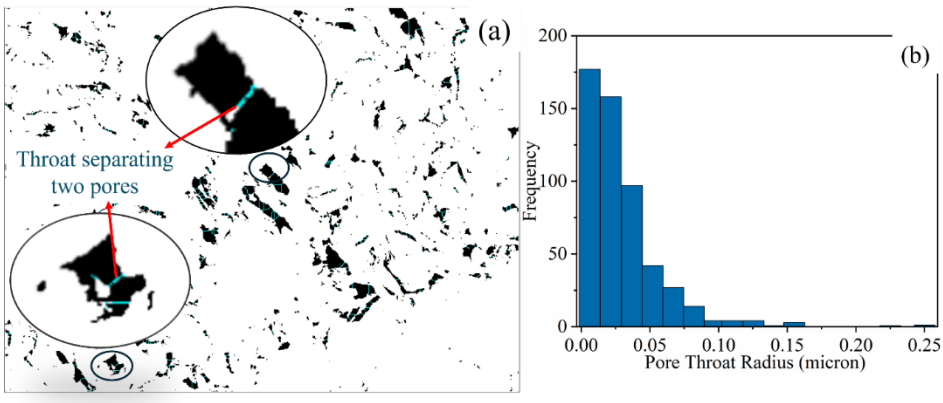

Figure 7.13. *Throat analysis from FE-SEM image processing: (**a**) throat segmentation derived from the binary segmented image, and (**b**) corresponding throat size distribution.*

The geometrical complexity of the pore network was quantified through fractal dimension analysis. Unlike the conventional binary (2D) box-counting method, which accounts only for pore width and length, the DBC method was employed to incorporate variations in grayscale intensity, thereby considering the box height as an additional dimension. In this approach, a 2D grayscale FE-SEM image is treated as a 3D surface, enabling a more realistic estimation of pore complexity and allowing direct comparison with fractal dimensions derived from LPGA and SAXS analyses. In the DBC algorithm, a structured grid of square boxes is superimposed on the image, and the number of boxes required to cover the pore structures is counted at different scales. The fractal dimension (Df) is obtained from the slope of the best-fit line between the total number of boxes (Nε) and the scaling factor (1/ε) on a log-log plot (Figure 7.14), where the scaling factor represents the ratio of the original box size to the total image size. For the analyzed shale FE-SEM image (Figure 7.11a), a strong linear correlation ($R^2 = 0.99$) with a calculated fractal dimension of 2.52 indicates that the pores possess a moderately complex and self-similar structure (Table 7.3).

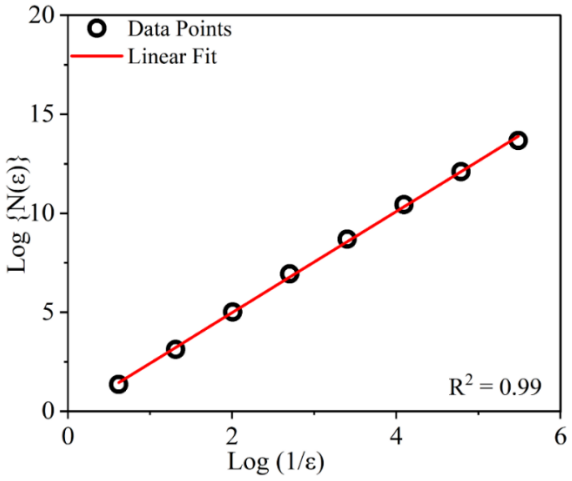

Figure 7.14. *Fractal fitting of the data represented on a log-log plot.*

Table 7.3. *Summary of pore parameters with their respective ranges and average values derived from multiple FE-SEM image analyses.*

Pore Parameter	Range	Average	Remark
Equivalent pore radius	18–255 nm	42 nm	Dominant small nanoscale pores
Pore circularity	0.09–0.24	0.2	Irregular/elongated pores
Pore coordination number	1.25–2.98	1.96	Low/moderate pore connectivity
Pore throat radius	8–250 nm	24 nm	Restrict permeability but contribute to storage capacity
Fractal dimension	2.37–2.61	2.55	Moderate complex structure

7.3.5. Micro-CT analysis

Micro-CT scanning was performed on a representative sub-volume with dimensions of 7.72 mm * 7.72 mm * 5.54 mm (width * height * depth), extracted from a core sample with a diameter of 35 mm. This technique was selected for its capability to characterize macropores larger than 10^3 nm. To achieve a comprehensive multi-scale pore assessment, micro-CT results were integrated with LPGA, SAXS, and FE-SEM analyses. The 16-bit micro-CT images were processed using Dragonfly software (workflow in Figure 7.15). The analysis quantified mean Feret diameter, equivalent spherical diameter, pore volume, and connectivity in terms of connected and total porosity. The mean Feret diameter represents the average of all Feret diameters within a pore or fracture, where each Feret diameter is defined as the distance between two parallel tangents touching the object's projected outline. For irregular shapes, it provides a representative measure of pore size (Maddirala et al., 2024). As shown in Figure 7.16a, the mean Feret diameter ranges from 0.07 mm to 0.62 mm, with a dominant frequency of ~ 99 % at 0.07 mm, rapidly declining to < 0.0001 % as size increases.

The equivalent spherical diameter (Figure 7.16b) exhibits a similar distribution but within a smaller range (0.02–0.24 mm). This is because irregular or elongated voids, when represented as equivalent spheres, yield smaller diameters. The highest frequency (~ 90–95 %) occurs at 0.02 mm, dropping sharply to < 7 % with increasing size. The pore volume distribution (Figure 7.16c) reflects the total void space available for fluid storage

within the rock matrix, a key reservoir property. Nearly the entire measured volume (~ 100 %) corresponds to a pore size of ~ 0.02 mm^3.

Pore connectivity refers to the degree of interlinkage among individual pores within the rock matrix. The 3D reconstructed profiles of connected pores and total pores, along with their few representative orthogonal 2D cross-sections, are shown in Figure 7.17. As shown in Figure 7.17a, the connected pores, particularly near the margins, form continuous pathways extending across the rock volume. However, their distribution is sparse throughout the profile, reflecting the inherently low connectivity typical of shale formations. The connected porosity of the sample is 1.96 %, indicating limited fluid flow pathways. In contrast, the total porosity shown in Figure 7.17b is 4.55 %, which includes both connected and isolated pores.

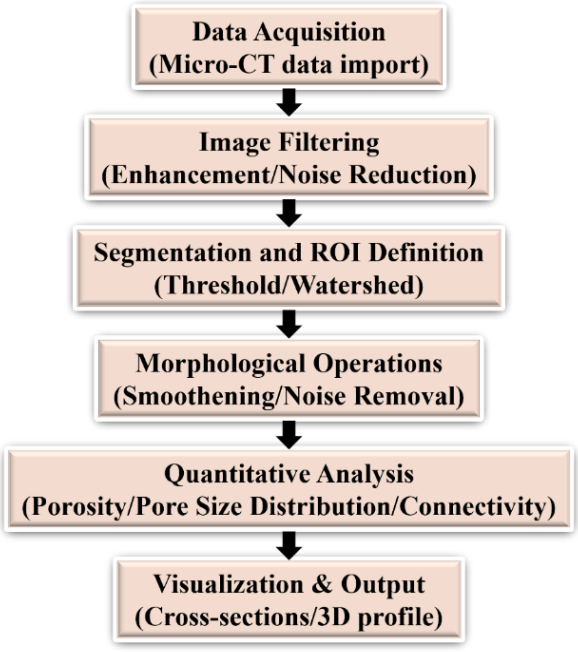

Figure 7.15. *Flowchart illustrating the working principle of the Dragonfly algorithm for micro-CT data analysis.*

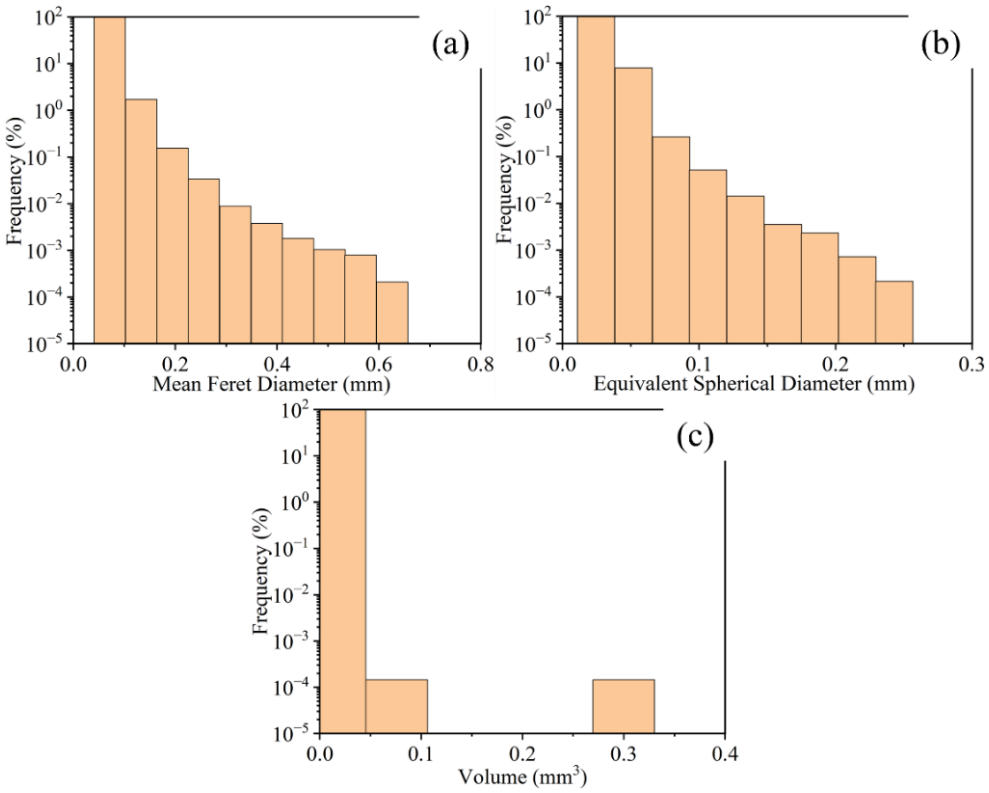

Figure 7.16. *Micro-CT-based quantitative analysis of the shale sample showing: (**a**) mean Feret diameter, (**b**) equivalent spherical diameter, and (**c**) pore volume.*

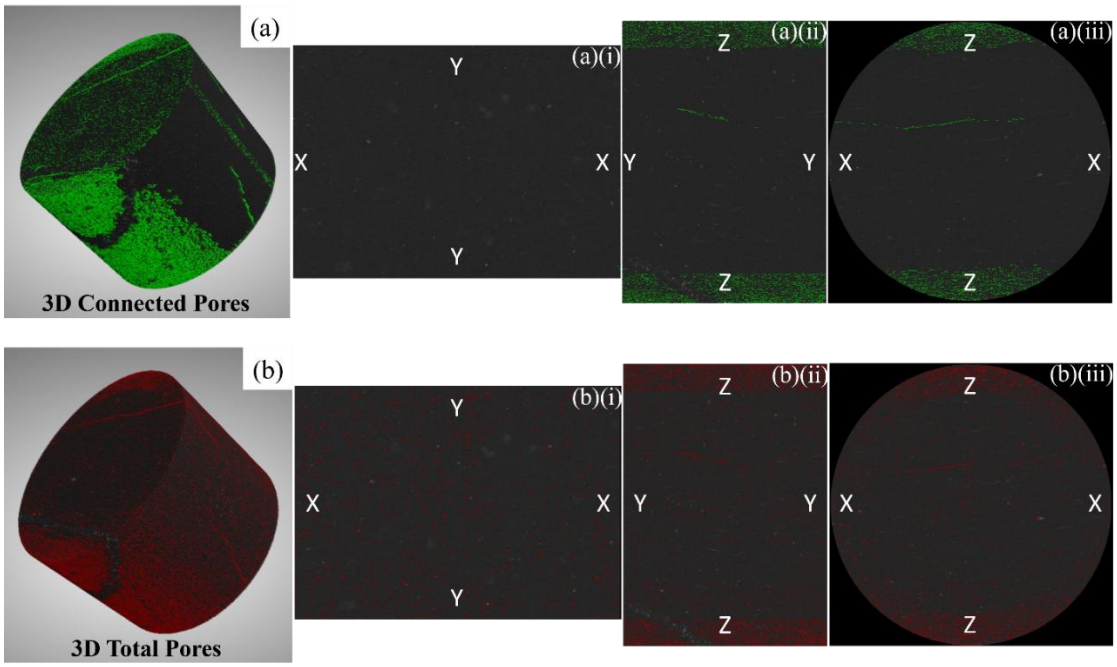

Figure 7.17. *Micro-CT-derived 3D reconstructed profiles of (**a**) connected and (**b**) total pores in the shale sample, along with their few representative orthogonal 2D cross-sections.*

7.4. Discussions

In this study, an integrated approach combining LPGA, SAXS, FE-SEM, and micro-CT analyses was used to characterize the pore structure of Lesser Himalayan shale. Each technique targets a specific pore size range. LPGA effectively characterizes fine micropores to mesopores, while SAXS extends the range to include mesopores and small macropores, capturing both accessible and inaccessible pores. FE-SEM provides detailed images and quantitative data on meso- and macropore geometries, and micro-CT identifies macropores larger than 10^3 nm. When used individually, each method gives only a partial view of the pore network. Therefore, integrating these techniques has allowed a comprehensive understanding of the overall pore system in the Neoproterozoic Krol Formation Shale of the Lesser Himalaya.

7.4.1. Pore System and its Connectivity in the Krol Shale

The pyritic black Krol Shale shows a complex and multi-scale pore system. The pore sizes range from ultra-micropores (< 1 nm) to large macropores (> 10^3 nm). The overall pore network is highly heterogeneous in geometry. The pores have irregular shapes and a hierarchical distribution. Such a structure allows significant gas storage within the rock.

The LPGA results from N_2 and CO_2 adsorption confirm a wide range of pores. The pores extend from ultra-micropores to small macropores. The N_2 adsorption isotherm is of Type IIB (Figure 7.5). This type suggests that the shale mainly contains mesopores, which cause hysteresis. It also includes a few macropores, indicated by the sharp increase in adsorption at a high relative pressure (0.98–1.00 P/Po) and the absence of a plateau (Rouquerol et al., 1998; Kuila and Prasad, 2013). Type IIB isotherms usually show low adsorption capacity at low relative pressure. The adsorption capacity increases rapidly at

pressures above 0.8 P/Po. Within the mesopores, multilayer adsorption and capillary condensation occur. Interactions between the gas molecules and the pore walls drive these processes. The interaction between gas molecules also contributes. This leads to gas condensation into a liquid-like phase at a pressure lower than the bulk saturation pressure (Po) (Vishal et al., 2019). The H3 hysteresis loop identified in the N_2 isotherm indicates slit-shaped and wedge-shaped pores. Such pores are typical of non-rigid, plate-like aggregates commonly found in clay minerals. These slit-shaped pores are visible in the FE-SEM image (Figure 7.10). The presence of a significant proportion of clay minerals is confirmed by FTIR and XRD analyses (Figures 7.18 and 7.19). In the FTIR spectra, O-H stretching vibrations between 3700 and 3500 cm^{-1} indicate the presence of clay minerals. The XRD pattern shows a strong intensity peak at $2\theta = 19.8°$, confirming the presence of illite. Semi-quantitative XRD analysis indicates that clay minerals account for about 17 % of the shale. In addition to clay minerals, FTIR spectra also aid in identifying kerogen. Absorbance bands between 3000 and 2800 cm^{-1} correspond to aliphatic C-H stretching, confirming the presence of kerogen. Kuila (2013) stated that clay minerals contribute most to shale's total porosity. The open hysteresis loop at low P/Po further supports this. The incomplete closure of the loop is due to the swelling behavior of clay minerals (Cao et al., 2020). In the case of CO_2 adsorption, the isotherm is of Type I. It shows a steep rise in adsorbed volume at very low P/Po. This indicates strong interactions between the adsorbent and adsorptive within ultra-micropores (< 1 nm). It also suggests micropore filling during the initial stage of adsorption (Chandra et al., 2022). The Type I isotherm confirms the presence of micropores (Clarkson et al., 2013; Rani et al., 2020). Unlike N_2 adsorption, the CO_2 isotherm shows no pronounced hysteresis. This is because CO_2 molecules are smaller in kinetic diameter. They interact more strongly with the pore surfaces and effectively probe ultra-micropores (< 1 nm).

PSD analysis reveals a complex pattern. The distribution is bimodal in the BJH model for N_2 and multimodal in the DFT model for N_2 and CO_2. The PSD peaks occur mainly within the micro- and mesopore ranges. These pores contribute most to the total pore volume and surface area of the shale. According to Wang et al. (2014), shale PSDs are often bimodal or multimodal. Pore volume is mainly controlled by micro- and mesopores. Tian et al. (2013) and Nilankar et al. (2024b) also reported that smaller pores control the specific surface area. Li et al. (2016) further noted that most micropores are hosted within the organic matter of shale.

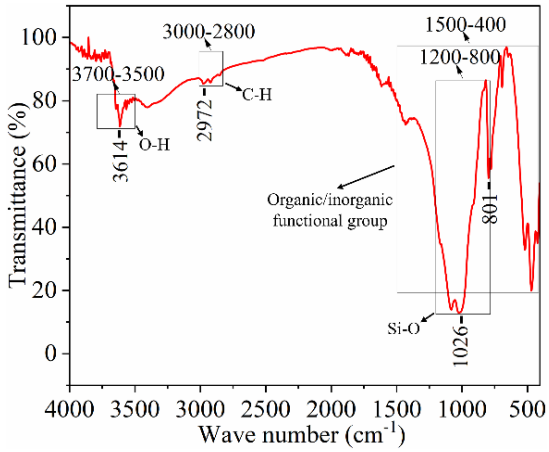

Figure 7.18. *Representative FTIR spectra of the Lesser Himalayan Krol Shale.*

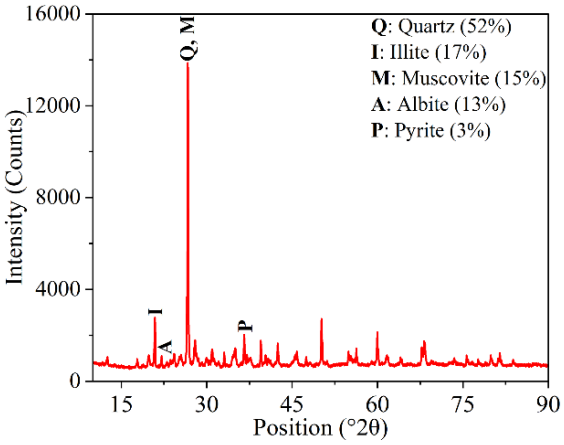

Figure 7.19. *Representative XRD pattern of Lesser Himalayan Krol Shale.*

The SAXS analysis provided useful information about the pore system of the shale samples. The 2D SAXS pattern (Figure 7.7) is isotropic and evenly distributed. The intensity gradually decreases from the center outward. This indicates that the pores are randomly oriented and vary from fine to coarse sizes. Similar results were also reported by Chandra et al. (2020a) for shale samples. SAXS cannot effectively detect micropores. However, PSD shows that mesopores are dominant in the samples. These mesopores are the main contributors to the overall storage capacity. Their dominance also reflects the shale's high adsorption potential. This is further supported by the LPGA results (Figure 7.6). In the LPGA curves, multilayer adsorption and capillary condensation within mesopores play a major role in gas storage. Chandra et al. (2022) also observed a similar trend. They reported an increase in pore volume with increasing pore size based on both SAXS and LPGA-derived PSD curves.

The FE-SEM-based image analysis provided critical insights into the pore system and its influence on storage and fluid flow behavior. The dominance of small nanoscale pores, mostly below 50 nm, reflects the characteristic feature of organic-rich shale. In such rocks, gas molecules are preferentially retained within confined nanoscale domains rather than in free pore spaces. The pore geometry, including circularity, aspect ratio, coordination number, and throat radius, reveals a highly heterogeneous and anisotropic pore network. The low circularity and aspect ratio indicate that most pores are irregular and elongated instead of equidimensional. Similar observations were reported by Jiang et al. (2024), who demonstrated that elongated pores are the dominant pore type in shale based on quantitative FE-SEM analysis. The FE-SEM image analysis supports these quantitative findings (Figure 7.12). The phyllosilicate framework of micaceous minerals, mainly illite, controls the development of elongated and subparallel pore structures (Chukwuma et al., 2018). Curtis et al. (2012) also emphasized that pores associated with

sheet-like phyllosilicate minerals form interconnected pore networks. The coordination number suggests low to moderate pore connectivity in the studied shale. This indicates that while isolated pores enhance gas storage, only a limited fraction of pores actively contribute to fluid migration. The small throat radius, mostly below 50 nm (Table 7.3), further signifies restricted fluid permeability. Overall, the irregular pore geometry and low connectivity contribute to the shale's heterogeneous, anisotropic nature.

The micro-CT analysis is particularly valuable for shale samples. While most fluid storage occurs within nanoscale pores, fluid flow is mainly controlled by large macropores and fractures. These features can only be captured through micro-CT imaging. Micropores and mesopores primarily store gas, whereas macropores facilitate gas drainage (Mazumder et al., 2026). Gou et al. (2019) pointed out that most pore structure studies in shale have focused on the nano to submicron scale. In contrast, the role of larger pores and fractures in the overall pore system has received limited attention. Despite differences in pore-size measurement ranges, the equivalent spherical diameter histogram from micro-CT analysis shows a dominance of irregular and elongated pores. This trend agrees well with the LPGA, SAXS, and FE-SEM results. Pore volume distribution is another key parameter that controls the fluid storage capacity of shale. Most of the total pore volume is concentrated in voids around 0.02 mm^3. This indicates that fine microfractures contribute significantly to the total pore volume. In addition to these microfractures, some macropores also contribute to fluid storage. Loucks et al. (2012) reported that with increasing thermal maturity, many smaller pores merge, resulting in a higher overall macropore volume. The 3D micro-CT profile in Figure 7.17 shows that some pores, especially those near the margins, are interconnected and form continuous pathways across the rock. However, most pores remain isolated. The connected porosity is only 1.96 %, confined mainly to the margins due to fine microfractures seen in the 3D

image. Similar low pore connectivity has been reported for other shale formations worldwide (Lan et al., 2015; Davudov et al., 2020). Wang et al. (2018) in their micro-CT study also stated that black shale typically possesses extremely low permeability (< 100 millidarcy) and low porosity (< 10 %). The higher total porosity (4.55 %) compared to the connected porosity in this study indicates that many pores act as isolated storage sites with limited fluid-flow pathways.

The total porosity of the samples was also measured using SAXS (4.98 %) and FE-SEM (5.64 %) analyses, along with micro-CT (Figure 7.20), providing a comprehensive evaluation of porosity in the Krol Shale. Similar porosity ranges have been reported for other shale formations by various researchers, using different analytical techniques (Nilankar et al., 2024b; Wang et al., 2025b). This consistency highlights the strength of a multi-analytical approach for characterizing the pore system in shale reservoirs.

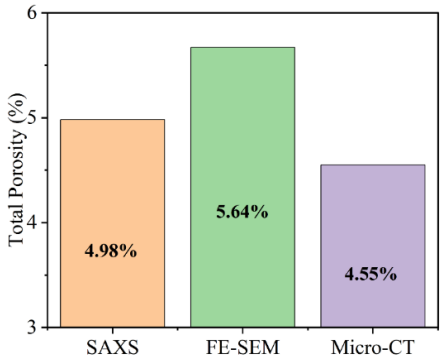

Figure 7.20. *Total Porosity in the studied shale from SAXS, FE-SEM, and micro-CT analyses.*

7.4.2. Comparison between Lesser Himalayan Krol Shale and other Explored Shale Basins

The geochemical and pore structure parameters indicate that the studied Himalayan shale (HS) from Krol Formation exhibits very close similarities with

previously explored shales from different basins of India, such as the Cambay Basin Shale (CBS), Raniganj Basin Shale (RBS), and Krishna-Godavari Basin Shale (KGBS) (Figure 7.21). Although the TOC wt % of the HS is lower than that of the RBS and KGBS, it is significantly higher than that of the CBS. The moderate TOC content thus reflects a fair degree of organic richness in the Krol Shale, which is essential for hydrocarbon generation. The high vitrinite reflectance and Type III kerogen indicate that the HS is a potential gas reservoir compared to other oil-prone shales. The pore characteristics of HS also show significant similarities to those of other shales. The LPGA showing a Type IIB isotherm curve is similar to the RBS isotherm, while CBS shows a Type II isotherm curve, and KGBS shows a Type IV isotherm curve. The Type IIB curve indicates the dominance of slit-shaped pores, which facilitates significant gas storage. The fractal dimension of HS is highly comparable to other shales, all of which show a moderately complex nature of the pore. This comparative study suggests that HS has a promising gas-generating capacity.

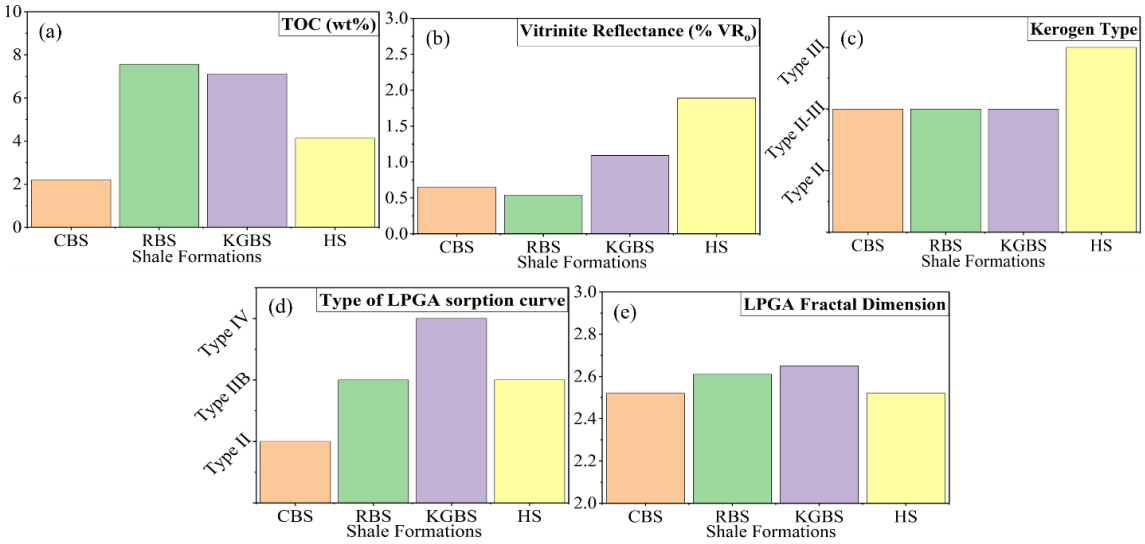

Figure 7.21. *Comparison of the characteristic properties: (**a**) TOC, (**b**) vitrinite reflectance, (**c**) kerogen type, (**d**) type of LPGA sorption curve, and (**e**) LPGA fractal dimension, of the untapped Lesser Himalayan Krol Shale with previously explored potential shale basins of India.*

7.4.3. Implications of this Study for Enhanced Gas Recovery with CO2 Sequestration

The pore system of shale governs gas storage, transport, and long-term retention behavior. The integrated pore characterization in this study provides a comprehensive understanding of the thermally matured Krol Shale of the Lesser Himalaya, which is critical for Enhanced Gas Recovery (EGR) and CO_2 sequestration applications. The multiscale pore system characterization, encompassing micropores (< 1 nm) to macropores (> 10^3 nm), reveals key insights into the storage and migration mechanisms of gas molecules. Pores within shale act as both storage domains and flow pathways, thereby controlling the overall gas production efficiency (Darabi et al., 2012). The predominance of micaceous minerals with elongated, slit-shaped pores enhances the sorptive capacity and diffusion behavior. The extensive development of the Krol Formation, stretching from Solan (Himachal Pradesh) to Nainital (Uttarakhand), represents a geologically significant unit for possible shale gas generation. Despite its thickness and organic richness, this black shale remains largely underexplored compared to other Indian basins. A systematic evaluation of its pore attributes can contribute meaningfully to the energy security framework of the country. The pore network characterization undertaken in this study is not only applicable for assessing methane storage and flow behavior but also demonstrates the feasibility of CO_2 sequestration. Carbon sequestration has emerged as a key technological intervention to mitigate atmospheric CO_2 concentrations (Rani et al., 2020; Shaw and Mukherjee, 2022). Nuttall et al. (2005) reported that CO_2 injection in unconventional reservoirs such as shale can synergistically enhance methane recovery while achieving permanent CO_2 storage. In this dual process, the dense and highly adsorptive CO_2 molecules preferentially occupy adsorption sites within nanopores, effectively displacing the pre-adsorbed methane. This exchange enhances methane recovery and concurrently traps CO_2 within the shale matrix.

A schematic representation of this process is illustrated in Figure 7.22. The Himalayan shale formations offer several advantages for CO_2 sequestration. Their complex pore network system with multiple structural and stratigraphic traps suggests a significant storage capacity. Additionally, the low-temperature climatic regime of the region minimizes geochemical reactivity, thereby promoting the long-term stability of the sequestered CO_2. In general, this study highlights the dual significance of the Krol Shale as both a promising gas formation and a potential CO_2 storage reservoir. Findings from this study provide critical insights for future exploitation strategies aimed at achieving sustainable gas production coupled with carbon management in the Himalayan basin.

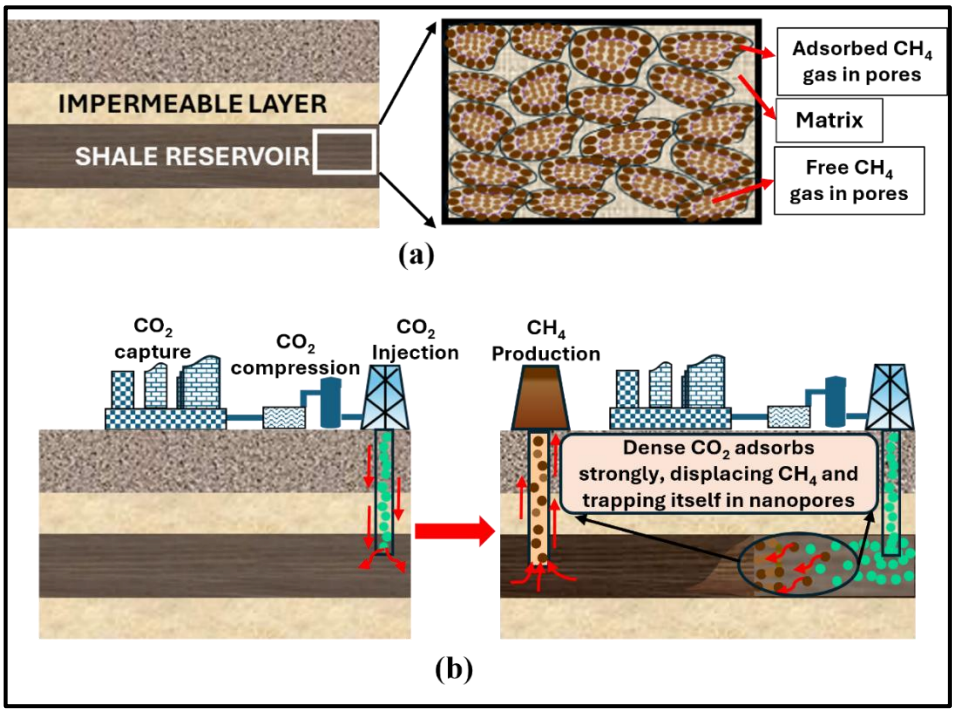

Figure 7.22. *Schematic illustration* ***(a)*** *adsorbed/free gas in pores of shale and* ***(b)*** *enhanced gas recovery coupled with CO_2 sequestration.*

7.5. Summary

The pore network system, defined by Pore Size Distribution (PSD), geometry, and connectivity, plays a crucial role in controlling the storage and transport behavior of shale

gas. Despite extensive investigations of shale formations across various Indian basins, pore characterization studies in the Lesser Himalaya remain largely unexplored. In particular, the Neoproterozoic Krol Shale from the northwestern Lesser Himalaya represents one of the untapped units with promising gas-bearing characteristics. In this study, shale samples from the Krol Formation were systematically analyzed for pore characteristics across nano- to macroscales using a combination of LPGA with N_2 and CO_2, SAXS, FE-SEM, and Micro-Computed Tomography (Micro-CT). LPGA N_2 adsorption exhibited Type IIB isotherms with H3 hysteresis loops, indicating slit- and wedge-shaped mesopores, while CO_2 adsorption revealed Type I isotherms, reflecting micropore filling. PSD derived from LPGA showed bimodal and multimodal patterns using Barrett-Joyner-Halenda (BJH) and Density Functional Theory (DFT) models, respectively. SAXS, sensitive to both open and closed pores, effectively captured the PSD, and the Porod-Debye Scattering Profile (PDSP) model confirmed the dominance of mesopores. FE-SEM observations revealed irregular to elongated nanopores (37–54 nm) and a moderately complex pore structure, as supported by fractal dimensions derived from LPGA, SAXS, and FE-SEM. Micro-CT analysis further indicated the presence of macropores and fractures ($\geq 10^3$ nm), with a mean Feret diameter of 0.07 mm and a pore volume of 0.02 mm^3. Porosity values estimated from SAXS, FE-SEM, and micro-CT were 4.98 %, 5.64 %, and 4.55 %, respectively. This integrated multiscale characterization, bridging nano to macroscale pore systems, provides new insights into the storage and transport behavior of gas and emphasizes the Krol Shale as a future shale gas formation in the Lesser Himalaya.

Chapter: 8
Multiscale Characterization of Pore Evolution in Lesser Himalayan Black Shale from Krol Formation under Oxic Thermal Heating: Relevance to Untapped Shale Gas Extraction

8.1. Introduction

Shale gas holds considerable potential as an unconventional energy source, yet it has received less attention compared to other alternatives like solar, wind, and biofuels. However, advancements in extraction technologies can highlight its untapped potential. Intricate pore network systems and fluid flow mechanisms in shale play a key role in storing and transporting fluids, which govern its fluid storage and transport behavior. These characteristics directly influence their capacity to store hydrocarbons or CO2 sequestration (Chen et al., 2016; Deng et al., 2016; Ji et al., 2016; Bai et al., 2019; Chandra et al., 2021). Developing and utilizing these unconventional energy sources could strengthen global energy security and advance energy diversification to reduce dependency on fossil fuels (Wang and Li, 2017; Nilankar et al., 2024a).

The pore system encompassing factors such as pore size, shape, connectivity, roughness, and adsorption-desorption capacity (Figure 8.1) forms the fundamental framework driving the processes of shale gas development, storage, and production (Mishra et al., 2018). Abundant nanoscale pores play a vital role in governing gas migration and transport within the shale. These pores include micropores (pore width < 2 nm) and mesopores (pore width 2–50 nm), which are predominant within the shale matrix (Kuila and Prasad, 2013). Gas is stored in three distinct phases in the shale: (1) as free gas within the micropores, (2) as adsorbed gas on the surfaces of organic matter and minerals, and (3) as dissolved gas within organic matter and minerals (Boruah et al., 2019; Huang et al., 2020). Among these, Bowker (2003) emphasized that the free gas phase represents the primary storage form of shale gas. Although extracting gas from shale

formations is challenging, numerous techniques have been developed to enhance recovery.

Conventional hydraulic fracturing relies on water and chemicals to create fractures for gas recovery, which can have significant environmental impacts. As an alternative, researchers have proposed thermal treatment techniques to improve gas recovery from shale reservoirs (Chen et al., 2016). Shale being a water-sensitive formation, the thermal treatment technique is highly preferable over others. Jamaluddin et al. (2000) noted that thermal treatment results in the vaporization of capillary-blocked water, which causes the dehydration of clay-bound water and damages the lattice structure of clay, ultimately producing thermally induced microfractures. Thermal stimulation involves both pyrolysis and combustion, and extensive global research utilizing multiple approaches has been carried out to understand the effects of pyrolysis on the pore structure of shales (Tiwari et al., 2013; Chen and Xiao, 2014; Sun et al., 2015; Bai et al., 2017; Chandra et al., 2021; Lei et al., 2021; Zhang et al., 2023; Zhuoke et al., 2023; Hazra et al., 2024). However, the impact of combustion-induced processes remains relatively underexplored, with only a few studies available (Chen et al., 2017; Chen et al., 2018; Cao et al., 2020; Chandra et al., 2021; Hazra et al., 2023).

Given the potential of combustion-driven thermal alterations in enhancing shale pore structures, further investigation is essential to bridge the knowledge gap and optimize shale gas recovery strategies. Combustion leads to the oxidation of kerogen, thereby causing the bitumen to burn fast and resulting in the opening of small and isolated pores and the development of new pores. At the same time, pyrolysis preserves the bitumen for a longer time, resulting in the blocking up of pores (Chandra et al., 2021). Chen et al. (2017) and Chen et al. (2018) studied the effects of low- and high-temperature combustion on shale. They reported that thermal treatment promotes gas desorption from

pores, enhances permeability, and induces fractures through thermal effects, thereby improving recovery.

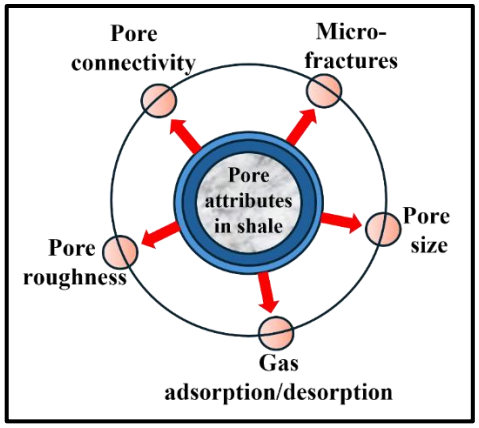

Figure 8.1. *A schematic representation of the pore attributes in shale.*

Over the past few decades, shales from various regions worldwide have been characterized through combustion techniques to enhance gas and oil recovery (Chen et al., 2017; Chen et al., 2018; Cao et al., 2020; Chandra et al., 2021; Hazra et al., 2023). Chen et al. (2017) conducted low-pressure N_2 adsorption and FE-SEM analyses on shale combusted at 800 °C. Their results showed a gradual increase in average pore diameter and pore size, accompanied by an increase in the volume of larger pores. In a subsequent study, Chen et al. (2018) observed a reduction in surface area through low-pressure N_2 adsorption when shale was combusted at 500 °C. Similarly, Cao et al. (2020) reported that combustion at 450 °C led to the oxidation of organic matter, resulting in the development of mesopores and macropores due to the enlargement of organic matter pores. Chandra et al. (2021) observed decreased average pore diameter and increased pore volume and surface area as the combustion temperature was raised to 300 °C. Furthermore, Hazra et al. (2023) highlighted that higher combustion temperatures

reduced the discernibility between mineral and organic matter while also driving significant evolution in pore structures.

Existing literature states that combustion alters shale's pore characteristics and surface morphology. Still, the extent and nature of the alteration depend strongly on the composition and internal structure of specific shale formations. The highly heterogeneous nature of shale suggests that there is a need for a thorough investigation of the individual formation that may facilitate gas recovery because even within the same reservoir, accurate assessment of shale characteristics is a challenging task due to its highly heterogeneous behavior (Mevawala et al., 2019).

In the Indian context, despite the significant shale gas potential, only a few studies have been conducted to understand the effect of combustion on the characteristic behavior of shale for enhanced gas recovery (Kar et al., 2022). Furthermore, the existing research has been limited to a few regions, primarily the Raniganj Basin of the Lower Gondwana sequence and the Bikaner-Nagaur Basin in Rajasthan. However, numerous shale formations across India remain inadequately explored, potentially holding substantial gas reserves. One such notable sequence of shale formation belonging to the Proterozoic age lies in the Lesser Himalayan region, within the Infra-Krol, Krol, and Tal formations, extending from Solan in the west to Nainital in the east, with exposures in and around Solan, Mussoorie, Garhwal, and Nainital.

Himalaya is known for its complex geological structures and diverse rock types, including igneous, sedimentary, and metamorphic rocks. One such rock type, i.e., black shale of Krol Formation and Infra Krol Formation, has received relatively little attention over time, primarily due to the challenges associated with their exploration. Black shale formations hold significant importance in shale gas, typically in the deep marine and lacustrine settings. However, Himalayan black shales remain underexplored compared to

similar formations in other Indian regions. This is primarily due to their inaccessibility and heterogeneous composition. A deeper understanding of their organic matter content, thermal maturity, and microstructural characteristics is essential for evaluating their energy resource potential. Evaluating pore systems in black shales, particularly those found in the Himalayan region, is critical for understanding their potential as unconventional energy resources and their suitability for geological carbon storage.

In recent years, only a few studies have assessed the source rock potential of black shales in the Himalayan region. Preliminary investigations suggest that the black shales of the Subathu Formation have the potential to generate dry gas (Hafiz et al., 2022). Mani et al. (2014) examined the shale gas potential of Proterozoic and Phanerozoic shales in the NW Himalaya, concluding that the region possesses minimal gas resources due to low total organic carbon (TOC) content and unfavorable Rock-Eval parameters, including S_1, S_2, and hydrogen index (HI). Similarly, Pandey et al. (2018) evaluated the hydrocarbon potential of carbonaceous shales from the Spiti and Chikkim Formations in the Tethys Himalaya. Their experimental investigations revealed the presence of methane as both free and fixed hydrocarbons, with findings further supported by Fourier Transform Infrared Spectroscopy (FTIR) and Nuclear Magnetic Resonance (NMR) studies. Therefore, comprehensive characterization of black shales in the Himalayan region is essential to assess shale gas potential and suitability for gas extraction.

In this study, block samples of shale from the Neoproterozoic Krol Formation were collected from the Kaudiyala area in the Garhwal region of Uttarakhand for thermal treatment (combustion) to determine the optimal temperature strategy for enhanced gas recovery. Based on Thermogravimetric Analysis (TGA), a maximum combustion temperature of 400 °C was selected, as mass loss beyond this point showed a sharp decline, indicating significant alteration in the shale's fundamental properties. After

thermal treatment, the shale samples were characterized for pore-scale structural evaluation using two advanced analytical techniques: Low-Pressure Gas Adsorption (LPGA) through the fluid-injection technique and Small Angle X-ray Scattering (SAXS) through the non-injection technique. Additionally, Field Emission Scanning Electron Microscopy (FE-SEM) provided microscopic imaging to support the pore-scale structural evaluation further.

8.2. Experimental Procedures

8.2.1. Sample Preparation

Total eight block samples of Krol Shale, collected from the study area (Figure 2.2) described in Section 2.2 of Chapter 2, were initially analyzed in the lab using techniques such as TOC and XRD to confirm their lithology and nature of the Krol Shale. Subsequently, portions from each collected block were combined and homogenized using the conning and quartering method to create a representative bulk sample. This approach ensured the sample was uniform and representative of the overall formation. The representative bulk sample was further powdered to < 75 µm for analysis, including LPGA, SAXS, TGA, and X-ray Diffraction (XRD). FE-SEM analyses were performed on chip samples of thickness 5 mm prepared from each block.

The combustion of shale was carried out in an electric muffle furnace at various temperatures: 25 °C (room temperature), 100 °C, 200 °C, 300 °C, and 400 °C. Both powder and chip samples were maintained at each temperature for four hours. The heating rate was set at 10 °C per minute until the target temperature was reached. After combustion, the samples were cooled within the furnace at the same rate of 10 °C per minute until they returned to room temperature. Maintaining consistent heating and

cooling rates ensured uniform thermal decomposition and prevented shocks. Figure 8.2 illustrates the schematic of the methodology adopted in this study.

8.2.2. Shale Petrography

The shale samples were mounted for petrographic analysis, including maceral identification, mineral matter assessment, vitrinite reflectance measurements, and photomicrograph documentation. Samples were prepared using one mm-sized particles embedded in an epoxy resin and hardener mixture. Petrological investigations were conducted using a Leica DM 4500P polarizing microscope under monochromatic and UV-reflected light, with 50x oil immersion objectives. Vitrinite reflectance measurements were performed using a J&M TIDAS photometer integrated with MSP 200 software.

8.2.3. LPGA analysis

To characterize the pores of Lesser Himalayan shale subjected to thermal treatment, low-pressure N_2 adsorption (LPGA) techniques were employed. LPGA analyses were conducted on 0.5–2 g powdered samples using the MicrotracBEL BELSORP Max II (Figure 8.2). Thermally treatment often leads to the formation and expansion of pores and fractures, making N_2 adsorption highly suitable for LPGA analyses. Kuila and Prasad (2013) also emphasized that nitrogen adsorption is the most effective and widely used gas for shale and clay pore characterization.

Isotherms were obtained at an ultra-low operating temperature of -194 °C, with relative pressure (P/P_0) ranging from 0.001 to 1. Initially, the samples were degassed at 100 °C before analysis. PSD was analyzed using the Barrett-Joyner-Halenda (BJH) model, the most commonly applied model in LPGA analyses for shale (Kuila and Prasad, 2013; Boruah et al., 2019; Chandra et al., 2021; Zhang et al., 2023; Zhuoke et al., 2023). Fractal geometry parameters were employed to assess pore irregularity, as they provide

an efficient and widely used tool for pore characterization (Mandelbrot and Wheeler, 1983). This study specifically utilized the Frenkel-Halsey-Hill (FHH) model, based on the gas adsorption technique established by Avnir and Jaroniec to determine fractal dimension characteristics (Avnir and Jaroniec, 1989).

8.2.4. SAXS analysis

SAXS analyses were performed using 0.1–1.0 g powder samples in XENOCS, Xuess 3.0 HR apparatus (Figure 8.2). Further, the powder samples were packed with Kapton tape and mounted over the sample holder with a sample-to-detector distance of ~ 1.5 m, and the profile was recorded. The measurements were conducted using a 30 W Cu X-ray source paired with a Pilatus 300K 1M hybrid pixel detector with single photon counting capability. Raw data in intensity (I(Q)) as a function of Q was recorded. Here, Q is the scattering vector equal to $4\pi\sin\theta/\lambda$, where λ is the wavelength of the X-rays and θ is half of the total scattering angle. In this experiment, Q ranges between 0.0001 $Å^{-1}$ to 0.181 $Å^{-1}$. The data was processed using XSACT software, and after performing background correction and noise removal, the pore attributes were computed using MATSAS, a MATLAB-based code (Rezaeyan et al., 2021). The Porod-Debye Scattering Profile (PDSP) model has been used to calculate the PSD, the most suitable model for the particles within shale (Chandra et al., 2020a). The fractal dimension is also computed to understand the irregularity/surface roughness in pores. In this investigation, SAXS served as a crucial tool for studying the structure of shale at the nanoscale (meso to macro) level, where thermal heating has resulted in an expansion of pre-existing pores along with the development of newer ones.

Chandra et al. (2023) emphasized that the SAXS technique, which utilizes X-ray scattering in the small-angle regime to account for the heterogeneous nature of pores, is

better suited for characterizing shale pores than imaging and adsorption methods. This approach provides a more realistic representation of the pore structure. Additionally, they noted that the SAXS-derived fractal dimension ("Dsaxs") is influenced by pore surface roughness, similar to the fractal dimension obtained from LPGA.

8.2.5. FE-SEM analysis

The morphology of thermally treated shale was assessed through JEOL JSM-7900F FE-SEM analyses. Under thermal treatment, this analysis becomes crucial to investigate the changes in the surficial features, including pore size and shape, along with the changes in the organic matter and boundaries of minerals (Nilankar et al., 2024a). Chip samples were dried and Au-coated to enhance the surface conductivity for better resolution and imaging. The operating voltage of 5 keV and the working distance of ~ 10 mm were used to obtain the images. Using FE-SEM analysis, a quantitative characterization of pore structure is possible when high-resolution images at the microscopic level are combined with the statistical analysis method (Fredrich et al., 1995; Vishal et al., 2019). Within the sample, the area/region with poor conductivity is represented by darker pixels, such as pore spaces and organic matter. In comparison, those areas/regions possessing better conductivity are represented by brighter pixels, such as mineral matters within shale (Chandra et al., 2023).

8.2.6. TGA analysis

Analyzing kinetics through a decrease in mass with increasing temperature during combustion is useful in characterizing the thermal behavior of shale, particularly in terms of its organic and inorganic matters. The thermogravimetric analytical technique was adopted for combustion kinetics using the Linseis TGA, PT1000 model (Figure 8.2). A

quantity of 16–20 mg of untreated powder samples was heated up to 550 °C in the presence of air at the rate of 10 °C min^{-1} with a precision of ± 0.1 °C.

8.2.7. X-ray diffraction (XRD)

The mineralogical changes in the thermally treated shale were performed using an Empyrean Panalytical X-ray Diffraction (XRD) apparatus (Figure 8.2). Around 2–4 mg of treated powder samples were taken to obtain the diffractogram. The apparatus has a monochromatic X-ray source with a maximum operating voltage of 60 kV. The intensity peaks were measured within the 2θ range of 10° to 90° at a scan step size of 0.0131° sec^{-1}. The semiquantitative mineralogical analysis of the untreated shale was performed using the Rietveld refinement technique in PANanalytical X-pert HighScore software (version 4023 000 04613, 2020).

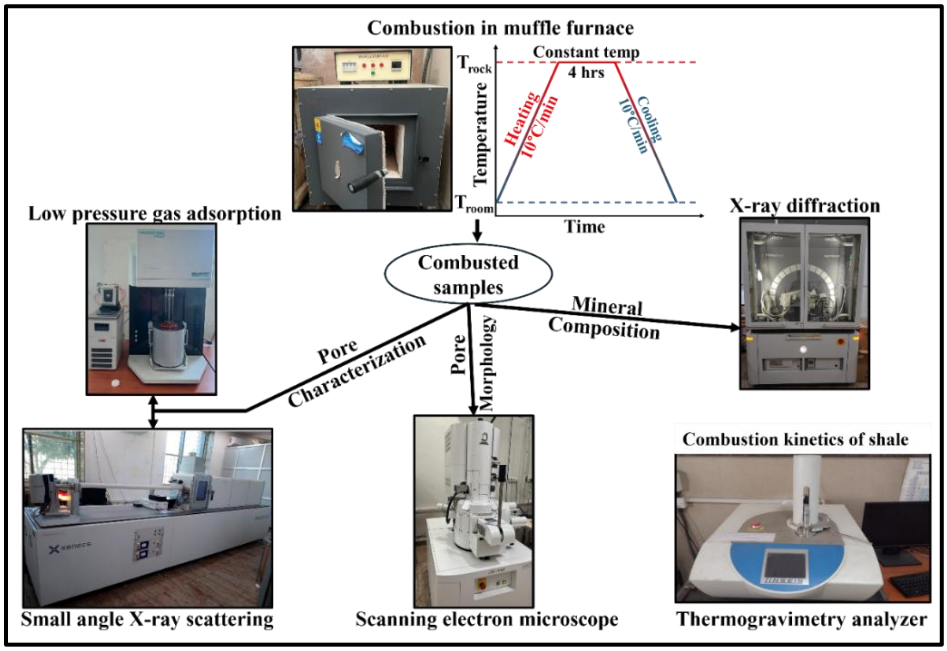

Figure 8.2. *A flowchart illustrating the detailed experimental procedure followed in this study.*

8.3. Results

8.3.1. Petrographic Characterization and TOC analysis

The Neoproterozoic black shale subjected to combustion primarily aimed at finding out pore structure evolution for enhanced recovery. Before the thermal treatment, it is essential to understand the initial geochemical properties of the samples. Figure 8.3 represents the vitrinite reflectance (% VR_o) *vs.* total organic carbon (TOC) plot showing the thermal maturity of the Lesser Himalayan shale to understand the critical insights into their potential for hydrocarbon generation and suitability for extraction. The results of the vitrinite reflectance range between 1.51 and 2.01, indicating that the study area's shale constitutes a gas-prone kerogen based on the Dow (1977) standard classification (Table 8.1). The average % VR_o shows that the specimen lies in the wet gas region and at the boundary of wet-to-dry regions. In contrast, the TOC within the samples indicated the presence of sufficient organic matter for hydrocarbon generation.

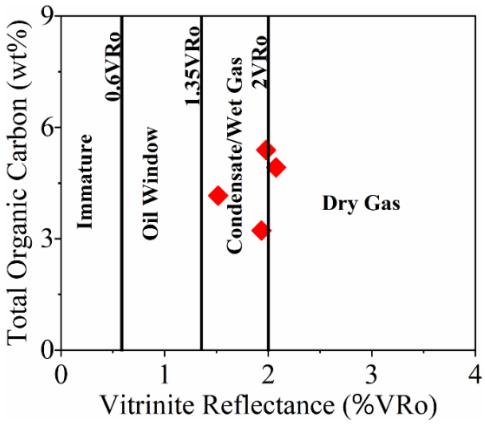

Figure 8.3. *Geochemical analysis based on Total organic carbon (TOC) vs. vitrinite reflectance (% VRo) showing thermal maturity of shale.*

Table 8.1. *Hydrocarbon generation potential and maturity classification scheme after Dow (1977).*

Oil Prone Generation		**Gas Prone Generation**	
Generation Stage	VR_o (%)	Generation Stage	VR_o (%)
Immature	< 0.6	Immature	< 0.8
Early oil	0.6–0.8	Early gas	0.8–1.2
Peak oil	0.8–1.0	Peak gas	1.2–2.0
Late oil	1.0–1.35	Late gas	➢ 2.0
Wet gas	1.35–2		
Dry gas	➢ 2.0		

To further understand the nature of shale, a petrographic analysis was conducted to identify the organic matter and kerogen types present in the samples (Figure 8.4). The petrographic images predominantly show vitrinite (Figures 8.4a, b), with evidence of thermal alteration (Figures 8.4g, i), often coated with pyrite (Figure 8.4h) or occasionally encased within pyrite (Figure 8.4e). Pyrite and clay minerals dominate among the mineral components, while liptinite and inertinite macerals are rarely observed or absent. Microscopic examination reveals a groundmass primarily composed of clay, with grey to yellowish-grey patches representing vitrinite. Pyrite appears golden, with highly reflective patches (Figure 8.4d) and framboidal pyrite (Figure 8.4f), characterized by its granular, rounded structure. Consequently, geochemical analysis, supported by petrography and TOC data, highlights the hydrocarbon potential of the shale. The findings place it within the gas window zone, indicating its viability as a source rock.

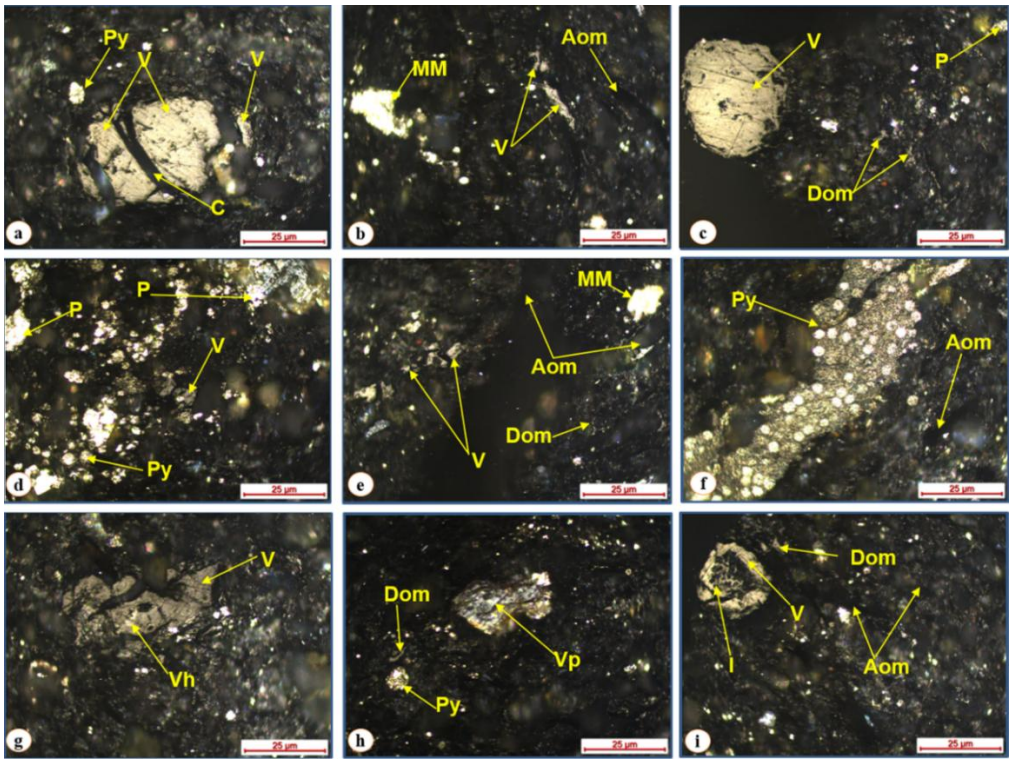

Figure 8.4. *Petrographic images of the studied shale samples: (**a**) showing vitrinite grain with oxidation crack, (**b**) vitrodetrinite-a small fragment of vitrinite with mineral matter and AOM, (**c**) rounded vitrinite pach with fine pyrite grains and DOM, (**d**) massive pyrite with fine pyrite grains, (**e**) vitrodetrinite, carbonate mineral and AOM, (**f**) framboidal pyrite, (**g**) vitrinite grain showing alternation due to heat effect, (**h**) vitrinite grain coated with mineral matter, (**i**) vitrinite grain converting into inertinite. [V-Vitrinite; I-Inertinite; P-Pyrite; Py-Framboidal Pyrite; Vh-Heat effect on vitrinite patch; Dom-Dispersed organic matter; Aom-Amorphous organic matter; Vp-Pyrite coating on vitrinite patch; C-Cracks in vitrinite; MM-Mineral Matter].*

8.3.2. TGA analysis

Figure 8.5 shows the thermogravimetric curve, where mass loss (in percentage) is plotted against increasing temperature. The graph is divided into two stages, each representing thermal events that occur as the temperature rises. In stage I, 25–400 °C, almost all the moisture/volatile components were liberated. Although the mass loss in stage I was insignificant compared to stage II, most of the loss in this stage was observed between 25 °C and 200 °C. In the range of 25–200 °C, mass loss up to 100–150 °C was attributed to the liberation of volatiles from the open pores/fractures, followed by the liberation of volatiles from interlayer clay minerals up to 200 °C. After 200 °C, the drop

in mass loss was less, mainly due to the removal of volatiles from the structure of hydrophilic minerals. In stage II (400–550 °C), the decline in the mass loss curve was sharp. The sharp decline in the curve indicated a substantial amount of kerogen within the sample. Moreover, the mass loss curve also reflects changes in density with increasing temperature. A sharp decline in the curve beyond 400 °C indicated a rapid reduction in density due to the splitting of the sample under thermal heating.

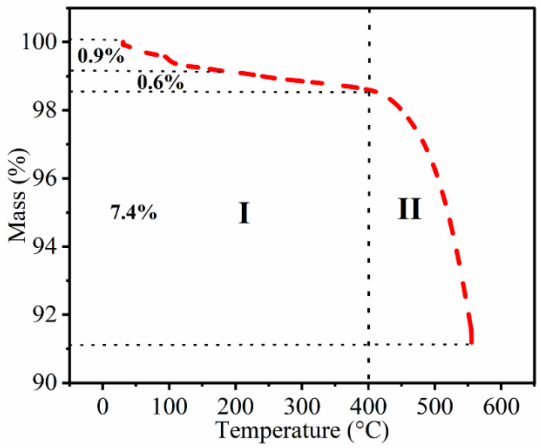

Figure 8.5. *Cumulative mass-loss during combustion using the thermogravimetric curve.*

8.3.3. XRD analysis

Figure 8.6a shows the XRD analysis of thermally treated Neoproterozoic Himalayan shale, highlighting mineral phases through their intensity peaks. Using PANalytical X'Pert HighScore software (version 4023 000 04613, 2020), the dominant minerals identified were quartz (2θ = 27°, 50°), illite (2θ = 12°, 20°), muscovite (2θ = 28°, 43°), albite (2θ = 22°), and pyrite (2θ = 37°). Rietveld refinement of untreated shale confirmed that quartz was the most abundant mineral, followed by illite, muscovite, albite, and pyrite. The pie chart in Figure 8.6b represents the mineral composition of untreated shale. The mineral phase analysis indicated that no significant phase changes happened at the selected combustion temperature. However, mineral intensity peaks

weakened as the temperature increased, with illite showing the most significant reduction, nearly disappearing at 400 °C.

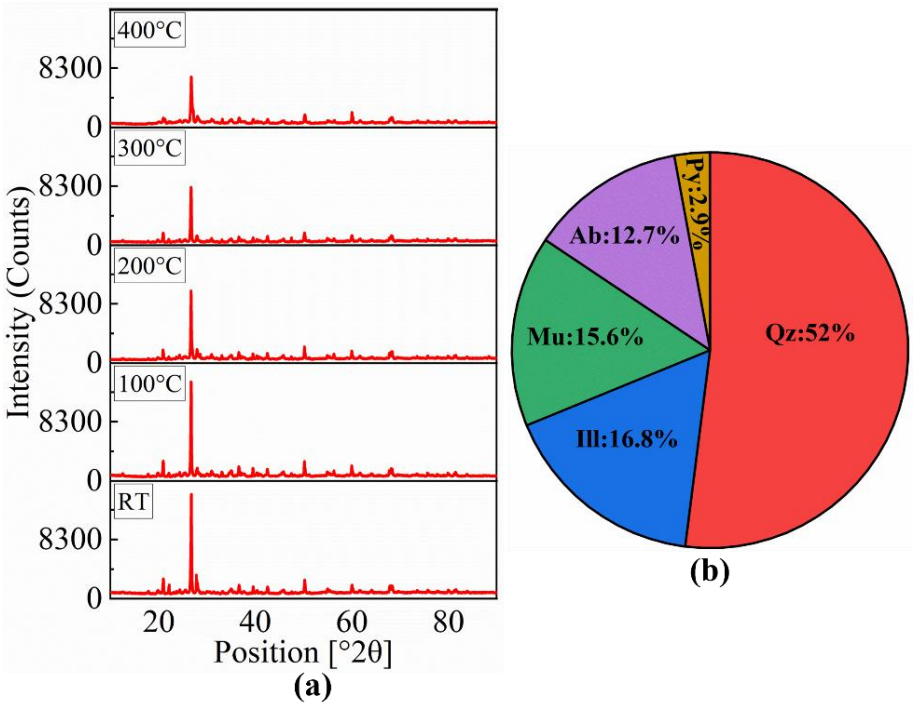

Figure 8.6. *(**a**) Intensity peaks of different mineral phases during combustion and (**b**) Percentage of dominant mineral phases in a representative sample (Qz: Quartz, Ill: Illite, Mu: Muscovite, Ab: Albite, Py: Pyrite).*

8.3.4. FE-SEM analysis

The surface morphology of thermally treated shale, including pores and fractures, was investigated using FE-SEM analysis. High-resolution photomicrographs captured at the microscale level provided a detailed visualization of the microstructural changes, emphasizing the impact of temperature on the pore system and the overall morphology of the shale. Before examining the thermal effects on surface morphology, key features of the samples, such as pore types, shapes, and organic matter pores, were analyzed. According to the Loucks classification scheme, interparticle, intraparticle, and organic matter pores were abundant (Figures 8.7a, b). Among these, organic matter pores were

the most prevalent, underscoring their critical role in determining the gas potential. Various pore shapes, including cylindrical, rounded, complex, and slit-shaped, were also identified in the sample (Figures 8.7c, d).

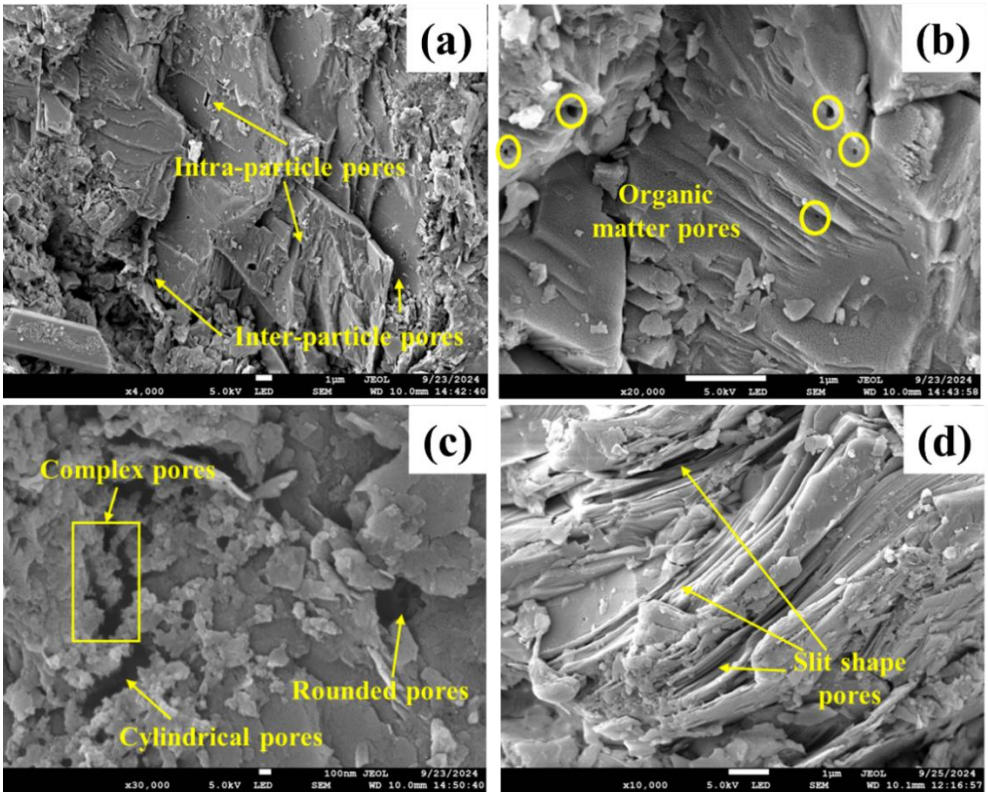

Figure 8.7. *A photomicrograph showing the characteristic features of the shale: (**a**) intra-particle and inter-particle pores, (**b**) organic matter pores, (**c**) complex, rounded, and cylindrical pores, (**d**) slit-shaped pores.*

A notable alteration in the morphology of pores, fractures, and organic matter pores was observed as the temperature increased (Figure 8.8). The photomicrographs taken at a 200x magnification revealed initial compaction of pores and fractures, followed by subsequent expansion. For the untreated shale (Figure 8.8a), smaller pores were observed throughout the surface. Upon heating the shale to 100 °C, a significant reduction in pores and fractures was observed (Figure 8.8b), indicative of compaction within the sample. The temperature range of 100 °C was insufficient to induce thermal degradation

of organic or mineral components, with the observed changes being limited to the compaction primarily attributed to removing free moisture from open pores and fractures. As the temperature increased beyond 100 °C, significant alterations in the surface morphology were observed. Coalescence of adjacent pores formed larger pores (Figure 8.8c). Thermally induced heat not only expanded pre-existing pores but also facilitated the development of numerous nanoscale pores within the shale matrix, as evidenced by the photomicrographs (Figure 8.8c). Further, the FE-SEM images demonstrated that combustion phenomena not only resulted in increased pore diameter or development of new pores within the shale but also resulted in thermal cracking (Figure 8.8c).

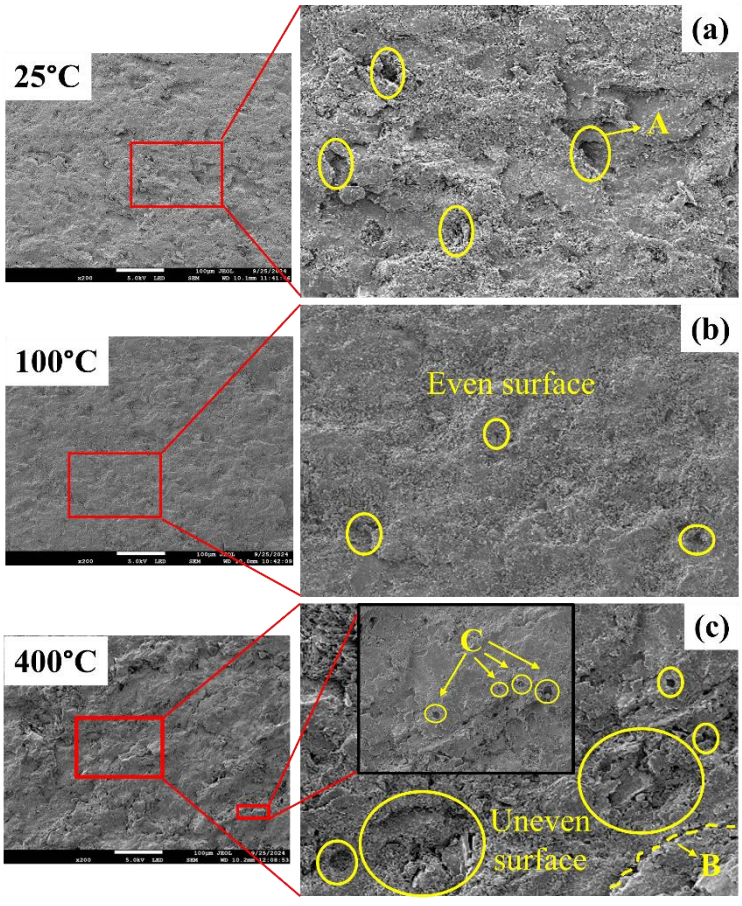

Figure 8.8. *Representative photomicrographs at combustion temperatures: **(a)** 25 °C, **(b)** 100 °C, **(c)** 400 °C. [A: micro pore, B: micro fracture, C: remnant of organic matter within organic pores after oxic heating].*

At ~ 400 °C, the shale exhibited marked changes in surface morphology. Evidence of organic decomposition (reduced contrast between mineral and organic matter pores) was evident, along with the generation of a network of larger, interconnected pores due to thermal heating. The degree of alteration in the samples demonstrated a direct correlation with surface evenness. Samples subjected to lower thermal alteration at 100 °C exhibited a relatively smooth and even surface. However, the visual interpretation from the photomicrographs indicates that surface roughness progressively increases as thermal breakdown intensifies with increasing temperature.

8.3.5. N2-LPGA analysis

The LPGA analysis in this study has proven to be a robust technique for understanding the thermal effects on the pore characteristics of Krol Shale. Heating facilitated the formation of larger pores by expanding pre-existing pores and generating new ones. Increasing temperature notably altered the adsorption-desorption isotherm, PSD, and fractal dimension.

The shape of isotherms and hysteresis loops plays a crucial role in the International Union of Pure and Applied Chemistry (IUPAC) classification scheme. Based on their shape, adsorption isotherms are categorized into six types (Type I–Type VI), reflecting the adsorption process's nature and the adsorbent material's structural properties. Hysteresis loops are classified into four types (Type H1 to Type H4). Figure 8.9 presents the isotherm curves of the shale sample combusted from 100 °C to 400 °C. The isotherms, which depict the quantity of N_2 adsorbed ($cm^3\ g^{-1}$) versus relative pressure (P/P_0), indicate that all follow Type IIB isotherms {as per the IUPAC classification by Rouquerol et al. (1998)}, despite thermal treatment. Unlike Type IIB isotherms, which appear at all temperatures, the hysteresis loop shifted from H4 (100 °C) to H3 (at 200 °C

and above) (Figure 8.9). The presence of Type IIB isotherms indicated the dominance of mesopores along with the presence of some macro- and microscale pores. Meanwhile, the transition of the hysteresis loop from H4 to H3 suggested a shift from narrow slit-shaped pores to slit/wedge-shaped pores, implying greater adsorption-desorption capacity at higher temperatures. Additionally, up to 200 °C, the hysteresis loop lacked closure at low relative pressures (Figure 8.9b). This effect was most pronounced in the sample tested at 100 °C, with a gradual reduction observed in samples treated at 200 °C. Although the isotherms from 100 °C to 400 °C showed similar patterns, all lacked a plateau at high P/Po. The adsorption amounts continuously increased with rising temperature. Notably, the isotherm for the sample treated at 400 °C exhibited a sharp increase at high P/Po values (> 0.9).

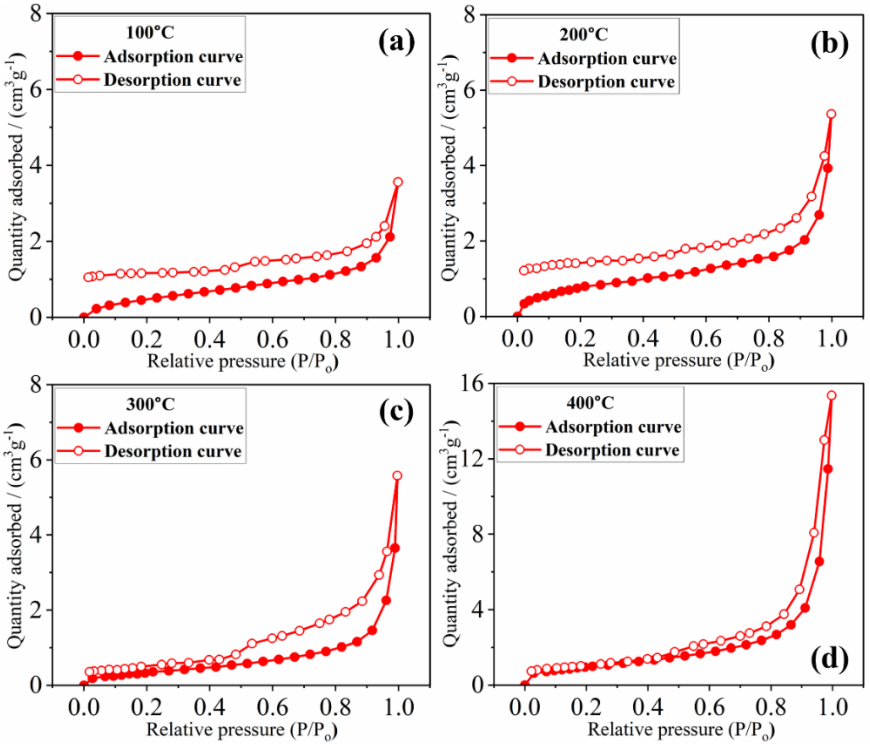

Figure 8.9. *Low-pressure N2 sorption isotherms of Neoproterozoic shale samples subjected to different combustion temperatures:* ***(a)*** *100 °C,* ***(b)*** *200 °C,* ***(c)*** *300 °C,* ***(d)*** *400 °C.*

The PSD of thermally treated shale is presented in Figure 8.10, providing a clear understanding of how combustion affects pore size evolution. Variations in micro, meso, and some macropores were observed as the temperature increased from 100 °C to 400 °C. Up to 100 °C, only micropores remained dominant with few mesopores. The average pore diameter, calculated using the BJH model, was 2.17 nm for samples treated at 100 °C. Above 100 °C, the distribution of larger pores increased continuously with rising combustion temperatures. In samples treated at 200 °C, the mesopore range exhibited dominant peaks between 2–7 nm, with an average pore diameter of 5.14 nm. At 300 °C, the mesopore range expanded further, showing dominant peaks between 2–15 nm with an average pore diameter of 11.14 nm. For samples treated at 400 °C, a single peak corresponding to the macropore range was also identified in addition to the prominent peaks within the mesopore range. Furthermore, peaks within the micropore range were also observed in samples treated at 200 °C and above, with their intensity increasing as the temperature increased. This was further supported by the Specific Surface Area (SSA) data obtained using the Brunauer-Emmett-Teller (BET) model. The SSA values showed a continuous increase with temperature, having a value of 2.01 $m^2 g^{-1}$ at 100 °C, 3.00 $m^2 g^{-1}$ at 200 °C, 3.27 $m^2 g^{-1}$ at 300 °C, and 3.53 $m^2 g^{-1}$ at 400 °C.

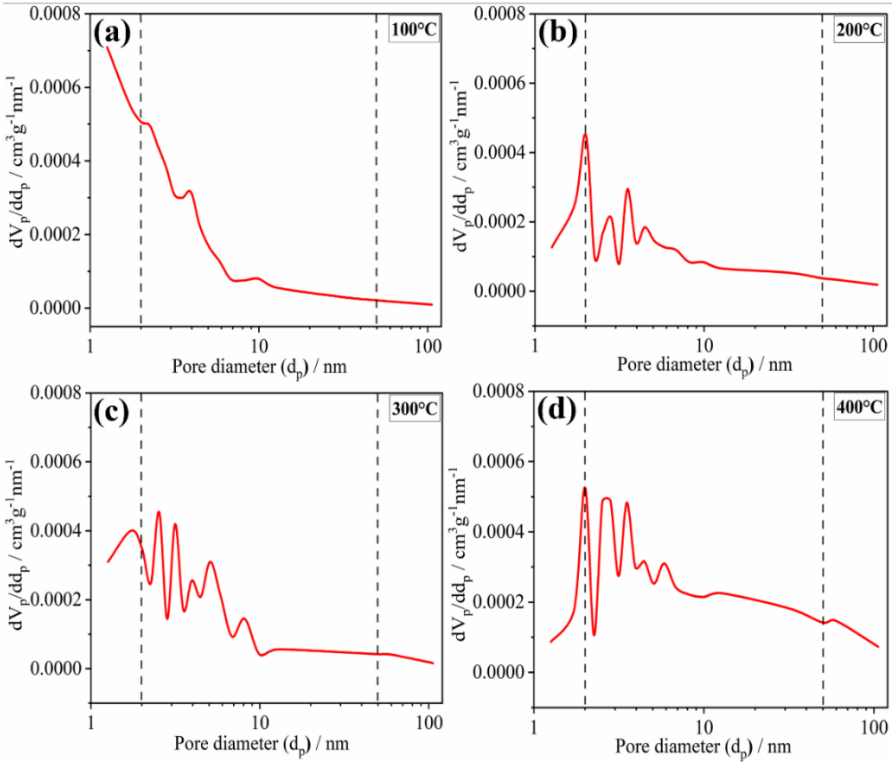

Figure 8.10. *PSD using the BJH model of the combusted shale samples: **(a)** 100 °C, **(b)** 200 °C, **(c)** 300 °C, **(d)** 400 °C.*

The fractal dimension quantifies the irregularity of pore structures in terms of roughness and complexity and can be determined using the equation D = A + 3, where D represents the fractal dimension (D1: surface fractal dimension, D2: pore fractal dimension), and A is the slope of the fitted line (Qi et al., 2002; Yao et al., 2008). The fractal fitting curve, based on the FHH model for combusted shale (Figure 8.11), is divided into two domains. The first domain (D1), with a P/Po range of 0–0.5, reflects the surface roughness characteristics of shale and corresponds to a mono-multilayer adsorption system dominated by van der Waals forces, while the second domain (D2), with a P/Po range of 0.5–1, represents the complexity of the pore structure and corresponds to a capillary condensation system where surface tension forces prevail (Sun et al., 2015; Wang et al., 2015). It may be noted that the fractal values vary between 2 to 3. A higher fractal value indicates a more complex and highly irregular pore structure.

The correlation coefficient for the fitting was found to be strong in regions D1 and D2, ranging from 0.9744 to 0.9983 for D1 and 0.9488 to 0.9824 for D2. Both D1 and D2 consistently increased with temperature, showing the increased complexity and irregularity with rising temperature. At 100 °C, the D1 value was 2.2035, followed by 2.3154 at 200 °C, 2.3596 at 300 °C, and 2.5182 at 400 °C. While the D2 value at 100 °C was 2.5393, followed by 2.5484 at 200 °C, 2.6121 at 300 °C, and 2.6915 at 400 °C.

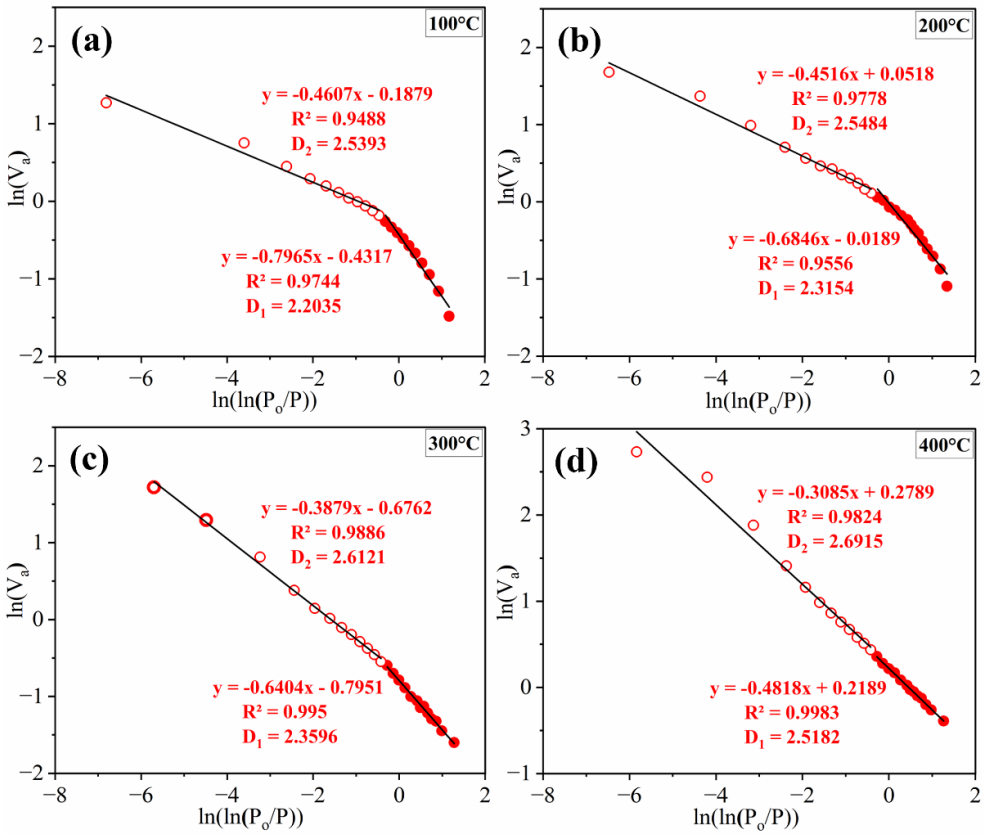

Figure 8.11. *Fractal results showing ln (Po/P)) vs. ln (Va) of low-pressure N2 sorption for thermally combusted shale:* ***(a)*** *100 °C,* ***(b)*** *200 °C,* ***(c)*** *300 °C,* ***(d)*** *400 °C.*

8.3.6. SAXS analysis

SAXS has proven invaluable for providing a detailed nanoscale characterization of combusted shale, particularly at the meso and macro scales. The Porod-Debye Scattering Profile (PDSP) model was applied to the scattering behavior shown in Figure 8.12. The logarithmic plot (log of intensity 'I(Q)' versus log of the scattering vector 'Q')

of the scattering profile under combustion reveals that the shale sample follows a power-law dependency ($I(Q) \propto Q^{-D}$, where D is the fractal dimension). The obtained scattering plot showed a linear trend, suggesting that the structure of shale exhibits a fractal nature. The intensity profile reached its maximum value at 400 °C, indicating the highest structural variation at this temperature. In comparison, the minimum scattering intensity was observed at 100 °C, reflecting the least structural variation. The fractal nature of the intensity profiles at higher temperatures indicated the complexity of the thermally induced pore system in terms of pore surface roughness. The fractal dimension values were 2.29, 2.24, 2.30, 2.32, and 2.35 for the samples combusted at 25 °C, 100 °C, 200 °C, 300 °C, and 400 °C, respectively.

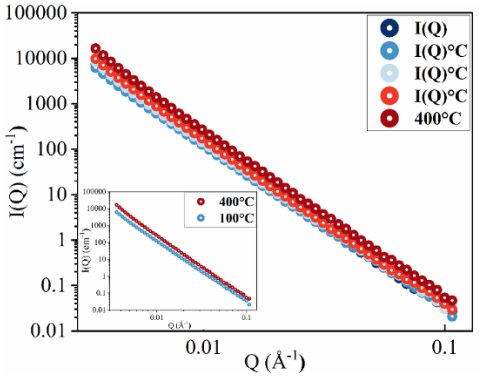

Figure 8.12. *A PDSP model-based scattering profile of shale subjected to different combustion temperatures.*

The SAXS analysis of combusted shales reveals significant variations in PSD with respect to temperature. The PSD results are calculated and presented in terms of pore volume ('dV/dlogD') and pore area ('dA/dlogD'), as shown in Figure 8.13. In general, the PSD indicates the formation of new pores and the expansion of pre-existing ones with increasing temperature, emphasizing the impact of thermal heating on shale gas recovery. The pore volume and area profiles exhibited similar trends with increasing temperature,

showing a slight initial decrease up to 100 °C, followed by an increase at higher temperatures. Up to 100 °C, both pore volume and area in the meso and macropore ranges decreased significantly, indicating structural compaction. Beyond 100 °C, both pore volume and area began to increase. Between 100 °C and 300 °C, a notable increase in pore volume and area was observed, particularly within the mesopore range. However, the increase in pore volume beyond the mesopore range was minimal between 100 °C and 300 °C. After 300 °C, the change in pore volume and area became more pronounced in the mesopore as well as the macropore ranges. At 400 °C, a significant increase in both mesopore volume and area was observed (Figure 8.13). Additionally, a sharp rise in pore volume and area was noted as the graph shifted from the mesopore to the macropore range, indicating extensive structural changes due to thermal heating. This suggests transitioning from a predominantly compact shale structure to a highly porous matrix.

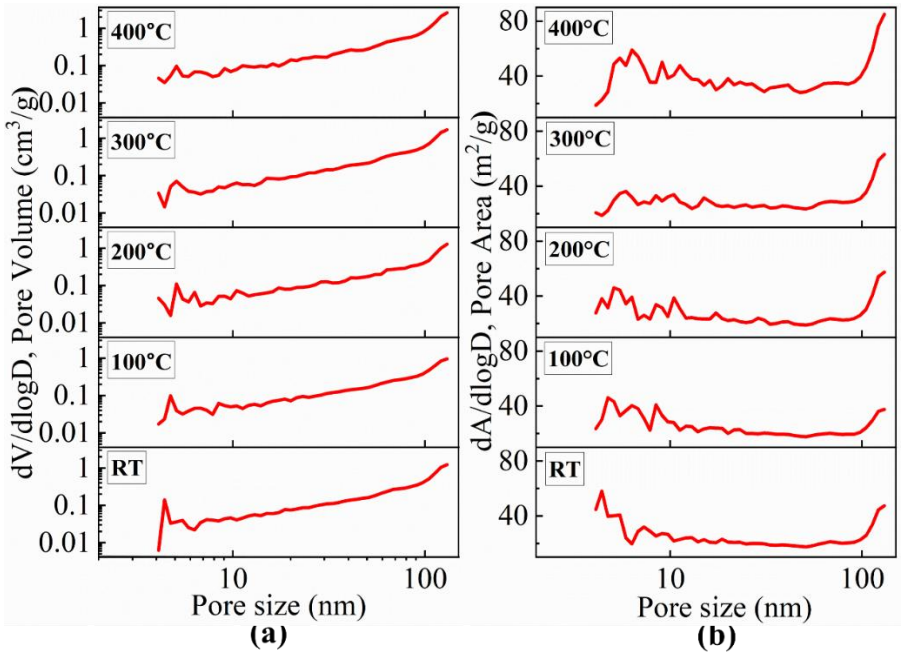

Figure 8.13. *Represents the PSD of the combusted shale based on* ***(a)*** *pore volume (dV/dlogD) and* ***(b)*** *pore area (dA/dlogD) of the SAXS analysis.*

8.4. Discussions

The evolution of pore structures in oil-bearing and gas-bearing shales is critical to controlling the flow pathways during migration/extraction. The low-porous nature of shale significantly impacts the overall efficiency of hydrocarbon storage, migration, and extraction. The combustion technique employed in this study has played a pivotal role in pore structure evolution. A schematic diagram in Figure 8.14 illustrates how thermal treatment influences the structural characteristics of shale, ultimately enhancing gas flow.

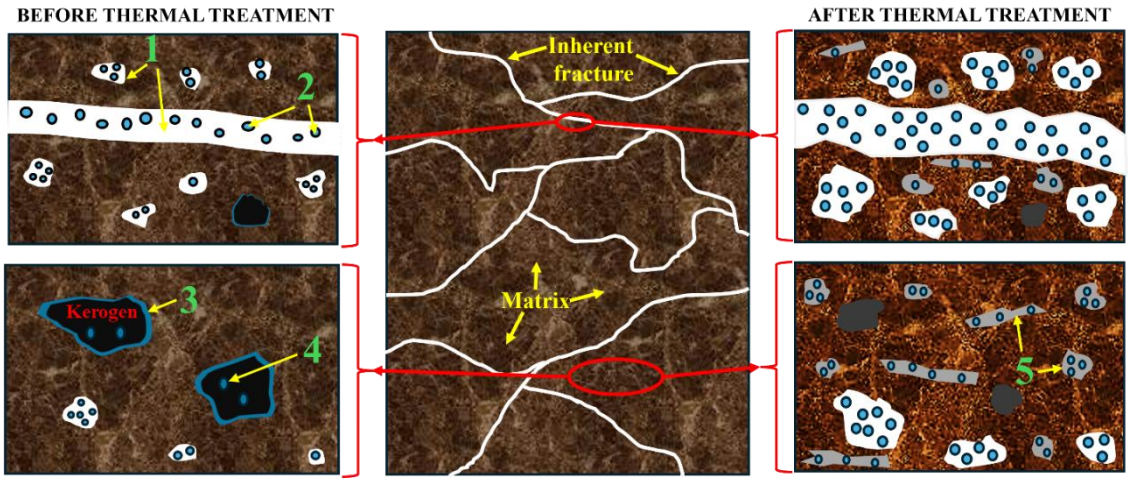

Figure 8.14. *The schematic diagram illustrates the effect of thermal treatment on the structural characteristics of shale, ultimately enhancing gas flow: (1: Zone of free gas within inherent micropores and microfractures, 2: Gas molecules, 3: Zone of adsorbed gas on or near the surface of organic matter, 4: Zone of dissolved gas within organic matter, 5: Thermally induced new pores and microfractures with gas flow).*

The combined LPGA and SAXS analysis has served as a tool for pore evolution studies examining the effects of thermal treatment. Both SAXS and LPGA techniques have proven valuable in pore structure evolution during combustion. The SAXS analysis has proven to be a more appropriate technique as it can access both accessible as well as inaccessible pores (Clarkson et al., 2013; Ruppert et al., 2013; Zhao et al., 2017). In contrast, in the LPGA technique, the gas molecules do not enter each pore space during adsorption (Chandra et al., 2020a). Hence, the higher accessibility of the pores through

the SAXS technique has resulted in the higher pore volume and pore area of the thermally combusted shale compared to the pore volume and pore area obtained through LPGA analysis. Besides, the visual microstructural changes through surface morphological analysis using FE-SEM have supported the LPGA and SAXS analysis in understanding the pore structural changes with temperature. The thermogravimetric curve and mineralogical changes have also crucially supported the pore attribute alteration during combustion. The following subsection elaborates on the discussion of the above-stated findings and supports them with existing meta-studies.

8.4.1. Compositional Variation with Combustion

The XRD analysis demonstrates that combustion induces significant variation in the mineralogical characteristics of shale. The dominant mineral phases, including quartz, illite, muscovite, albite, and pyrite, highlight the complex composition of Neoproterozoic Krol shale. No significant change appeared even at the highest combustion temperature of 400 °C. However, the weakening of the mineral peaks was observed (Figure 8.6). This weakening was most pronounced in the clay mineral illite due to the dihydroxylation process, which led to the disappearance of its peaks at 400 °C (Nilankar et al., 2024a). During the dihydroxylation process, the removal of structural/bound water from the lattice of clay minerals results in the diminishing or disappearance of peaks (Bai et al., 2017). The weakening in the intensity of the peaks due to changes in the mineral lattice after thermal heating leads to the collapse or alteration of the crystal structure (Ruan et al., 2002).

The thermal events in the thermogravimetric curve provided critical insights into the thermal behavior and mass loss pattern during combustion (Figure 8.5). Stage I (< 400 °C) primarily involved the release of moisture and volatiles, resulting in relatively

minor mass loss compared to Stage II (> 400 °C), which marked the decomposition of organic matter. < 400 °C, the release of volatiles primarily involves the removal of (i) free water from open pores and fractures, (ii) interlayer water between clay minerals, and (iii) bound water from the mineral lattice structure (Zhang et al., 2021; Jin et al., 2022). > 400 °C, the curve indicated the presence of a sufficient amount of kerogen/organic matter, which started to decompose, resulting in the sharp decline of the curve (Herdes et al., 2018; Srinivasan et al., 2020). The sudden drop in the curve also indicated the thermal breakdown of the specimen, leading to a rapid decrease in material density (Nilankar et al., 2024a).

8.4.2. Morphological Variation with Combustion

SEM analysis in this study revealed that combustion causes significant microstructural changes in shale (Hazra et al., 2023). Specifically, photomicrographs showed the development and expansion of pore networks in samples combusted up to 400 °C (Figure 8.8). This transformation was dynamic and varied significantly across different temperature ranges. All coexisting pore types (inter, intra, and organic pores) within shale were significantly affected under the effect of thermal treatment in terms of enlargement and opening (Loucks et al., 2012; Cao et al., 2016). Coalescence of the adjacent pores was significant at higher temperatures, resulting in the formation of large pores and establishment of an interconnected pore network. Bai et al. (2017) reported the collapse and coalescence of existing pores during shale combustion. Furthermore, his findings on developing new pores and expanding pre-existing ones with temperature were consistent with current investigations. However, slight compactness was observed in the photomicrographs of the shale sample treated at 100 °C. Though this compactness was due to the removal of free moisture, it had an insignificant impact on the overall pore

structure (Nilankar et al., 2024a). In addition to inefficient thermal degradation temperature (up to 100 °C), causing only the removal of free moisture from the open space/fractures, Feng et al. (2020) noted that a temperature range of 100 °C often leads to reversible deformation, resulting in the closure of existing pores and fractures. Beyond 100 °C, the effect of thermal degradation was pronounced within the samples. Thermal heating altered the pore structure of shale by increasing the pore diameter and thermal fracking on the surface of the shale (Figure 8.8c). The evidence of significantly small pores in the photomicrographs of the shale sample treated at 400 °C further indicated that thermal heating not only led to the expansion of pre-existing pores and thermal cracking but also resulted in new pore development (Figure 8.8c). Chen et al. (2017) stated that the decarbonization of shale samples leads to pore enlargement and improved connectivity. The morphological alterations due to combustion observed in this study are consistent with previous findings (Yang et al., 2021; Vishal et al., 2022; Nilankar et al., 2024a). The photomicrographs in Figure 8.8c also suggest significant decomposition of organic matter at 400 °C, as evidenced by the significantly reduced contrast between organic matter pores and the surrounding mineral matrix. This interpretation is further supported by TGA, which confirmed the thermal decomposition of organic matter at or above this temperature. This decomposition, resulting from the oxidation of organic matter, led to the collapse of organic pores, which in turn caused the enlargement of existing pore dimensions (Tian et al., 2013; Chen et al., 2017).

The fractal dimension is an important parameter used to express the roughness and complexity of a material's surface. It quantitatively measures structural/surface morphology changes due to temperature variations. It also captures slight variations in the pore system or structural changes in fractal values. Higher fractal values indicate a rougher and more complex surface, while lower values correspond to a smoother surface.

To analyze morphological variations during combustion, the fractal dimensions of combusted shale from 100 °C to 400 °C were calculated using N_2-LPGA and from 25 °C to 400 °C was calculated using SAXS techniques, as presented in Figure 8.15. It is evident from Figure 8.15 that the fractal nature of the sample was strongly influenced by combustion, as indicated by the increasing fractal dimension values, which reflect enhanced roughness and pore complexity. Shale is well known for its intricate behavior and fractal nature, which depends on the connectivity, nature, and transport properties of pores (Radlinski et al., 2004). This complexity further increased with combustion. The LPGA-derived fractal dimensions (D_{LPGA}) and the SAXS-derived fractal dimensions (D_{SAXS}) showed a continuous increment with temperature (except at 100 °C in the case of D_{SAXS}), suggesting that the increased thermal alteration results in the development of complex structures with rough surfaces. The FE-SEM observations were entirely consistent with the results of the fractal dimension. Chandra et al. (2021) stated that forming new mesopores increases surface roughness, whereas pore amalgamation may often lead to reduced surface roughness. A rise in temperature increases surface fractal dimensions due to the widening of pre-existing pores (Choi and Park, 2020). The coalescence and collapse of the pre-existing pores not only resulted in widening but also increased the complexity with temperature. Mazumder et al. (2024) stated that increased pore surface complexity with increasing temperature indicates enhanced gas storage potential and recovery.

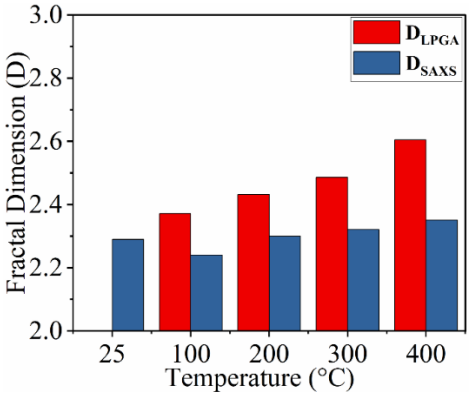

Figure 8.15. *A bar plot illustrates the variation of the fractal dimension measured by LPGA and SAXS with combustion temperature.*

8.4.3. Pore Structural Evolution with Combustion

The combined LPGA and SAXS analyses have proven effective in understanding the complete pore evolution from the micro to macro scale of thermally treated Himalayan shale. Although LPGA is an intrusive (injection-based) technique, while SAXS is non-intrusive (non-injection-based), both methods revealed nearly identical alterations in pore characteristics. Figure 8.16 presents a bar plot comparing porosity values obtained from LPGA and SAXS across different combustion temperatures. Although the absolute percentage values varied due to differences in measurement techniques, both methods exhibited a similar porosity trend with temperature. This variation in porosity highlights the pore evolution occurring during combustion at selected temperatures.

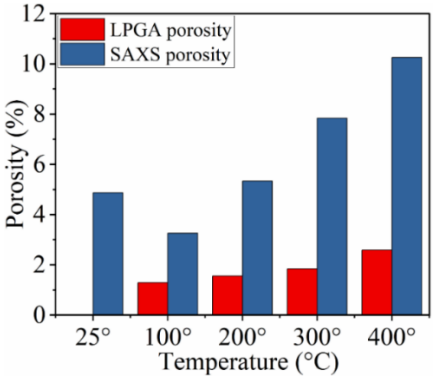

Figure 8.16. *A bar plot illustrates the variation in porosity derived from LPGA and SAXS analyses across different temperatures.*

LPGA demonstrated a clear progression in pore development with combustion. The type IIB isotherm pattern with hysteresis loop shifting from H4 to H3 with increasing combustion temperature is evidence of thermal alteration (Figure 8.9). Type IIB isotherm indicates that the material contains mainly mesopores without forming a plateau at a higher relative pressure (P/P_o) (Rouquerol et al., 1998). Although the isotherm type remained unchanged, the steepness at a higher relative pressure (P/Po = 0.9–1) varied with temperature. The notable rise in steepness within the sample treated at 400 °C indicates enhanced adsorption/desorption of the gas, likely due to the formation and expansion of pores. In their thermal investigation, Chandra et al. (2021) also observed a sharp rise in the P/Po value of the isotherm. The shift from an H4 hysteresis loop to an H3 hysteresis loop with increasing temperature indicates pore widening or the formation of new pores (Sing, 1985; Lowell et al., 2004; Liu and Gadikota, 2018; Mishra et al., 2018; Yu et al., 2019). This transition from narrow slit-shaped pores in H4 to slit-shaped pores in H3 with temperature aligns with the findings of Nilankar et al. (2024b). Yu et al. (2019) stated that a slit-shaped pore structure has greater gas transportation capacity than others.

There was a lack of closure in the hysteresis loop at low relative pressure within the samples treated at low temperatures. The primary cause of this lack of closure is likely due to the porous structures, such as clay minerals, within the shale. The swelling of clay minerals is the primary cause of the lack of closure at low relative pressure (Chen et al., 2015; Cao et al., 2020). As the temperature increased, the swelling intensity diminished, ultimately disappearing at 300 °C and above. Therefore, at these higher temperatures, the combustion process effectively removed all moisture from the clay minerals, thereby eliminating their swelling properties. A continuous rise in the adsorption-desorption

isotherm of LPGA analysis was observed with rising temperatures from 100 °C to 400 °C. Whereas in the case of SAXS analysis, which was carried out from 25 °C (room temperature) to 400 °C, an initial reduction in the scattering profile up to 100 °C was observed, followed by a continuous increase in temperature. Although the gradient of the profiles remained consistent across different thermal treatment temperatures, variations in intensity indicated modifications in the pore structure (Figure 8.12). A reduction in the scattering profile up to 100 °C is because of initial compaction due to the removal of moisture from the pores. Feng et al. (2017) stated that when water escapes from the pores, a drop in the pore pressure is observed along with the rise in effective stress, thereby resulting in the packed mineral grains. Zhang et al. (2021) and Chandra et al. (2023) analyzed SAXS scattering profiles under combustion, such that their findings were consistent with the present study, suggesting that significant alterations in the pore structure of shale occur with increasing temperatures.

The analysis of PSD using LPGA and SAXS proved highly effective. Despite employing different models, both techniques yielded remarkably similar patterns in their results. Table 8.2 compares the PSD results from LPGA and SAXS. The BJH model was used for LPGA analysis, while the PDSP model was applied to SAXS. In LPGA-derived PSD, primarily using pore volume indicated the presence of some micropores, with limited mesopores within specimens treated at 100 °C. The temperature up to 100 °C was insufficient to alter pore structures, only facilitating moisture loss, and thereby leading to overall compactness. Despite this, the SSA value at 100 °C remained appreciable, mainly due to the presence of small micropores. Tian et al. (2013) stated that small micropores contribute significantly to SSA.

Table 8.2. *PSD of thermally combusted shale analyzed by LPGA and SAXS.*

Temp (°C)	Volume ($cm^3 g^{-1}$)				Area ($m^2 g^{-1}$)			
	LPGA		SAXS		LPGA	SAXS		
	Micro	Meso	Meso	Macro	SSA	Meso	Macro	Average
25	–	–	0.07128	0.44386	–	25.43	25.19	25.31
100	0.00061	0.00012	0.07435	0.39097	2.01	24.68	22.98	23.83
200	0.00038	0.00026	0.07845	0.44086	3	26.83	29.04	27.93
300	0.00037	0.00032	0.08744	0.61289	3.27	27.08	34.31	30.69
400	0.00048	0.00039	0.11933	0.85667	3.53	37.14	43.33	40.23

The SAXS-derived PSD, which is based on pore area and volume and primarily sensitive to meso- and macropores, indicates that the untreated samples contain lesser mesopores compared to those subjected to thermal treatment. Beyond 100 °C, both LPGA and SAXS-derived PSD showed shifting towards larger pores. Both analyses indicated the formation of new pores and the expansion of existing ones. Cao et al. (2020) and Nilankar et al. (2024b) carried out the LPGA analysis of shale with increasing temperature, and their study demonstrated a significant enhancement in the PSD with an increase in the pore volume of micro-, meso-, and a few macropores, leading to efficient flow transport channels. Hence, shale gas adsorption is highly sensitive to temperature variations, and understanding this temperature effect is crucial for optimizing shale gas resource development (Xia et al., 2024). Based on SAXS-derived PSD, Chandra et al. (2023) observed a substantial increase in mesopore volume when subjected to combustion at 300 °C. Furthermore, Chandra et al. (2023) confirmed their findings by comparing them with the LPGA-derived PSD. Chandra et al. (2021) also observed a massive rise in the total pore volume of mesopores and micropores within a combusted shale compared to a pyrolyzed shale. The LPGA-derived SSA was minimum at 100 °C due to the initial compactness of pores. Beyond this point, it gradually increased with rising temperature, indicating the formation of new pores along with the expansion of pre-existing ones. A sharp increase in the SAXS-PSD was observed at 400 °C, primarily due to structural alterations in clay minerals initiated above 300 °C and the intense oxidation of organic

matter at 400 °C, both of which contribute to the significant enlargement of inorganic and organic pores(Sun et al., 2016; Liu and Hou, 2020; Nilankar et al., 2024b). Thermal cracking of organic matter not only improves gas accessibility but also increases permeability, allowing free gas to flow (Mazumder et al., 2024). As a result, the combined effects of clay minerals structural deterioration and organic matter decomposition led to a sharp increase in total pore volume and pore area across micro, meso, and macropore regions.

8.5. Summary

Thermal stimulation under oxic heating has emerged as a transformative approach for enhancing gas recovery from tight shale reservoirs, which is typically challenging due to their complex pore structures, low permeability, and inherent anisotropy. Considering this, an untapped Neoproterozoic shale from the Lesser Himalayan region was heated up to 400 °C to investigate pore structure evolution using a combination of SAXS, LPGA, and FE-SEM. Given the shale's fair hydrocarbon generation potential, as indicated by total organic carbon (TOC) and vitrinite reflectance (% VRo) data, understanding its thermal-induced pore structure evolution is critical for enhancing gas extraction efficiency. The outcomes of this study demonstrate that oxic heating significantly alters the pore structure of shale, marked by a progressive shift from micropores to meso- and macropores. SAXS and LPGA analyses reveal a strong positive correlation between pore size distribution (PSD) and thermal treatment. The increased steepness in LPGA-derived BET isotherms and hysteresis loop transition from H4 to H3 confirms the development of larger pores. These substantial changes result from the coalescence and collapse of the adjacent pores during combustion. Along with the expansion of pre-existing pores, new pores were also developed during combustion, which was obvious with the findings of

pore area and SSA derived from SAXS and LPGA analysis. Furthermore, a notable rise in the pore area at 400 °C was also observed, suggesting the breakdown of organic matter and the formation of numerous organic matter pores. This organic matter breakdown was evident with the TGA, where a rapid mass loss was observed at 400 °C. The FE-SEM photomicrographs with widened pores, fractures, and numerous finer pores at higher temperatures further supported the above findings. This study highlights the potential of combustion-induced thermal stimulation and suggests that oxic thermal treatment can effectively alter shale microstructure, thereby offering a viable enhancement technique for shale gas recovery.

Chapter: 9
Conclusions and Future Scope

9.1. Conclusions

In view of rapid infrastructure development within the Chandpur Phyllite and the hydrocarbon potential of the untapped Krol Shale, detailed characterization of these rock masses is very crucial. Lack of adequate knowledge of these rock masses in terms of their physico-mechanical, geochemical, morphological, and pore characteristics may often lead to serious drawbacks. In compliance with this, six objectives were thought about: (*i*) a comprehensive investigation of the multiscale weathering-grade classification of Chandpur Phyllite by integrating *in situ* observations with laboratory investigations; (*ii*) to understand the influence of water saturation on the physico-mechanical behavior of Chandpur Phyllite at different foliation angles (β); (*iii*) investigation of the effect of specimen geometry on the point load strength and anisotropy behavior of phyllite; (*iv*) to perform a multiscale mechanical characterization of Krol Shale using Conventional and Non-conventional analytical techniques; (*v*) characterization of the pore system of the Krol Shale using an integrated multiscale analytical method; (*vi*) evolution of pore structure in Krol Formation Shale under oxic thermal conditions through multiscale analysis. The major conclusions with reference to each objective are mentioned below.

9.1.1. Multiscale Weathering-grade Classification of Chandpur Phyllite: Insights from In situ Observation and Laboratory Investigation

This study presents a comprehensive weathering-grade classification for phyllites, integrating conventional *in situ* observation with conventional and non-conventional laboratory analysis. The key findings of this investigation are as follows:

- *In situ* mechanical testing demonstrated a progressive decline in rock strength with weathering. The decreasing rebound values with increased weathering-grade reflect the breakdown of intergranular bonds and increased microcracks within the matrix of phyllite. Scratch testing also emerged as a highly effective field method for differentiating weathering-grades of phyllite.
- Progressive weathering resulted in a significant increase in the intensity of clay minerals, particularly kaolinite. As weathering advanced, minerals like mica, chlorite, and feldspar transformed into clay minerals.
- Wettability measurements confirmed an increase in surface hydrophilicity from W1–4. This is attributed to the formation of clay minerals and surface microfractures during weathering, which enhanced water adsorption capacity. The adsorption-desorption isotherms from LPGA analysis also confirm increased hydrophilicity with weathering.
- Surface roughness parameters (R_a and R_q) exhibited a progressive increase from W1–3, primarily due to intensified mineral fragmentation and microcracking associated with weathering. However, at W4, a noticeable reduction in roughness was observed, attributed to the filling of surface asperities by secondary clay minerals. These structural changes are further supported by tribological data, which indicate a maximum CoF in the W1 sample and a minimum in the W4 sample, with a continuous increase in wear volume from W1–4.
- Multiscale structural analysis, like petrography, SEM, and AFM, revealed structural degradation in phyllite from W1–4. W1 samples showed intact micaceous foliations and sharp grain-to-grain contact, while weathering led to grain disintegration, foliation distortion, and clay mineral accumulation. In W4

samples, the rock matrix was dominated by secondary clays, resulting in a smoother, homogenized surface texture.

9.1.2. Impact of Water Saturation on Physico-mechanical Properties of Chandpur Phyllite at Varying Foliation Angles

The present study investigated the directional dependency on the rock behavior of highly foliated Himalayan phyllite, which was significantly influenced by water saturation. The key findings of this investigation are as follows:

- The Chandpur Phyllite is primarily composed of micaceous (muscovite and illite) and brittle (quartz) minerals. The major concentration of such platy/flaky micaceous minerals is present in the form of well-developed foliations, responsible for the directional variation in the physico-mechanical properties.
- P-wave velocity under normal and saturated conditions displays a decreasing trend with increasing β. The wave velocities are relatively higher under saturated conditions than under normal conditions.
- The strength parameters of Chandpur Phyllite exhibit a strong anisotropic nature under normal and saturation conditions. However, the values under saturation states were lower than under normal state. UCS and BTS exhibit a "U-shoulder" type anisotropy indicating the high anisotropic nature with strength first decreasing and then continuously increasing with increasing β having a maximum value at 90º and minimum value at β=30º.
- It could be inferred that although the water saturation altered the strength of phyllite, its effect on the failure mode was found insignificant. Rather, the examined failure modes correspond to the orientation of the foliation planes.

- In specimens that generally fail at lower strength, failure occurs along the foliation or non-central, especially within specimens of β = 30°. In contrast, those specimens that failed at higher strength values, in that case, failure occurred across the foliation or central, especially within specimens of β = 60° or 90°. Weak foliation planes are responsible for the failure of the specimens at lower strength, while rock matrices play a major role in the failure at higher strength.

9.1.3. Influence of Specimen Geometry on the Point Load Strength Anisotropy of Phyllite

The present study investigates the influence of specimen geometry on the point load strength of anisotropic phyllite through integrated experimental and mathematical analyses. Three different specimen geometries of t/d ratio of 1, 0.8, and 0.6 have been selected, and axial PLI tests across various β between 0 to 90° have been performed. The key findings of this investigation are as follows:

- The point load strength index "$I_{S(50)}$" for t/d ratios of 0.8 and 1 increased within 0° ≤ β ≤ 60°, followed by a decrease at β =75° and 90°. Meanwhile, for the t/d ratio of 0.6, $I_{S(50)}$ consistently increases with the increase of β from 0 to 90°.
- Regardless of the t/d ratio, valid failure modes occurred along the foliation up to β =30°. However, at higher β (≥ 45°), the specimens with t/d ratios of 0.8 and 1 possess invalid failure modes, which are attributed to non-uniform stress distribution at higher angles. Conversely, the specimens with a t/d ratio of 0.6 maintained valid failure modes even at higher angles, attributed to uniform stress distribution.
- Furthermore, the Student's t-test indicated a significant difference between the strength indices of the different ratios. Specifically, the specimens with a t/d ratio

of 0.6 demonstrated a relatively better strength index than those with a t/d ratio of 0.8 and 1.

- Based on experimental data from this study, a generalized empirical relationship between the t/d ratio and β has been developed to estimate $I_{S(50)}$ in cases of valid rock failure.

9.1.4. Multiscale Mechanical Characterization of Krol Shale using Brazilian Tensile Strength and Nano-indentation Tests: Implications in Hydrocarbon Recovery and CO_2 Sequestration

This study introduces multiscale analysis to understand the mechanical response of Krol Shale at the macro- and microscales by combining conventional BTS and non-conventional nano-indentation techniques. The key findings of this study are as follows:

- The Neoproterozoic Krol Shale exhibits a hydrocarbon gas potential nature with a significant proportion of clay minerals along with other major minerals. It represents the marine depositional environment with terrestrial organic matter.
- The average low elastic modulus values derived from the nano-indentation, BTS, and ultrasonic pulse velocity tests indicate the low-to-moderate stiffness of the Krol Shale with a semi-ductile nature.
- Characteristic features in the nano-indentation load-displacement response, including pop-in and elbow events, provide insight into microscale deformation behavior. Pop-in events are linked to the presence of pores and microstructural heterogeneities. The elbow event on the other end indicates the phase transformation during the unloading stage.
- Statistical clustering-based deconvolution of the nano-indentation elastic modulus data identified two distinct mechanical phases in the BS1 sample and three phases in the BS2 sample. For the BS1 sample, the mean elastic moduli of phase 1 and

phase 2 are 5.50 GPa and 15.99 GPa, respectively. In contrast, the BS2 sample exhibits mean elastic moduli of 5.71 GPa, 20.05 GPa, and 38.45 GPa for phases 1, 2, and 3, respectively.

- The relatively low average BTS values of 5.16 MPa and 5.92 MPa for the BS1 and BS2 samples support the elastic modulus results of this study and indicate a low-to-moderate stiffness of the Krol Shale. The layer-activation failure during the BTS tests indicates a low strength value, with fractures propagating along bedding planes.
- Low average BI values were obtained from both the BTS and nano-indentation load-displacement curves. For the BTS tests, the average BI values for the BS1 and BS2 samples were 0.38 and 0.42, respectively, while for the nano-indentation tests, the average BI values were 0.13 and 0.17, overall indicating the semi-ductile mechanical behavior of Krol Shale.
- AFM analysis captured detailed topographical heterogeneity of the Krol Shale through quantitative surface roughness parameters. The measured R_a and R_q values indicate that both BS1 and BS2 samples exhibit a high surface asperity density and pronounced surface irregularities, which promote microscale stress concentration sites and may act as initiation points for microcrack development under applied loading.
- The probabilistic distribution approach for multiscale integration successfully links the microscopic and macroscopic properties and indicates that the predicted macroscopic values are consistent with the experimentally observed data.

9.1.5. Pore System Characterization of Untapped Krol Shale Using an Integrated Multi-analytical Approach: Bridging Nano- to Macroscale Investigation

The pore system of an untapped Neoproterozoic Lesser Himalayan shale from the Krol Formation was effectively characterized using LPGA, SAXS, FE-SEM, and micro-CT analyses. These techniques effectively bridged the gap between nano- and macro-scale pores. The key findings of this investigation are as follows:

- Geochemical and petrographic analyses indicate that the pyrite-rich black shale of the Krol Formation contains Type III kerogen within a post-oil (gas) maturity window. The dominance of vitrinite macerals with high reflectance (% VRo > 1.5 %) and the absence of liptinite and inertinite confirm advanced thermal maturity and strong gas-generation capacity. High sulfur content (> 10 wt %) and TOC (> 1 %) further classify the Krol Shale as a marine-influenced coaly facies.
- The sample exhibits a dominance of highly irregular and elongated pore geometries, primarily slit- and wedge-shaped pores. The LPGA-derived N_2 adsorption isotherm of Type IIB with an H3 hysteresis loop confirms the abundance of slit and wedge-shaped mesopores. FE-SEM imaging, supported by MATLAB-based quantitative analysis, further reveals numerous irregular and elongated nanoscale pores.
- The PSD reveals a hierarchical pore system dominated by micropores and mesopores, which primarily control the storage capacity. LPGA-derived CO_2 adsorption identifies ultra-micropores (< 1 nm) through DFT-PSD, whereas LPGA-N_2 adsorption indicates bimodal to multimodal mesopore distributions using BJH and DFT-PSD analyses. SAXS-based PSD, interpreted through the PDSP model, further confirms that the shale is largely dominated by mesopores.
- The SEM-based quantitative analysis of pore coordination number and throat radius indicates low to moderate pore connectivity. Micro-CT results showing low

connected porosity (1.96 %) relative to total porosity (4.55 %) further support this observation.

- Micro-CT analysis effectively identifies natural microfractures and macropores > 103 nm, which play a key role in governing fluid flow within the shale reservoir. The 3D reconstruction shows that connected porosity is primarily concentrated along margins due to these microfractures. Consistent with nanoscale observations from LPGA, SAXS, and FE-SEM, the small equivalent spherical diameter (~ 0.02 mm) from micro-CT further emphasizes the dominance of irregular and elongated pores and fractures.

9.1.6. Multiscale Characterization of Pore Evolution in Lesser Himalayan Black Shale from Krol Formation under Oxic Thermal Heating: Relevance to Untapped Shale Gas Extraction

Combustion-induced thermal stimulation is crucial for creating pathways for gas migration and increasing overall efficiency. The key findings of this investigation are as follows:

- The geochemical analysis of the Lesser Himalayan shale signifies hydrocarbon potential, indicating a gas-prone kerogen type that forms a basis for studying pore structure evolution during combustion to enhance the hydrocarbon extraction efficiency.
- The mass loss during combustion highlights the thermal behavior of shale, demonstrating the volatile release patterns and kerogen decomposition in two distinct phases/stages. Stage I (25–400 °C) is attributed to loss due to the liberation of moisture, while Stage II (400–550 °C) is attributed to loss due to organic matter decomposition.

- Combustion significantly affects the surface morphology, with noticeable changes in the pore system. At 100 °C, thermal degradation is inefficient, and pore compaction occurs as free moisture is removed. Above 100 °C, pores expand due to thermal-induced heat, leading to the merging of adjacent pores. The reduced contrast between organic matter pores and the surrounding mineral matrix within photomicrographs of shale treated at 400 °C suggests organic matter decomposition, leading to the formation of abundant organic pores. The surface becomes increasingly irregular and complex with combustion, as indicated by fractal values, showing the evolution of the pore structure with temperature. The fractal nature and FE-SEM images suggest that higher temperatures enhance pore connectivity, improving gas storage and recovery potential.
- Thermally treated shale's PSD provides valuable insights into gas recovery potential. At room temperature and 100 °C, micropores dominate. Beyond 100 °C, there is a noticeable shift toward larger meso and macropores. A sharp rise in PSD at 400 °C indicates extensive pore development due to structural deformation and oxidation of organic matter within the shale, resulting in significant pore expansion.
- Thermally induced heat not only widens existing pores but also creates new pores. The pore area initially decreases and then steadily increases with temperature, indicating the formation of new pores along with the expansion of existing ones.

9.2. Scope for Future Work

Although the research carried out in this thesis provides a comprehensive characterization of the Chandpur Phyllite and Krol Shale, some future studies can help in strengthening the findings. As the studied Krol Shale has a wide geographical stretch

extending from Solan (Himachal Pradesh) in the west to Nainital (Uttarakhand) in the east, with prominent exposures in the Mussoorie and Garhwal regions, the current investigations are limited to a single region (i.e., Garhwal region). Therefore, future work should incorporate sampling of the Krol Shale from multiple locations from different regions along the entire stretch to yield more reliable, representative conclusions. Furthermore, only oxic thermal heating under combustion has been carried out for the Krol Shale to enhance the pore structure, but anoxic heating under pyrolysis is equally important to understand the pore development. Therefore, future research should focus on anoxic thermal heating of the Krol Shale to compare the changes in the pore structure and gas recovery potential with oxic conditions. The Himalaya also experience considerable and regular variations in seasonal and diurnal temperature, which strongly affect the behavior of such weak and anisotropic rock masses. Therefore, such rock masses should undergo cyclic heating-cooling and freeze-thaw phenomenon before characterization to understand their durability, compositional changes, microstructural changes, and pore structure evolution under such environmental conditions. The above-mentioned future scope will help develop a comprehensive understanding of the behavior of Chandpur Phyllite and Krol Shale to enhance their applicability for different purposes.

References

Abbas, H. A., & Mohamed, Z. (2022). Anisotropic index strength behaviour and failure mode validation of weathered shale. *Geomechanics and Geoengineering*, *17*, 658–676.

Agliardi, F., Zanchetta, S., & Crosta, G. B. (2014). Fabric controls on the brittle failure of folded gneiss and schist. *Tectonophysics*, *637*, 150–162.

Akbay, D. (2023). Investigating the accuracy of specimen shape for point load index test in predicting the uniaxial compressive strength for rocks using regression analysis and machine learning. *Mining, Metallurgy & Exploration*, *40*, 2107–2115.

Akbay, D. (2024). Point load index applicability to predicting rocks' uniaxial compressive and tensile strengths: available data analysis and FEM-based validity check. *Strength of Materials*, *56*, 1045–1054.

Åkesson, U., Stigh, J., Lindqvist, J. E., & Göransson, M. (2003). The influence of foliation on the fragility of granitic rocks, image analysis and quantitative microscopy. *Engineering Geology*, *68*, 275–288.

Altindag, R. (2010). Assessment of some brittleness indexes in rock-drilling efficiency. *Rock Mechanics and Rock Engineering*, *43*, 361–370.

American Society for Testing and Materials (ASTM). (2001). *ASTM standards on disc* (Vol. 04.08). ASTM International.

Anand, A., Balikram, A., & Ojha, K. (2023). Evaluation of pore characteristics of deeper Cambay shale under simulated pre/postsorption conditions by CH4 and CO2 gases. *Energy & Fuels*, *37*, 16536–16550.

Anon (1995). The description and classification of weathered rocks for engineering purposes-Geological Society Engineering Group Working Party Report. *Quarterly Journal of Engineering Geology*, *28*, 207–242.

Ansari, T., Kainthola, A., Singh, K. H., Singh, T. N., & Sazid, M. (2021). Geotechnical and micro-structural characteristics of phyllite derived soil; implications for slope stability, Lesser Himalaya, Uttarakhand, India. *Catena*, *196*, 104906.

Auden, J. (1934). *Geological Survey of India* (Vol. 77). Rec.

Avnir, D., & Jaroniec, M. (1989). An isotherm equation for adsorption on fractal surfaces of heterogeneous porous materials. *Langmuir*, *5*, 1431–1433.

Avşar, E., Ulusay, R., & Mutlutürk, M. (2015). An experimental investigation of the mechanical behavior and microstructural features of a volcanic soil (Isparta, Turkey) and stability of cut slopes in this soil. *Engineering Geology*, *189*, 68–83.

Aydin, N. S. D., Aydin, A., & Malpas, J. (2002). Distribution of clay minerals along a weathered pyroclastic profile, Hong Kong. *Catena*, *50*, 17–41.

Azhar, M. U., Zhou, H., Yang, F., Younis, A., Lu, X., Fang, H., & Geng, Y. (2020). Water-induced softening behavior of clay-rich sandstone in Lanzhou Water Supply Project, China. *Journal of Rock Mechanics and Geotechnical Engineering*, *12*, 557–570.

Bahadur, J., Radlinski, A. P., Melnichenko, Y. B., Mastalerz, M., & Schimmelmann, A. (2015). Small-angle and ultrasmall-angle neutron scattering (SANS/USANS) study of New Albany shale: a treatise on microporosity. *Energy & Fuels*, *29*, 567–576.

Bai, F., Sun, Y., Liu, Y., & Guo, M. (2017). Evaluation of the porous structure of Huadian oil shale during pyrolysis using multiple approaches. *Fuel*, *187*, 1–8.

Bai, J., Kang, Y., Chen, M., Liang, L., You, L., & Li, X. (2019). Investigation of multi-gas transport behavior in shales via a pressure pulse method. *Chemical Engineering Journal*, *360*, 1667–1677.

Bakshi, T., & Vishal, V. (2021). A review on the role of organic matter in gas adsorption in shale. *Energy & Fuels*, *35*, 15249–15264.

Bakshi, T., Prusty, B. K., Pathak, K., & Pal, S. K. (2018). Pore characteristics of Damodar valley shale and their effect on gas storage potential. *Journal of Petroleum Science and Engineering*, *162*, 725–735.

Bal, A., Misra, S., & Sen, D. (2024). Nanopore heterogeneity and accessibility in oil and gas bearing cretaceous kg (raghampuram) shale, kg basin, india: An advanced multi-analytical study. *Natural Resources Research*, *33*, 1131–1154.

Baldermann, A., Dietzel, M., & Reinprecht, V. (2021). Chemical weathering and progressing alteration as possible controlling factors for creeping landslides. *Science of the Total Environment*, *778*, 146300.

Basu, A., & Aydin, A. (2006). Predicting uniaxial compressive strength by point load test: significance of cone penetration. *Rock Mechanics and Rock Engineering, 39,* 483–490

Basu, A., & Kamran, M. (2010). Point load test on schistose rocks and its applicability in predicting uniaxial compressive strength. *International Journal of Rock Mechanics and Mining Sciences*, *47*, 823–828.

Basu, A., Celestino, T. B., & Bortolucci, A. A. (2009). Evaluation of rock mechanical behaviors under uniaxial compression with reference to assessed weathering-grades. *Rock Mechanics and Rock Engineering*, *42*, 73–93.

Basu, A., Mishra, D. A., & Roychowdhury, K. (2013). Rock failure modes under uniaxial compression, Brazilian, and point load tests. *Bulletin of Engineering Geology and the environment*, *72*, 457–475.

Bates, R. L., & Jackson, J. A. (1984). Dictionary of geological terms. *Knopf Doubleday Publishing Group, 584.*

Behrestaghi, M. H. N., Rao, K. S., & Ramamurthy, T. (1996). Engineering geological and geotechnical responses of schistose rocks from dam project areas in India. *Engineering Geology*, *44*, 183–201.

Bennett, K. C., Berla, L. A., Nix, W. D., & Borja, R. I. (2015). Instrumented nanoindentation and 3D mechanistic modeling of a shale at multiple scales. *Acta Geotechnica*, *10*, 1–14.

Beucher, S. (1992). The watershed transformation applied to image segmentation. *Scanning microscopy*, *1992*, 28.

Bhat, G. M. (2019). Hydrocarbons exploration and production in India: Future Prospect. *Journal of the Geological Society of India*, *94*, 113–116.

Bhattacharya, S. N., & Chandra, K. (1979). Geochemical investigations for petroleum exploration in the Himalayan region. *Himalayan Geological Seminar, 3*, 217.

Bhowmick, S., Ram, B. K., & Mondal, T. K. (2022). An experimental approach to evaluate the role of rock failure modes in mechanical characterization of metabasalts. *Geotechnical and Geological Engineering*, *40*, 2867–2880.

Bian, K., Liu, J., Zhang, W., Zheng, X., Ni, S., & Liu, Z. (2019). Mechanical behavior and damage constitutive model of rock subjected to water-weakening effect and uniaxial loading. *Rock Mechanics and Rock Engineering*, *52*, 97–106.

Bieniawski, Z. T. (1974). Estimating the strength of rock materials. *Journal of the Southern African Institute of Mining and Metallurgy*, *74*, 312–320.

Bieniawski, Z. T. (1975). The point-load test in geotechnical practice. *Engineering geology*, *9*, 1–11.

Bieniawski, Z. T. (1989). Engineering rock mass classifications: a complete manual for engineers and geologists in mining, civil, and petroleum engineering. *John Wiley & Sons*.

Bobko, C., & Ulm, F. J. (2008). The nano-mechanical morphology of shale. *Mechanics of Materials*, *40*, 318–337.

Borrelli, L., Greco, R., & Gullà, G. (2007). Weathering-grade of rock masses as a predisposing factor to slope instabilities: Reconnaissance and control procedures. *Geomorphology*, *87*, 158–175.

Boruah, A., Rasheed, A., Mendhe, V. A., & Ganapathi, S. (2019). Specific surface area and pore size distribution in gas shales of Raniganj Basin, India. *Journal of Petroleum Exploration and Production Technology*, *9*, 1041–1050.

Bose, N., & Mukherjee, S. (2019). Field documentation and genesis of the back-structures from the Garhwal Lesser Himalaya, Uttarakhand, India. *The Geological Society of London, 481,* 111–125.

Bowker, K. A. (2003). Recent development of the Barnett shale play, Fort Worth Basin. *West Texas Geological Society Bulletin, 2,* 6.

Brace, W. F., Paulding Jr, B. W., & Scholz, C. H. (1966). Dilatancy in the fracture of crystalline rocks. *Journal of geophysical research*, *71*, 3939–3953.

Broch, E., & Franklin, J. A. (1972). The point-load strength test. In *International Journal of Rock Mechanics and Mining Sciences & Geomechanics Abstracts, 9,* 669–676.

BSI (1981). Code of practice for site investigations (British Standard BS5930:1981). *British Standards Institute, London*.

Buades, A., Coll, B., & Morel, J. M. (2005). A review of image denoising algorithms, with a new one. *Multiscale Modeling & Simulation*, *4*, 490–530.

Burchfiel, B. C., Zhiliang, C., Hodges, K. V., Yuping, L., Royden, L. H., Changrong, D., & Jiene, X. (1992). The South Tibetan detachment system, Himalayan orogen: Extension contemporaneous with and parallel to shortening in a collisional mountain belt. *Geological Society of America Special Paper, 269,* 1–41.

Cai, X., Zhou, Z., Liu, K., Du, X., & Zang, H. (2019). Water-weakening effects on the mechanical behavior of different rock types: phenomena and mechanisms. *Applied Sciences*, *9*, 4450.

Cao, T., Song, Z., Wang, S., & Xia, J. (2016). Characterization of pore structure and fractal dimension of Paleozoic shales from the northeastern Sichuan Basin, China. *Journal of Natural Gas Science and Engineering*, *35*, 882–895.

Cao, Y. H., Chen, W., Wang, T. X., & Yuan, Y. N. (2020). Thermally enhanced shale gas recovery: microstructure characteristics of combusted shale. *Petroleum Science*, *17*, 1056–1066.

Cargill, J. S., & Shakoor, A. (1990). Evaluation of empirical methods for measuring the uniaxial compressive strength of rock. In *International Journal of Rock Mechanics and Mining Sciences & Geomechanics Abstracts*, 27, 495–503.

Carosi, R., Lombardo, B., Musumeci, G., & Pertusati, P. C. (1999). Geology of the higher Himalayan crystallines in Khumbu Himal (eastern Nepal). *Journal of Asian Earth Sciences*, *17*, 785–803.

Carvalho, T. R. R., Leao, M. F., & Gomes Marques, E. A. (2020). Characterization of phyllite weathering profiles developed under tropical climate on Quadrilatero Ferrifero region, MG, Brazil. *Journal of South American Earth Sciences*, *103,* 102727.

Chandra, D., Bakshi, T., & Vishal, V. (2021). Thermal effect on pore characteristics of shale under inert and oxic environments: Insights on pore evolution. *Microporous and Mesoporous Materials*, *316*, 110969.

Chandra et al. (2023). Pore morphology in thermally-treated shales and its implication on CO2 storage applications: A gas sorption, SEM, and small-angle scattering study. *Fuel*, *331*, 125877.

Chandra, D., Vishal, V., Bahadur, J., & Sen, D. (2020a). A novel approach to identify accessible and inaccessible pores in gas shales using combined low-pressure sorption and SAXS/SANS analysis. *International Journal of Coal Geology*, *228*, 103556.

Chandra, D., Vishal, V., Bahadur, J., Agrawal, A. K., Das, A., Hazra, B., & Sen, D. (2022). Nano-scale physicochemical attributes and their impact on pore heterogeneity in shale. *Fuel*, *314*, 123070.

Chandra, D., Vishal, V., Debbarma, A., Banerjee, S., Pradhan, S. P., & Mishra, M. K. (2020b). Role of composition and depth on pore attributes of Barakar Formation Gas Shales of Ib Valley, India, using a combination of low-pressure sorption and image analysis. *Energy & Fuels*, *34*, 8085–8098.

Chauhan, O. S., Patil, S. K., & Suneethi, J. (2004). Fluvial influx and weathering history of the Himalaya since Last Glacial Maxima-isotopic, sedimentological and magnetic records from the Bay of Bengal. *Current Science*, *87,* 509–515.

Chen, J., & Xiao, X. (2014). Evolution of nanoporosity in organic-rich shales during thermal maturation. *Fuel*, *129*, 173–181.

Chen, S., Li, X., Chen, S., Wang, Y., Gong, Z., & Zhang, Y. (2021). A new application of atomic force microscopy in the characterization of pore structure and pore contribution in shale gas reservoirs. *Journal of Natural Gas Science and Engineering*, *88*, 103802.

Chen, W., Lei, Y., Chen, Y., & Sun, J. (2016). Pyrolysis and combustion enhance recovery of gas for two China shale rocks. *Energy & Fuels*, *30*, 10298–10305.

Chen, W., Lei, Y., Ma, L., & Yang, L. (2017). Experimental study of high temperature combustion for enhanced shale gas recovery. *Energy & Fuels*, *31*, 10003–10010.

Chen, W., Zhou, Y., Yang, L., Zhao, N., & Lei, Y. (2018). Experimental study of low-temperature combustion characteristics of shale rocks. *Combustion and Flame*, *194*, 285–295.

Chen, Y., Wei, L., Mastalerz, M., & Schimmelmann, A. (2015). The effect of analytical particle size on gas adsorption porosimetry of shale. *International Journal of Coal Geology*, *138*, 103–112.

Chen, Z., He, C., Xu, G., Ma, G., & Wu, D. (2019). A case study on the asymmetric deformation characteristics and mechanical behavior of deep-buried tunnel in phyllite. *Rock Mechanics and Rock Engineering*, *52*, 4527–4545.

Choi, Y. C., & Park, B. (2020). Effects of high-temperature exposure on fractal dimension of fly-ash-based geopolymer composites. Journal of Materials Research and Technology, 9, 7655–7668.

Chong, K. P., Chen, J. L., Dana, G. F., & Weber, J. A. (1984). Indirect and direct tensile behavior of Devonian oil shales (No. DOE/LC/10877–1567). *Wyoming Univ., Laramie (USA)*.

Chowdhury, M., Sarkar, K., Hazra, B., Sadeghpour, F., Panda, M., Vishal, V., & Ostadhassan, M. (2025). Effects of Rapid Thermal Exposure from Igneous Intrusions on the Pore Structure, Thermal Maturity, and Nanomechanical Properties of Coal and Shale. *Energy & Fuels*, *39*, 15689–15705.

Chukwuma, K., Bordy, E. M., & Coetzer, A. (2018). Evolution of porosity and pore geometry in the Permian Whitehill Formation of South Africa-A FE-SEM image analysis study. *Marine and Petroleum Geology*, *91*, 262–278.

Clarkson et al. (2013). Pore structure characterization of North American shale gas reservoirs using USANS/SANS, gas adsorption, and mercury intrusion. *Fuel*, *103*, 606–616.

Curtis, M. E., Cardott, B. J., Sondergeld, C. H., & Rai, C. S. (2012). The development of organic porosity in the Woodford Shale related to thermal maturity. In *SPE Annual Technical Conference and Exhibition,* SPE-160158.

Darabi, H., Ettehad, A., Javadpour, F., & Sepehrnoori, K. (2012). Gas flow in ultra-tight shale strata. *Journal of Fluid Mechanics*, *710*, 641–658.

Davudov, D., Moghanloo, R. G., & Zhang, Y. (2020). Interplay between pore connectivity and permeability in shale sample. *International Journal of Coal Geology*, *220*, 103427.

Dearman, W. R. (1995). Description and classification of weathered rocks for engineering purposes: the background to the BS5930: 1981 proposals. *Quarterly Journal of Engineering Geology and Hydrogeology*, *28*, 267–276.

DeCelles, P. G., Robinson, D. M., Quade, J., Ojha, T. P., Garzione, C. N., Copeland, P., & Upreti, B. N. (2001). Stratigraphy, structure, and tectonic evolution of the Himalayan fold-thrust belt in western Nepal. *Tectonics*, *20*, 487–509.

Deere, D. U., & Deere, D. W. (1989). *Rock Quality Designation (RQD) after Twenty Years* (No. WESCRGL891).

Deng, H., Hu, X., Li, H. A., Luo, B., & Wang, W. (2016). Improved pore-structure characterization in shale formations with FESEM technique. *Journal of Natural Gas Science and Engineering*, *35*, 309–319.

Dey, S., Dasgupta, P., Das, K., Goto, K. T., Matin, A., Suzuki, K., & Kubota, M. (2022). Krol Sandstone-black shale association of the Lesser Himalayan Neoproterozoic

succession, Himachal Pradesh, India: An unexplored record of the hothouse aftermath. *Marine and Petroleum Geology*, *141*, 105723.

Domnich, V., Gogotsi, Y., & Dub, S. (2000). Effect of phase transformations on the shape of the unloading curve in the nanoindentation of silicon. *Applied Physics Letters*, *76*, 2214–2216.

Dow, W. G. (1977). Kerogen studies and geological interpretations. *Journal of geochemical exploration*, *7*, 79–99.

Du, J., Luo, S., Hu, L., Guo, B., Guo, D., & Zhang, G. (2022). Multiscale mechanical properties of shales: grid nanoindentation and statistical analytics. *Acta Geotechnica*, *17*, 339–354.

Duan, X., Wang, W., Liu, S., Cao, Y., Zheng, Z., & Zhu, Q. (2023). Experimental investigation on mechanical behavior, energy evolution and gas permeability of anisotropic phyllite subjected to triaxial compression and cyclic loading. *Geomechanics for Energy and the Environment*, *35*, 100483.

Egli, M., Fitze, P., & Mirabella, A. (2001). Weathering and evolution of soils formed on granitic, glacial deposits: results from chronosequences of Swiss alpine environments. *Catena*, *45*, 19–47.

Erarslan, N., Liang, Z. Z., & Williams, D. J. (2012). Experimental and numerical studies on determination of indirect tensile strength of rocks. *Rock Mechanics and Rock Engineering*, *45*, 739–751.

Fan, M., Jin, Y., Chen, M., & Geng, Z. (2019). Mechanical characterization of shale through instrumented indentation test. *Journal of Petroleum Science and Engineering*, *174*, 607–616.

Fener, M. U. S. T. A. F. A., Kahraman, S., Bilgil, A., & Gunaydin, O. (2005). A comparative evaluation of indirect methods to estimate the compressive strength of rocks. *Rock Mechanics and Rock Engineering*, *38*, 329–343.

Feng, G., Kang, Y., Meng, T., Hu, Y. Q., & Li, X. H. (2017). The influence of temperature on mode I fracture toughness and fracture characteristics of sandstone. *Rock Mechanics and Rock Engineering*, *50*, 2007–2019.

Feng, G., Kang, Y., Wang, X., Hu, Y., & Li, X. (2020). Investigation on the failure characteristics and fracture classification of shale under Brazilian test conditions. *Rock Mechanics and Rock Engineering*, *53*, 3325–3340.

Fereidooni, D., Khanlari, G. R., Heidari, M., Sepahigero, A. A., & Kolahi-Azar, A. P. (2016). Assessment of inherent anisotropy and confining pressure influences on mechanical behavior of anisotropic foliated rocks under triaxial compression. *Rock Mechanics and Rock Engineering*, *49*, 2155–2163.

Forster, I. R. (1983). The influence of core sample geometry on the axial point-load test. *Intl J of Rock Mech & Mining Sci & Geomechanic Abs*, *20*.

Fredrich, J. T., Menéndez, B., & Wong, T. F. (1995). Imaging the pore structure of geomaterials. *Science*, *268*, 276–279.

Gao et al. (2017). Estimation of the equivalent elastic modulus in shale formation: Theoretical model and experiment. *Journal of Petroleum Science and Engineering*, *151*, 468–479.

Gao, Q., Zhou, Z., Han, Y., Zhou, D., Ghassemi, A., & Sun, Q. (2025). Study on hydraulic fracture propagation under the influence of natural fractures in fractured reservoirs. *Environmental earth sciences*, *84*, 425.

Garrido, M. E., Petnga, F. B., Martínez-Ibáñez, V., Serón, J. B., Hidalgo-Signes, C., & Tomás, R. (2022). Predicting the uniaxial compressive strength of a limestone exposed to high temperatures by point load and Leeb rebound hardness testing. *Rock Mechanics and Rock Engineering*, *55*, 1–17.

Garum, M., Glover, P. W., Lorinczi, P., Scott, G., & Hassanpour, A. (2020). Ultrahigh-resolution 3D imaging for quantifying the pore nanostructure of shale and predicting gas transport. *Energy & Fuels*, *35*, 702–717.

Ghosh Dastidar, S., Sarkar, K., Chandra, D., Hazra, B., & Vishal, V. (2025). Investigating Pore Characteristics and Their Dependence on Shale Composition: Case Study from a Permian Basin in India. *ACS Omega*, *10*, 4395–4405.

Goel, R. K., & Mitra, S. (2015, October). Importance of weathering in rock engineering. In *Int. Conf. on Engineering Geology in New Millennium* (pp. 231–245).

Gong, F. Q., Wang, Y. L., Luo, S. (2020). Rockburst proneness criteria for rock materials: Review and new insights. *Journal of Central South University, 27*, 2793–2821.

Goodarzi, M., Rouainia, M., Aplin, A. C., Cubillas, P., & de Block, M. (2017). Predicting the elastic response of organic-rich shale using nanoscale measurements and homogenisation methods. *Geophysical Prospecting*, *65*, 1597–1614.

Gou et al. (2019). Full-scale pores and micro-fractures characterization using FE-SEM, gas adsorption, nano-CT and micro-CT: A case study of the Silurian Longmaxi Formation shale in the Fuling area, Sichuan Basin, China. *Fuel*, *253*, 167–179.

Graham, S. P., Rouainia, M., Aplin, A. C., Cubillas, P., Fender, T. D., & Armitage, P. J. (2021). Geomechanical characterisation of organic-rich calcareous shale using AFM and nanoindentation. *Rock mechanics and rock engineering*, *54*, 303–320.

Greminger, M. (1982). Experimental studies of the influence of rock anisotropy on size and shape effects in point-load testing. *International Journal of Rock Mechanics and Mining & Geomechanics Abstracts*, *19*.

Guglielmin, M., Worland, M. R., Convey, P., & Cannone, N. (2012). Schmidt Hammer studies in the maritime Antarctic: application to dating Holocene deglaciation and estimating the effects of macrolichens on rock weathering. *Geomorphology*, *155*, 34–44.

Guo et al. (2023). Mechanical behavior and constitutive model of shale under real-time high temperature and high stress conditions. *Journal of Petroleum Exploration and Production Technology*, *13*, 827–841.

Gupta, A. S., & Rao, S. K. (1998). Index properties of weathered rocks: inter-relationships and applicability. *Bulletin of Engineering Geology and the Environment*, *57*, 161–172.

Gupta, A. S., & Rao, S. K. (2001). Weathering indices and their applicability for crystalline rocks. *Bulletin of Engineering Geology and the Environment*, *60*, 201–221.

Hack, R., & Price, D. (1997). Quantification of weathering. In *Engineering geology and the environment* (pp. 145–150). Balkema Publishers.

Hafiz et al. (2022). An assessment of the source potential and reservoir characterization for tight gas exploration in the Subathu Formation shale, Himalayan Foreland Basin, Northwestern India. *Journal of Asian Earth Sciences*, *230*, 105205.

Hall, K., Thorn, C., & Sumner, P. (2012). On the persistence of 'weathering'. *Geomorphology*, *149*, 1–10.

Han, L., Shi, X., Ni, H., Jiang, S., Che, M., & Qu, F. (2025). Fracture toughness evaluation of shale based on machine learning and micromechanical approach. *Engineering Fracture Mechanics*, *323*, 111194.

Hazra, B., Chandra, D., Lahiri, S., Vishal, V., Sethi, C., & Pandey, J. K. (2023). Pore evolution during combustion of distinct thermally mature shales: insights into potential *In situ* conversion. *Energy & Fuels*, *37*, 13898–13911.

Hazra et al. (2024). Experimental study on pore structure evolution of thermally treated shales: implications for CO2 storage in underground thermally treated shale horizons. *International Journal of Coal Science & Technology*, *11*, 61.

Hazra, B., Vishal, V., & Singh, D. P. (2020). Applicability of low-pressure CO2 and N2 adsorption in determining pore attributes of organic-rich shales and coals. *Energy & Fuels*, *35*, 456–464.

He, J., & Afolagboye, L. O. (2018). Influence of layer orientation and interlayer bonding force on the mechanical behavior of shale under Brazilian test conditions. *Acta Mechanica Sinica*, *34*, 349–358.

Herdes, C., Petit, C., Mejía, A., & Muller, E. A. (2018). Combined experimental, theoretical, and molecular simulation approach for the description of the fluid-phase behavior of hydrocarbon mixtures within shale rocks. *Energy & fuels*, *32*, 5750–5762.

Hoek, E., & Brown, E. T. (1980). Empirical strength criterion for rock masses. *Journal of the geotechnical engineering division*, *106*, 1013–1035.

Hoek, E., & Brown, E. T. (1997). Practical estimates of rock mass strength. *International journal of rock mechanics and mining sciences*, *34*, 1165–1186.

Hu, K., Feng, Q., & Wang, X. (2017). Experimental research on mechanical property of phyllite tunnel surrounding rock under different moisture state. *Geotechnical and Geological Engineering*, *35*, 303–311.

Hu et al. (2024). From micropores to macropores: Investigating pore characteristics of Longmaxi shale in the Sichuan Basin. *Energy & Fuels*, *38*, 3961–3981.

Huang, J., Jin, T., Barrufet, M., & Killough, J. (2020). Evaluation of CO2 injection into shale gas reservoirs considering dispersed distribution of kerogen. *Applied Energy*, *260*, 114285.

HUANG, L. Q. (2021). Mechanical properties and rockburst proneness of phyllite under uniaxial compression. *Transactions of Nonferrous Metals Society of China*, *31*(12), 3862–3878.

Hutton, A. C. (1995). Organic petrography of oil shales. In *Composition, Geochemistry and Conversion of Oil Shales*, 17–33.

International Society for Rock Mechanics (ISRM). (1978). Suggested methods for determining hardness and abrasiveness of rocks. In *International Journal of Rock Mechanics and Mining Sciences & Geomechanics Abstracts*, *15*, 89–97.

International Society for Rock Mechanics (ISRM). (1985). Suggested method for determining point load strength. In *International Journal of Rock Mechanics and Mining Sciences & Geomechanics Abstracts*, *22*, 51–60.

International Society for Rock Mechanics (ISRM). (2007). The complete ISRM suggested methods for rock characterization, testing and monitoring: 1974–2006.

International Society for Rock Mechanics (ISRM). (2014) The ISRM Suggested Methods for Rock Characterization, Testing and Monitoring: 2007–2014.

International Society for Rock Mechanics (ISRM). (2015) The ISRM Suggested Methods for Rock Characterization, Testing and Monitoring: 2007–2014.

Irfan, T. Y. (1996). Mineralogy, fabric properties and classification of weathered granites in Hong Kong. *Quarterly Journal of Engineering Geology and Hydrogeology*, *29*, 5–35.

Iverson, R. M. (2000). Landslide triggering by rain infiltration. *Water resources research*, *36*, 1897–1910.

Jain, A. K. (2014). When did India-Asia collide and make the Himalaya?. *Current Science*, 254–266.

Jamaluddin, A. K. M., Bennion, D. B., Thomas, F. B., & Ma, T. Y. (2000). Application of heat treatment to enhance permeability in tight gas reservoirs. *Journal of Canadian Petroleum Technology*, *39*.

Jamshidi, A. (2022). A comparative study of point load index test procedures in predicting the uniaxial compressive strength of sandstones. *Rock Mechanics and Rock Engineering*, *55*, 4507–4516.

Jamshidi, A., & Sousa, L. (2024). Accuracy of point load index and Brazilian tensile strength in predicting the uniaxial compressive strength of the rocks: A comparative study. *Materials*, *17*, 5081.

Jarvie, D. M., Hill, R. J., Ruble, T. E., & Pollastro, R. M. (2007). Unconventional shale-gas systems: The Mississippian Barnett Shale of north-central Texas as one model for thermogenic shale-gas assessment. *AAPG bulletin*, *91*, 475–499.

Ji et al. (2016). Fractal characteristics of nano-pores in the Lower Silurian Longmaxi shales from the Upper Yangtze Platform, south China. *Marine and Petroleum Geology*, *78*, 88–98.

Jiang, K., Zhou, W., Jia, N., Liu, R., Wang, H., Zhou, Q., & Tang, C. (2024). Analytical model of shale gas permeability based on the pore size distribution from FE-SEM and image analysis. *Arabian Journal for Science and Engineering*, *49*, 8661–8677.

Jin, J., Liu, J., Jiang, W., Cheng, W., & Zhang, X. (2022). Evolution of the anisotropic thermal conductivity of oil shale with temperature and its relationship with anisotropic pore structure evolution. *Energies*, *15*, 8021.

Jin, X., Shah, S. N., Roegiers, J. C., & Zhang, B. (2014). Fracability evaluation in shale reservoirs-an integrated petrophysics and geomechanics approach. In *SPE hydraulic fracturing technology conference and exhibition*, SPE-168589.

Karakul, H., Ulusay, R., & Isik, N. S. (2010). Empirical models and numerical analysis for assessing strength anisotropy based on block punch index and uniaxial compression tests. *International Journal of Rock Mechanics and Mining Sciences*, *47*, 657–665.

Kar et al. (2022). Source rock properties and kerogen decomposition kinetics of Eocene shales from petroliferous Barmer basin, western Rajasthan, India. *Journal of Natural Gas Science and Engineering*, *100*, 104497.

Kaufman, A. J., Jiang, G., Christie-Blick, N., Banerjee, D. M., & Rai, V. (2006). Stable isotope record of the terminal Neoproterozoic Krol platform in the Lesser Himalaya of northern India. *Precambrian Research*, *147*, 156–185.

Kaushal, H., Singh, A., & Samadhiya, N. K. (2024). Minero-petrographic, geochemical, and physical alteration of himachal gneiss an impact on uniaxial strength due to weathering. *Bulletin of Engineering Geology and the Environment*, *83*, 458.

Khadka et al. (2025). Impacts of Himalayan tectonism on Eocene gas shale and its pore structure within the Lesser Himalaya, Nepal: Insights for shale gas accumulation and preservation. *Petroleum Science, 23,* 103–126.

Khanlari, G. R., Heidari, M., & Momeni, A. A. (2012). Assessment of weathering processes effect on engineering properties of Alvand granitic rocks (west of Iran), based on weathering indices. *Environmental Earth Sciences*, *67*, 713–725.

Khanlari, G. R., Heidari, M., Sepahi-Gero, A. A., & Fereidooni, D. (2014a). Determination of geotechnical properties of anisotropic rocks using some index tests. *Geotechnical Testing Journal*, *37*, 242–254.

Khanlari, G. R., Heidari, M., Sepahigero, A. A., & Fereidooni, D. (2014b). Quantification of strength anisotropy of metamorphic rocks of the Hamedan province, Iran, as determined from cylindrical punch, point load and Brazilian tests. *Engineering Geology*, *169*, 80–90.

Khanlari, G., Rafiei, B., & Abdilor, Y. (2015). Evaluation of strength anisotropy and failure modes of laminated sandstones. *Arabian Journal of Geosciences*, *8*, 3089–3102.

Kong, L., Hadavimoghaddam, F., Li, C., Liu, K., Liu, B., Semnani, A., & Ostadhassan, M. (2021). AFM vs. Nanoindentation: Nanomechanical properties of organic-rich Shale. *Marine and Petroleum geology*, *132*, 105229.

Kuila, U. (2013). Measurement and interpretation of porosity and pore-size distribution in mudrocks: The hole story of shales. *Colorado School of Mines*.

Kuila, U., & Prasad, M. (2013). Specific surface area and pore-size distribution in clays and shales. *Geophysical prospecting*, *61*, 341–362.

Kumar, R., Bhargava, K., & Choudhury, D. (2017). Correlations of uniaxial compressive strength of rock mass with conventional strength properties through random number generation. *International Journal of Geomechanics*, *17*, 06016021.

Kumar, S., Chandra, D., Hazra, B., Vishal, V., & Pathegama Gamage, R. (2024). Nanopore characteristics of Barakar Formation shales and their impact on the gas storage potential of Korba and Raniganj Basins in India. *Energy & Fuels*, *38*, 3833–3847.

Kumar, S., Das, S., Bastia, R., & Ojha, K. (2018). Mineralogical and morphological characterization of Older Cambay Shale from North Cambay Basin, India: Implication for shale oil/gas development. *Marine and Petroleum Geology*, *97*, 339–354.

Kumar, U., Kumar, B., & Mallick, N. (2013). Groundwater prospects zonation based on RS and GIS using fuzzy algebra in Khoh River watershed, Pauri-Garhwal District, Uttarakhand, India. *Global perspectives on geography (GPG)*, *1*, 37–45.

Kumar, V., Curtis, M. E., Gupta, N., Sondergeld, C. H., & Rai, C. S. (2012). Estimation of elastic properties of organic matter and Woodford shale through nano-indentation measurements. In *SPE Canada unconventional resources conference*, SPE-162778.

Kundu, J., Mahanta, B., Sarkar, K., & Singh, T. N. (2018). The effect of lineation on anisotropy in dry and saturated Himalayan schistose rock under Brazilian test conditions. *Rock Mechanics and Rock Engineering*, *51*, 5–21.

Kuuskraa, V., Stevens, S. H., & Moodhe, K. D. (2013). Technically recoverable shale oil and shale gas resources: an assessment of 137 shale formations in 41 countries outside the United States. *US Energy Information Administration, US Department of Energy.*

Kwiecińska, B., Pusz, S., & Valentine, B. J. (2019). Application of electron microscopy TEM and SEM for analysis of coals, organic-rich shales and carbonaceous matter. *International Journal of Coal Geology*, *211*, 103203.

Lan, Q., Xu, M., Binazadeh, M., Dehghanpour, H., & Wood, J. M. (2015). A comparative investigation of shale wettability: The significance of pore connectivity. *Journal of Natural Gas Science and Engineering*, *27*, 1174–1188.

Lei et al. (2021). A comprehensive analysis of the pyrolysis effects on oil shale pore structures at multiscale using different measurement methods. *Energy*, *227*, 120359.

Li, B., Liu, J., Bian, K., Ai, F., Hu, X., Chen, M., & Liu, Z. (2019a). Experimental study on the mechanical properties weakening mechanism of siltstone with different water content. *Arabian Journal of Geosciences*, *12*, 656.

Li, C., Ostadhassan, M., Gentzis, T., Kong, L., Carvajal-Ortiz, H., & Bubach, B. (2018). Nanomechanical characterization of organic matter in the Bakken formation by microscopy-based method. *Marine and Petroleum Geology*, *96*, 128–138.

Li, C., Ostadhassan, M., Kong, L., & Bubach, B. (2019b). Multi-scale assessment of mechanical properties of organic-rich shales: A coupled nanoindentation, deconvolution analysis, and homogenization method. *Journal of Petroleum Science and Engineering*, *174*, 80–91.

Li, C., Zhong, S., Xie, H., Zhou, C., & Hu, J. (2026). Microscopic time-dependent mechanical behavior of shale derived from nanoindentation. *Deep Underground Science and Engineering*, *5*, 160–175.

Li, D., & Wong, L. N. Y. (2013). The Brazilian disc test for rock mechanics applications: review and new insights. *Rock mechanics and rock engineering*, *46*, 269–287.

Li, H., Lai, B., Lin, S. (2016). Shale mechanical properties influence factors overview and experimental investigation on water content effects. *Journal of Sustainable Energy Engineering 3*, 275–298

Li, H., Lai, B., Liu, H. H., Zhang, J., & Georgi, D. (2017). Experimental investigation on Brazilian tensile strength of organic-rich gas shale. *Spe Journal*, *22*, 148–161.

Li, L. (2001). Microscopic study and numerical simulation of the failure process of granite. *HKU Theses Online (HKUTO)*.

Li et al. (2022a). Nanoscale mechanical property variations concerning mineral composition and contact of marine shale. *Geoscience Frontiers*, *13*, 101405.

Li et al. (2022b). Pore structure characteristics and their controlling factors of deep shale: A case study of the Lower Silurian Longmaxi Formation in the Luzhou area, southern Sichuan Basin. *ACS omega*, *7*, 14591–14610.

Li, Z., Xu, G., Dai, Y., Zhao, X., & Fu, Y. (2021). Effects of foliation on deformation and failure mechanism of silty slates. *International Journal of Rock Mechanics and Mining Sciences*, *141*, 104703.

Lin, J., Huang, Y., Wang, M. K., Jiang, F., Zhang, X., & Ge, H. (2015). Assessing the sources of sediment transported in gully systems using a fingerprinting approach: an example from South-east China. *Catena*, *129*, 9–17.

Liu, G., Peng, Y., Zuo, Q., Su, Y., & Wu, L. (2022a). Dynamic mechanics and energy dissipation of saturated layered phyllite. *Minerals*, *12*, 1246.

Liu et al. (2022b). Microstructural analysis of organic matter in shale by SAXS and WAXS methods. *Petroleum Science*, *19*, 979–989.

Liu, K., Ostadhassan, M., & Kong, L. (2018). Multifractal characteristics of Longmaxi Shale pore structures by N2 adsorption: A model comparison. *Journal of Petroleum Science and Engineering*, *168*, 330–341.

Liu, M., & Gadikota, G. (2018). Probing the influence of thermally induced structural changes on the microstructural evolution in shale using multiscale X-ray scattering measurements. *Energy & Fuels*, *32*, 8193–8201.

Liu, Q., Liang, B., Sun, W., & Zhao, H. (2021a). Experimental study on the difference of shale mechanical properties. *Advances in Civil Engineering*, *2021*, 6677992.

Liu, X., Deng, Y., & Zou, B. (2023a). Implementation of a constitutive model for anisotropic rocks based on modified Lade failure criterion. *Scientific Reports*, *13*, 3210.

Liu, X., Zhou, Y., & Xu, D. (2023b). Anisotropic mechanical properties of quartz mica schist subjected to true triaxial compression. *Environmental Earth Sciences*, *82*, 204.

Liu et al. (2014). An improved differential box-counting method to estimate fractal dimensions of gray-level images. *Journal of visual communication and Image Representation*, *25*, 1102–1111.

Liu, Y., & Hou, J. (2020). Selective adsorption of CO2/CH4 mixture on clay-rich shale using molecular simulations. *Journal of CO2 Utilization*, *39*, 101143.

Liu, Y., Liu, S., & Kang, Y. (2021b). Probing nanomechanical properties of a shale with nanoindentation: heterogeneity and the effect of water-shale interactions. *Energy & Fuels*, *35*, 11930–11946.

Liu, Z., Liu, D., Cai, Y., Yao, Y., Pan, Z., & Zhou, Y. (2020). Application of nuclear magnetic resonance (NMR) in coalbed methane and shale reservoirs: A review. *International Journal of Coal Geology*, *218*, 103261.

Loucks, R. G., Reed, R. M., Ruppel, S. C., & Hammes, U. (2012). Spectrum of pore types and networks in mudrocks and a descriptive classification for matrix-related mudrock pores. *AAPG bulletin*, *96*, 1071–1098.

Lowell, S., Shields, J. E., Thomas, M. A., & Thommes, M. (2012). Characterization of porous solids and powders: surface area, pore size and density. *Springer Science & Business Media, 16*.

Lu, Y., Li, Y., Wu, Y., Luo, S., Jin, Y., & Zhang, G. (2020). Characterization of shale softening by large volume-based nanoindentation. *Rock Mechanics and Rock Engineering*, *53*, 1393–1409.

Luo et al. (2020). Quantitative assessment of weathering degree of the Touzhai rock-avalanche deposit in Southwest China. *Geomorphology*, *359*, 107162.

Maddirala, R., Shukla, R., Pramanik, R., Mishra, D. A., Sharma, A., Jain, R., & Kakati, H. (2024). Impact of Pulse Plasma-Based Shockwave Technology on Sandstone Porosity and Pore Connectivity Using Ultrasonic Compressional Wave Velocity and Microtomography. *Energy & Fuels*, *38*, 20433–20448.

Mahanta, B., Singh, T. N., Ranjith, P. G., & Vishal, V. (2018). Experimental investigation of the influence of strain rate on strength; failure attributes and mechanism of Jhiri shale. *Journal of Natural Gas Science and Engineering*, *58*, 178–188.

Makumbi, M. N., & Jackson, M. L. (1977). Weathering of Karroo argillite under equatorial conditions. *Geoderma*, *19*, 181–197.

Mandelbrot, B. B., Wheeler, J. A. (1983). The Fractal Geometry of Nature. *American Journal of Physics, 51*, 286–287.

Mani, D., Patil, D. J., Dayal, A. M., Kavitha, S., Hafiz, M., Hakhoo, N., & Bhat, G. M. (2014). Gas potential of Proterozoic and Phanerozoic shales from the NW Himalaya, India: Inferences from pyrolysis. *International journal of coal geology*, *128*, 81–95.

Manjunath, G. L., & Jha, B. (2019). Geomechanical characterization of gondwana shale across nano-micro-meso scales. *International Journal of Rock Mechanics and Mining Sciences*, *119*, 35–45.

Marques, E. A. G., & Williams, D. J. (2015). Weathering profiles of Bunya Phyllite in southwest Brisbane-A geotechnical approach. In *12th Australia New Zealand Conference on Geomechanics. Wellington. Anais... Wellington: Changing the Face of the Earth*, 1–8.

Marques, E. A. G., Williams, D. J., Assis, I. R., & Leão, M. F. (2017). Effects of weathering on characteristics of rocks in a subtropical climate: weathering

morphology, *In situ*, laboratory and mineralogical characterization. *Environmental Earth Sciences*, *76*, 602.

Martin, R. P., & Hencher, S. R. (1986). Principles for description and classification of weathered rock for engineering purposes. *Geological Society, London, Engineering Geology Special Publications*, *2*, 299–308.

Masoumi, H., Roshan, H., Hedayat, A., & Hagan, P. C. (2018). Scale-size dependency of intact rock under point-load and indirect tensile Brazilian testing. *International Journal of Geomechanics*, *18*, 04018006.

Mastalerz, M., Drobniak, A., & Hower, J. C. (2021). Controls on reservoir properties in organic-matter-rich shales: Insights from MICP analysis. *Journal of Petroleum Science and Engineering*, *196*, 107775.

Mazumder, M., Bal, A., Tripathy, A., Liu, S., & Singh, T. N. (2024). Multiscale assessment of transformation in pore system of shale during combustion: An insight into poromechanical response and sorption dynamics. *Energy & Fuels*, *38*, 17510–17524.

Mazumder, M., Tripathy, A., Bal, A., Liu, S., Singh, T. N., & Pan, Z. (2026). Multi-proxy assessment of thermal and microstructural evolution in sub-bituminous coal affected by igneous Intrusion: Implications for CBM storage and transport. *Fuel*, *405*, 136414.

Mehrotra, V. K., Mitra, S., & Agrawal, C. K. (1991, September). Need of long-term evaluation of rock parameters in the Himalaya. In *ISRM Congress*, *ISRM-7CONGRESS*.

Meng, F., Wong, L. N. Y., & Zhou, H. (2021). Rock brittleness indices and their applications to different fields of rock engineering: A review. *Journal of rock mechanics and geotechnical Engineering*, *13*, 221–247.

Mevawala, C., Jiang, Y., & Bhattacharyya, D. (2019). Techno-economic optimization of shale gas to dimethyl ether production processes via direct and indirect synthesis routes. *Applied Energy*, *238*, 119–134.

Mishra, D. A., & Basu, A. (2012). Use of the block punch test to predict the compressive and tensile strengths of rocks. *International Journal of Rock Mechanics and Mining Sciences*, *51*, 119–127.

Mishra, D. A., & Ram, B. K. (2024). A review on evaluation of microstructural parameters to estimate the strength of virtually isotropic rock materials. *Geotechnical and Geological Engineering*, *42*, 4627–4649.

Mishra, D. K., Samad, S. K., Varma, A. K., & Mendhe, V. A. (2018). Pore geometrical complexity and fractal facets of Permian shales and coals from Auranga Basin, Jharkhand, India. *Journal of Natural Gas Science and Engineering*, *52*, 25–43.

Mishra, P., & Mukhopadhyay, D. K. (2012). Structural evolution of the frontal fold-thrust belt, NW Himalaya from sequential restoration of balanced cross-sections and its

hydrocarbon potential. *Geological Society, London, Special Publications, 366,* 201-228.

Mitra, S. (1991). Studies on long-term behaviour of underground powerhouse cavities in soft rocks. *Ph.D. Thesis, University of Roorkee (now IIT Roorkee), Roorkee, India.*

Mitra, S., Singh, B., Rajvanshi, U. S. (1988). Performance of Chhibro Underground Powerhouse Cavities after Charging Water Conductor System - A Case Study. *In: International Symposium on Underground Engineering, New Delhi, India, Vol. I,* 425–430.

Momeni, A., Hashemi, S. S., Khanlari, G. R., & Heidari, M. (2017). The effect of weathering on durability and deformability properties of granitoid rocks. *Bulletin of Engineering Geology and the Environment*, *76*, 1037–1049.

Moses, C., Robinson, D., & Barlow, J. (2014). Methods for measuring rock surface weathering and erosion: A critical review. *Earth-Science Reviews*, *135*, 141–161.

Mukherjee, S. (2013). Channel flow extrusion model to constrain dynamic viscosity and Prandtl number of the Higher Himalayan Shear Zone. *International Journal of Earth Sciences*, *102*, 1811-1835.

Navarre-Sitchler, A. K., Cole, D. R., Rother, G., Jin, L., Buss, H. L., Brantley, S. L. (2013). Porosity and surface area evolution during weathering of two igneous rocks. *Geochimica et Cosmochimica Acta 109*, 400–413.

Nilankar, K., Singh, D., Singh, H. K., & Han, G. (2024a). Characterization and behavior of Raniganj shale under heated environment. *Fuel*, *366*, 131377.

Nilankar, K., Singh, D., Singh, H. K., Kumar, A., & Mustapha, K. A. (2024b). Evolution of pore morphometry and compositional changes in immature Raniganj Shale under heated environment: Implications for enhanced gas recovery. *Energy & Fuels*, *38*, 22128–22145.

Nuttal, B. C., Eble, C., Bustin, R. M., & Drahovzal, J. A. (2005). Analysis of Devonian black shales in Kentucky for potential carbon dioxide sequestration and enhanced natural gas production. In *Greenhouse Gas Control Technologies 7*, 2225–2228.

Obradors-Prats, J., Rouainia, M., Aplin, A. C., & Crook, A. J. (2017). Assessing the implications of tectonic compaction on pore pressure using a coupled geomechanical approach. *Marine and Petroleum Geology*, *79*, 31–43.

Oliver, W. C., & Pharr, G. M. (1992). An improved technique for determining hardness and elastic modulus using load and displacement sensing indentation experiments. *Journal of materials research*, *7*, 1564–1583.

Otsu, N. (1975). A threshold selection method from gray-level histograms. *Automatica*, *11*, 285–296.

Ozturk, C. A., & Nasuf, E. (2013). Strength classification of rock material based on textural properties. *Tunnelling and Underground Space Technology*, *37*, 45–54.

Pandey, B., Pathak, D. B., Mathur, N., Jaitly, A. K., Singh, A. K., & Singh, P. K. (2018). A preliminary evaluation on the prospects of hydrocarbon potential in the carbonaceous shales of Spiti and Chikkim formations, Tethys Himalaya, India. *Journal of the Geological Society of India*, *92*, 427–434.

Paul, A., Mukherjee, S., & Biswas, M. (2025). Global review on shale: Focus on hydrocarbon geoscience & carbon sequestration. *Results in Earth Sciences*, *3*, 100088.

Paul, D., Malik, S., Mishra, D. K., & Hiwale, R. (2021). Shale gas: An indian market perspective. *International Journal of Energy Economics and Policy*, *11*, 126–136.

Pei et al. (2025). Multiscale anisotropic mechanical properties of oil shale: new insights from nanoindentation profiling. *Petroleum Science, 23,* 33–51.

Perri, F., Borrelli, L., Gullà, G., & Critelli, S. (2014). Chemical and minero-petrographic features of Plio-Pleistocene fine-grained sediments in Calabria, southern Italy. *Italian Journal of Geosciences*, *133*, 101–115.

Pöhl, F. (2019). Pop-in behavior and elastic-to-plastic transition of polycrystalline pure iron during sharp nanoindentation. *Scientific reports*, *9*, 15350.

Puniya, N., Sharma, S., Mukherjee, S., Patidar, A. K., & Puniya, M. K. (2026). Highway expansion and landslide susceptibility in the lesser himalaya: geospatial modelling and structural analysis along the Chamba-Sainj corridor. *Engineering Research Express*, *8*, 125112.

Qi, H., Ma, J., & Wong, P. Z. (2002). Adsorption isotherms of fractal surfaces. *Colloids and Surfaces A: Physicochemical and Engineering Aspects*, *206*, 401–407.

Qiu, J., Li, D., & Li, X. (2017). Dynamic failure of a phyllite with a low degree of metamorphism under impact Brazilian test. *International Journal of Rock Mechanics and Mining Sciences*, *94*, 10–17.

Rabbani, A., & Ayatollahi, S. (2015). Comparing three image processing algorithms to estimate the grain-size distribution of porous rocks from binary 2D images and sensitivity analysis of the grain overlapping degree. *Special Topics & Reviews in Porous Media: An International Journal*, *6*, 71–89.

Rabbani, A., & Salehi, S. (2017). Dynamic modeling of the formation damage and mud cake deposition using filtration theories coupled with SEM image processing. *Journal of Natural Gas Science and Engineering*, *42*, 157–168.

Radlinski et al. (2004). Application of SAXS and SANS in evaluation of porosity, pore size distribution and surface area of coal. *International journal of coal geology*, *59*, 245–271.

Radliński, A. P., Radlińska, E. Z., Agamalian, M., Wignall, G. D., Lindner, P., & Randl, O. G. (1999). Fractal geometry of rocks. *Physical Review Letters*, *82*, 3078.

Raiverman, V., Kunte, S. V., & Mukherjea, A. (1984). Basin geometry, Cenozoic sedimentation and hydrocarbon prospects in north western Himalaya and Indo-Gangetic plains. *Petroleum Asia Journal*, *6*, 67–92.

Ram, B. K., & Basu, A. (2019a). A modified JRC-JCS model and its applicability to weathered joints of granite and quartzite. *Bulletin of Engineering Geology and the Environment*, *78*, 6089–6099.

Ram, B. K., & Basu, A. (2019b). Shear behavior of unfilled-planar quartzitic rock joints with reference to weathering-grade of joint surfaces. *Rock Mechanics and Rock Engineering*, *52*, 4113–4121.

Ram, B. K., & Gupta, V. (2024). Physico-mechanical characterization of Higher Himalayan granite under the thermal treatments of different heating-cooling conditions. *Acta Geotechnica*, *19*, 2841–2854.

Ramamurthy, T., Rao, G. V., & Singh, J. (1993). Engineering behaviour of phyllites. *Engineering Geology*, *33*, 209–225.

Rana, N., Singh, S., Sundriyal, Y. P., Rawat, G. S., & Juyal, N. (2016). Interpreting the geomorphometric indices for neotectonic implications: An example of Alaknanda valley, Garhwal Himalaya, India. *Journal of Earth System Science*, *125*, 841–854.

Rani, S., Prusty, B. K., & Pal, S. K. (2020). Characterization of shales from Damodar valley coalfields for CH4 recovery and CO2 sequestration. *Environmental Technology & Innovation*, *18*, 100739.

Rastegar, F., Nejati, H. R., & Nazerigivi, A. (2020). On applicability of some indirect tests for estimation of tensile strength of anisotropic rocks. *Journal of Mining and Environment, 11*, 711–720.

Read, J. R. L., Thornton, P. N., & Regan, W. M. (1980). A rational approach to the point load test. In *Australia-New Zealand Conference on Geomechanics (3rd: 1980: Wellington, NZ)*, 2–35.

Reeves, M. J. (1985, December). Rock surface roughness and frictional strength. In *International Journal of Rock Mechanics and Mining Sciences & Geomechanics Abstracts*, *22*, 429–442.

Regmi, A. D., Yoshida, K., Dhital, M. R., & Pradhan, B. (2014). Weathering and mineralogical variation in gneissic rocks and their effect in Sangrumba Landslide, East Nepal. *Environmental Earth Sciences*, *71*, 2711–2727.

Rezaeyan, A., Pipich, V., & Busch, A. (2021). MATSAS: a small-angle scattering computing tool for porous systems. *Applied Crystallography*, *54*, 697–706.

Robyr, M., Vannay, J. C., Epard, J. L., & Steck, A. (2002). Thrusting, extension, and doming during the polyphase tectonometamorphic evolution of the High Himalayan Crystalline Zone in NW India. *Journal of Asian Earth Sciences*, *21*, 221–239.

Rouquerol, J., Rouquerol, F., & Sing K. S. W. (1998). Absorption by Powders and Porous Solids. *Academic press, ISBN 0080526012*.

Ruan, C. D., & Ward, C. R. (2002). Quantitative X-ray powder diffraction analysis of clay minerals in Australian coals using Rietveld methods. *Applied Clay Science*, *21*, 227–240.

Ruppert, L. F., Sakurovs, R., Blach, T. P., He, L., Melnichenko, Y. B., Mildner, D. F., & Alcantar-Lopez, L. (2013). A USANS/SANS Study of the Accessibility of Pores in the Barnett Shale to Methane and Water. *Energy & Fuels*, *27*, 772–779.

Şahin, M., Ulusay, R., & Karakul, H. (2020). Point load strength index of half-cut core specimens and correlation with uniaxial compressive strength. *Rock Mechanics and Rock Engineering*, *53*, 3745–3760.

Santi, P. M. (2006). Field methods for characterizing weak rock for engineering. *Environmental & Engineering Geoscience*, *12*, 1–11.

Saroglou, H., & Tsiambaos, G. (2006). Point load strength determination of anisotropic rocks. In *EUROCK*, 603–608.

Sati, S. P., Sundriyal, Y. P., & Rawat, G. S. (2007). Geomorphic indicators of neotectonic activity around Srinagar (Alaknanda basin), Uttarakhand. *Current Science, 92*, 824–829.

Schuh, C. A. (2006). Nanoindentation studies of materials. *Materials today*, *9*, 32–40.

Searle, M. P. (1986). Structural evolution and sequence of thrusting in the High Himalayan, Tibetan—Tethys and Indus suture zones of Zanskar and Ladakh, Western Himalaya. *Journal of structural geology*, *8*, 923–936.

Shah, S. K. (1991). Stratigraphic setting of the Phanerozoic rocks along the northern boundary of the Indian plate. *Physics and Chemistry of the Earth*, *18*, 317–328.

Sharma, K. K. (1998). Geologic and tectonic evolution of the Himalaya before and after the India-Asia collision. *Proceedings of the Indian Academy of Sciences-Earth and Planetary Sciences*, *107*, 265–282.

Shaw, R., & Mukherjee, S. (2022). The development of carbon capture and storage (CCS) in India: A critical review. *Carbon Capture Science & Technology*, *2*, 100036.

Shekhar, S., Saklani, P. S., & Bhola, A. M. (2006). Geology and structure of Srinagar, Garhwal Himalaya. *Himalaya (geological aspects)*, *117*, 1267–1269.

Shi, X., He, Z., Long, S., Peng, Y., Li, D., & Jiang, S. (2019). Loading rate effect on the mechanical behavior of brittle longmaxi shale in nanoindentation. *International Journal of Hydrogen Energy*, *44*, 6481–6490.

Shukla, P., Kumar, V., Curtis, M., Sondergeld, C. H., & Rai, C. S. (2013, June). Nanoindentation studies on shales. In *ARMA US Rock Mechanics/Geomechanics Symposium*, ARMA-2013.

Sing, K. S. (1985). Reporting physisorption data for gas/solid systems with special reference to the determination of surface area and porosity (Recommendations 1984). *Pure and Applied Chemistry*, *57*, 603–619.

Singh, D., Nilankar, K., Ram, B. K., Singh, H. K., Sharma, A., & Srivastava, P. (2025a). Influence of Specimen Geometry on the Point Load Strength Anisotropy of Phyllite. *Geotechnical and Geological Engineering*, *43*, 464.

Singh, D., Nilankar, K., Singh, H. K., & Ram, B. K. (2025b). Impact of water saturation on physico-mechanical properties of fragile Chandpur Phyllite at varying foliation angles. *Geotechnical and Geological Engineering*, *43*, 2.

Singh, D., Nilankar, K., Singh, H. K., Kumar, A., Vishal, V., & Mustapha, K. A. (2025c). Multiscale Characterization of Pore Evolution in Lesser Himalayan Black Shale from Krol Formation under Oxic Thermal Heating: Relevance to Untapped Shale Gas Extraction. *Energy & Fuels*, *39*, 11723–11738.

Singh, D., Singh, H. K., Kumar, A., Mishra, D. A., & Vishal, V. (2026). Pore System Characterization of Untapped Himalayan Shale Using an Integrated Multianalytical Approach: Bridging Nano-to Macro-Scale Investigation. *Energy & Fuels*, *40*, 4594–4612.

Singh, H. O., Ansari, T. A., Singh, T. N., & Singh, K. H. (2022). Development of statistical models to predict the mechanical properties of some metamorphic rocks from P-wave velocity and certain physical properties. *Geotechnical and Geological Engineering*, *40*, 4247–4268.

Singh, I. B., & Rai, V. (1983). Fauna and biogenic structures in Krol-Tai succession (Vendian-Early Cambrian), Lesser Himalaya: their biostratigraphic and palaeoecological significance. *Journal of the Palaeontological Society of India*, *28*, 67-90.

Singh, J., Ramamurthy, T., & Venkatappa Rao, G. (1989). Strength anisotropies in rocks. *Indian Geotechnical Journal*, *19*, 147–166.

Singh, M., Samadhiya, N. K., Kumar, A., Kumar, V., & Singh, B. (2015). A nonlinear criterion for triaxial strength of inherently anisotropic rocks. *Rock Mechanics and Rock Engineering*, *48*, 1387–1405.

Singh, V. K., & Singh, D. P. (1993). Correlation between point load index and compressive strength for quartzite rocks. *Geotechnical and geological Engineering, 11*, 269–272.

Srinivasan, V., Tripathy, A., Gupta, T., & Singh, T. N. (2020). An investigation on the influence of thermal damage on the physical, mechanical and acoustic behavior of Indian Gondwana shale. *Rock Mechanics and Rock Engineering*, *53*, 2865–2885.

Sun, B., Ren, F., & Wang, H. (2022). Experimental investigation on anisotropic characteristics of carbonaceous slate under uniaxial compression. *Environmental Earth Sciences*, *81*, 405.

Sun, Q., Zhang, W., & Qian, H. (2016). Effects of high temperature thermal treatment on the physical properties of clay. *Environmental Earth Sciences*, *75*, 610.

Sun, W., Feng, Y., Jiang, C., & Chu, W. (2015). Fractal characterization and methane adsorption features of coal particles taken from shallow and deep coalmine layers. *Fuel*, *155*, 7–13.

Takahashi, M., Mizoguchi, K., Kitamura, K., & Masuda, K. (2007). Effects of clay content on the frictional strength and fluid transport property of faults. *Journal of Geophysical Research: Solid Earth*, *112,* 148–227.

Tandon, R. S., & Gupta, V. (2015). Estimation of strength characteristics of different Himalayan rocks from Schmidt hammer rebound, point load index, and compressional wave velocity. *Bulletin of Engineering Geology and the Environment*, *74*, 521–533.

Tavallali, A., & Vervoort, A. (2010). Effect of layer orientation on the failure of layered sandstone under Brazilian test conditions. *International journal of rock mechanics and mining sciences*, *47*, 313–322.

Thommes, M., Kaneko, K., Neimark, A. V., Olivier, J. P., Rodriguez-Reinoso, F., Rouquerol, J., & Sing, K. S. (2015). Physisorption of gases, with special reference to the evaluation of surface area and pore size distribution (IUPAC Technical Report). *Pure and applied chemistry*, *87*, 1051–1069.

Tian, H., Pan, L., Xiao, X., Wilkins, R. W., Meng, Z., & Huang, B. (2013). A preliminary study on the pore characterization of Lower Silurian black shales in the Chuandong Thrust Fold Belt, southwestern China using low pressure N2 adsorption and FE-SEM methods. *Marine and Petroleum Geology*, *48*, 8–19.

Tian, X., He, X., Song, D., Li, Z., Khan, M., Liu, H., & Qiu, L. (2022). AFM characterization of surface mechanical and electrical properties of some common rocks. *International Journal of Mining Science and Technology*, *32*, 435–445.

Tian, X., Song, D., He, X., Khan, M., Li, Z., Liu, H., & Liu, X. (2021). Presenting *In situ* AFM investigations for the evolution of micro-surface topography and elastic modulus of rock under variable loads. *Engineering Fracture Mechanics*, *258*, 108107.

Tiwari, P., Deo, M., Lin, C. L., & Miller, J. D. (2013). Characterization of oil shale pore structure before and after pyrolysis by using X-ray micro CT. *Fuel*, *107*, 547–554.

Tuğrul, A. (2004). The effect of weathering on pore geometry and compressive strength of selected rock types from Turkey. *Engineering geology*, *75*, 215–227.

Upreti, B. N. (1999). An overview of the stratigraphy and tectonics of the Nepal Himalaya. *Journal of Asian Earth Sciences*, *17*, 577–606.

Valdiya, K. S. (1983). Lesser Himalayan geology: crucial problems and controversies. *Current science, 52*, 839–857.

Vicente, M. A. (1983). Clay mineralogy as the key factor in weathering of 'arenisca dorada'(golden sandstone) of Salamanca, Spain. *Clay Minerals*, *18*, 215–217.

Viles, H. A. (2013). Linking weathering and rock slope instability: non-linear perspectives. *Earth Surface Processes and Landforms*, *38*, 62–70.

Vishal, V., Chandra, D., Bahadur, J., Sen, D., Hazra, B., Mahanta, B., & Mani, D. (2019). Interpreting pore dimensions in gas shales using a combination of SEM imaging, small-angle neutron scattering, and low-pressure gas adsorption. *Energy & Fuels*, *33*, 4835–4848.

Vishal, V., Rizwan, M., Mahanta, B., Pradhan, S. P., & Singh, T. N. (2022). Temperature effect on the mechanical behavior of shale: Implication for shale gas production. *Geosystems and Geoenvironment*, *1*, 100078.

Wahengbam, A., Singh, Y. R., Singh, L. S., & Singh, C. K. (2025). Source rock and palaeoecology of the Permian Damuda Formation, Group, Sikkim: Rock-Eval pyrolysis and organic matter approach. *Journal of Earth System Science*, *134*, 62.

Wang, J. A., & Park, H. D. (2001). Comprehensive prediction of rockburst based on analysis of strain energy in rocks. *Tunnelling and underground space technology*, *16*, 49–57.

Wang et al. (2025a). Examining the reliability of current micro-and nano-indentation-based rock mechanical upscaling schemes: a comprehensive comparison with uniaxial/triaxial macroscopic mechanical testing. *Geomechanics and Geophysics for Geo-Energy and Geo-Resources*, *11*, 28.

Wang, J., Yang, C., Liu, Y., Li, Y., & Xiong, Y. (2022). Using nanoindentation to characterize the mechanical and creep properties of shale: load and loading strain rate effects. *ACS Omega*, *7*, 14317–14331.

Wang et al. (2024a). Point Load Strength Test Power Index of Irregular Sandy Dolomite Blocks: M. Wang et al. *Rock Mechanics and Rock Engineering*, *57*, 5279–5290.

Wang, M., Xue, H., Tian, S., Wilkins, R. W., & Wang, Z. (2015). Fractal characteristics of Upper Cretaceous lacustrine shale from the Songliao Basin, NE China. *Marine and Petroleum Geology*, *67*, 144–153.

Wang, Q., & Li, R. (2016). Natural gas from shale formation: A research profile. *Renewable and Sustainable Energy Reviews*, *57*, 1–6.

Wang, Q., & Li, R. (2017). Research status of shale gas: A review. *Renewable and Sustainable Energy Reviews*, *74*, 715–720.

Wang et al. (2025b). Integrated experimental studies of pore structure and fluid uptake in the Bossier Shale in eastern Texas, USA. *Fuel*, *384*, 133926.

Wang, Y., Hou, Z. Q., & Hu, Y. Z. (2018). *In situ* X-ray micro-CT for investigation of damage evolution in black shale under uniaxial compression. *Environmental Earth Sciences*, *77*, 717.

Wang et al. (2024b). Recent techniques on analyses and characterizations of shale gas and oil reservoir. *Energy Reviews*, *3*, 100067.

Wang, Y., Zhu, Y., Chen, S., & Li, W. (2014). Characteristics of the nanoscale pore structure in Northwestern Hunan shale gas reservoirs using field emission scanning electron microscopy, high-pressure mercury intrusion, and gas adsorption. *Energy & Fuels*, *28*, 945–955.

Wei, M., Zhang, L., Xiong, Y., Li, J., & Peng, P. A. (2016). Nanopore structure characterization for organic-rich shale using the non-local-density functional theory by a combination of N2 and CO2 adsorption. *Microporous and mesoporous materials*, *227*, 88–94.

Wei, W. E. I., & Algeo, T. J. (2020). Elemental proxies for paleosalinity analysis of ancient shales and mudrocks. *Geochimica et Cosmochimica Acta*, *287*, 341–366.

Weijermars, R., Wang, J., & Nelson, R. (2020). Stress concentrations and failure modes in horizontal wells accounting for elastic anisotropy of shale formations. *Earth-Science Reviews*, *200*, 102957.

Welivitiya, W. D. P., & Hancock, G. R. (2024). Quantifying mine waste rock physical weathering rate and processes for improved geomorphic post-mining landforms. *Geomorphology*, *463*, 109357.

Wen, G., Hu, J., Wu, Y., Zhang, Z. X., Xu, X., & Xiang, R. (2022). Mechanical properties and failure behavior of dry and water-saturated foliated phyllite under uniaxial compression. *Materials*, *15*, 8962.

Wild, K. M., & Amann, F. (2018). Experimental study of the hydro-mechanical response of Opalinus Clay-Part 1: Pore pressure response and effective geomechanical properties under consideration of confinement and anisotropy. *Engineering Geology*, *237*, 32–41.

Wilson, M. J. (2004). Weathering of the primary rock-forming minerals: processes, products and rates. *Clay minerals*, *39*, 233–266.

Wong, T. F., & Baud, P. (2012). The brittle-ductile transition in porous rock: A review. *Journal of Structural Geology*, *44*, 25–53.

Wu, G., Cui, K., Wang, P., & Chen, W. (2023). Weathering Processes and Mechanisms of Low-Grade Metamorphic Rock following Freeze-Thaw Processes. *Geofluids*, *2023*, 5814341.

Wu, R., Li, H., Li, X., Xia, X., & Liu, L. (2020). Experimental study and numerical simulation of the dynamic behavior of transversely isotropic phyllite. *International Journal of Geomechanics*, *20*, 04020105.

Xia, X., Jiao, X., Li, J., Shen, W., Xia, Y., & Wang, H. (2024). Gas adsorption behavior in shale reservoirs: Insights from molecular scale. *Capillarity*, *13*, 68–72.

Xiao et al. (2024). Systematic paleontology, acritarch biostratigraphy, and δ13C chemostratigraphy of the early Ediacaran Krol A Formation, Lesser Himalaya, northern India. *Journal of Paleontology*, *98*, 159–220.

Xu, G., He, C., Su, A., & Chen, Z. (2018). Experimental investigation of the anisotropic mechanical behavior of phyllite under triaxial compression. *International Journal of Rock Mechanics and Mining Sciences*, *104*, 100–112.

Xue, Y., Kong, F., Li, S., Zhang, L., Zhou, B., Li, G., & Gong, H. (2020). Using indirect testing methods to quickly acquire the rock strength and rock mass classification in tunnel engineering. *International Journal of Geomechanics*, *20*, 05020001.

Xue, Y., Kong, F., Qiu, D., Gong, H., & Ning, Z. (2022). Assessing the effect of grain size or anisotropy on the correlated equations between uniaxial compressive strength and point load test. *Bulletin of Engineering Geology and the Environment*, *81*, 325.

Yang, C., Xiong, Y., Wang, J., Li, Y., & Jiang, W. (2020). Mechanical characterization of shale matrix minerals using phase-positioned nanoindentation and nano-dynamic mechanical analysis. *International Journal of Coal Geology*, *229*, 103571.

Yang, L., Yang, D., Li, Y., Cai, J., & Jiang, X. (2024). Nanoindentation study on microscopic mineral mechanics and bedding characteristics of continental shales. *Energy*, *312*, 133614.

Yang, S., Yang, D., & Kang, Z. (2021). Experimental investigation of the anisotropic evolution of tensile strength of oil shale under real-time high-temperature conditions. *Natural Resources Research*, *30*, 2513–2528.

Yao, Y., Liu, D., Tang, D., Tang, S., & Huang, W. (2008). Fractal characterization of adsorption-pores of coals from North China: An investigation on CH4 adsorption capacity of coals. *International Journal of Coal Geology*, *73*, 27–42.

Yee et al. (2023). Preliminary analysis of rock mass weathering-grade using image analysis of CIELAB color space with the validation of Schmidt hammer: A case study. *Physics and Chemistry of the Earth, Parts a/b/c*, *129*, 103291.

Yu, H., Zhu, Y., Jin, X., Liu, H., & Wu, H. (2019). Multiscale simulations of shale gas transport in micro/nano-porous shale matrix considering pore structure influence. *Journal of Natural Gas Science and Engineering*, *64*, 28–40.

Zeng, L., Zhao, J., Zhu, S., Xiong, W., He, Y., & Chen, J. (2008). Impact of rock anisotropy on fracture development. *Progress in Natural Science*, *18*, 1403–1408.

Zhang, D., Ranjith, P. G., & Perera, M. S. A. (2016). The brittleness indices used in rock mechanics and their application in shale hydraulic fracturing: A review. *Journal of Petroleum Science and Engineering*, *143*, 158–170.

Zhang, G., Wei, Z., & Ferrell, R. E. (2009). Elastic modulus and hardness of muscovite and rectorite determined by nanoindentation. *Applied Clay Science*, *43*, 271–281.

Zhang et al. (2021). Evolution of shale microstructure under *In situ* heat treatment: synchrotron small angle X-ray scattering. *Energy & Fuels*, *35*, 4345–4357.

Zhang, P., Lu, S., Li, J., Wang, J., Zhang, J., & Yin, Y. (2023). Pore structure characterizations of shale oil reservoirs with heat treatment: a case study from dongying sag, Bohai Bay Basin, China. *ACS Omega*, *8*, 26508–26525.

Zhang, S., & Sheng, J. J. (2018). Effect of water imbibition on fracture generation in Mancos shale under isotropic and anisotropic stress conditions. *Journal of Geotechnical and Geoenvironmental Engineering*, *144*, 04017113.

Zhao, J., Jin, Z., Hu, Q., Jin, Z., Barber, T. J., Zhang, Y., & Bleuel, M. (2017). Integrating SANS and fluid-invasion methods to characterize pore structure of typical American shale oil reservoirs. *Scientific Reports*, *7*, 15413.

Zhao, J., Zhang, D., Wu, T., Tang, H., Xuan, Q., Jiang, Z., & Dai, C. (2019). Multiscale approach for mechanical characterization of organic-rich shale and its application. *International Journal of Geomechanics*, *19*, 04018180.

Zhu, J., Deng, J., Ning, P., Fu, Z., Li, X., & Pak, R. Y. (2024). Effects of water saturation and loading condition on rock tensile strength: insights from acoustic emission analysis. *Rock Mechanics and Rock Engineering*, *57*, 163–179.

Zhuoke et al. (2023). High-temperature-induced pore system evolution of immature shale with different total organic carbon contents. *ACS Omega*, *8*, 12773–12786.

Publications in Referred Journal

Publications from Thesis Outcomes

1. **Singh, D.,** Nilankar, K., Singh, H. K., & Ram, B. K. (2025). Impact of Water Saturation on Physico-mechanical Properties of Fragile Chandpur Phyllite at varying Foliation Angles. ***Geotechnical and Geological Engineering***, *43*, 2.
2. **Singh, D.,** Nilankar, K., Ram, B. K., Singh, H. K., Sharma, A., & Srivastava, P. (2025). Influence of Specimen Geometry on the Point Load Strength Anisotropy of Phyllite. ***Geotechnical and Geological Engineering***, *43*, 464.
3. **Singh, D.,** Nilankar, K., Singh, H. K., Kumar, A., Vishal, V., & Mustapha, K. A. (2025). Multiscale Characterization of Pore Evolution in Lesser Himalayan Black Shale from Krol Formation under Oxic Thermal Heating: Relevance to Untapped Shale Gas Extraction. ***Energy & Fuels***, *39*, 11723–11738.
4. Ram, B. K., † **Singh, D.,** † Singh, H. K., Gupta, V., Mishra, D. A., & Kumar, S. (2026). Engineering Properties of Himalayan Rocks: A Comprehensive Review across Tectono-stratigraphic Zones. ***Journal of Earth System Science****, 135,* 110. (†Contributed equally).
5. **Singh, D.,** Singh, H. K., Kumar, A., Mishra, D. A., & Vishal, V. (2026). Pore System Characterization of Untapped Himalayan Shale Using an Integrated Multianalytical Approach: Bridging Nano-to Macro-Scale Investigation. ***Energy & Fuels***, *40*, 4594–4612.
6. **Singh, D.,** Ram, B. K., Singh, H. K., & Nilankar, K. (2026). Multiscale Weathering-grade Classification of Chandpur Phyllite: Insights from *In situ* Observation and Laboratory Investigation. ***Physics and Chemistry of the Earth, Parts A/B/C****, 144*, 104569.
7. **Singh, D.,** Singh, H. K., Srivastava, P., & Kumar, R. (2026). Multiscale Mechanical Characterization of Krol Shale using Brazilian Tensile Strength and Nano-indentation Tests: Implications in Hydrocarbon Recovery and CO_2 Sequestration. ***Energy & Fuels***, *40*, 15699–15715.

Other Publications

1. Nilankar, K., **Singh, D.,** Singh, H. K., & Han, G. (2024). Characterization and behavior of Raniganj shale under heated environment. ***Fuel***, *366*, 131377.
2. Nilankar, K., **Singh, D.,** Singh, H. K., Kumar, A., & Mustapha, K. A. (2024). Evolution of pore morphometry and compositional changes in immature Raniganj Shale under heated environment: Implications for enhanced gas recovery. ***Energy & Fuels***, *38*, 22128–22145.

Divyanshoo Singh (Ph.D.)

Geology (Experimental Rock Mechanics, Geomechanics, Engineering Geology, & Subsurface Energy Resources)
Rajiv Gandhi Institute of Petroleum Technology, Jais, Amethi, Uttar Pradesh, India, 229304
Phone: +91 7054565096
singhdivyanshoo2323@gmail.com & divyanshoos@rgipt.ac.in
https://scholar.google.com/citations?user=I3saGaAAAAAJ&hl=en
https://researchgate.net/profile/Divyanshoo-Singh?ev=hdr_xprf

Education

Ph.D. in *Experimental Rock Mechanics, Geomechanics, Engineering Geology, & Subsurface Energy Resources*, Department of Petroleum Engineering and Geoengineering, Rajiv Gandhi Institute of Petroleum Technology (RGIPT), Jais, India (August 2021 to Present) (***Thesis Submitted on 30th June 2026***).

- **Thesis Topic**: Multiscale Characterization of Anisotropic Rocks with Emphasis on Phyllite and Shale from the Lesser Himalaya, Uttarakhand, India.
- **Supervisor**: Dr. Hemant Kumar Singh, Asst. Professor, RGIPT, Jais.

M.Sc. in *Geology* (Div: **First**), Department of Geology, Hemvati Nandan Bahuguna Garhwal University (HNBGU), Srinagar, Garhwal, Uttarakhand, India (Completed in 2019).

- **Dissertation Topic**: Morphometric analysis of Bal Ganga River (a tributary of Bhilangana) using Remote Sensing and GIS Techniques.
- **Supervisor**: Prof. Harish Chandra Nainwal, Professor, HNBGU, Srinagar.

B.Sc. in *Geology, Physics, and Mathematics* (Div: **First**), University of Lucknow, Lucknow, Uttar Pradesh, India (Completed in 2017).

Research Overview

My doctoral research is focused on a comprehensive multiscale understanding of anisotropic rocks from the Himalayan region by considering the effects of weathering, directional anisotropy, water saturation, specimen geometry, and thermal treatment. I have carried out both in-situ investigation and advanced laboratory characterization to understand the physico-mechanical, mineralogical, morphological, petrographic, and microstructural properties of rocks. The outcomes of the research contribute to safe and sustainable infrastructure development, hydrocarbon recovery, and CO_2 sequestration in the Himalayan region and support the nation's strategic initiatives towards socio-economic development. Beyond my doctoral research, I have a strong interest in the broader fields of Engineering Geology, Geomechanics, Experimental Rock Mechanics, and Subsurface Energy Resources. In the future, I aim to expand my research by applying advanced experimental and analytical techniques to better understand rock behavior for engineering and energy-related applications.

Research Interest

- Experimental Rock Mechanics

- Geomechanics
- Engineering Geology
- Geotechnical Engineering
- Petroleum Geology
- Reservoir Characterization
- Unconventional Energy Resources
- Carbon Capture and Sequestration (CCS)

Publications in Peer-Reviewed Journals:

1. **Singh, D.,** Singh, H. K., Srivastava, P., & Kumar, R. (2026). Multiscale Mechanical Characterization of Krol Shale using Brazilian Tensile Strength and Nano-indentation Tests: Implications in Hydrocarbon Recovery and CO_2 Sequestration. *Energy & Fuels, 40*(29), 15699-15715. https://doi.org/10.1021/acs.energyfuels.6c01829. (***IF 6, Q1***).
2. **Singh, D.,** Ram, B. K., Singh, H. K., & Nilankar, K. (2026). Multiscale weathering grade classification of Chandpur phyllite: Insights from in-situ observation and laboratory investigation. *Physics and Chemistry of the Earth, Parts A/B/C*, *144*, 104569. https://doi.org/10.1016/j.pce.2026.104569. (***IF 4.6, Q1***).
3. Ram, B. K.†, **Singh, D.†,** Singh, H. K., Gupta, V., Mishra, D. A., & Kumar, S. (2026). Engineering properties of Himalayan rocks: a comprehensive review across tectono-stratigraphic zones. *Journal of Earth System Science*, *135*(2), 110. https://doi.org/10.1007/s12040-026-02808-1. (***IF 2.1, Q2***).
4. **Singh, D.,** Singh, H. K., Kumar, A., Mishra, D. A., & Vishal, V. (2026). Pore System Characterization of Untapped Himalayan Shale Using an Integrated Multianalytical Approach: Bridging Nano-to Macro-Scale Investigation. *Energy & Fuels*, *40*(9), 4594-4612. https://doi.org/10.1021/acs.energyfuels.5c06422. (***IF 6, Q1***).
5. **Singh, D.,** Nilankar, K., Ram, B. K., Singh, H. K., Sharma, A., & Srivastava, P. (2025). Influence of Specimen Geometry on the Point Load Strength Anisotropy of Phyllite. *Geotechnical and Geological Engineering*, *43*(8), 464. https://doi.org/10.1007/s10706-025-03485-5. (***IF 3.2, Q1***).
6. **Singh, D.,** Nilankar, K., Singh, H. K., Kumar, A., Vishal, V., & Mustapha, K. A. (2025). Multiscale Characterization of Pore Evolution in Lesser Himalayan Black Shale from Krol Formation under Oxic Thermal Heating: Relevance to Untapped Shale Gas Extraction. *Energy & Fuels*, *39*(24), 11723-11738. https://doi.org/10.1021/acs.energyfuels.5c01632. (***IF 6, Q1***).
7. **Singh, D.,** Nilankar, K., Singh, H. K., & Ram, B. K. (2025). Impact of water saturation on physico-mechanical properties of fragile chandpur phyllite at varying foliation angles. *Geotechnical and Geological Engineering*, *43*(1), 2. https://doi.org/10.1007/s10706-024-02985-0. (***IF 3.2, Q1***).
8. Nilankar, K., **Singh, D.,** Singh, H. K., Kumar, A., & Mustapha, K. A. (2024). Evolution of pore morphometry and compositional changes in immature Raniganj Shale under heated environment: Implications for enhanced gas recovery. *Energy & Fuels*, *38*(22), 22128-22145. https://doi.org/10.1021/acs.energyfuels.4c04095. (***IF 6, Q1***).
9. Nilankar, K., **Singh, D.,** Singh, H. K., & Han, G. (2024). Characterization and behavior of Raniganj shale under heated environment. *Fuel*, *366*, 131377. https://doi.org/10.1016/j.fuel.2024.131377. (***IF 7.8, Q1***).

Book Chapters

1. **Singh, D.,** Nilankar, K., Singh, H. K., Kumar, A., & Pandey, A. (2026). Variations in

Physico-Mechanical Properties of Jodhpur Limestone Under Simulated Acid Rain Condition. In: R. Singh et al. (Eds.): Geosciences for Sustainable World (GSW) 2024. *Springer Proceedings in Earth and Environmental Sciences*. https://doi.org/10.1007/978-3-032-07259-7_27.

Conference Presentations

1. **Singh, D.,** & Singh, H. K. Pore Structure Evolution in Lesser Himalayan Krol Shale under Combustion: Implications for Untapped Shale Gas Recovery. *UrjaVarta-2025*. July 17, 2025.
2. **Singh, D.,** & Singh, H. K. Physico-mechanical Characterization of Precambrian Granite: An Implication to HDR Geothermal Reservoir. *International Conference on Earth: From Archaean to Proterozoic (ICEAP-2024)*. December 19-21, 2024.
3. **Singh, D.,** Nilankar, K., & Singh, H. K. Influence of Water Saturation on Characteristic Behavior of Himalayan Phyllite. *National Geo-Research Scholars Meet (NGRSM-2024)*. November 22-25, 2024.
4. **Singh, D.,** Nilankar, K., & Singh, H. K. (2024). Recommendation of Specimen Geometry in Determining Point Load Strength Index for Anisotropic Rocks. In *ARMA/DGS/SEG International Geomechanics Symposium* (pp. ARMA-IGS). ARMA. November 18-20, 2024. https://doi.org/10.56952/IGS-2024-0303.
5. **Singh, D.,** & Singh, H. K. Thermal Effects on Pore Attributes and Surface Morphology of Lesser Himalayan Shale. *International Conference on Transforming Upstream: Breakthrough Technologies and Sustainability (ICTU-2024)*. September 30-October 01, 2024.
6. **Singh, D.,** Nilankar, K., Singh, H. K., Kumar, A., & Pandey, A. Variations in Physico-Mechanical Properties of Jodhpur Limestone Under Simulated Acid Rain Condition. *National Conference on Geosciences for Sustainable World (GSW-2024)*. March 06-07, 2024.
7. Nilankar, K., **Singh, D.,** & Singh, H. K. A comparative study of Pore attributes between Gondwana Shale and Lesser Himalayan Shale. *National Conference on Geosciences for Sustainable World (GSW-2024)*. March 06-07, 2024.
8. **Singh, D.,** Singh, H. K., & Ansari, T. A. Impact of Normal and Hot Water Saturation on Physico-Mechanical Properties of Fine-grained Sandstone Rock. *International Conference on Geotechnical Issues in Energy, Infrastructure, and Disaster Management (ICGEID-2024)*. January 18-20, 2024.
9. **Singh, D.,** Nilankar, K., & Singh, H. K. Characterization of Himalayan Phyllite with reference to Foliation Planes. *International Conference on Himalayan Environment in Changing Climate Scenario (HECCS-2023)*. September 19-23, 2023.
10. **Singh, D.,** & Singh, H. K. A comprehensive review on the recent development of non-destructive empirical techniques in estimating geo-mechanical properties of shales. *International Conference on Engineering Geology and Geotechniques for safe and sustainable infrastructures (EGCON-2022)*. November 16-17, 2022.

Awards/Fellowships/Academic Achievements

- Awarded the Best Poster Presentation Award in the National Conference on Geosciences for Sustainable World (GSW-2024), held at Banaras Hindu University, Varanasi, Uttar Pradesh, India.

- Awarded a Gold Medal (1st Rank Holder) in Master of Science (M.Sc.) at the overall University level.
- Received the Department of Science and Technology (DST) Inspire Fellowship for pursuing a Ph.D. degree.
- Qualified Graduate Aptitude Test in Engineering (GATE) in the years 2020, 2021, and 2023.

Instruments Handled/Softwares Used

- Skilled in operating instruments like Compression Testing Machine, Triaxial Testing Machine, Point Load Tester, Block Punch Tester, Brazilian Tensile Strength Tester, Schmidt Rebound Hammer, Ultrasonic Pulse Velocity Tester, Tilt Tester, Slake Durability Apparatus, Physical Properties Measurement Setup, Helium Porosimeter, Liquid/Gas Permeameter, Atomic Force Microscope, Optical Microscope, and other rock characterization instruments.
- Experienced in specialized software packages, including MATLAB, OriginPro, ArcGIS Pro, CorelDRAW, X'Pert HighScore, Gwyddion, and ImageJ, for data processing and analysis.
- Proficient in Microsoft Office (MS Word, Excel, PowerPoint) for scientific writing and data analysis.

Academic Responsibilities/Teaching Experiences

- Frequently reviewing research papers for the journals “Scientific Reports”, “Frontiers in Earth Science”, “Earth Science Informatics”, “Marine Geoscience and Energy Resources”, “Carbonates and Evaporites”, etc.
- Engineering Workshop laboratory for first-year B.Tech. Students of RGIPT. Provided practical guidance in basic engineering operations, tool handling, and laboratory safety.
- Geology Practical laboratory for second-year B.Tech. Students of RGIPT. Provided hands-on training in rock and mineral identification, thin-section analysis, etc.

Trainings/Workshops/Internships Attended

- Workshop on Carbon Capture & Storage - From Concepts to Field Implementation, organized by Indian Institute of Science Education and Research, Bhopal. October 13-16, 2025.
- Training Programme on Geotechnical Sampling and Laboratory Techniques, organized by the Geological Survey of India. July 24-30, 2024.
- Workshop on Capacity Building in Scientific Writing & Communication skills, organized by Banaras Hindu University. November 25-30, 2022.
- Workshop on Research-Related Solutions for Faculty and Research Scholars, organized by Rajiv Gandhi Institute of Petroleum Technology. January 31-February 4, 2022.
- Specialized training in structural mapping and various mine visits during geological field work across the Neem Ka Thana and Udaipur area of Rajasthan in M.Sc.
- Hands-on practice in measuring dip and strike of bedding planes and training in rock/mineral sampling during geological field work across the Jabalpur area of Madhya Pradesh in B.Sc.

Professional Memberships

- European Association of Geoscientists & Engineers (EAGE).
- Federation of Indian Petroleum Industry (FIPI).

References:

Dr. Hemant Kumar Singh Department of Petroleum Engineering and Geoengineering, Rajiv Gandhi Institute of Petroleum Technology, Jais Email: hemantks@rgipt.ac.in Mo.: +91 9641186063	**Prof. Deepak Amban Mishra** Department of Petroleum Engineering and Earth Sciences, Indian Institute of Petroleum & Energy, Visakhapatnam Email: dam.geo@iipe.ac.in Mo.: +91 8912856035

Declaration

I hereby declare that the above information is correct to the best of my knowledge.

Date:
Place: Divyanshoo Singh